UNIVERSIDAD COMPLUTENSE DE MADRID

FACULTAD DE CIENCIAS FÍSICAS

TESIS DOCTORAL

Selective contacts for undoped photovoltaic cells fabricated by high-pressure sputtering

Contactos selectivos para células fotovoltaicas sin dopado fabricadas mediante pulverización catódica de alta presión

MEMORIA PARA OPTAR AL GRADO DE DOCTOR

PRESENTADA POR

Francisco José Pérez Zenteno

DIRIGIDA POR

Eric García Hemme
Enrique San Andrés Serrano

© Francisco José Pérez Zenteno, 2025

Universidad Complutense de Madrid

Facultad de Ciencias Físicas

Selective contacts for undoped photovoltaic cells fabricated by high-pressure sputtering

Contactos selectivos para células fotovoltaicas sin dopado fabricadas mediante pulverización catódica de alta presión

---

Francisco José Pérez Zenteno

Supervisors:

Dr. Eric García Hemme

Dr. Enrique San Andrés Serrano

Madrid, 2025

Universidad Complutense de Madrid

Facultad de Ciencias Físicas

Tesis Doctoral

Programa de doctorado en Física

Selective contacts for undoped photovoltaic cell fabricated by high-pressure sputtering

Contactos selectivos para células fotovoltaicas sin dopado fabricadas mediante pulverización catódica de alta presión

Memoria para optar al grado de doctor en física

presentada por

Francisco José Pérez Zenteno

Directores

Dr. Eric García Hemme

Dr. Enrique San Andrés Serrano

Madrid, 2025

A mi familia

AGRADECIMIENTOS

Este trabajo, de cierta manera, es el legado de mis abuelos José Pérez Nava y Concepción Guilló Deza, los cuales se conocieron cuando mi abuelo estaba haciendo su doctorado en la facultad de derecho de la UCM, allá por la década los sesenta del siglo pasado. Él, de origen tlaxcalteca; ella, madrileña; y yo, por ende, una mezcla de ambos. Me siento orgulloso de ser parte de los dos grandes pueblos que dieron origen Nueva España (México). Allá donde quiera que estén, espero que se sientan orgullosos de que su nieto haya seguido la tradición familiar.

Hay muchas otras personas que quiero agradecer ya que de una u otra forma también han influido para la culminación de esta tesis. De antemano pido disculpas si me he olvidado de alguno. Primero que nada, quiero agradecer al grupo de láminas delgadas y microelectrónica de la UCM por haberme tratado tan bien desde el momento que los conocí. Todos ustedes no solo me han enseñado sobre microelectrónica sino también cómo ser un buen investigador. Gracias Rodrigo García, Javier Olea David Pastor, Álvaro del Prado, Ignacio Martil y Germán González. Especial agradecimiento a mis directores de tesis, Eric García y Enrique San Andrés. Fue su exigencia y su excelente calidad como profesores lo que me motivó para hacer un doctorado con ustedes. Agradezco también haber compartido despacho con excelentes personas que hoy considero mis amigos. Por orden cronológico, pero no por eso en importancia: Daniel Caudevilla, Sari Algaidy, Rafael Benítez, Guillermo Godoy y Núria Roca. Con cada uno de ustedes he compartido maravillosos momentos que siempre recordaré. También a Sebastian Duarte Cano que, aunque lo conocí en la universidad como compañero de doctorado se ha vuelto como de mi familia. Otras personas de la UCM con las que siempre estaré agradecido son los técnicos del CAI de *técnicas físicas*, Pablo Fernández Sáez y Rosa Cimas Cuevas. Siempre me recibieron con una sonrisa cuando bajaba a pedirles cualquier servicio. A Fernando Herrera y Antonio Paz que también me ayudaron muchísimo. Y a Mar Gálvez por haberme facilitado toda la burocracia y por las buenas charlas.

Al ser un trabajo netamente experimental, quiero darle las gracias a las siguientes personas que me han ayudado con las medidas experimentales. A José y Laura del CAI *de espectroscopia y correlación* por la medidas de FTIR, a Irene del *Centro Nacional de Investigaciones Metalúrgicas* por las medidas de XPS, a Ignacio del CAI *de difracción de rayos X* por su gran ayuda en GIXRD y XRR, a Isabel del *Laboratorio de Microscopía Avanzada* de la Universidad de Zaragoza por la fabricación de las lamelas. A Adrián del *Centro Nacional de Microscopía Electrónica* por las medidas con TEM. Un agradecimiento muy especial para Rocío y Nacho de la *Unidad de dispositivos energéticos y medioambientales* del *CIEMAT* que sin quienes este trabajo no habría sido posible.

También quiero agradecer a todas las personas del *PV-Lab* de la EPFL que me recibieron de maravilla durante los cuatro meses que estuve en Neuchâtel. Especialmente a Dr. Franz-Josef Haug por haberme aceptado para hacer la estancia y que siempre estuve en la disposición de ayudarme. *Merci beaucoup pour tout.*

A lo largo de estos cinco años también conocido a muchas personas en Madrid que también me han motivado para seguir con este proyecto. Entre ellos quiero agradecer a Andrés Ospina, Miguel Bobonis, José Jauregui, Félix Segura, Oibar Martínez y Lucía Álvarez. Con cada uno de ustedes viví gratos momentos de mi vida en Madrid.

Finalmente, quiero darle las gracias a mi familia que, sin ellos este trabajo nunca hubiera sido posible. A mi tío Antonio, doctor en electrónica, que sin duda influyó en mi para querer estudiar una ingeniería y hacer un doctorado. A mis abuelos materno, Socorro y Antonio que siempre me motivaron y me dieron buenos consejos. A mi hermano Fernando, que para este momento estará comenzando su doctorado en genética y continuando la tradición familiar. A mis primos pequeños, Santiago, Luis, Gerardo y Sofía que espero se puedan inspirar para seguir una carrera de ciencias. Y a mis padres, Edith y Francisco que siempre han sido un ejemplo para mí. Sin ustedes, nunca hubiera llegado hasta aquí.

Francisco J. Pérez Zenteno

ABSTRACT

The most widely adopted silicon solar cell architectures, such as TOPCon and HJT, rely on doped layers to serve as carrier-selective contacts that facilitate the extraction of photogenerated charge carriers. However, the fabrication of these doped layers typically requires high-temperature processes and the use of toxic precursor gases (e.g., $POCl_3$, PH_3, or BBr_3), which increase manufacturing complexity and require strict safety protocols. From a technological perspective, heavily doped silicon layers generally exhibit relatively low bandgaps, which lead to parasitic optical absorption, particularly in the short-wavelength range. In addition, high doping concentrations can enhance Auger recombination, contributing to increased recombination losses. Both effects ultimately reduce the efficiency of the solar cell. Therefore, the investigation of undoped wide-bandgap materials as selective contacts presents a promising strategy to enhance device performance while simplifying the fabrication process and improving environmental compatibility.

The main objective of this thesis was the fabrication and characterization of dopant-free carrier-selective contacts for c-Si solar cells. For this, the uncommon technique of high-pressure sputtering (HPS) was used as deposition method. Two materials were studied during this work: indium tin oxide (ITO) as a transparent conductive oxide (TCO) and titanium oxide (TiO_x) as an electron-selective contact (ESC). HPS is characterized by a significantly higher working pressure than conventional sputtering. During this thesis, the working pressure in HPS was in the 1 mbar range. Such working pressure leads to sputtered particles with a lower kinetic energy that can reduce the ion bombardment damage of the substrate. Potentially, this can translate into heterojunctions with a lower interfacial density of defects, which is key to obtaining high-quality solar cells.

Although TiO_x and ITO have been studied for photovoltaic applications, their structural, optical, and electrical properties are highly dependent on the deposition technique employed. Parameters such as crystallinity, stoichiometry, defect density, and carrier concentration can vary significantly between methods like sol-gel, atomic layer deposition (ALD), conventional sputtering, and pulsed laser deposition (PLD). These variations directly impact the material's performance as transparent electrodes or carrier-selective contacts in solar cell architectures. In this context, HPS emerges as an alternative technique with unique features, most notably, the thermalization of sputtered species due to the high working pressure. This results in low-energy particle flux that enables the deposition of uniform and low-damage films at low temperatures. Investigating the properties of TiO_x and ITO deposited by HPS is thus essential to assess their viability in low-temperature solar cell fabrication routes.

To evaluate the suitability of TiO_x and ITO as electron-selective contacts and transparent conductive oxides in silicon solar cells, several key parameters must be studied. The specific contact resistivity

(ρ_c) provides information on the efficiency of majority carrier extraction at the interface, while the minority carrier lifetime (τ_{eff}) reflects the level of recombination losses introduced by the material. For TCO applications, a high transparency in the visible light range is essential to ensure efficient light transmission to the absorber layer, and a low sheet resistance is required to achieve lateral conduction of photogenerated carriers. Together, these parameters offer a better understanding of the optoelectronic performance of the material and its potential integration in high-efficiency solar cell architectures.

For the electrical characterization, several techniques were employed. The four-point probes method for obtaining the sheet resistance, Hall effect measurements (with van der Pauw configuration) to measure the mobility and carrier concentration, transfer length method (TLM) and Cox & Strack method (C&S) to obtain the specific contact resistivity. For the optical characterization ellipsometry was used to determine refractive index and film thickness, and spectrophotometry in UV-Vis-NIR to measure the transmittance, reflectance and absorptance of the films. The band gap was also calculated through the Tauc's plot fitting. Finally, the structural characterization of TiOx and ITO thin films was carried out using several complementary techniques. X-ray photoelectron spectroscopy (XPS) was employed to determine the elemental composition and stoichiometry of the films. Grazing incidence X-ray diffraction (GIXRD) was used to assess the crystallographic nature of the layers, distinguishing between amorphous and polycrystalline phases. Fourier transform infrared spectroscopy (FTIR) provided information on the vibrational modes and chemical bonding within the films. Transmission electron microscopy (TEM) was also conducted to obtain high-resolution images of the film morphology and microstructure. Regarding the passivation, photoconductance measurements (quasi-steady state) were used to obtain the minority carrier lifetime, the implied open-circuit voltage and the recombination current density of the samples.

For the ITO films, different working pressures were investigated. It was observed that higher working pressures promoted the formation of amorphous films with low resistivity values on the order of $\sim 10^{-4}$ Ωcm and relatively high carrier mobility (~40 cm^2/Vs). In contrast, parameters such as the Sn/In atomic ratio, optical transmittance in the visible range, and optical bandgap showed minimal variation with changes in working pressure, indicating that the electrical improvements were primarily related to morphological or microstructural changes rather than compositional or optical modifications.

TiO_x films were deposited using a two-step process consisting of the deposition of a thin metallic Ti layer followed by low-temperature plasma oxidation to form the TiO_x layer. This approach was found to significantly reduce the oxidation of the silicon surface compared to direct TiO_x deposition (i.e., without the Ti capping layer), which is critical for achieving low specific contact resistivity at the heterojunction interface. Substrate temperatures of 150 °C and 200 °C were investigated, along with varying oxidation durations ranging from 15 minutes to 2 hours. While extended oxidation times led

to the appearance of certain crystalline planes, the TiO_x films remained predominantly amorphous. Both the specific contact resistivity and the effective minority carrier lifetime exhibited dependencies on the oxidation conditions, indicating the importance of fine-tuning the process parameters for optimal electronic performance.

Using the best films, heterojunction solar cell prototypes were fabricated incorporating either ITO as transparent conductive oxide (TCO) or TiO_x as the electron-selective contact (ESC).The illuminated current-voltage (IV) characteristics were measured, and the key photovoltaic parameters were extracted. Additionally, the external quantum efficiency (EQE) of the solar cells was measured to evaluate the spectral response and carrier collection efficiency across different wavelengths.

In addition to ITO deposited by HPS, this thesis also explores the use of hydrogenated indium tin oxide (ITO:H) deposited by standard RF sputtering as a multifunctional passivating-TCO layer. The motivation lies in the possibility of integrating ITO:H into TOPCon architectures to reduce the number of processing steps. Typically, hydrogenation in such devices is achieved through a SiN_x:H capping layer and a subsequent high-temperature firing step, followed by HF etching prior to TCO deposition. ITO:H, on the other hand, can serve both as a transparent conducting electrode and as a hydrogen reservoir for defect passivation, thereby eliminating the need for separate hydrogenation and etching steps. Experimental results show that ITO:H films deposited with optimized O_2 and H_2 gas flows exhibit low resistivity (~10^{-3} Ωcm) and good optical transparency. Annealing processes at 400 °C for 20 - 90 minutes enable effective hydrogen diffusion into poly-Si(n)/c-Si(n) structures. This leads to significant improvements in minority carrier lifetime (>5 ms), implied V_{oc} (>720 mV), and reduced recombination current densities ($J_0 \approx 4$ fA·cm^{-2}), validating the dual functionality of ITO:H in passivating contact solar cell architectures.

In summary, this thesis investigates the potential of using HPS for fabricating TiOx and ITO layers as dopant-free selective contacts in c-Si solar cells, while also proposing an alternative approach using RF-sputtered ITO:H as a passivating-TCO to simplify and improve the fabrication of TOPCon devices.

RESUMEN

Las arquitecturas de célula solar de silicio más ampliamente utilizadas, como TOPCon y HJT, se basan en capas dopadas que actúan como contactos selectivos para facilitar la extracción de cargas fotogeneradas. Sin embargo, la fabricación de estas capas dopadas generalmente requiere procesos a alta temperatura y el uso de gases precursores tóxicos (por ejemplo, $POCl_3$, PH_3 o BBr_3), lo que incrementa la complejidad del proceso de fabricación y exige estrictos protocolos de seguridad. Desde una perspectiva tecnológica, las capas de silicio fuertemente dopado presentan en general bandas prohibidas relativamente bajas, lo que conduce a una absorción óptica parasitaria, particularmente en el rango de longitud de onda corta. Además, altas concentraciones de dopado pueden potenciar la recombinación Auger, contribuyendo a un aumento de las pérdidas por recombinación. Ambos efectos reducen finalmente la eficiencia de la célula solar. Por tanto, la investigación de materiales no dopados con bandas prohibidas amplias como contactos selectivos representa una estrategia prometedora para mejorar el rendimiento del dispositivo, simplificar su fabricación y aumentar su compatibilidad medioambiental.

El objetivo principal de esta tesis fue la fabricación y caracterización de contactos selectivos de portadores sin dopado para células solares de silicio cristalino (c-Si). Para ello, se empleó la técnica poco común de pulverización catódica a alta presión (HPS, por sus siglas en inglés) como método de depósito. Durante este trabajo se estudiaron dos materiales: el óxido de indio y estaño (ITO) como óxido conductor transparente (TCO) y el óxido de titanio (TiO_x) como contacto selectivo de electrones (ESC). La HPS se caracteriza por trabajar a una presión significativamente superior a la pulverización convencional. En esta tesis, la presión de trabajo estuvo en el orden de 1 mbar. Esta elevada presión provoca que las especies pulverizadas tengan una menor energía cinética, lo que puede reducir el daño por bombardeo iónico sobre el sustrato. Potencialmente, esto se traduce en heterouniones con una menor densidad de defectos interfaciales, lo cual es clave para lograr células solares de alta calidad.

Aunque el ITO y el TiO_x han sido ampliamente estudiados para aplicaciones fotovoltaicas, sus propiedades estructurales, ópticas y eléctricas dependen fuertemente de la técnica de depósito empleada. Parámetros como la cristalinidad, estequiometría, densidad de defectos y concentración de portadores pueden variar significativamente entre métodos como sol-gel, depósito por capas atómicas (ALD), pulverización convencional (Sputtering) y depósito por láser pulsado (PLD). Estas variaciones impactan directamente en el rendimiento del material como electrodo transparente o como contacto selectivo de portadores en arquitecturas de células solares. En este contexto, la HPS emerge como una técnica alternativa con características particulares, destacando la termalización de las especies pulverizadas debido a la elevada presión de trabajo. Esto da lugar a un flujo de partículas de baja energía que permite el depósito de capas uniformes y con bajo daño a bajas temperaturas.

Para evaluar la idoneidad del TiO_x y del ITO como contactos selectivos de electrones y óxidos conductores transparentes en células solares de silicio, deben estudiarse varios parámetros clave. La resistividad de contacto específica (ρ_c) proporciona información sobre la eficiencia en la extracción de portadores mayoritarios en la interfaz, mientras que el tiempo de vida de los portadores minoritarios (τ_{eff}) refleja el nivel de pérdidas por recombinación introducidas por el material. En aplicaciones como TCO, se requiere una alta transmitancia en el rango visible para garantizar una eficiente transmisión de luz hacia la capa absorbente, así como una baja resistencia en hoja para lograr la conducción lateral de los portadores fotogenerados. En conjunto, estos parámetros permiten comprender mejor el desempeño optoelectrónico del material y su posible integración en arquitecturas de células solares de alta eficiencia.

Para la caracterización eléctrica se utilizaron diversas técnicas: el método de las cuatro puntas alineadas para obtener la resistencia en hoja, medidas de efecto Hall (con configuración van der Pauw) para determinar la movilidad y la concentración de portadores, el método de longitud de transferencia (TLM) y el método de Cox & Strack para obtener la resistividad de contacto específica. Para la caracterización óptica se empleó elipsometría para determinar el índice de refracción y el espesor de las capas, y espectrofotometría UV-Vis-NIR para medir la transmitancia, reflectancia y absortancia de las láminas. El ancho de la banda prohibida se estimó mediante ajuste con el método de Tauc. Finalmente, la caracterización estructural del TiO_x y del ITO se realizó mediante técnicas complementarias: la espectroscopía de fotoelectrones de rayos X (XPS) para determinar la composición elemental y estequiometría, la difracción de rayos X en incidencia rasante (GIXRD) para evaluar la naturaleza cristalográfica de las capas, la espectroscopía infrarroja por transformada de Fourier (FTIR) para analizar los modos vibracionales y enlaces químicos, y microscopía electrónica de transmisión (TEM) para obtener imágenes de alta resolución de la morfología y microestructura de las capas. Para evaluar la pasivación, se emplearon medidas de fotoconductancia en régimen cuasi estacionario para obtener el tiempo de vida de portadores minoritarios, la tensión de circuito abierto implícita y la densidad de corriente de recombinación.

En el caso del ITO, se investigaron diferentes presiones de trabajo. Se observó que presiones de trabajo más elevadas promovían la formación de películas amorfas con valores de resistividad bajos ($\sim 10^{-4}$ Ωcm) y una movilidad de portadores relativamente alta (~ 40 cm^2/Vs). En contraste, parámetros como la relación Sn/In, la transmitancia óptica en el rango visible y el ancho de banda prohibida mostraron variaciones mínimas con la presión, lo que indica que las mejoras eléctricas se debieron principalmente a cambios morfológicos o microestructurales y no tanto a modificaciones composicionales u ópticas.

Las láminas de TiO_x se depositaron mediante un proceso en dos etapas: depósito de una delgada capa metálica de Ti seguida por una oxidación con plasma a baja temperatura para formar el TiO_x. Este

enfoque demostró reducir significativamente la oxidación de la superficie de silicio en comparación con el depósito directo de TiO_x (sin capa de Ti), lo cual es fundamental para lograr una baja resistividad de contacto específica en la interfaz de la heterounión. Se estudiaron temperaturas del sustrato de 150 °C y 200 °C, junto con tiempos de oxidación que variaron entre 15 minutos y 2 horas. Aunque los tiempos de oxidación prolongados condujeron a la aparición de ciertos planos cristalinos, las películas de TiO_x se mantuvieron mayoritariamente amorfas. Tanto la resistividad de contacto específica como el tiempo de vida efectivo mostraron dependencia con las condiciones de oxidación, lo que resalta la importancia de afinar los parámetros del proceso para optimizar el desempeño electrónico.

Utilizando las mejores láminas, se fabricaron prototipos de células solares de heterounión que incorporaron ITO como TCO o TiO_x como contacto selectivo de electrones. Se midieron las curvas corriente-voltaje (IV) bajo iluminación y se extrajeron los parámetros fotovoltaicos clave. Adicionalmente, se midió la eficiencia cuántica externa (EQE) de las células para evaluar la respuesta espectral y la eficiencia de recolección de portadores a diferentes longitudes de onda.

Además del ITO depositado por HPS, esta tesis explora también el uso de óxido de indio y estaño hidrogenado (ITO:H) depositado mediante pulverización RF convencional como una capa TCO pasivante multifuncional. La motivación radica en la posibilidad de integrar el ITO:H en arquitecturas TOPCon para reducir el número de etapas de procesamiento. Típicamente, la hidrogenación en estos dispositivos se realiza mediante una capa de SiN_x:H seguida de un tratamiento térmico a alta temperatura, tras el cual se elimina el SiN_x mediante HF antes de depositar el TCO. El ITO:H, en cambio, puede cumplir simultáneamente la función de electrodo transparente conductor y de reservorio de hidrógeno para pasivar defectos, eliminando así la necesidad de pasos separados de hidrogenación y limpieza con HF. Los resultados experimentales muestran que las láminas de ITO:H depositadas con flujos optimizados de O_2 y H_2 presentan baja resistividad ($\sim 10^{-3}$ Ωcm) y buena transparencia óptica. Procesos de recocido a 400 °C durante 20 a 90 minutos permiten una difusión efectiva de hidrógeno hacia estructuras de tipo poly-Si(n)/c-Si(n), lo que conduce a mejoras significativas en el tiempo de vida de portadores minoritarios (>5 ms), la tensión de circuito abierto implícita (>720 mV) y la reducción de la densidad de corriente de recombinación ($J_0 \approx 4$ fA·cm^{-2}), validando la funcionalidad dual del ITO:H en arquitecturas con contacto pasivante.

En resumen, esta tesis investiga el potencial del uso de la HPS para fabricar capas de TiO_x e ITO como contactos selectivos sin dopado para células solares de silicio cristalino, y propone además un enfoque alternativo basado en ITO:H depositado por sputtering RF como capa TCO pasivante para simplificar y mejorar la fabricación de dispositivos TOPCon.

Content

AGRADECIMIENTOS .... **I**

ABSTRACT .... **III**

RESUMEN .... **VI**

CHAPTER I: INTRODUCTION **1**

1.1 Climate emergency and photovoltaics 1

1.2 Solar cells and their limitations 3

1.2.1 Solar cell characterization *5*

1.2.2 Main loss mechanisms in c-Si solar cells *8*

1.3 Solar cell architecture 13

1.3.1 Perovskite – Silicon tandem solar cells *16*

1.3.2 Dopant-free asymmetric heterocontact (DASH) solar cells *18*

1.4 Transparent conductive oxides in solar cells 19

1.4.1 Indium tin oxide (ITO) *21*

1.4.2 Hydrogenated indium tin oxide (ITO:H) for solar cell applications *22*

1.5 Selective contacts in Si-based heterojunction solar cells 23

1.5.1 Physical origin of selectivity *23*

1.5.2 Materials acting as carrier selective contacts *26*

1.5.3 Titanium oxide (TiO_x) as selective contact *28*

1.6 High-pressure sputtering 29

1.7 Motivation and objectives 31

1.8 Thesis structure 32

1.9 References 34

CHAPTER II: FABRICATION TECHNIQUES **41**

2.1 Substrates 41

2.2 Substrate Cleaning Process 41

2.3 Sputtering 43

2.3.1 Reactive sputtering *43*

2.3.2 RF sputtering *45*

2.4 High-Pressure Sputtering (HPS) 46

2.5 Ion Implantation 48

2.5.1 Rapid Thermal Annealing *51*

2.6 Thermal/Electron-beam Evaporator 52

2.7 Plasma Enhanced Chemical Vapor Deposition (PECVD) 53

2.8 Photolithography 56

2.9 Flash Lamp Annealing 58

2.10 Reference 59

CHAPTER III: CHARACTERIZATION TECHNIQUES **62**

3.1 Plasma characterization 62

3.1.1 Optical Emission Spectroscopy (OES) *62*

3.2 Structural characterization ... 63
3.2.1 Profilometer ... 63
3.2.2 X-ray photoemission spectroscopy (XPS) ... 64
3.2.3 Grazing Incidence X-ray diffraction (GIXRD) ... 66
3.2.4 Transmission Electron Microscopy (TEM) ... 67
3.3 Electrical characterization ... 68
3.3.1 Four-point probe ... 68
3.3.2 Hall effect and the van der Pauw configuration ... 70
3.3.3 Transfer Length Method (TLM) ... 73
3.3.4 Cox & Strack Method (CSM) ... 74
3.3.5 Photoconductance ... 77
3.3.6 Current-voltage characteristics of solar cell ... 79
3.4 Optical characterization ... 80
3.4.1 Ellipsometry ... 80
3.4.2 UV-Vis-IR Spectrophotometry ... 81
3.4.3 Fourier Transform Infrared Spectroscopy (FTIR) ... 82
3.4.4 Photoluminescence (PL) ... 83
3.5 References ... 84
CHAPTER IV: ITO DEPOSITED BY HIGH-PRESSURE SPUTTERING ... 87
4.1 Structural and electrical characterization of ITO deposited by high-pressure sputtering ... 87
4.2 Optical characterization of ITO deposited by high-pressure sputtering ... 93
4.3 Electrical and optical characterization of a-Si:H(i)/ITO ... 95
4.4 Si heterojunction solar cell with ITO deposited by high-pressure sputtering ... 98
4.5 Summary and conclusions ... 102
4.6 References ... 103
CHAPTER V: ITO:H DEPOSITED BY RF SPUTTERING ... 106
5.1 Motivation ... 106
5.2 Experimental results ... 106
5.2.1 Characterization of ITO deposited with Ar atmosphere ... 108
5.2.2 Characterization of ITO deposited with Ar/O_2 atmosphere ... 112
5.2.3 Characterization of ITO deposited with Ar/O_2/H_2 atmosphere ... 117
5.2.4 ITO:H films (~80 nm) on poly-Si(n)/c-Si(n) junctions ... 127
5.2.5 Summary and conclusions ... 133
5.3 References ... 135
CHAPTER VI: TiO_X DEPOSITED BY HIGH-PRESSURE SPUTTERING USING LOW-TEMPERATURE OXYGEN PLASMA ... 137
6.1 Characterization of Ti deposition with high-pressure sputtering ... 137
6.2 Oxidation of Ti thin film through low-temperature O_2 plasma ... 139
6.3 Structural characterization of TiO_x fabricated by the two-step oxidation process ... 142
6.4 Optical characterization of TiO_x fabricated by the two-step oxidation process ... 151

6.5 Minority carrier lifetime measurements of Si/TiO_x and Si/SiO_x/TiO_x by quasi-steady state photoconductance ... 156
6.6 Optimization of the rear contact for Cox & Strack samples for determining the contact resistivity of Si(n)/TiO_x junction. ... 161
6.7 Extraction of contact resistivity of c-Si(n)/TiO_x and c-Si(n)/SiO_x/TiO_x by Cox & Strack method.... 165
6.8 Summary and conclusions ... 168
6.9 References ... 169
CHAPTER VII: TIO_X/A-SI:H(I) AS ELECTRON SELECTIVE CONTACT FOR SI HETEROJUNCTION SOLAR CELL 174
7.1 Minority carrier lifetime and contact resistivity measurements of TiO_x/a-Si:H(i) (~ 10 nm) ... 174
7.2 Minority carrier lifetime measurements of TiO_x/a-Si:H(i) (~ 7 nm) ... 178
7.3 Flash Lamp Annealing process of a-Si:H(i) and TiO_x/a-Si:H(i) samples ... 182
7.4 Heterojunction solar cell with TiO_x as electron-selective contact ... 184
7.4.1 Evolution of J_{sc}, V_{oc}, FF, efficiency and resistances with low temperature annealing steps. ... 185
7.4.2 Comparison between Si solar cells with TiO_x as ESC and HIT solar cell ... 188
7.5 Summary and conclusions ... 192
7.6 References ... 193
CHAPTER VIII: SUMMARY, CONCLUSIONS, AND FUTURE WORK ... 196
8.1 Conclusions ... 197
8.1.1 ITO deposited by HPS: ... 197
8.1.2 ITO:H deposited by RF sputtering: ... 197
8.1.3 TiO_x deposited by HPS: ... 198
8.1.4 HPS - TiO_x with a-Si:H(i) passivating layer: ... 199
8.2 Future work ... 200
LIST OF PUBLICATIONS ... 201
9.1 Journal papers ... 201
9.1.1 Related to this thesis ... 201
9.1.2 Others ... 202
9.2 Contributions in conferences ... 204

CHAPTER I: INTRODUCTION

1.1 Climate emergency and photovoltaics

The global warming emergency is becoming one of the most pressing issues for all societies. The Intergovernmental Panel on Climate Change (IPCC) from the United Nations has promoted actions to reduce global warming below 1.5 ºC in comparison to the preindustrial era by 2030 [1]. Unfortunately, the current trend is not very encouraging for achieving this goal, mainly due to insufficient actions. According to the 2023 IPCC report, it is more likely that the mean global temperature will exceed 1.5 ºC within the 2030s if no extensive actions are taken [2]. One of the main problems is the still-growing emission of anthropogenic greenhouse gas (GHG), mainly CO_2, from transport and industry, as it can be seen in Figure 1-1.

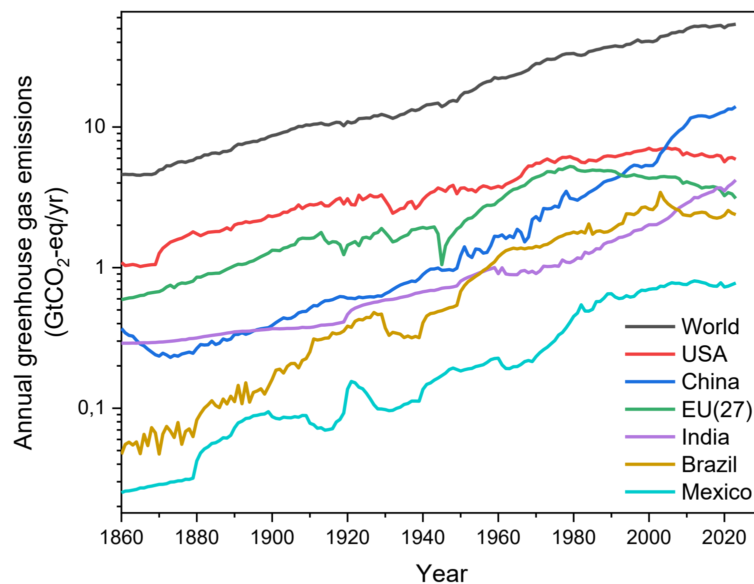

Figure 1-1 Annual greenhouse gas emissions per year for different countries. Data from [3]

A greater penetration of renewable energy sources in the energy mix is now a reality that can mitigate the effects of global warming. Among all the renewable energy sources, solar PV stands out as the spearhead of the energy transition. In many countries, the levelized cost of energy (LCOE) of solar PV

is already the lowest among all technologies. The mean LCOE around the world for PV has reduced from 0.46 $/kWh to 0.04 $/kWh in the last decade [4], as it is depicted in the following graph.

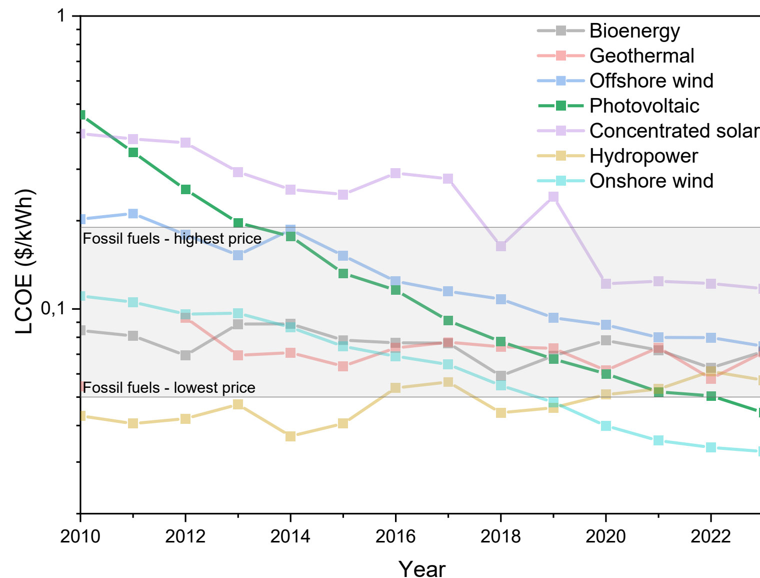

Figure 1-2 Evolution of global average levelized cost of energy (LCOE) for different renewable energy sources. The grey band shows the range of fossil fuel-fired power generation cost in 2023. Data from [4]

For that reason, research on PV technology plays a crucial role in further reducing the LCOE, which remains a key metric for evaluating the economic competitiveness of energy sources. Achieving a lower LCOE can be pursued through multiple complementary strategies. For instance, increasing the power conversion efficiency enables more electricity to be generated from the same area, directly impacting energy yield. Reducing fabrication costs (whether through material optimization, simpler processing steps, or scalable manufacturing techniques) can significantly lower capital expenditures. Extending the operational lifetime of PV modules enhances the system's cost-effectiveness over time, as the initial investment is amortized over a longer period of energy production. Or even exploring novel approaches to minimize material consumption during solar cell fabrication. Together, these approaches contribute to making solar energy more affordable, accessible, and sustainable on a global scale.

By the end of 2024, the cumulative installed photovoltaic capacity worldwide had surpassed 2.2 TW, following a record addition of between 554 GW and 602 GW during the year, representing an annual growth rate of approximately 30% [5]. China alone accounted for 357 GW of new installations, contributing to nearly 60% of the global capacity additions. Other leading markets were the European Union (62.6 GW), the United States (47.1 GW), and India (31.9 GW) [5]. In early 2025, China's cumulative solar capacity surpassed 1 TW, accounting for nearly half of the global total capacity [6].

Projections by organizations such as Solar Power Europe anticipate further acceleration, forecasting 655 GW of solar power expected to be added globally by 2025 [7]. This exponential growth consolidates PV as the most rapidly deployed renewable energy technology, highlighting its increasing role in the global energy transition toward a low-carbon future.

1.2 Solar cells and their limitations

Ever since the first solar cell was developed in the 1950s, the research on PV has accomplished astonishing improvements in efficiency, from the first Si solar cell with only 6% [8] to 33.8 % with Si/Perovskite tandems fabricated by *Longi* [9]; or even as high as 47.6% for III-V semiconductor multijunction under concentration [10]. This development has been made possible by a better understanding of the physical phenomena that governs the operation of a solar cell.

The basic operating principle of a solar cell relies on the photovoltaic effect in a semiconductor material, typically crystalline silicon. When the material absorbs photons with energies equal to or greater than its bandgap energy (E_{gap}), electrons in the valence band are excited to the conduction band, leaving behind holes in the valence band. This process results in the generation of electron–hole pairs. These charge carriers are then separated by the electrochemical gradient of the device and subsequently transported to the respective electrodes. Once collected at the external contacts, the carriers give rise to a photocurrent, thereby converting the absorbed solar energy into usable electrical power.

In equilibrium conduction, i.e., under no illumination, a semiconductor is described by the electron (n_0) and hole concentration (p_0) through the law of mass action ($n_0 p_0 = n_i^2$). In turn, the electron and hole concentrations are described by the following expressions:

$$n = n_0 = N_c e^{-\left(\frac{E_F - E_c}{k_B T}\right)}$$
$$p = p_0 = N_v e^{-\left(\frac{E_v - E_F}{k_B T}\right)} \quad 1.1$$

Where N_C and N_V are the densities of states for the conduction and valence bands, respectively. E_C and E_V are the conduction and valence band energies, E_F is the Fermi level, k_B is the Boltzmann constant, and T is the temperature of the semiconductor.

Under illumination, the semiconductor transitions into a non-equilibrium state in which excess electrons (Δn) and holes (Δp) are generated. As a result, the Fermi level splits into two distinct quasi-Fermi levels: one for electrons (E_{Fn}) and one for holes (E_{Fp}). This separation reflects the different carrier populations, and the following expressions describe it:

$$n = n_0 + \Delta n = N_c e^{-\left(\frac{E_{Fn}-E_c}{k_B T}\right)}$$

$$p = p_0 + \Delta p = N_v e^{-\left(\frac{E_v-E_{Fp}}{k_B T}\right)} \tag{1.2}$$

The concept of quasi-Fermi levels plays a fundamental role in solar cell design, as the energy separation between the electron and hole quasi-Fermi levels determines the theoretical limit of the implied open circuit voltage ($i\text{-}V_{oc}$).

$$iV_{oc} = \frac{E_{Fn}-E_{Fp}}{q} = \frac{k_B T}{q} ln\left(\frac{(n_0 + \Delta n)(p_0 + \Delta p)}{n_i^2}\right) \tag{1.3}$$

Where q is the elementary charge.

Historically, the separation of photogenerated charge carriers has been primarily attributed to the action of an internal electric field, such as that established in a pn junction [8]. However, the underlying physics of charge separation is more complex. As discussed by Würfel [11], carrier transport must account for the motion due to electric field (drift) and concentration gradient (diffusion), or via quasi-Fermi level gradient which unifies both effects. In this context, the most comprehensive expression describing charge carrier flow is given by the generalized current density equation expressed in terms of quasi-Fermi levels [12]:

$$j_n = q\mu_n n \frac{d\phi}{dx} + qD_n \frac{dn}{dx} = \mu_n n \frac{dE_{Fn}}{dx}$$

$$j_p = q\mu_p p \frac{d\phi}{dx} - qD_p \frac{dp}{dx} = \mu_p p \frac{dE_{Fp}}{dx} \tag{1.4}$$

$$j_{total} = j_n + j_p = \frac{\sigma_n}{q}\frac{dE_{Fn}}{dx} + \frac{\sigma_p}{q}\frac{dE_{Fp}}{dx}$$

Where D_n and D_p are the diffusion coefficients, $\frac{dn}{dx}$ and $\frac{dp}{dx}$ are the carrier concentration gradients, μ_n and μ_p are the carrier mobilities, $\frac{d\phi}{dx}$ is the electrostatic potential gradient, σ_n and σ_p are the carrier conductivities, $\frac{dE_{Fn}}{dx}$ and $\frac{dE_{Fp}}{dx}$ are the quasi-Fermi levels gradients.

1.2.1 Solar cell characterization

To characterize the performance of a solar cells, the characteristic JV curve should be measured under standard conditions. The most typical condition is the AM1.5G, which is the most used reference spectrum for terrestrial solar cell testing, particularly in Europe and North America. It represents the average solar spectral irradiance received at the Earth's surface at mid-latitudes. It assumes a global irradiance (direct + diffuse sunlight) of 1000 W/m^2, and a cell temperature of 25 ºC.

The simplest description of a solar cell can be done with the one-diode model:

$$j(V) = j_L - j_0\left(e^{\frac{qV}{nk_BT}} - 1\right) \tag{1.5}$$

Where j_L is the light-generated current density, j_0 is the reverse saturation current density, V is the voltage across the solar cell, n is the ideality diode factor with a typical value 1 for diffusion-dominated mechanism, k_B is the Boltzmann constant, T is the temperature of the solar cell, and q is the elementary charge.

Although, the one-diode model is simple to implement, this does not include the recombination that takes place in the depletion region (p-n junction). For that reason, a more accurate description can be done by the two-diode model which can also include the influences of series (Rs) and parallel resistance (R_p).

$$j(V) = j_L - j_{01}\left(e^{\frac{qV-j(V)R_s}{n_1k_BT}} - 1\right) - j_{02}\left(e^{\frac{qV-j(V)R_s}{n_2k_BT}} - 1\right) - \frac{V - j(V)R_s}{R_p} \tag{1.6}$$

In this expression, the $j(V)$ is an implicit term, and thus numerical methods are required for solving. The terms j_{01} and j_{02} are the saturation current densities of the diffusion mechanism (bulk) and recombination in the depletion region (Shockley-Read-Hall recombination), respectively, n_1 and n_2 are the ideality factors for both mechanisms, typically $n_1 = 1$ and $n_2 = 2$. The electrical circuit that represents equation 1.6 is shown in Figure 1-3.

Rs accounts for all the possible ohmic losses in the devices, i.e., resistance from the bulk, contact resistance between different materials, and metal grid resistance. While the Rp is associated to pinholes, grain boundaries, or other leakage paths that allow current to bypass the p-n junction.

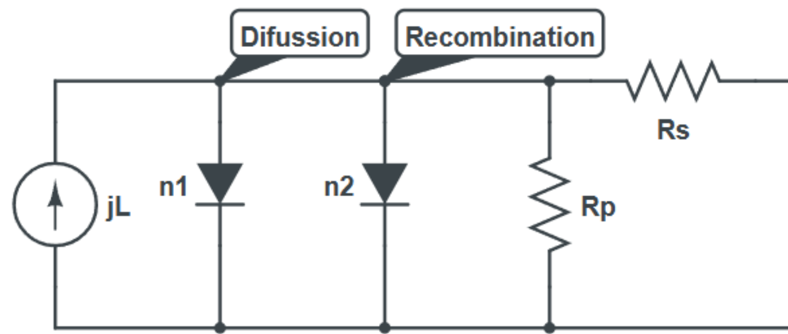

Figure 1-3 Circuit diagram of the double diode model including the parasitic series (R_s) and parallel resistances (R_p)

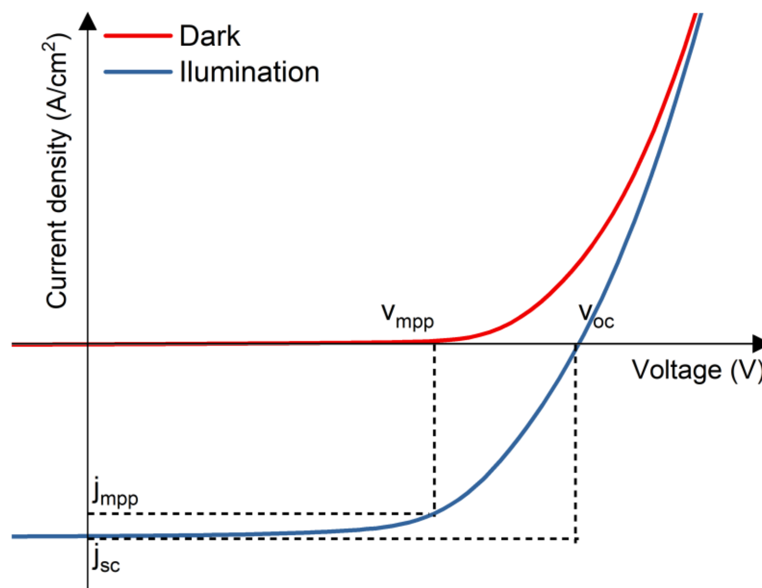

Figure 1-4 JV curve of a solar cell measured in darkness and under illumination.

The most important parameters of a solar cell can be extracted from its current-voltage (JV) curve, as shown in Figure 1-4. To obtain this curve, the solar cell is swept over a range of voltages while measuring the corresponding current, typically using a source-measure unit (SMU).

Short circuit current density (j_{sc}): This is the maximum obtained current from a solar cell when the voltage is zero. In an ideal solar cell with $R_s = 0$ and $R_p = \infty$, the short circuit current density is identical to the photogenerated current. This can be affected by different factors such as the active area of the cell (shading), the light intensity, and optical properties (parasitic absorption and reflection). For Si solar cells under AM1.5G (standard conditions) the maximum j_{sc} that can be obtained is 42 mA/cm^2 [13].

Open circuit voltage (V_{oc}): This is the maximum voltage that is obtained when there is no current flowing through the external circuit. From the one-diode model, V_{oc} is obtained with the following expression:

$$V_{oc} = \frac{k_B T}{q} \ln\left(\frac{j_{sc}}{j_0} + 1\right) \quad 1.7$$

From this expression, it is evident that V_{oc} is highly sensitive to the reverse saturation current density (j_0), which is directly influenced by the recombination processes within the solar cell. Therefore, the value of V_{oc} serves as an indicator of the effectiveness of surface and bulk passivation. In laboratory, high-quality Si solar cells can achieve V_{oc} value up to 764 mV under standard conditions [14].

Fill factor (FF): This describes the ratio between the maximum power ($P_{mpp} = j_{mpp} V_{mpp}$) and the product of V_{oc} and j_{sc}.

$$FF = \frac{V_{mpp} j_{mpp}}{V_{oc} j_{sc}} \quad 1.8$$

Considering that the JV curve follows the one-diode model, the FF can also be described by the following expression [13].

$$FF_0 = \frac{v_{oc} - \ln(v_{oc} + 0.72)}{v_{oc} + 1}$$
$$v_{oc} = \frac{V_{oc} q}{n k_B T} \quad 1.9$$

Nevertheless, in real solar cells, resistive losses (particularly due to series and shunt resistances) can significantly impact the FF. Therefore, alternative expressions that incorporate the effect of series resistance provide a more accurate and practical estimation of FF under realistic operating conditions [15].

$$FF_S = FF_0(1 - 1.1 r_S) + \frac{r_S^2}{5.4}$$
$$r_S = \frac{R_S j_{sc}}{V_{oc}} \quad 1.10$$

Conversion efficiency (η): Is the main parameter to compare the performance of different solar cells. This represents the ratio between the maximum output power density and the incident light power. In the case of standard conditions, P_{in} is equal to 1000 W/m^2.

$$\eta = \frac{P_{out}}{P_{in}} = \frac{V_{oc} j_{sc} FF}{P_{in}} \tag{1.11}$$

1.2.2 Main loss mechanisms in c-Si solar cells

In the classical detailed-balance treatment by Shockley and Queisser from 1961, radiative recombination is the sole loss mechanism, which sets an efficiency limit of 30% for the 1.12 eV band gap of crystalline Si [16]. In recent years, the theoretical limit has lowered due to the incorporation of non-radiative recombination effects, mainly Auger recombination. Recent works, such as those by Richter et al. [17] and Niewelt et al. [18], converge on an efficient limit of ~29.4% for defect-free Si wafers. State-of-the-art laboratory devices are now within ~2–3 absolute percentage points of that value: certified heterojunction solar cell prototypes reported efficiencies of 27.09 % in late 2024, underscoring how narrow the remaining margin is [19]. Closing this gap is no longer a question of bulk perfection but of mitigating extrinsic losses, minimising surface/interface recombination through advanced passivating contacts, reducing contact and lateral resistances, and optimizing light management (texturing, antireflection, rear reflectors), as summarised in recent reviews on passivating-contact architectures [20].

1.2.2.1 Recombination losses

A key parameter in the fabrication of solar cells is the minority carrier lifetime, which quantifies the average time that photogenerated carriers can survive before recombining. Since recombination directly limits the number of carriers that can be collected at the contacts, the lifetime is intrinsically linked to the recombination mechanisms present in the device. A longer lifetime indicates lower overall recombination rates, thereby increasing the probability that carriers will reach the electrodes and contribute to the photocurrent. In semiconductors, recombination can occur through various pathways, which are commonly classified into two main categories: bulk recombination, occurring within the

volume of the material, and surface recombination, taking place at the interfaces or surfaces. Both types must be minimized to achieve long carrier lifetimes and, consequently, high solar cell efficiencies.

Bulk recombination encompasses three distinct mechanisms: radiative recombination, Shockley-Read-Hall (SRH) recombination, and Auger recombination.

Radiative recombination: This recombination takes places when an electron from the conduction band combines with a hole in the valence band producing a photon. This mechanism dominates in direct bandgap semiconductors such as GaAs, however for indirect bandgap semiconductors like Si, radiative recombination is really low and usually it is neglected. The rate of radiative recombination can be expressed as follows [21]

$$U_{rad} = B(np - n_i^2)$$
$$U_{rad} \approx BN_D\Delta n \quad if \;\; \Delta n \ll N_D \tag{1.12}$$
$$U_{rad} \approx B\Delta n^2 \quad if \;\; \Delta n \gg N_D$$

Where B is the radiative recombination coefficient and the approximation is given for a n-type material for a low injection ($\Delta n << N_D$) and high injection ($\Delta n >> N_D$) condition.

Auger recombination: This recombination involves three carriers. When an electron and a hole recombine, the remaining energy is given to a third carrier (an electron in the conduction band) instead of emitting heat or a photon. Following this excitation, the electron thermalizes back down to the conduction band. Auger recombination is the most important mechanism with heavy doping or under concentrated sunlight which ultimately limits the minority carrier lifetime and efficiency of the solar cell. This can be expressed as follows [22]

$$U_{Auger} = C_n n^2 p + C_p p^2 n$$
$$U_{Auger} \approx C_n N_D^2 \Delta n \qquad if \;\; \Delta n \ll N_D \tag{1.13}$$
$$U_{Auger} \approx (C_n + C_p)\Delta n^3 \quad if \;\; \Delta n \gg N_D$$

Where C_n and C_p are the Auger recombination coefficient for electrons and holes and the approximation is given for a n-type material for a low injection ($\Delta n << N_D$) and high injection ($\Delta n >> N_D$) condition

Shockley-Read-Hall recombination: This mechanism occurs via localized defect states within the bandgap, typically introduced by impurities or structural defects. In this process an electron (or hole) is captured by the impurity state and subsequently a hole (or electron) is captured. The SRH

recombination rate depends on the trap energy level, the density of defect states, and electron (hole) capture cross section [21].

$$U_{SRH} = \frac{V_t N_t (np - n_i^2)}{\frac{1}{\sigma_p}(n + n_1) + \frac{1}{\sigma_n}(p + p_1)} \quad with \quad \begin{matrix} n_1 = n_i e^{\frac{E_t - E_{Fi}}{k_B T}} \\ p_1 = n_i e^{\frac{E_{Fi} - E_t}{k_B T}} \end{matrix} \qquad 1.14$$

Where V_t is the thermal voltage ($V_t = \frac{k_B T}{q}$), σ_n and σ_p are the electron and hole capture cross section, N_t is the defect density, E_t is the energy level of the defect, and E_{Fi} is the intrinsic Fermi level of the material.

Taking these effects into account, the bulk lifetime can be expressed as follows

$$\frac{1}{\tau_{bulk}} = \frac{1}{\tau_{rad}} + \frac{1}{\tau_{Auger}} + \frac{1}{\tau_{SHR}} \qquad 1.15$$

$$where \frac{1}{\tau_x} = \frac{U_x}{\Delta n}$$

These three mechanisms will determine the bulk lifetime, as depicted in Figure 1-5. At a low-injection level, SRH recombination dominates the effective lifetime; meanwhile, at a high-injection level, the Auger recombination is the most important recombination mechanism.

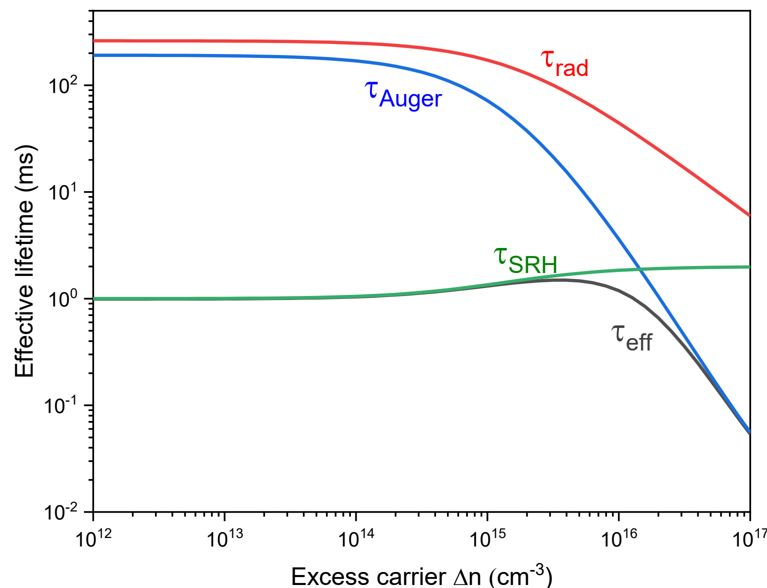

Figure 1-5 Effective lifetime in the bulk and its contributions. Plotted using the PV-Lighthouse recombination calculator [23] *(n-type c-Si, 2.5 Ωcm, τ_{min} = 1 ms).*

Surface recombination: This occurs at the interfaces of a semiconductor where the periodic crystal lattice is interrupted, leading to the formation of localized defect states or dangling bonds that can trap carriers. These states introduce energy levels within the bandgap and act as efficient non-radiative recombination centers. This mechanism is particularly relevant at semiconductor/metal interfaces, where Fermi-level pinning and high interface state densities enhance carrier recombination. The rate at which excess carriers recombine at the surface is described by the surface recombination velocity (S) which is defined with the following expression:

$$U_{surf} = (\sigma_{surf} v_{th} N_{t,surf})\Delta n_{surf} = S\Delta n_{surf} \qquad 1.16$$

Where σ_{surf} is the capture cross-section of the traps at the surface, v_{th} is the thermal velocity ($v_{th} = \sqrt{\frac{3kT}{m^*}}$), m^* is the effective mass of the carrier, $N_{t,surf}$ is the density of surface states, and Δn_{surf} is the excess minority carrier concentration at the interface.

The maximum surface recombination velocity is approximately $S_{max} \approx v_{th}$ which is about 10^7 cm/s at room temperature [22]. Thus, to reduce the recombination rate at the surface is necessary to minimize the σ_{surf} and/or $N_{t,surf}$. In practice, this is achieved through chemical passivation (a-Si:H(i), SiO_x) where the dangling bonds are saturated or via field-effect passivation (doped a-Si:H, Al_2O_3) where a fixed charge repels minority carrier away from the surface [24]. The following schematic (Figure 1-6) summarized the recombination mechanism explained so far.

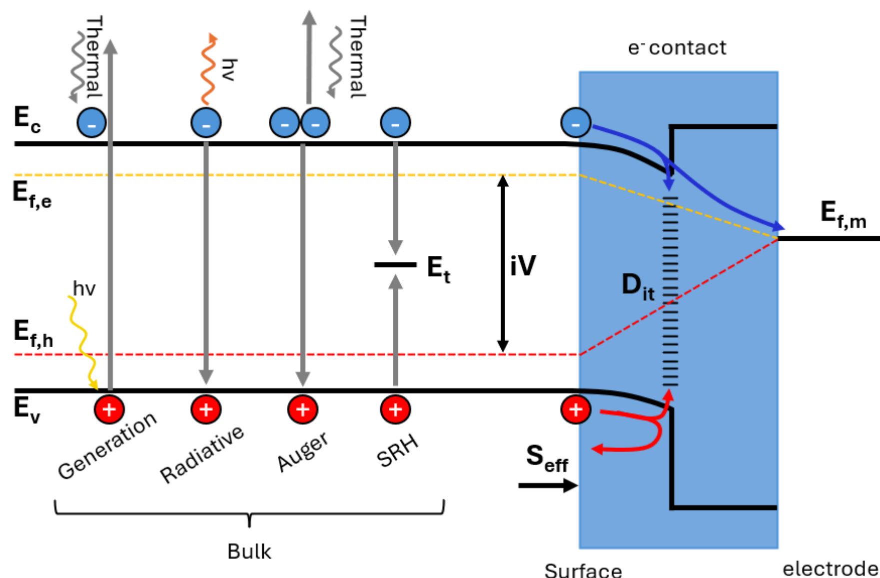

Figure 1-6 Schematic representation of the main carrier recombination mechanisms in a semiconductor. D_{it} represents the density of surface defects. Adapted from [25]

1.2.2.2 Optical losses

Optical losses in a solar cell refer to the fraction of incident light that does not contribute to the generation of electron-hole pairs. These losses can be broadly classified into two main categories: reflective losses and absorption losses. Reflective losses occur when light is reflected at the surface before entering the absorber layer. This reflection may be caused by shadowing from the front metal contact grid, suboptimal performance of the anti-reflective coating (ARC), or insufficient surface texturing that limits light trapping. Absorption losses arise when light penetrates the cell but is not absorbed effectively. This can result from a low absorption coefficient of the material at certain wavelengths, insufficient absorber thickness, or inadequate surface texturing that reduces the optical path length. Additional sources of optical loss include sub-bandgap photons, which have insufficient energy to excite electrons across the bandgap, and parasitic absorption in non-active layers such as transparent conductive oxides, passivation layers, or metal contacts. In optimized solar cells, an ARC layer is typically deposited on the rear side to reflect the coming light and increase the probability to be absorbed in the active layer. The Figure 1-7 depicts the main optical losses in a solar cell as well as the effect in the absorptance due to texturized surfaces. Although Figure 1-7 b) shows an increase in absorptance in the sub-bandgap region, this is an artificial effect resulting from the textured surface, which causes part of the incident light to be scattered outside the detection range. As a result, this scattered light is neither recorded as reflected nor transmitted, leading to an overestimation of absorptance[26].

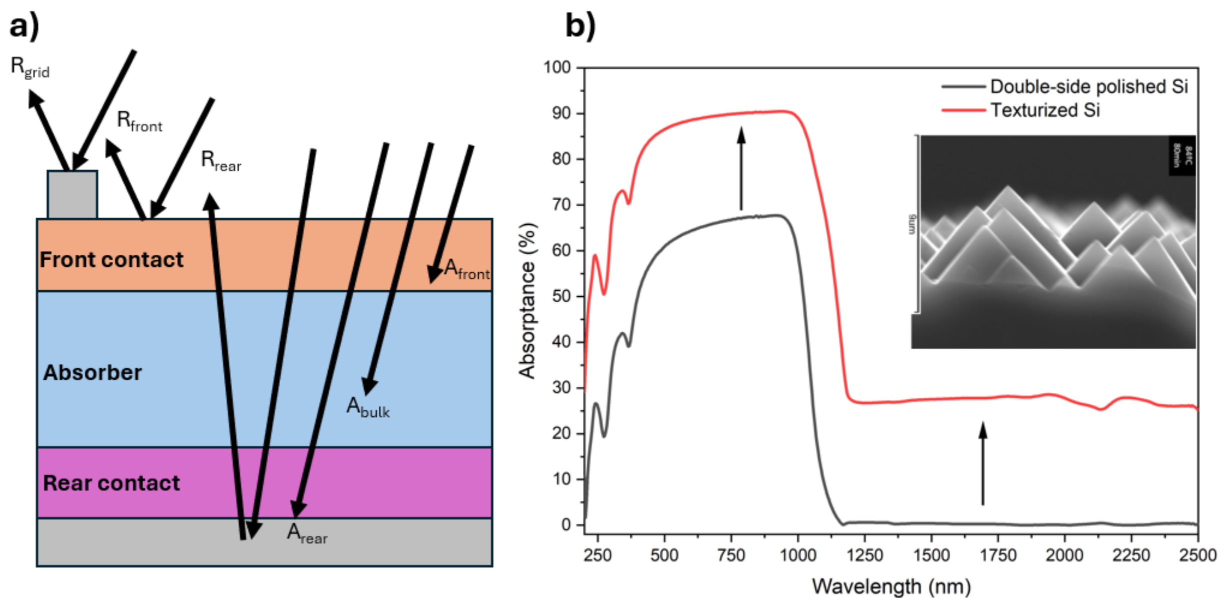

Figure 1-7 a) Schematic illustration of the main optical loss mechanisms in a polished silicon (Si) solar cell, and b) measured absorptance spectra of a double-side polished (DSP) silicon wafer and a texturized Si wafer. The inset shows a cross-sectional SEM image of the texturized surface.

1.2.2.3 Resistive losses

Resistive losses in solar cells come from all voltage drops caused by electrical resistance within the device and are a critical factor limiting the fill factor and overall efficiency. These losses can be broadly divided into series resistance (R_s) and parallel resistance (R_p) components.

The series resistance includes contributions from several sources. First, the sheet resistance (R_{sh}) of the transparent conductive oxide (TCO) layer plays a significant role in determining lateral carrier transport losses, particularly over large areas. Second, the contact resistivity (ρ_c) at interfaces, such as between the TCO and the metal grid or between passivating/contact layers and the absorber, can introduce additional current drops if the interface is poorly engineered. Third, the resistance of the metal grid itself contributes to the total series resistance and depends on the grid design (finger width, spacing, and height) and the metal conductivity. These resistive components collectively reduce the maximum power point (MPP) by limiting current flow.

On the other hand, parallel resistance (R_p) also known as shunt resistance, represents unwanted leakage paths that allow current to bypass the depletion region, typically due to pinholes, defects, or impurities creating low-resistance paths across the junction. While parallel resistance predominantly affects the slope of the JV curve near the short-circuit current, series resistance primarily affects the curve near V_{oc}. Proper optimization of material properties, contact engineering, and device layout is essential to minimize both types of resistive losses and enhance solar cell performance.

1.3 Solar cell architecture

By the end of 2025, there are four solar cell architectures that dominate the market. Among them, the Tunnel Oxide Passivated Contact (TOPCon) is the main architecture in the market, with 80 % of the PV modules [27]. Following this technology, it can be still found (the once dominant) Passivated Emitted and Rear Contact (PERC), the Heterojunction with Intrinsic Thin Layer (HJT), and all the technologies which include Back Contact architecture (xBC). The market share for these PV technologies is shown in Figure 1-8. Although, the market share of Perovskite/Si tandem is still testimonial, it is expected that this technology will start to be commercially profitable by 2031 with an efficiency of nearly 30 % [28].

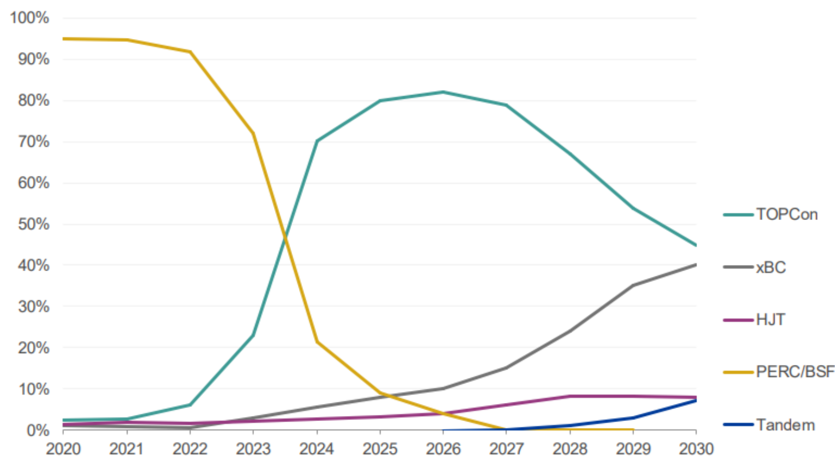

Figure 1-8 Market shares for mainstream PV technologies. Taken from [27]

TOPCon technology is currently the most relevant Si-based technology in the market. This technology is the clear successor of the so-far dominant PERC technology. This is due to the advantages of the TOPCon structure. The inclusion the SiO_x/poly-Si (doped) stack between the metal contact and the Si absorber has improved efficiency by reducing the recombination of the photogenerated carriers, thus increasing the minority carrier lifetime and the V_{oc}. Recently, V_{oc} values of 748.6 mV and efficiency of 26.07 % for commercial TOPCon panels have been reported [29]. Additionally, the fabrication route can be implemented in the present PERC technology factories due to the similarity of the process (diffusion and metallization lines).

The Heterojunction with Intrinsic Thin Layer (HJT), also known as Heterojunction with Intrinsic Thin Layer (HIT), is another well studied technology already present in the market. This technology shows advantages over TOPCon such as lowering the thermal budget by replacing diffused junctions with thin, doped hydrogenated amorphous silicon (a-Si:H) layers deposited by plasma enhanced chemical vapour deposition (PECVD) at 150-250 °C. However, pyrophoric and highly toxic precursor gases are still necessary to deposit doped a-Si:H layers. For depositing a-Si:H(n), which acts as electron selective contact (ESC) in HJT solar cells, SiH_4 (silane) + PH_3 (phosphine) mixture is required. For depositing a-Si:H(p), acting as hole selective contact (HSC), SiH_4 + TMB (trimethylborane) mixture is required. In the past, diborane (B_2H_6) was also used for the a-Si:H(p) deposition; however now it is largely avoided due to highly toxicity. All this implies that PECVD systems require complex and robust systems for storage of precursor gases and leak detection. The main advantage of HJT technology over PERC and TOPCon lies in its superior surface passivation, provided by the thin intrinsic a-Si:H layers and the reduction in energy consumption due to much lower manufacturing temperatures. This results in a significant reduction in surface recombination which leads to an increase in the V_{oc}. Nevertheless,

the relatively narrow bandgap of a-Si:H (~1.7–1.8 eV) causes parasitic absorption, particularly in the short-wavelength region, which can reduce the photogenerated current density (j_{sc}) [30].

In interdigitated back contact (IBC) solar cells, both the electron and hole collecting electrodes are positioned on the rear side of the wafer in an interdigitated pattern, thereby eliminating front side metallization and avoiding optical shading losses. The back side is formed by alternating p-type and n-type regions, separated by dielectrics spacers to prevent shunting. As the p-type and n-type regions can be fabricated either by poly-Si(n/p)/SiO_x, similar to TOPCon, or a-Si:H(i)/a-Si:H(n/p), similar to HJT, there is not a standard design for IBC. Although this design enables record efficiencies above 26 % when combined with a-Si:H(i)/a-Si:H(n/p) approaches [31], it requires complex processing steps, including precise photolithography or laser patterning, making fabrication more challenging compared to TOPCon or HJT. The Figure 1-9 depicts the solar architectures explain so far.

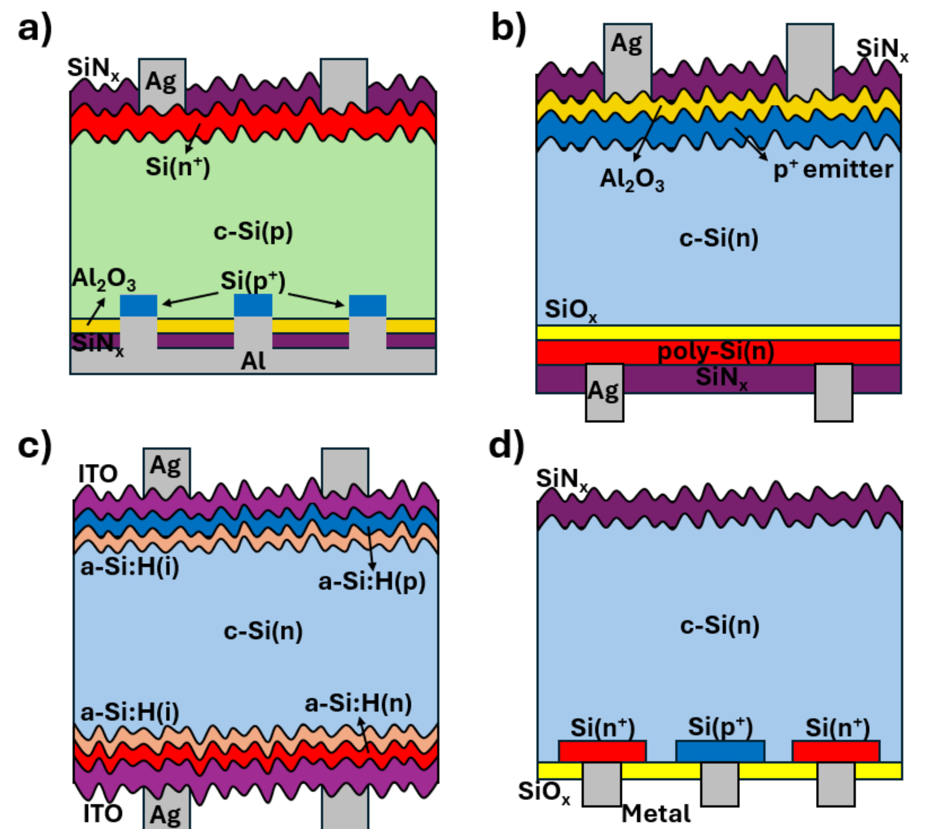

Figure 1-9 Main solar cell design found in the market. a) Passivated Emitted and Rear Contact (PERC), b) Tunnel Oxide Passivated Contact (TOPCon), c) Heterojunction with Intrinsic Thin Layer (HJT), and d) Interdigitated Back Contact (IBC).

1.3.1 Perovskite – Silicon tandem solar cells

In recent years, perovskite (PK) solar cells have attracted much attention in the scientific community. Their ease of fabrication and low manufacturing costs make them a candidate to replace Si-based solar cells. However, these materials still present challenges for large-scale implementation. Some of them are the instability they present when operating in real conditions (humidity and oxygen degrade perovskites), the scalability to manufacture perovskites, and the replacement of lead by another non-toxic material [32]. Since perovskites can be tuned to have different bandgap values, creating Si/PK tandems is another idea being investigated [33]. In this way, Si would absorb low-energy photons, while PK would absorb high-energy photons. The use of Si/perovskite tandem solar cells enables overcoming the recombination-limited efficiency ceiling of single-junction crystalline silicon devices (~29.4%), with theoretical efficiencies reaching up to ~45% [34]. However, for a module a more conservative efficiency of ~30 % would be expected by 2030 [28].

Two basic configurations are commonly used to manufacture Si/PK tandem cells. On the one hand, there is the four-terminal configuration. In this structure, the bottom cell (Si-based) and the top cell (perovskite) are electrically isolated and are mechanically joined once they are both finished. The drawback of this configuration lies in the number of connections needed to extract the charges [35]. On the other hand, the two-terminal configuration, shown in Figure 1-10, connects optically and electrically the bottom and top cells. This way, the perovskite cell can be fabricated just above the Si-based cell. To fabricate this type of structure, a recombination junction is necessary. The purpose of the recombination junction is to electrically connect the cells in series. For this, the majority carriers of each cell need to recombine without producing the recombination of the minority carriers [36]. On the other hand, it also requires low absorption in the infrared and a refractive index adapted to avoid reflections in the interfaces [37]. The film thickness must also be optimized to avoid increasing the series resistance of the devices [38].

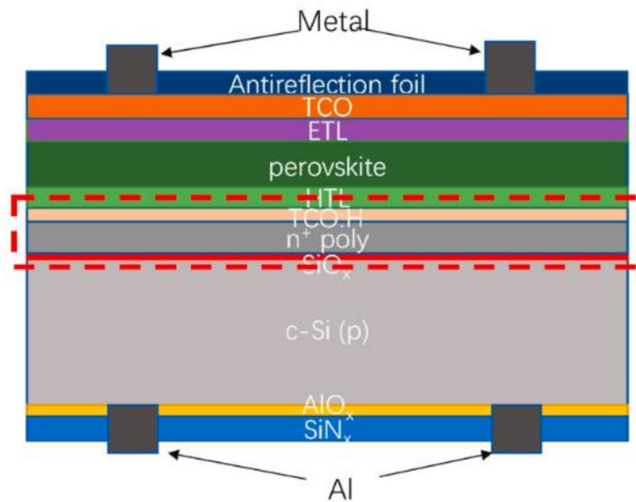

Figure 1-10 Structure of a two-terminal Si/PK tandem solar cell, including TOPCon as the bottom cell, Perovskite as the top cell, and TCO:H as the recombination junction. Adapted from [39]

Recombination junctions can be divided into two main groups based on diffused contacts and passivated contacts. The first type is basically the structure of a tunnel diode (Esaki diode) where two highly doped semiconductors (degenerate semiconductors) come into contact, allowing conduction by tunnelling mechanism [40]. The second type (passivated contact) is the junction of n-type semiconductors (ITO, IZO) with the hole transport layer (HTL) of the perovskite cell. This creates a bending in the energy bands in the junction (Figure 1-11) that allows the conduction by means of trap-assisted tunnelling (TAT), thus allowing the extraction of the photogenerated carriers [36].

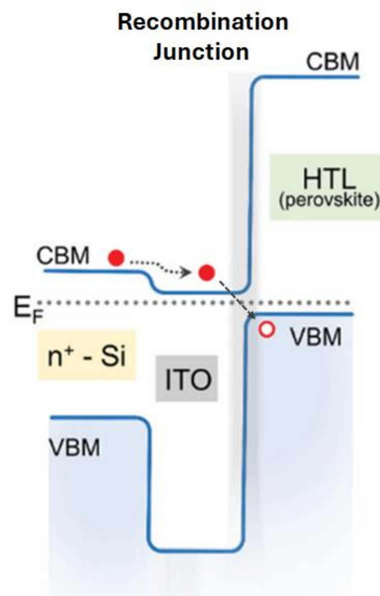

Figure 1-11 Energy diagram of a recombination junction in a Si/Pk tandem solar cell. Adapted from [36].

1.3.2 Dopant-free asymmetric heterocontact (DASH) solar cells

Until now, all solar cell architectures described require processes involving toxic gases (SiH_4, PH_3, TMB, etc.) and/or high temperatures to deposit poly-Si(n/p) or a-Si:H(n/p). Ideally, these drawbacks could be avoided with the dopant-free asymmetric heterocontact (DASH) architecture. The concept of DASH relays on replacing the conventional doped semiconductor layers with wide bandgap materials that provide selectivity, i.e. extract one type of charge while the other is blocked. These materials, also kwon as selective contacts (SC), are generally transition metal oxides (TMO), transparent conductive oxide (TCO) or fluorides.

This architecture would simplify the fabrication process since toxic dopant precursor are not required, and the materials can be deposited at low temperature (≤ 200 ºC). Furthermore, from a physics point of view, wide bandgap SC will reduce the parasitic absorption and Auger recombination losses. A problem typically found with heavily doped layers (poly-Si and a-Si:H). One of the first reference to DASH terminology was in 2016 with the work of Bullock, A. et al [41]. In this study, a thin MoO_x layer was used as hole selective contact (HSC), while LiF_x acted as electron selective contact (ESC). This research showed that dopant-free contact concept was viable to reach efficiencies above 15 %. A basic DASH design is depicted in the following figure.

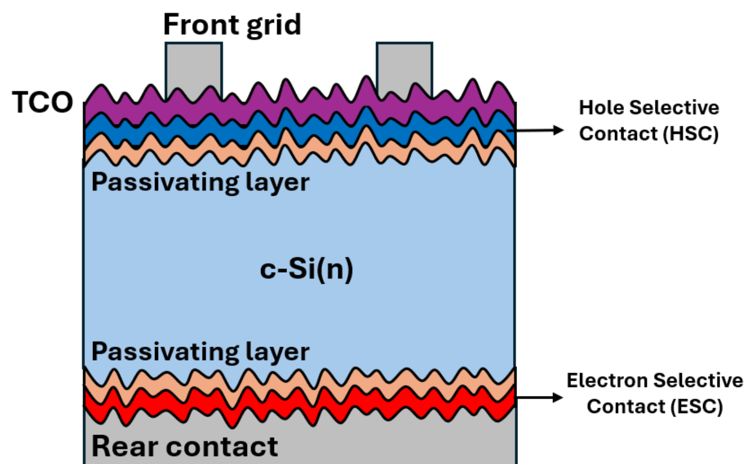

Figure 1-12 Basic dopant-free asymmetric heterocontact solar cell design.

A detail description on the physics of selectivity and different materials acting as selective contacts will be described in the following sections.

1.4 Transparent conductive oxides in solar cells

Transparent conductive oxides (TCOs) are materials widely used in solar cell structures due to their unique combination of optical and electrical properties. Their large bandgap energy (typically > 3 eV) ensures high transparency in the visible spectral range, allowing efficient light transmission to the absorber layer. Simultaneously, TCOs exhibit low sheet resistance, which enables effective lateral conduction of photogenerated charge carriers across the device surface. These characteristics make TCOs essential components for front contact layers in various photovoltaic technologies.

TCOs are degenerated doped oxide or nitride semiconductors [42]. This means that the E_F lies inside the conduction band. Additionally, TCOs exhibit highly dispersive conduction bands meaning that the energy *E(k)* of electrons changes rapidly with the state (*k*). This band structure has two important consequences: smaller effective mass (m^*) which leads to a higher mobility (μ) since $\mu = \frac{q\tau}{m^*}$ where τ is the average scattering time, and low optical absorption due to low density of states *g(E)* since $g(E)dE \propto m^{*3/2}$ which means that fewer photons will be absorbed via free carrier absorption because of fewer available states [43].

TCOs can also present the Burstein-Moss (BM) effect which causes a shift in the optical absorption toward higher photon energies (lower wavelengths). This occurs because the high electron concentration fills the low-energy states in the conduction band, preventing optical transitions from the valence band into these occupied states due to the Pauli exclusion principle. As a result, only transitions to higher-energy states are allowed, effectively increasing the apparent optical bandgap. This shift enhances transparency in the visible range; however, excessive doping may also lead to increased free-carrier absorption in the infrared. For a simple parabolic band, the BM shift is depicted in Figure 1-13 and it can be described as follow [44]:

$$\Delta E_{BM} = \frac{\hbar^2}{2m^*}(3\pi^2 n)^{\frac{2}{3}} \qquad 1.17$$

Where m^* is the effective mass of the carrier, n is the carrier concentration and $\hbar$ is the reduced Planck constant.

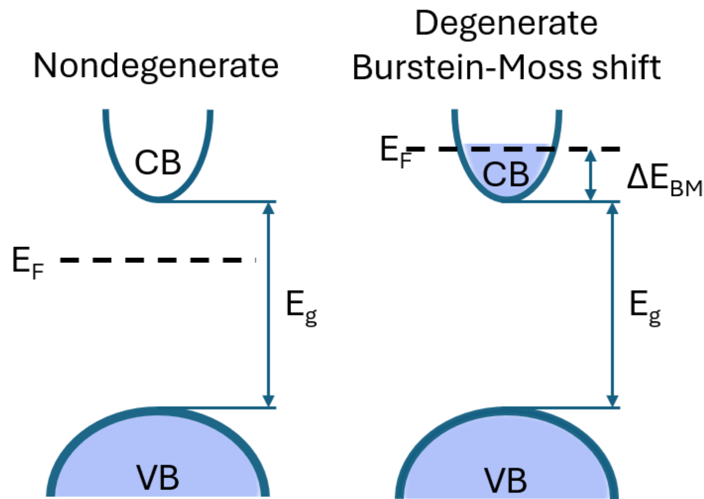

Figure 1-13 Schematic for a n-type nondegenerated semiconductor and degenerated with Burstein-Moss shift semiconductor.

For solar cell applications, TCOs must meet several key requirements, including high electrical conductivity, low optical absorption in both the ultraviolet (UV) and infrared (IR) spectral regions, low contact the TCO layer. Specifically, the electrical conductivity ($\sigma = qn\mu$) increases with both carrier concentration (n) and mobility (μ). Optical absorption in the UV region is influenced by the carrier concentration through mechanisms such as the Burstein–Moss shift, which modifies the apparent band gap. In the infrared region, absorption is governed by the plasma resonance of free carriers: when the photon energy approaches the plasma frequency, collective oscillations of conduction electrons induce strong reflection or absorption. As the carrier concentration increases, the plasma frequency shifts toward higher energies (shorter wavelengths), thereby reducing the IR transparency of the TCO [42]. This trade-off imposes a fundamental balance between electrical performance and optical transparency. The plasma frequency (ω_p), which determines the onset of infrared absorption, is given by resistance with adjacent layers, and a suitable refractive index to minimize optical reflection. Most of these properties are intrinsically linked to the free carrier concentration and mobility within

$$\omega_p\ [rad/s] = \sqrt{\frac{nq^2}{\varepsilon_0 m^*}} \quad 1.18$$

Where n is the free carrier concentration, q is the elementary charge, ε_0 is the vacuum permittivity, and m^* is the effective mass of the carrier. To express it in terms of wavelength, the following expression can be used:

$$\lambda_p = \frac{2\pi c}{\omega_p} \tag{1.19}$$

Where c is the speed of light in vacuum.

1.4.1 Indium tin oxide (ITO)

Among the various TCOs, indium tin oxide (ITO) remains the most widely used in photovoltaic devices due to its balance between high electrical conductivity and optical transparency. ITO is typically composed of ~90 wt% In_2O_3 and ~10 wt% SnO_2. Is a degenerate n-type semiconductor with a carrier concentration in the range of 10^{20}-10^{21} cm^{-3}, which results in low resistivity values down to ~10^{-4} Ωcm [45][46]. Its optical transmittance exceeds 85% in the visible range, and its bandgap is typically between 3.5–3.8 eV, enhanced by the Burstein–Moss effect due to the high doping level [46][42]. The plasma resonance of free carriers sets a transparency limit in the near-infrared region, typically around 1.5 µm, and this limit shifts with increasing carrier concentration. Thus, a trade-off between electrical and optical performance is necessary [42].

ITO films can be deposited using several techniques, RF and DC magnetron sputtering are the most common techniques for industrial applications due to scalability, uniformity, and tunability of electrical and optical properties [47]. The performance of ITO is strongly influenced by deposition parameters such as oxygen partial pressure, substrate temperature, and sputtering power. All of these parameters can affect the crystallinity, carrier concentration, and surface roughness of the film [45]. Furthermore, improper tuning of oxygen content can lead to either excessive oxygen vacancies (increasing free carrier absorption) or oxygen-rich conditions (reducing conductivity).

The primary application of ITO in solar cells is as a front contact, where it serves a dual function: it allows the transmission of incident light to the absorber layer due to its high transparency in the visible range, and it provides low-resistance lateral conduction of photogenerated charge carriers toward the metal grid for efficient extraction. Recent research has explored additional functionalities of ITO in advanced photovoltaic architectures. For instance, ITO has been employed as a recombination layer in Si/perovskite tandem solar cells, where it facilitates charge recombination between the sub-cells while maintaining optical transparency [36]. Moreover, ITO has also been investigated as a hydrogen reservoir, capable of releasing hydrogen during annealing to improve the chemical passivation in

Tunnel Oxide Passivated Contact (TOPCon) solar cells [48]. This is the main objective investigated in **Chapter V**.

Despite its high performance, the scarcity and cost of indium have motivated efforts to replace ITO with alternative TCOs such as Al-doped zinc oxide (AZO) or F-doped tin oxide (FTO) [47]. ITO remains the benchmark due to its low sheet resistance and excellent transparency. Novel deposition techniques can further improve the ITO characteristics or even make it suitable for sensitive solar cells materials such as Perovskite, this is the main purpose of the **Chapter IV**.

1.4.2 Hydrogenated indium tin oxide (ITO:H) for solar cell applications

In the context of Si/PK tandem solar cells, hydrogenated indium tin oxide (ITO:H) is gaining attention as a promising material for further research. Due to its wide use in other photovoltaic devices, ITO is often used to create the recombination junction in Si/PK structures. Unlike ITO deposited on the front side of single-layer solar cells, low lateral conduction is sought in ITO for recombination junctions. This is because lateral conduction can reduce the shut resistance of the tandem, reducing the fill factor and thus efficiency. For that reason, the deposition of ITO with an O_2 atmosphere has been investigated as an option to reduce lateral conduction and avoid absorption by free carriers in the infrared [49]. Nevertheless, a compromise must be made since the oxygen could affect the electrical parameters of the cell (reduction in V_{oc}), which could negatively affect the solar cell's performance [50].

The deposition of ITO:H on poly-Si contacts has been recently investigated to reduce the TOPCon fabrication steps. Typically, the TOPCon fabrication needs a hydrogenation step to passivate the defects resulting from the formation of the poly-Si passivating layer. This is achieved by depositing a hydrogen-rich silicon nitride (SiN_x:H) layer followed by a firing step carried out at high temperature (~ 800 ºC). After hydrogenation, the SiN_x:H layer should be removed by a chemical etching with diluted HF before the deposition of a conventional TCO. In that sense, an ITO:H could hit two targets with one shot since the hydrogen contained inside the ITO could passivate the defects at the interfaces while the ITO layer acts as the recombination junction. Although ITO:H has not been extensively explored, the work of Tusch et al. has shown positive results with respect to the passivation of poly-Si/ITO:H joints with annealing at relatively low temperature (300 ºC) [51]. This topic was investigated during the predoctoral research stay at EPFL-PVlab and the results are explained in **Chapter V**.

1.5 Selective contacts in Si-based heterojunction solar cells

Carrier-selective contacts (CSCs) act as energy-selective membranes: they provide a low-resistance extraction (high conductivity) path for one type of photogenerated carriers while creating a large potential barrier for the opposite carrier, thereby suppressing interfacial recombination and reducing series resistance. Traditionally the function of charge separation (selectivity) was achieved by highly doped films as in the case of n^+ emitter in Passivated Emitter and Rear Cell (PERC) p-type Si solar cells. Typically, these films are fabricated in diffusion furnaces at very high temperatures (> 800 °C) with highly toxic and hazardous precursor gases such as $POCl_3$ (phosphorus oxychloride) for n^+ emitter or BBr_3 (boron tribromide) for p^+ emitter. Furthermore, these high-doped layers enhance the Auger recombination losses due to high concentration of dopants, which leads to an increase in the recombination current (J_0) and thus a reduction in open circuit voltage (V_{oc}).

In this context, CSC materials have attracted attention of the scientific community due to their excellent selectivity, compatibility with low-temperature fabrication and absence of toxic precursor. These materials have been extensively studied for emerging solar cell structures, such as organic and perovskite solar cells, because they are well-suited for integration with chemically and thermally sensitive absorber layers [52]. Their integration into silicon solar cells has not been as widespread and only began to gain traction in the mid-2010s, following the first reports demonstrating the application of dopant-free CSCs in silicon-based devices [53][41]. This marked the beginning of the Dopant-free Asymmetric Heterojunction (DASH) solar cell architecture.

1.5.1 Physical origin of selectivity

The concept of carrier selectivity refers to the ability of a contact to preferentially extract one type of charge carrier (either electrons or holes) while effectively blocking the other. From a physical perspective, this selectivity arises from the asymmetry in carrier conductivities within the contact region. Specifically, when a material exhibits a high conductivity for majority carriers and a low conductivity for minority carriers, the likelihood of recombination at the contact is significantly reduced. This is because the minority carriers encounter a transport barrier, preventing them from reaching the interface where recombination could occur with the majority carriers. A detailed explanation of carrier selectivity can be found in the work of Würfel et al. [11].

Diverse mechanisms can create large asymmetry between electron and hole conductivities. Among the most relevant are the following [54]:

- **Highly doped regions**: This is the primary selectivity mechanism employed in PERC and TOPCon solar cells. In these architectures, highly doped regions are introduced at the silicon surface to increase the concentration of a specific type of charge carrier, electrons in n-type doping or holes in p-type doping. As a result, strong band bending occurs near the interface, shifting the Fermi level closer to the conduction band (for n-type) or to the valence band (for p-type). This high carrier concentration leads to a significant increase in the conductivity of the majority carrier, while the minority carrier experiences a reduction in conductivity due to a higher potential barrier. In this way, a conductivity asymmetry is established, which enables the effective carrier selectivity at the contact. See Figure 1-14 a).

- **Band offset**: Using wide-bandgap materials with conduction or valence band offsets at the interface with c-Si can selectively extract carriers. For example, materials like TiO_2, electron selective contact, exhibit a large valence band offset ($\Delta E_v > 2$ eV) with n-type silicon and a small conduction band offset ($\Delta E_c \approx 0.1$ eV). Such band offset will favor the extraction of only one kind of carrier (electrons for the case of TiO_x) while impeding the transport of the other (holes) as an energy barrier is created for one of them. Similarly, a small ΔE_v and large ΔE_c would lead to a hole selective contact. This is the case for NiO_x or Cu_2O with c-Si(n) [55]. See Figure 1-14 b).

- **Fixed charges**: Some dielectric materials contain immobile fixed charges that induce band bending, facilitating the accumulation of one carrier type and repelling the other. This has been demonstrated in systems like Al_2O_3/ZnO or polymer-based Lewis acids/bases [56]. See Figure 1-14 c).

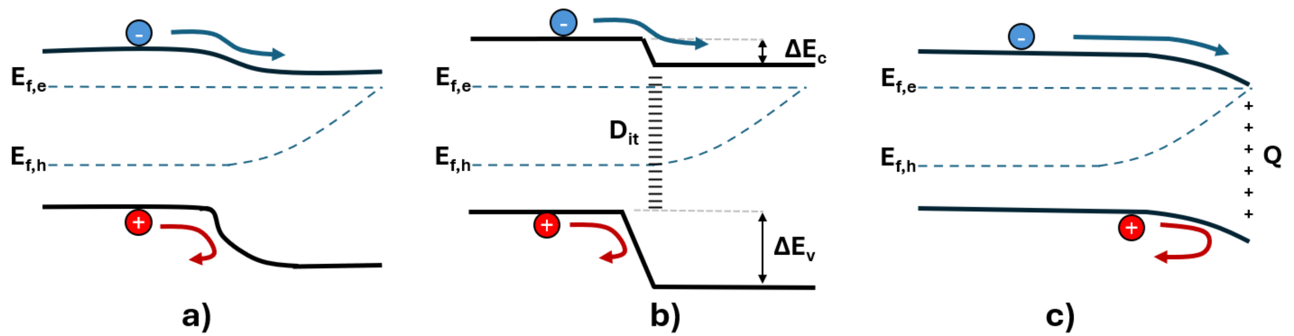

Figure 1-14 Diverse mechanism to obtain carrier selectivity: a) high doped region, b) band offset, and c) due to fixed charges.

- **Work function**: Metals or compounds with extreme work functions (*Φ*) can induce accumulation or depletion of carriers at the Si interface, although Fermi level pinning (FLP) often limits this effect. To mitigate FLP, thin interfacial layers (e.g., native SiO_2, Al_2O_3, or transition metal oxides) are introduced to suppress metal-induced gap states (MIGS). [56] In general materials with high *Φ* tend to be used as hole selective contacts while low *Φ* are used as electron selective contacts.

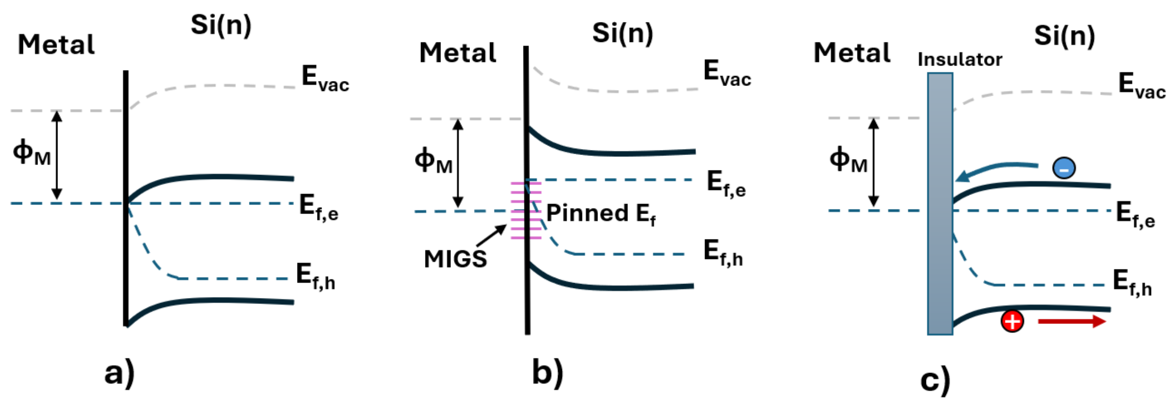

Figure 1-15 Band diagram of a low work function metal (Φ_M) and c-Si(n) junction: a) ideal case, b) with the Fermi level pinning effect due to metal induced gap states (MIGS), and c)including an insulator to avoid Fermi level pinning.

Among the high *Φ* materials, MoO_x is one of the most studied materials which has shown impressive performance when this is tested as hole selective contact. A good explanation on the selectivity mechanism for MoO_x can be found in Wang et al. work [55]. When MoO_x is deposited on c-Si(n), the large work function difference between MoO_x and Si causes a strong upward band bending in the silicon near the interface. This results in an approach of the Fermi level at the surface to the valence band, effectively inverting the surface region of the c-Si(n) and thus behaving as a p-type Si. This

inversion layer allows holes (minority carriers in c-Si(n)) to be collected efficiently, while it creates a potential barrier for electrons (majority carriers), thus blocking electron transport from c-Si(n) into MoO_x. This is depicted in the following band energy diagram.

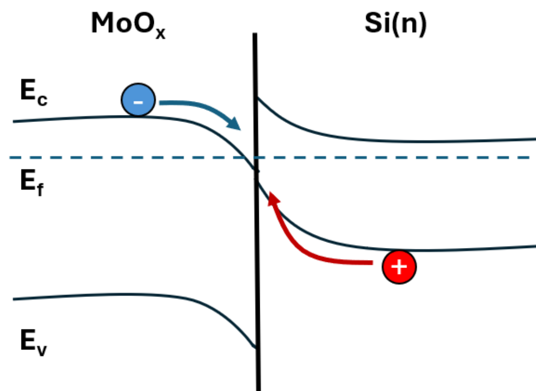

Figure 1-16 Energy band diagram for MoO_x/c-Si(n) junction. The selectivity is achieved via the type inversion of Si at the junction.

Theoretically, carrier selectivity can also be achieved through a strong mobility asymmetry between electrons and holes; however, empirically this approach remains largely unexplored [11].

Experimentally, the selectivity of CSC materials is typically determined by measuring two key parameters:

Specific contact resistivity (ρ_c): This represents the resistivity between the absorber and the CSC, and it directly reflects the quality of the majority carrier extraction. The proper methodology to obtain this parameter will be explained in **Chapter III**.

Recombination current density (J_0): In an absorber with few defects, this parameter indicates the recombination losses at the CSC/absorber junction. Thus, it can be directly linked to the effective minority carrier lifetime (τ_{eff}). Again, the methodology to obtain the J_0 and τ_{eff} is explained in **Chapter III.**

1.5.2 Materials acting as carrier selective contacts

Among the various material under investigation, CSCs for solar cell applications can be broadly classified into two main families based on their composition and functional mechanisms:

Alkali/alkaline-earth: These materials are ionic compounds composed of positively charged ions (cations) and negatively charged ions (anions), typically involving elements with high electronegativity. They exhibit very wide band gaps (often exceeding 5 eV), which makes them electrically insulating and optically transparent in the visible range. Due to their low work functions and the ability to form interfacial dipoles, many of these compounds such as LiF_x, KF_x, and CsF_x, are primarily employed as ESCs in solar cell architectures [56][57].

Transition metal oxides (TMOs): Transition metals are d-block elements in the periodic table that form cations with partially filled d orbitals. The availability of multiple d electrons enables these elements to exhibit a wide range of oxidation states, typically from –III to +VIII [56]. The oxidation state of an atom reflects the number of electrons it has effectively lost (positive oxidation state) or gained (negative oxidation state) when forming a compound. This flexibility in oxidation states allows TMOs to exhibit diverse electronic behavior, ranging from metallic to semiconducting or insulating (dielectric) properties. One of the most critical factors that determines whether a TMO functions as an electron-selective contact or a hole-selective contact is its work function. In general, TMOs with high work functions tend to act as HSCs, while those with low work functions are suitable for ESC applications [58]. The most studied TMOs acting as HSC are MoO_{3-x} [41], V_2O_{5-x} [59], and WO_{3-x} [60], while TiO_{2-x} [61], Nb_2O_{5-x} [62], and Ta_2O_{5-x} [63] are commonly used as ESC.

Figure 1-17 illustrates several materials that have been explored as carrier-selective contacts for integration with crystalline silicon solar cells.

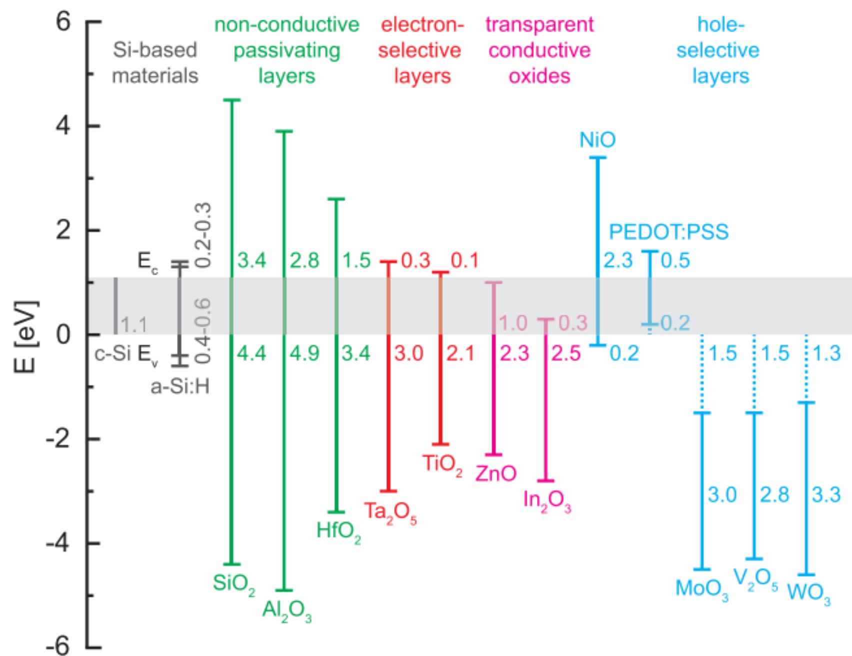

Figure 1-17 Conduction and valence band offsets of various materials with respect to c-Si. Graph from [54]

1.5.3 Titanium oxide (TiO_x) as selective contact

Titanium oxide (TiO_x), particularly in its sub-stoichiometric form (TiO_{2-x}), has been widely studied as a multifunctional material in photovoltaic devices. Historically, TiO_x was first used as an anti-reflective coating (ARC) due to its high transparency and refractive index (~2.5), which improves light trapping on textured silicon surfaces [64]. Later, TiO_x gained prominence as an ESC in perovskite solar cells because of its favorable conduction band alignment, chemical stability, and ease of deposition at low temperatures [56]. In the perovskite community, it is commonly referred to as electron transport layer (ETL) instead of ESC. In recent years, TiO_x has been explored as ESC for crystalline silicon (c-Si) solar cells. Its ability to block holes while selectively extracting electrons is primarily governed by its large bandgap (> 3.0 eV) and low work function (~4.1–4.4 eV). When deposited on c-Si(n), TiO_x forms a heterojunction with significant band bending, which promotes electron transport while impeding hole injection due to an energy barrier at the valence band edge. TiO_x/c-Si(n) junction exhibit large valence band offset ($\Delta E_v > 2$ eV) with and a small conduction band offset ($\Delta E_c \approx 0.1$ eV) [65]. The energy band diagram of c-Si(n)/TiO_x junction is depicted in Figure 1-18.

The performance of TiO_x as a selective contact is highly dependent on its deposition method, which affects stoichiometry, defect density, and interfacial passivation. Techniques such as thermal evaporation, sol-gel, atomic layer deposition (ALD), and sputtering have been explored. For instance, ALD enables excellent control over stoichiometry and thickness, often leading to better passivation and lower J_0 [56]. On the other hand, sputtering techniques are compatible with large-area processing but may require additional post-deposition treatments to enhance passivation quality and reduce contact resistivity [55].

Several high-efficiency solar cell structures have successfully incorporated TiO_x contacts. Notably, one of the first practical demonstration of dopant-free asymmetric heterocontact (DASH) solar cell architecture utilizes TiO_x as the electron contact and MoO_x as the hole contact, achieving efficiencies exceeding 20% [58]. Further improvements have been reported by optimizing interlayers (e.g., a-Si:H(i) or SiO_2) between TiO_x and c-Si, which mitigate Fermi-level pinning and enhance chemical passivation [54]. A simulated heterojunction solar cell using TiO_x as the rear contact and MoO_x as the front contact achieved 22.6% efficiency, with V_{oc} of 723 mV and J_{sc} of 39.2 mA/cm². This demonstrates the potential of TiO_x as electron selective contact in DASH solar cell structures [65].

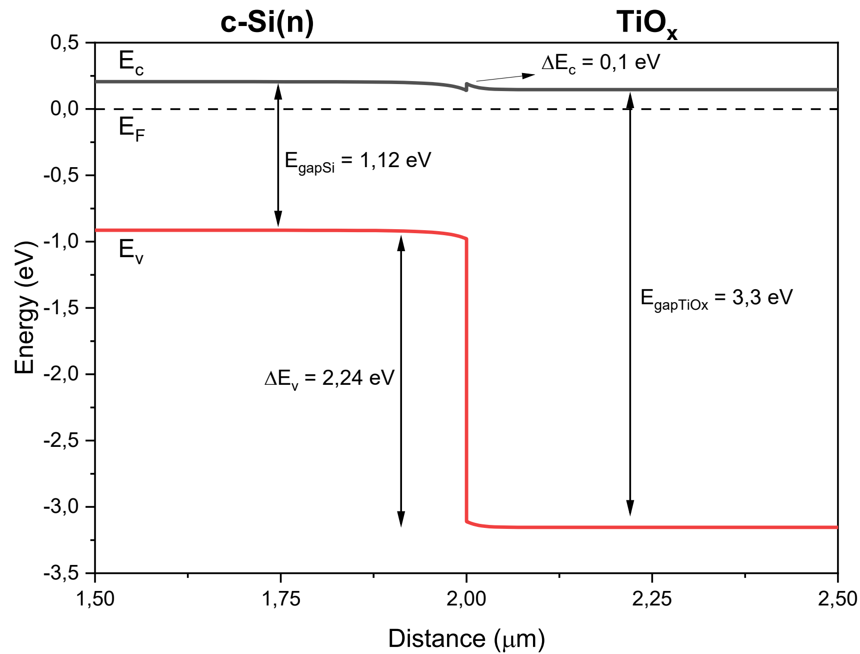

Figure 1-18 Energy band diagram for the c-Si(n)/TiO_x junction.

In summary, TiO_x emerges as a promising candidate for dopant-free ESCs in crystalline silicon photovoltaics, due to its favorable band alignment, high optical transparency, and compatibility with scalable deposition techniques. Nevertheless, further investigation is needed to enhance its interfacial passivation quality to meet the requirements of industrial implementation. In this context, exploring TiO_x films deposited by HPS presents an attractive research topic, given the potential advantages of this technique in tailoring film properties and interface quality. The results of TiO_x films deposited by HPS will be presented in **Chapter VI** and **Chapter VIII.**

1.6 High-pressure sputtering

Sputtering is a well-known deposition technique in the semiconductor industry. In the solar cell fabrication industry, sputtering is commonly used for depositing TCOs such as indium tin oxide (ITO) [66], and aluminium-doped zinc oxide (AZO) [67], or metal contacts such as Al, Ti, Ag, or Ni. Also, few works used conventional sputtering for the deposition of selective contacts materials such as TiO_2 [61], MoO_3 [68], and V_2O_5 [69]. Among the advantages of this technique, we can highlight the good uniformity and adhesion of the layer and the fine-tuning that can be made if the sputtering parameters (power, pressure, and temperature) are modified. On the contrary, relatively low deposition rates and damage caused by ion bombardment and UV exposure are some of the main drawbacks. New solar

cell architectures include thin and sensitive layers, such as a-Si:H in HIT cells, poly-Si in TOPCon or perovskite and thus the ion bombardment damage and UV exposure produced by sputtering can be a problem for these novel cells [70]. However, the ionic bombardment can be handled by reducing the kinetic energy of the sputtered particles that eventually arrive at the substrate. One way to achieve this is to ensure that the sputtered particles undergo multiple collisions before reaching the substrate. In this manner, the energy of these particles is transferred to the particles of the working gas. This can be quantified through the mean free path using the following expression [71]:

$$\lambda = \frac{1}{\sqrt{2}\pi d^2 n_v} \quad 2.1$$

Where λ is the mean free path, d is the particle's kinetic diameter, and n_v is the number of particles per volume. From equation 2.1 and considering the ideal gas law, we can obtain the following equation:

$$\lambda = \frac{kT}{\sqrt{2}\pi d^2 p} \quad 2.2$$

Where k is the Boltzmann constant, T is the plasma temperature, and p is the pressure. This expression shows that the mean free path will be reduced if the sputtering system's pressure increases. In that sense, there would be many collisions between particles that would reduce their kinetic energy.

As the name suggests, HPS differs from conventional magnetron sputtering mainly in its working pressure. HPS working pressure is in the ~1 mbar range while conventional sputtering works at two to three orders of magnitude below (10^{-3}–10^{-2} mbar range). During this thesis, the working pressure was kept in the 0.5 - 2 mbar range, which reduced the mean free path to the order of 10^{-2} cm. This is considerably lower than a mean free path of 1 -10 cm from traditional sputtering. With the working pressure of HPS, the mean free path of sputtered species becomes very short, so atoms ejected from the target undergo many collisions with the process gas. These gas-phase collisions thermalize the flux, reducing the kinetic energy of arriving particles to values on the order of $k_B T$ [72]. The resulting quasi-diffusive transport delivers the sputtered atoms gently to the substrate, suppressing bombardment-induced damage, lowering the defects formation, and promoting dense, uniform films even at low substrate temperature. These attributes are particularly advantageous for fabricating high-quality materials for CSCs or TCOs applications. As an example, the mean free path of Ti and In atoms as a function of pressure are depicted in the Figure 1-19.

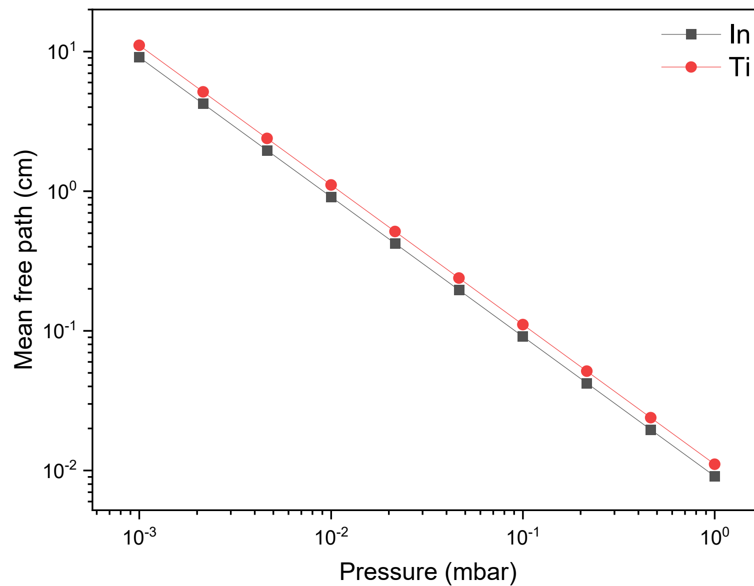

Figure 1-19 Mean free path at 300 K of In and Ti as a function of pressure. The particle kinetic diameter for In and Ti is 0.32 nm and 0.29 nm respectively.

The original idea behind high-pressure sputtering (HPS) is attributed to Dr Poppe's research group at Forschungszentrum Jülich (Germany) for the growth of $YBa_2Cu_3O_7$ as high-temperature superconductor [73], [74]. Given the promising results, the *láminas delgadas and microeletrónica* research group at *Universidad Complutense de Madrid* upgraded the system to deposit high-k dielectrics for metal/insulator/semiconductor (MIS) structures. With this technique, various high-k dielectrics such as TiO_x [75], HfO_2 [76], Gd_2O_3 [77], and $Gd_xSc_{2-x}O_3$ [78] were studied. Those studies consistently reported low interface-state densities (D_{it}), showing the excellent film quality obtained with HPS. In the framework of several research projects, where this thesis is included, HPS has been used for the growth of materials for solar cell applications, such as ITO as TCO [79], MoO_x [80] as hole-selective contact (HSC) and TiO_x as ESC [61], which is the core of this work.

A detailed description of the HPS system, process window, and diagnostic tools employed in this work is provided in **Chapter II**.

1.7 Motivation and objectives

The current global demand for low-cost and high-efficiency solar cells has driven the scientific community to search for new materials. Among various materials being explored, the integration of carrier selective contacts into Si solar cells has emerged as a promising approach to fabricate high-

efficiency devices while reducing the complexity, and with less environmental impact. In this context, dopant-free electron-selective materials such as titanium oxide (TiO_x) and transparent conductive oxides (TCOs) like indium tin oxide (ITO) have gained significant attention due to their favorable band alignments, high transparency, and potential to minimize parasitic absorption and recombination losses. However, the properties of these materials are highly sensitive to the deposition technique and conditions employed. As explained before, high-pressure sputtering (HPS) offers interesting properties worth investigating for the TCO and CSC deposition with reduced substrate damage.

Despite its potential, this thesis work presents the first demonstration of the use of HPS for the fabrication of functional layers in solar cells. This thesis is motivated to better understand the HPS-deposited TiO_x and ITO layers, optimize their structural, electrical, and optical properties, and evaluate their performance as selective contacts in silicon-based photovoltaic devices.

The main objectives of this thesis are the following:

- To characterize the HPS deposition of ITO and TiO_x varying the working pressure, the RF power, and the substrate temperature.
- To characterize the structural, optical, and electrical properties of the as-deposited films using techniques such as X-ray diffraction (XRD), ellipsometry, UV-Vis-NIR spectroscopy, Hall effect measurements, and X-ray photoelectron spectroscopy (XPS).
- To evaluate the selectivity of ITO and TiO_x films deposited on Si substrates by measuring the contact resistivity and the minority carrier lifetime of the ITO and TiO_x films. This study allows to determine their viability as a TCO or selective contact respectively.
- To fabricate and test silicon solar cell prototypes incorporating HPS-deposited TiO_x and/or ITO, and to assess their impact on device performance in terms of short circuit current density, open circuit voltage, and overall efficiency.

1.8 Thesis structure

- **Chapter I** provides a brief introduction to the fundamental principles of solar cell physics and presents the key properties of transparent conductive oxides (TCOs), with a particular focus on indium tin oxide (ITO) thin films. The most relevant concepts related to carrier-selective

contacts in silicon solar cells are also discussed. Finally, the high-pressure sputtering (HPS) technique is introduced as the deposition method explored in this work.

- **Chapter II** describes the main **fabrication techniques** employed throughout the development of this thesis, with special emphasis on the HPS method. Additionally, the substrates used, and the corresponding cleaning procedures are detailed.

- **Chapter III** outlines the structural, electrical, and optical **characterization techniques** applied to ITO and TiO_x thin films. Particular attention is devoted to the Cox & Strack method for extracting specific contact resistivity and to photoconductance measurements for determining minority-carrier lifetime.

- **Chapter IV** gives all the results and analysis (structural, electrical, optical, and minority carrier lifetime) obtained from the characterization of **HPS-deposited ITO** layers. Also, the ITO is deposited on a HJT solar cell to assess the impact on the solar cell performance.

- **Chapter V** describes the work carried out at EPFL's PV-LAB on **hydrogen-saturated ITO (ITO:H)** deposited by conventional sputtering. The study focuses on structural, electrical, and lifetime properties, with the goal of integrating ITO:H into a TOPCon fabrication route where the layer serves both as a transparent conductive oxide and as a hydrogen reservoir to passivate underlying films during the firing step.

- **Chapter VI** gives all the results and analysis (structural, electrical, optical, and minority carrier lifetime) obtained from the **HPS-deposited TiO_x** on Si substrate (TiO_x/Si) and HPS-deposited TiO_x along with RCA-growth SiO_x as passivation layer (TiO_x/SiO_x/Si).

- **Chapter VII** investigates **HPS-deposited TiO_x on Si substrates featuring an intermediate a-Si:H(i)** passivation layer (TiO_x/a-Si:H(i)/Si). The resulting stack is subsequently used as an electron selective contact in heterojunction solar cells, and its structural, electrical, and lifetime characteristics are analysed.

- **Chapter VIII** summarizes the conclusions for each of the chapters and details future works

1.9 References

[1] IPCC, *Global Warming of 1.5°C.An IPCC Special Report on the impacts of global warming of 1.5°C above pre-industrial levels and related global greenhouse gas emission pathways, in the context of strengthening the global response to the threat of climate change,*. Cambridge, UK: Cambridge University Press, 2018.

[2] H. Lee *et al.*, *IPCC Sixth Assessment Report - Synthesis Report*. 2022.

[3] M. W. Jones *et al.*, "National contributions to climate change due to historical emissions of carbon dioxide, methane and nitrous oxide," doi: 10.5281/ZENODO.14054503.

[4] IRENA, *Renewable Generation Costs in 2022*. 2022.

[5] IEA, "Snapshot of Global PV Markets 2014," 2015. [Online]. Available: http://www.iea-pvps.org/fileadmin/dam/public/report/technical/PVPS_report_A_Snapshot_of_Global_PV_1992-2014.pdf.

[6] PVknowhow, "China solar growth Reaches 1 TW: Stunning 56.9% Increase in 2024," 2025. https://www.pvknowhow.com/news/china-solar-growth-reaches-1-tw-stunning-56-9-increase-in-2024/ (accessed Jun. 26, 2025).

[7] Solar Power Europe, "Global Market Outlook For Solar Power 2024 - 2028," 2024. [Online]. Available: http://www.solarpowereurope.org/insights/global-market-outlook/.

[8] D. M. Chapin, C. S. Fuller, and G. L. Pearson, "A new silicon p-n junction photocell for converting solar radiation into electrical power," *J. Appl. Phys.*, vol. 25, no. 5, pp. 676–677, 1954, doi: 10.1063/1.1721711.

[9] J. Liu *et al.*, "Perovskite-silicon tandem solar cells with bilayer interface passivation," *Nature*, vol. 635, no. November, 2024, doi: 10.1038/s41586-024-07997-7.

[10] Frauhofer-ISE, "Fraunhofer ISE Develops the World's Most Efficient Solar Cell with 47.6 Percent Efficiency," 2022. https://www.ise.fraunhofer.de/en/press-media/press-releases/2022/fraunhofer-ise-develops-the-worlds-most-efficient-solar-cell-with-47-comma-6-percent-efficiency.html (accessed Jul. 09, 2025).

[11] U. Wurfel, A. Cuevas, and P. Wurfel, "Charge carrier separation in solar cells," *IEEE J. Photovoltaics*, vol. 5, no. 1, pp. 461–469, 2015, doi: 10.1109/JPHOTOV.2014.2363550.

[12] S. M. Sze and M. K. Lee, *Semiconductor devices: Physics and technology*, 3rd ed. John Wiley and Sons Inc, 2012.

[13] A. H. M. Smets, K. Jäger, O. Isabella, R. A. van Swaaij, and M. Zeman, *Solar energy the physics and engineering of photovoltaic conversion technologies and systems*. Cambridge, UK, 2016.

[14] A. Augusto, S. Y. Herasimenka, R. R. King, S. G. Bowden, and C. Honsberg, "Analysis of the recombination mechanisms of a silicon solar cell with low bandgap-voltage offset," *J. Appl.*

Phys., vol. 121, no. 20, 2017, doi: 10.1063/1.4984071.

[15] M. A. Green, “Accurate expressions for solar cell fill factors including series and shunt resistances,” *Appl. Phys. Lett.*, vol. 108, no. 8, 2016, doi: 10.1063/1.4942660.

[16] W. Shockley and H. J. Queisser, “Detailed balance limit of efficiency of p-n junction solar cells,” *J. Appl. Phys.*, vol. 32, no. 3, pp. 510–519, 1961, doi: 10.1063/1.1736034.

[17] A. Richter, M. Hermle, and S. W. Glunz, “Reassessment of the limiting efficiency for crystalline silicon solar cells,” *IEEE J. Photovoltaics*, vol. 3, no. 4, pp. 1184–1191, 2013, doi: 10.1109/JPHOTOV.2013.2270351.

[18] T. Niewelt *et al.*, “Reassessment of the intrinsic bulk recombination in crystalline silicon,” *Sol. Energy Mater. Sol. Cells*, vol. 235, p. 111467, 2022, doi: 10.1016/j.solmat.2021.111467.

[19] G. Wang *et al.*, “27.09%-Efficiency Silicon Heterojunction Back Contact Solar Cell and Going Beyond,” *Nat. Commun.* , vol. 15, no. 1, pp. 1–12, 2024, doi: 10.1038/s41467-024-53275-5.

[20] D. Yan *et al.*, “Silicon solar cells with passivating contacts: Classification and performance,” *Prog. Photovoltaics Res. Appl.*, vol. 31, no. October 2021, pp. 310–326, 2022, doi: 10.1002/pip.3574.

[21] L. M. Antognini, “Contact Design for Silicon Heterojunction Solar Cells,” Ph.D. dissertation, École Polytechnique Fédérale de Lausanne, Lausanne, Switzerland, 2022.

[22] P. Wurfel, *Physics of Solar Cells: From Principles to New Concepts*, 1st ed. Weinheim, Germany: Wiley-VCH Verlag, 2005.

[23] PV lighthouse, “Recombination calculator,” 2025. https://www2.pvlighthouse.com.au/calculators/recombination calculator/recombination calculator.aspx (accessed Jul. 04, 2025).

[24] L. G. Gerling Sarabia, “Characterization of alternative carrier selective materials and their application to heterojunction solar cells,” Ph.D. dissertation, Universitat Politécnica de Catalunya, Barcelona, Spain, 2017.

[25] E. Genç, “Font Side Solutions for c-Si Solar Cells with High-Temperature Passivating Contacts,” Ph.D. dissertation, École Polytechnique Fédérale de Lausanne, Lausanne, Switzerland, 2024.

[26] L. Hanssen and S. Kaplan, “Problems posed by scattering transmissive materials for accurate transmittance and reflectance measurements,” *SPIE Conf. Opt. Diagnostic Methods InorganicTransmissive Mater.*, 1998.

[27] CRU and K. PVEL, “Hot topics and key questions for the solar industry in 2025 Solar Technology and Cost Service,” 2025. https://www.kiwa.com/globalassets/usa/pvel/resources/2025-q1-stac-webinar-slides-kiwa-pvel-cru-1.pdf (accessed Oct. 01, 2025).

[28] F. Fu *et al.*, "Monolithic Perovskite-Silicon Tandem Solar Cells: From the Lab to Fab?," *Adv. Mater.*, vol. 34, no. 24, 2022, doi: 10.1002/adma.202106540.

[29] E. Bellini, "JA Solar claims world record open-circuit voltage for TOPCon solar cell – pv magazine International," 2024. https://www.pv-magazine.com/2024/12/16/ja-solar-claims-world-record-open-circuit-voltage-for-topcon-solar-cell/ (accessed Feb. 15, 2025).

[30] Z. C. Holman *et al.*, "Current losses at the front of silicon heterojunction solar cells," *IEEE J. Photovoltaics*, vol. 2, no. 1, pp. 7–15, 2012, doi: 10.1109/JPHOTOV.2011.2174967.

[31] K. Yoshikawa *et al.*, "Silicon heterojunction solar cell with interdigitated back contacts for a photoconversion efficiency over 26%," *Nat. Energy*, vol. 2, no. 5, pp. 1–8, Mar. 2017, doi: 10.1038/nenergy.2017.32.

[32] R. A. Afre and D. Pugliese, "Perovskite Solar Cells: A Review of the Latest Advances in Materials, Fabrication Techniques, and Stability Enhancement Strategies," *Micromachines*, vol. 15, no. 2, 2024, doi: 10.3390/mi15020192.

[33] M. H. Miah, M. U. Khandaker, M. B. Rahman, M. Nur-E-Alam, and M. A. Islam, "Band gap tuning of perovskite solar cells for enhancing the efficiency and stability: issues and prospects," *RSC Adv.*, vol. 14, no. 23, pp. 15876–15906, 2024, doi: 10.1039/d4ra01640h.

[34] A. R. Zanatta, "The Shockley–Queisser limit and the conversion efficiency of silicon-based solar cells," *Results Opt.*, vol. 9, no. November, p. 100320, 2022, doi: 10.1016/j.rio.2022.100320.

[35] C. Li, Y. Wang, and W. C. H. Choy, "Efficient Interconnection in Perovskite Tandem Solar Cells," *Small Methods*, vol. 4, no. 7, pp. 1–19, 2020, doi: 10.1002/smtd.202000093.

[36] M. De Bastiani, A. S. Subbiah, E. Aydin, F. H. Isikgor, T. G. Allen, and S. De Wolf, "Recombination junctions for efficient monolithic perovskite-based tandem solar cells: Physical principles, properties, processing and prospects," *Mater. Horizons*, vol. 7, no. 11, pp. 2791–2809, 2020, doi: 10.1039/d0mh00990c.

[37] A. Puaud, "Understanding and Optimisation of transport mechanisms in Perovskite on Silicon Heterojunction Tandem Solar Cells Apolline Puaud To cite this version : HAL Id : tel-03462780 Compréhension et Optimisation des mécanismes de transport dans les cellules Tande," 2021.

[38] Ö. Ş. Kabaklı *et al.*, "Thickness Optimization of Front and Recombination ITO in Monolithic Perovskite/Silicon Tandem Solar Cells," *Sol. RRL*, vol. 2400454, pp. 1–10, 2024, doi: 10.1002/solr.202400454.

[39] W. Chen *et al.*, "N-type polysilicon passivating contact combined with hydrogen-containing TCO as the interconnected structure for perovskite/silicon tandem solar cells," *Sol. Energy Mater. Sol. Cells*, vol. 238, no. October 2021, p. 111622, 2022, doi:

10.1016/j.solmat.2022.111622.

[40] R. N. Hall, "Tunnel Diodes," *IRE Trans. Electron Devices*, vol. 7, no. 1, pp. 1–9, 1960, doi: 10.1109/T-ED.1960.14584.

[41] J. Bullock *et al.*, "Efficient silicon solar cells with dopant-free asymmetric heterocontacts," *Nat. Energy*, vol. 1, no. 3, 2016, doi: 10.1038/NENERGY.2015.31.

[42] E. Fortunato, D. Ginley, H. Hosono, and D. C. Paine, "Transparent Conducting Oxides for Photovoltaics," *Mrs Bull.*, vol. 32, no. March 2007, pp. 242–247, 2017.

[43] A. Facchetti and T. J. Marks, *Transparent Electronics From Synthesis to Applications*. Wiltshire, Great Britain: John Wiley & Sons, Ltd, 2010.

[44] P. K. Chakraborty, G. C. Datta, and K. P. Ghatak, "The simple analysis of the Burstein – Moss shift in degenerate n-type semiconductors," vol. 339, pp. 198–203, 2003, doi: 10.1016/j.physb.2003.07.001.

[45] J. Gwamuri, M. Marikkannan, J. Mayandi, P. K. Bowen, and J. M. Pearce, "Influence of oxygen concentration on the performance of ultra-thin RF magnetron sputter deposited indium tin oxide films as a top electrode for photovoltaic devices," *Materials (Basel).*, vol. 9, no. 1, 2016, doi: 10.3390/ma9010063.

[46] O. Tuna, Y. Selamet, G. Aygun, and L. Ozyuzer, "High quality ITO thin films grown by dc and RF sputtering without oxygen," *J. Phys. D. Appl. Phys.*, vol. 43, no. 5, 2010, doi: 10.1088/0022-3727/43/5/055402.

[47] G. T. Chavan *et al.*, "A Brief Review of Transparent Conducting Oxides (TCO): The Influence of Different Deposition Techniques on the Efficiency of Solar Cells," 2023.

[48] F. Meyer *et al.*, "Optimization of front SiNx/ITO stacks for high-efficiency two-side contacted c-Si solar cells with co-annealed front and rear passivating contacts," *Sol. Energy Mater. Sol. Cells*, vol. 219, 2021, doi: 10.1016/j.solmat.2020.110815.

[49] Ö. Ş. Kabaklı *et al.*, "Optimizing the Ito Interconnection Layer for Monolithic Perovskite Silicon," no. September, pp. 18–22, 2023.

[50] G. Huang *et al.*, "Influence of Deposition Parameters of ITO Films on the Performance of HJT Solar Cells," *Int. J. Photoenergy*, vol. 2023, 2023, doi: 10.1155/2023/1065503.

[51] L. Tutsch, F. Feldmann, B. MacCo, M. Bivour, E. Kessels, and M. Hermle, "Improved Passivation of n-Type Poly-Si Based Passivating Contacts by the Application of Hydrogen-Rich Transparent Conductive Oxides," *IEEE J. Photovoltaics*, vol. 10, no. 4, pp. 986–991, 2020, doi: 10.1109/JPHOTOV.2020.2992348.

[52] Z. Lu, "Universal energy-level alignment of molecules on metal oxides," *Nat. Mater.*, vol. 11, no. 1, pp. 76–81, 2011, doi: 10.1038/nmat3159.

[53] C. Battaglia *et al.*, "Silicon heterojunction solar cell with passivated hole selective MoO x

contact," *Appl. Phys. Lett.*, vol. 104, no. 11, Mar. 2014, doi: 10.1063/1.4868880.

[54] J. Melskens *et al.*, "Passivating Contacts for Crystalline Silicon Solar Cells: From Concepts and Materials to Prospects," *IEEE J. Photovoltaics*, vol. 8, no. 2, pp. 373–388, 2018, doi: 10.1109/JPHOTOV.2018.2797106.

[55] Y. Wang, S. T. Zhang, L. Li, X. Yang, L. Lu, and D. Li, "Dopant-free passivating contacts for crystalline silicon solar cells: Progress and prospects," *EcoMat*, vol. 5, no. 2, pp. 1–29, 2023, doi: 10.1002/eom2.12292.

[56] J. Ibarra Michel, J. Dréon, M. Boccard, J. Bullock, and B. Macco, "Carrier-selective contacts using metal compounds for crystalline silicon solar cells," *Prog. Photovoltaics Res. Appl.*, vol. 31, no. 4, pp. 380–413, 2022, doi: 10.1002/PIP.3552.

[57] B. Bilal and H. Najeeb-ud-Din, "Fundamentals of and Recent Advances in Carrier Selective Passivating Contacts for Silicon Solar Cells," *J. Electron. Mater.*, vol. 50, no. 7, pp. 3761–3772, Jul. 2021, doi: 10.1007/S11664-021-08933-5.

[58] S. Acharyya *et al.*, "Dopant-free materials for carrier-selective passivating contact solar cells: A review," *Surfaces and Interfaces*, vol. 28, no. August 2021, p. 101687, 2022, doi: 10.1016/j.surfin.2021.101687.

[59] X. Yang *et al.*, "Atomic Layer Deposition of Vanadium Oxide as Hole-Selective Contact for Crystalline Silicon Solar Cells," vol. 2000467, pp. 1–8, 2020, doi: 10.1002/aelm.202000467.

[60] D. K. Nandi and S. K. Sarkar, "Atomic layer deposition of tungsten oxide for solar cell application," *Energy Procedia*, vol. 54, pp. 782–788, 2014, doi: 10.1016/j.egypro.2014.07.321.

[61] F. Pérez-Zenteno *et al.*, "High-pressure sputtering deposition and in situ plasma oxidation of TiOx thin films as electron selective contact for photovoltaic applications," *Mater. Sci. Semicond. Process.*, vol. 186, no. October 2024, 2025, doi: 10.1016/j.mssp.2024.109038.

[62] C. J. Leach, B. E. Davis, B. M. Garland, R. Thorpe, and N. C. Strandwitz, "Ultrathin atomic layer deposited niobium oxide as a passivation layer in silicon based photovoltaics," *J. Appl. Phys.*, vol. 130, no. 21, Dec. 2021, doi: 10.1063/5.0067281.

[63] P. Tyagi, "Ultrathin TaOx film based photovoltaic device," *Thin Solid Films*, vol. 519, no. 7, pp. 2355–2361, Jan. 2011, doi: 10.1016/J.TSF.2010.11.039.

[64] W. Li *et al.*, "Passivating Contacts for Crystalline Silicon Solar Cells: An Overview of the Current Advances and Future Perspectives," *Adv. Energy Mater.*, vol. 14, no. 18, pp. 1–29, 2024, doi: 10.1002/aenm.202304338.

[65] H. Mehmood, H. Nasser, T. Tauqeer, and R. Turan, "Simulation of silicon heterostructure solar cell featuring dopant-free carrier-selective molybdenum oxide and titanium oxide contacts," *Renew. Energy*, vol. 143, pp. 359–367, 2019, doi: 10.1016/j.renene.2019.05.007.

[66] K. Tao *et al.*, "The impact of indium tin oxide deposition and post annealing on the passivation

property of TOPCon solar cells," *Sol. Energy*, vol. 176, no. July, pp. 241–247, 2018, doi: 10.1016/j.solener.2018.10.034.

[67] S. Zhong *et al.*, "Exploring co-sputtering of ZnO:Al and SiO 2 for efficient electron-selective contacts on silicon solar cells," *Sol. Energy Mater. Sol. Cells*, vol. 194, pp. 67–73, 2019, doi: 10.1016/j.solmat.2019.02.005.

[68] J. M. Pachlhofer *et al.*, "Non-reactive dc magnetron sputter deposition of Mo-O thin films from ceramic MoOx targets," *Surf. Coatings Technol.*, vol. 332, no. July, pp. 80–85, 2017, doi: 10.1016/j.surfcoat.2017.07.083.

[69] M. S. B. De Castro, C. L. Ferreira, and R. R. De Avillez, "Vanadium oxide thin films produced by magnetron sputtering from a V 2O5 target at room temperature," *Infrared Phys. Technol.*, vol. 60, pp. 103–107, 2013, doi: 10.1016/j.infrared.2013.03.001.

[70] Q. Yang *et al.*, "Origin of sputter damage during transparent conductive oxide deposition for semitransparent perovskite solar cells," *J. Mater. Chem. A*, vol. 12, no. 24, pp. 14816–14827, 2024, doi: 10.1039/d3ta06654a.

[71] B. J. H. Stadler, *Vapor Processes*. Elsevier Inc., 2016.

[72] P. Feijoo, "High permitivity dielectric for next generations of integrated circuits," Ph.D. dissertation, Universidad Complutense de Madrid, Madrid, Spain, 2013.

[73] U. Poppe *et al.*, "Direct production of crystalline superconducting thin films of YBa2Cu3O7 by high-pressure oxygen sputtering," *Solid State Commun.*, vol. 66, no. 6, pp. 661–665, 1988, doi: 10.1016/0038-1098(88)90228-1.

[74] U. Poppe *et al.*, "Low-resistivity epitaxial YBa2Cu3O7 thin films with improved microstructure and reduced microwave losses," *J. Appl. Phys.*, vol. 71, no. 11, pp. 5572–5578, 1992, doi: 10.1063/1.350535.

[75] S. Duẽas *et al.*, "A comparative study of the electrical properties of TiO2 films grown by high-pressure reactive sputtering and atomic layer deposition," *Semicond. Sci. Technol.*, vol. 20, no. 10, pp. 1044–1051, 2005, doi: 10.1088/0268-1242/20/10/011.

[76] F. L. Martínez *et al.*, "Optical properties and structure of HfO2 thin films grown by high pressure reactive sputtering," *J. Phys. D. Appl. Phys.*, vol. 40, no. 17, pp. 5256–5265, 2007, doi: 10.1088/0022-3727/40/17/037.

[77] Z. Gao, M. F. Romero, A. Redondo-Cubero, M. A. Pampillon, E. San Andres, and F. Calle, "Effects of Gd2O3 Gate Dielectric on Proton-Irradiated AlGaN/GaN HEMTs," *IEEE Electron Device Lett.*, vol. 38, no. 5, pp. 611–614, 2017, doi: 10.1109/LED.2017.2682795.

[78] M. A. Pampillón, E. San Andrés, P. C. Feijoo, and J. L. G. Fierro, "High-k gadolinium scandate on Si obtained by high pressure sputtering from metal targets and in-situ plasma oxidation," *Semicond. Sci. Technol.*, vol. 32, no. 3, 2017, doi: 10.1088/1361-6641/aa58cc.

[79] D. Caudevilla *et al.*, “Indium tin oxide obtained by high pressure sputtering for emerging selective contacts in photovoltaic cells,” *Mater. Sci. Semicond. Process.*, vol. 137, 2022, doi: 10.1016/j.mssp.2021.106189.

[80] F. J. P. Zenteno *et al.*, “High Pressure Sputtering of Mo Targets in Mixed Ar/O2/H2Atmospheres for Hole Selective Contacts in Photovoltaic Cells,” *14th Spanish Conf. Electron Devices, CDE 2023 - Proc.*, pp. 7–10, 2023, doi: 10.1109/CDE58627.2023.10339461.

CHAPTER II: FABRICATION TECHNIQUES

2.1 Substrates

During the development of this thesis, different substrates were used to determine the properties of the materials under study. The following is a brief description of each substrate and the type of measurements it was used for:

- Determination of deposition rate for ITO and Ti and verification of Ti oxidation: glass substrate 2.2 x 2.2 cm^2 with a thickness of ~ 0.16 mm from *AmScope.*

- Verification of Ti oxidation: n-type Si wafers, float zone, double side polish, high resistivity (1100 – 3000 Ωcm), <100> orientation and 300 µm thickness, purchased from ITME (*Institute of Electronic Materials Technology*).

- Optical characterization of ITO and TiO_x (absorption and band gap measurements): fused quartz 2.2 x 2.2 cm^2 with a thickness of ~0.5 mm from *Micro to Nano.* This substrate was used in lieu of a glass substrate since the fused quartz has a larger bandgap (~7.6 eV) [1] than optical glasses (~4.0 eV) [2]. This lower bandgap could affect the correct measurement of the thin film bandgap, leading to misinterpretations.

- Devices (Cox & Strack and solar cells): n-type Si wafer, float zone, double side polish, low resistivity (1 – 5 Ωcm), <100>, and 300 µm thickness, purchased from *TOPSIL.*

2.2 Substrate Cleaning Process

Substrate cleaning is a critical step before material deposition to ensure high-quality thin films with optimal adhesion, uniformity, and performance. Contaminants such as organic residues, particulates, and metal ions can lead to defects, poor film adhesion, and unwanted chemical reactions that degrade the deposited layers' electrical, optical, or mechanical properties. For instance, in semiconductor and

optoelectronic applications, surface contamination can introduce charge traps or scattering centres, affecting device efficiency [3].

During the development of this thesis, the glass and quartz substrates were cleaned using acetone dipping to remove organic residues from the surface. After this, isopropyl alcohol (C_3H_8O), also known as IPA, removes residual acetone, which may leave contaminants after evaporation. Finally, we performed a deionized water (DIW) rinse, followed by drying with Ar stream to remove any remaining solvent.

Proper cleaning is crucial before any deposition process with Si substrates. One of the most widely used recipes in the industry is the RCA (*Radio Corporation of America*) cleaning procedure, created by Werner Kern in the 1970s [4]. This cleaning aims to remove organic and metallic contaminants present on the surface of the Si and it has been the workhorse in Si device manufacturing. The cleaning steps used during the development of this thesis were as follows:

1. Immersion in IPA to remove the main organic contaminants. This is performed for a couple of minutes at room temperature.

2. Standard Clean 1 (SC-1): immersion in H_2O:NH_4OH:H_2O_2 (5:1:1) solution for 10 min at a temperature between 70-75ºC. This step eliminates organic contaminants and metals such as Cu, Au, Ag, Zn, and Ni. Besides, this process dissolves the wafer's native oxide while forming a new oxide.

3. Rinse with deionized water (DIW) to eliminate residues from SC1 and reduce the sample temperature. The DIW system provides water with a resistivity of 18.2 MΩcm.

4. Standard Clean 2 (SC-2): immersion in H_2O:HCl:H_2O_2 (5:1:1) solution for 10 min at a temperature between 70-75ºC. With this step, the ionic residues, metals such as Au and Ag, and metal hydroxides including $Al(OH)_3$, $Fe(OH)_3$, $Mg(OH)_2$, and $Zn(OH)_2$ are removed.

5. The last step is dipping the samples in DIW to remove SC-2 residuals and drying with Ar stream.

Before loading the sample to the vacuum chamber, it is immersed in HF:H_2O (1:50) for 1 min at room temperature to remove the oxide grown during the RCA cleaning process. This process produces a hydrophobic Si surface. After this step, it is important to introduce the sample to the processing chamber as fast as possible to avoid the regrowth of native oxide. Additionally, for the case of the high-pressure sputtering (HPS), before any process, the substrates were heated at 150 ºC in vacuum. The

goal was the H_2O desorption from the sample and the chamber walls. The H_2O might be introduced when the deposition chamber is opened to the clean room atmosphere during the sample loading.

2.3 Sputtering

Sputtering is a physical vapor deposition (PVD) technique widely used for depositing thin layers in semiconductor industries. It relies on extracting atoms of a specific target, such as titanium, by bombarding it with ionized particles. The mixture of all the ionized and excited particles creates the characteristic plasma. Since the ions are charged particles, when a voltage is applied between the target and the substrate holder, the particles will be accelerated toward the electrode with the opposite sign. There are typically two types of power sources to accelerate the ionized particles, alternating at radio frequency, typically 13.56 MHz, (RF) and direct current (DC). Normally, RF is preferred over DC when dielectric targets (oxides ort nitrides) want to be sputtered. The alternating electric field prevents charge buildup on the target surface by periodically reversing the polarization and thus avoiding plasma extinction. Additionally, the RF or DC power source is connected to an impedance-matching network to reduce the reflected power [5].

Thin films deposited by sputtering exhibit properties that clearly distinguish them from those obtained by evaporation techniques. Sputtered coatings are typically denser, less porous, and adhere more strongly to the substrate, while also providing improved uniformity over large areas. The resulting microstructure depends strongly on deposition conditions, in particular the working pressure and substrate temperature, which can lead to amorphous, nanocrystalline, or polycrystalline films. In conventional sputtering processes, the working pressure is usually in the 10^{-3} mbar range. As discussed in the previous section, variations in this parameter significantly affect both the growing film and the substrate surface. For example, an increase in working pressure has been correlated with a larger grain size, which in turn can modify key electrical and optical properties of the deposited films [6].

2.3.1 Reactive sputtering

Typically, noble gases such as Ar are used to bombard the target and thus deposit the material. These gases have the advantage of not reacting chemically with the target material or substrate. Nevertheless, in some cases, a reactive atmosphere is used to interact with the deposited material. For instance, for the deposition of TCOs, O_2 is usually introduced to keep the exact stoichiometry in the deposited

material as the one on the target material. Another example is an H_2 atmosphere, which is sometimes used to increase the conductivity of selective contacts such as MoO_x [7] or to induce the passivation of defects such as ITO:H [8]. Although this approach can be interesting for obtaining oxidated or hydrogenated layers, caution must be taken since the target could also interact with the plasma species. The interaction between O_2 and the target might create a thin layer on the surface that can hinder the target species extraction and thus the sputtering yield decreases. This effect has been observed when metal targets are used in a reactive atmosphere, and it is frequently referred as target poisoning [9]. Therefore, if the goal is to deposit the same material as the target, a conditioning step would be necessary to remove the layer that has grown on its surface.

The conditioning step typically involves sputtering the target with a non-reactive gas such as Ar until the unwanted surface layer is removed. It is important to monitor the voltage between the substrate and the target to determine when the target has been cleaned since this value changes as a function of the sputtered material. For instance, if the same power is used, dielectric materials such as TiO_2 need a higher voltage than metal targets. Figure 2-1 depicts this situation, where the voltage is shown as a function of RF power for a Ti and TiO_x target with and without an O_2 atmosphere. As soon as O_2 is introduced into the chamber, the voltage required for sputtering the Ti target increases. This can be explained by the growth of a TiO_x layer on the surface, which changes the sputtering yield. Since the e^- binding of the Ti-O molecule (459 eV) is higher than in the Ti-Ti molecule (454 eV) [10], the ion-induced secondary electron emission decreases, i.e., for each ion bombardment, fewer secondary electrons are coming from the target, making it more challenging to maintain plasma with the same ion energy (voltage) [9]. Therefore, it is necessary to increase the voltage to keep the RF power constant. This effect has also been observed in the deposition of VO_x through a V target with an O_2-reactive atmosphere [11]. When oxides targets such as TiO_x, there is no apparent change when O_2 is introduced into the chamber since the surface is already an oxide.

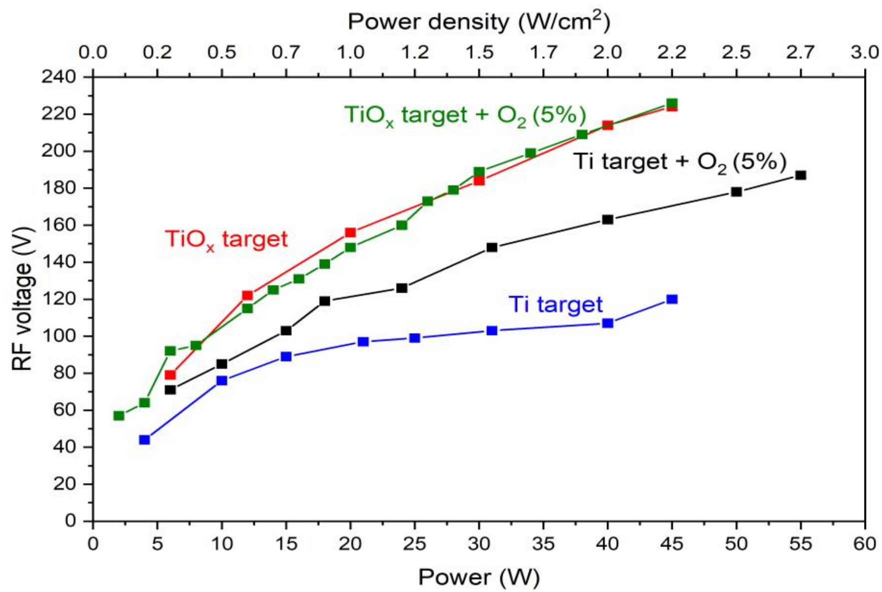

Figure 2-1 RF voltage as a function of the power for Ti and TiOx with and without O2, obtained from HPS system

2.3.2 RF sputtering

A standard RF sputtering system was used during the four-month stay at PV-Lab (EFPL) to deposit ITO:H. The system is a *Univex* RF sputtering from *Leybold*. This system was adapted to supply three gas lines: pure Ar, mixed Ar/O_2 (95%/5%), and mixed Ar/H_2 (95%/5%). Each gas line is controlled by a mass flow controller with a maximum mass flow rate of 50 sccm, 10 sccm, and 10 sccm, respectively. An ITO target (90 % In_2O_3 + 10 % SnO_2) manufactured by *Umicore* with a purity of 99.99 % was used. The deposition process was performed at room temperature with the substrate holder rotated at a velocity of 10 rpm to improve the homogeneity of the deposition. The distance between the substrate holder and the target is approximately 15 cm. The power of the RF source was always maintained below 200 W to mitigate the degradation of the ITO target. As it is common for sputtering targets, it has a circular shape with a 4” diameter (10.16 cm). Thus, the power density was kept in the 0.4 Wcm^{-2} to 2.4 Wcm^{-2} range. The following figure shows an image of the system.

Figure 2-2 RF sputtering system at PV-Lab (EPFL) used to deposit ITO:H

2.4 High-Pressure Sputtering (HPS)

The main deposition technique used during this thesis was HPS. This technique is explained in Chapter I from a physics point of view. In this section, the HPS system is described from a more technological (engineering) perspective.

The HPS system schematic and photograph are shown in Figure 2-3 and Figure 2-4 respectively. This system includes three targets attached to a robotized arm that allows the deposition of different combinations of films without breaking the vacuum. During this work, we used a Ti target from Kurt J. Lesker Company (50.8 mm diameter, 3.2 mm thick, and 99.995% purity) and an indium-tin oxide target 90-10% from Testbourne (50.8 mm diameter, 3.2 mm thick, and 99.99% purity). The residual pressure obtained after one day of pumping is typically ~10^{-6} mbar. This was the residual pressure before all the deposition processes performed during this work. To achieve this pressure, the deposition chamber is evacuated using two turbomolecular pumps connected in series. The first is a *HiCube* system from *Pfeiffer*, which includes a turbomolecular pump and a membrane pump that operates simultaneously. This setup is considered the backing pump. Additionally, the system is equipped with a second turbomolecular pump directly connected to the deposition chamber, backed by a membrane pump.

A *TRUMPF* Hüttinger PFG 300 radio frequency (RF) power source connected to a matching box is used to ignite the plasma. This power source's frequency is 13.56 MHz, and its maximum power is 300 W. However, due to target refrigeration limitations, the power during deposition was always under 50 W (~2.5 W/cm^2). Furthermore, this system includes three gas lines (Ar, O_2, and H_2) connected to a mass flow controller (MFC), with a maximum flux of 436 sccm for the Ar line and 40 sccm for the O_2 and H_2 lines.

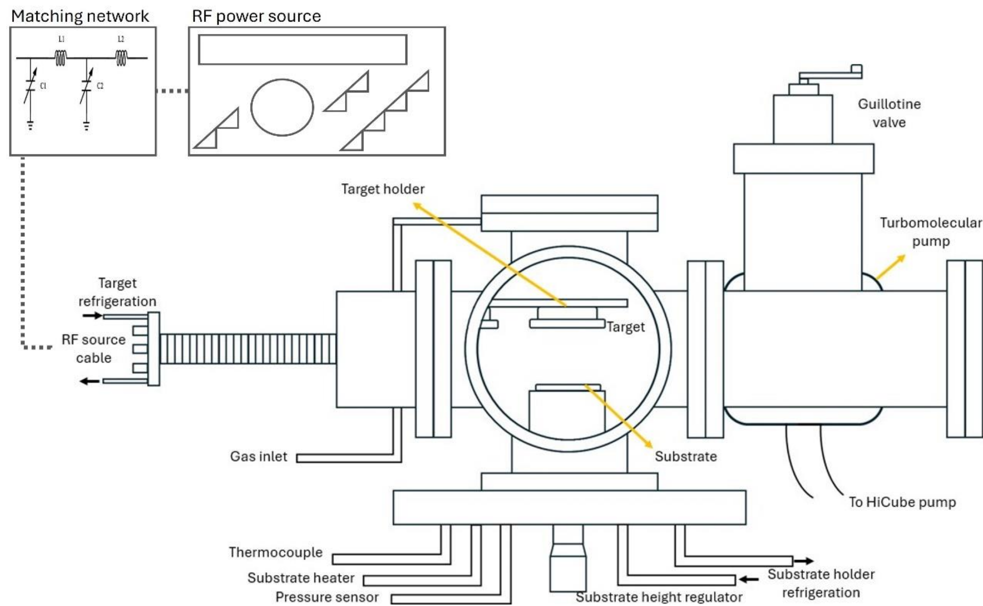

Figure 2-3 Schematic of the high-pressure sputtering system used during this thesis.

Figure 2-4 Photograph of the high-pressure sputtering system used during this thesis to deposit ITO and TiO_x films.

2.5 Ion Implantation

An essential technique used during this work was ion implantation. This technique introduces elements (dopants) into a substrate, typically a semiconductor such as Si or Ge. These dopants are the key to the success of the microelectronics and photovoltaic industries, as they allow for the modification of semiconductors' electrical and optical properties.

Specifically in the photovoltaic industry, dopants are often introduced using diffusion furnaces, as in PERC-type cells, where the emitter is typically fabricated through diffusion processes. However, this technique has the disadvantage of requiring high temperatures (~800 °C) to enable dopant diffusion. Moreover, the doping profile, i.e., the concentration of the diffused element as a function of depth, is less controllable than ion implantation [12].

For this reason, from a PV research point of view, ion implantation is an attractive technique for doping semiconductors at room temperature while achieving more controlled doping profiles. In this work, we used a *Varian IMC200* ion implanter, refurbished by Ion Beam Services (IBS) France, (Figure 2-5). This equipment is housed in *Centro de Asistencia a la Investigación* (CAI) *de técnicas físicas* facilities at the *Universidad Complutense de Madrid* (UCM). This ion implanter can introduce various elements at energies typically between 15 and 185 keV and temperatures between -196 °C and 400 °C, making it highly versatile for tailoring the doping process to specific material and device requirements.

During the development of this thesis, phosphorus was implanted on the rear side of the Si samples to ensure good ohmic contact for the Cox & Strack samples and obtain the specific contact resistivity of the TiO_x/c-Si(n) junction. The implantation condition was 32 keV, reaching a dose of $4x10^{15}$ cm^{-2}. Finally, the implanted impurities were activated with a Rapid Thermal Annealing (RTA) at 1000 °C for 120 s in an Ar atmosphere.

Figure 2-5 Ion implantation system at CAI of physical techniques from UCM.

The ion implantation process can briefly be described in the three following steps:

1. **Extraction and acceleration of ions**: In this stage, the ions to be implanted are generated and extracted. In the case of phosphorous, the precursor is P powder. It is heated in a ceramic vacuum tube from which P evaporates. Once the P is in the gas phase, it is injected directly into a Freeman ion source. This kind of ion source consists of a cylindrical chamber with a concentric filament that emits electrons by thermionic emission. The plasma is produced by applying a potential difference (around 60 V) between the filament and the inner wall of the chamber and an axial magnetic field. Typically, Ar is introduced as a carrier gas for starting the plasma as P is gradually introduced. Finally, the ions are extracted by applying a potential difference of 32 kV between the Freeman source and the extractor.

Figure 2-6 Freeman source employed to extract phosphorus.

2. **Ion selection and alignment**: Once the ions leave the Freeman source, they pass through an electromagnet that determines which ions will be implanted. This is possible because a magnetic field perpendicular to the ion flow exerts a force described by Lorentz's law, causing a curvature in their trajectory. The following formula can describe this curvature [13].

$$r = \frac{mv}{qB} \quad 2.3$$

   Where r is the radius of the curvature, B is the magnetic field, m is the mass, q is the ion charge, and v is the velocity of the ion. In that sense, an ion with a specific mass-charge relationship can be selected.

   After selecting the ion to be implanted, it is accelerated to the desired implantation energy. Additionally, the ion beam is aligned using magnetic quadrupoles. Finally, deflection plates scan the beam vertically and horizontally in a random pattern to assure uniform implantation across the entire sample.

3. **Substrate holder and dose calculation**: When the ions reach the substrate placed on the sample holder, the total dose can be measured with a Faraday cup. The ion beam hits a metal collector, which gains a small charge while the incoming ions are neutralized. Once the metal is discharged, the small current can be measured. This is proportional to the number of ions implanted. Then, the total doses can be measured with the following expression.

$$N = \frac{1}{A}\int_0^T \frac{I(t)}{q}\,dt \qquad 2.4$$

Where N is the implanted dose in cm^{-2}, I is the measured current, q is the charge of the ion, A is the implanted area, and t is the implantation time.

The ion beam impacting the sample can produce secondary electrons. Those electrons could alter the dose measurement. Therefore, the system includes a Faraday cup, which includes a collector cylinder with a ring polarized at -500 V on top of it. With these elements, the secondary electrons are trapped on the collector. This setup is concentric to the substrate holder.

2.5.1 Rapid Thermal Annealing

Once the material has been introduced into the substrate, it is necessary to activate the impurities to dope the substrate. Rapid thermal annealing (RTA) is an ideal technique to achieve that. With this technique, the heating occurs in a few minutes using halogen or infrared lamps. After keeping the annealing temperature for several seconds, the lamp heating stops and the sample cools down with a rate that depends on its thermal inertia. Caution must be taken to avoid thermal shock that could damage the sample. Typically, this equipment works in controlled atmospheres such as Ar or forming gas (10% H_2 and 90% N_2) to avoid sample oxidation. One aspect to consider is cross contamination, so ideally the substrate holders should be dedicated to process only one kind of sample.

Throughout this thesis, we used the MPTC RTP 600 equipment located in the facilities of the CAI of UCM. This equipment can work in temperatures from 250 to 1300 ºC, with a ramp-up between 0 and 150 ºC/s. The maximum time depends on the working temperature; for example, for a temperature of 1000ºC, the maximum processing time is 6 min.

Figure 2-7 Rapid thermal annealing system employed to activate the impurities introduced during the ion implantation process.

2.6 Thermal/Electron-beam Evaporator

Thermal or electron-beam evaporators are classified as physical vapor deposition since the deposited film comes from heating the material until it reaches its evaporation temperature. When the melted material is in a high vacuum, the evaporated atoms travel in a straight line until they reach the substrate and condense to produce the thin film. The deposition rate can be controlled by adjusting the temperature of the material being evaporated. The thickness of the deposited film is measured in real time using a quartz crystal microbalance (QCM). This consists of a crystal resonator connected to an alternating electric field, which creates mechanical oscillation in the quartz. When the evaporated material reaches the QCM, its mass increases, thus decreasing its resonant frequency. As the frequency shift is proportional to the density of the material, this value must be introduced in the control software to determine the final thickness.

The difference between thermal and e-beam evaporation is the heating source. In thermal evaporation, the material is placed in a crucible (normally Tungsten) and heated until the material evaporates; however, this is limited to low-melting-point materials as the crucible and material start to interact at high temperatures. In an electron-beam evaporator, a high-energy e-beam directly heats a localized area of the material and evaporates it. This technique allows the evaporation of materials with higher melting points, such as refractory metals (Mo, Ta, W) [14], oxides (SiO_2, TiO_2, Al_2O_3) [15], or

thermally stable materials (SiC) [16]. Many e-beam evaporators, such as the one used in this thesis, have a rotating crucible holder to evaporate different materials without breaking the vacuum.

During this thesis, we used a *Classic 250 evaporator* from *Pfeiffer*. This equipment includes a thermal evaporator and an e-beam evaporator (maximum e-beam power of 5 kW), allowing the deposition of two layers in the same process. The pressure required to start evaporation, typically 10^{-7} mbar, is obtained by a turbomolecular pump with the support of a rotary pump.

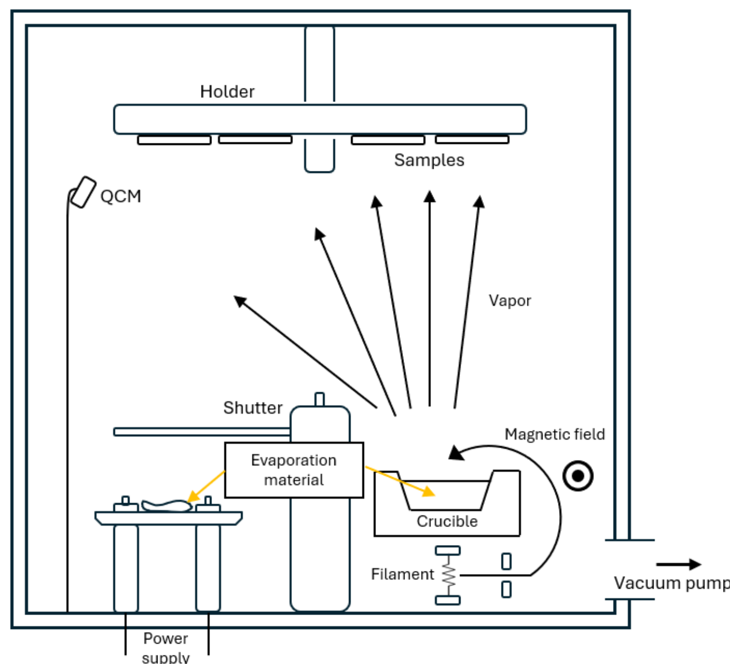

Figure 2-8 Scheme of the thermal/e-beam evaporator used for metal deposition

2.7 Plasma Enhanced Chemical Vapor Deposition (PECVD)

Another fabrication technique used during this thesis was plasma-enhanced chemical vapor deposition (PECVD). Unlike sputtering or evaporation, which are classified as physical vapor deposition, chemical vapor deposition (CVD) relies on the chemical reaction of different precursor gases to deposit the desired film. High temperatures are typically necessary when films are grown by classical CVD systems, generally between 600 ºC and 1000 ºC. These high temperatures promote a stronger reaction between the precursor gases and the substrate, producing the film. In contrast, PECVD is considered a low-temperature CVD since it is a plasma that promotes the growth of the film. This allows the deposition at lower substrate temperatures, typically between 100 ºC and 400 ºC. Nowadays, this

technique is widely used for the deposition of SiO_x [17], SiN_x [18], SiC [19], a-Si:H, and doped a-Si:H [20]. The following table shows the precursor gases commonly used for depositing these materials.

Table 2-1 Precursor gasses employed for depositing the materials normally fabricated by PECVD.

Material	Precursor gasses
SiO_x	SiH_4 / O_2
SiN_x	SiH_4 / N_2
SiC	SiH_4 / CH_4
a-Si:H	SiH_4/ H_2
a-Si:H (n)	SiH_4 / PH_3
a-Si:H (p)	SiH_4 / $B(CH_3)_3$

It is important to note that PECVD systems usually require several safety systems since many of the precursor gases used can be hazardous or even lethal. For example, silane (SiH_4) is pyrophoric in contact with air, while trimethylborane (TMB) ($B(CH_3)_3$), and phosphine (PH_3) are highly toxic.

In this thesis, two different PECVD systems were used. The first PECVD is located at *Centro de Investigaciones Energéticas, Medioambientales y Tecnológicas* (CIEMAT) from *Elettrorava s.p.a* house. This tool has a parallel-plate configuration with an electrode dimension of 17.5 x 17.5 cm^2 with a distance between both electrodes of 10 mm. An RF source (13.56 MHz) generates the plasma, and the system normally works with a pressure range between 2.6 and 3 mbar during the deposition. The temperature of the substrate is kept constant at 180 ºC for all the deposition processes. With this system, a-Si(i), a-Si(n), and a-Si(p) were deposited on top of n-type Si samples. The details on power density and gas fluxes are shown in the following table.

Table 2-2 Fabrication details of the materials fabricated with the PECVD system at CIEMAT. [1] amorphous silicon hydrogenated (a-Si:H) to inhibit the epitaxial growth, [2] a-Si:H to passivate dangling bonds at the interface

Material	Power density (mW/cm^2)	Precursor gases fluxes (sccm)
a-Si:H[1]	49	SiH_4 : 20 / H_2 : 20
a-Si:H[2]	10	SiH_4 : 20 / H_2 : 120
a-Si:H (n)	20	SiH_4 : 20 / H_2 : 150 / PH_3 (2% in H_2) : 8
a-Si:H (p)	15	SiH_4 : 5 / H_2 : 20 - 100 / TMB (2% in H_2) : 7.5

The second PECVD is located at EPFL – PVLab facilities, which was made by the company *Unaxis.* This system also has a parallel-plate configuration with electrode dimensions of 50.2 x 61.2 cm2 and a distance between them of 15 mm. An RF source generates plasma at a frequency of 40 MHz. The temperature was kept at 200 ºC for the experiments with a pressure of 0.7 mbar. With this system, a-SiCx:H(n) was deposited on top of n-type Si samples. Both PECVD systems used during this thesis have a parallel-plate configuration. A schematic of this kind of configuration is depicted in Figure 2-9.

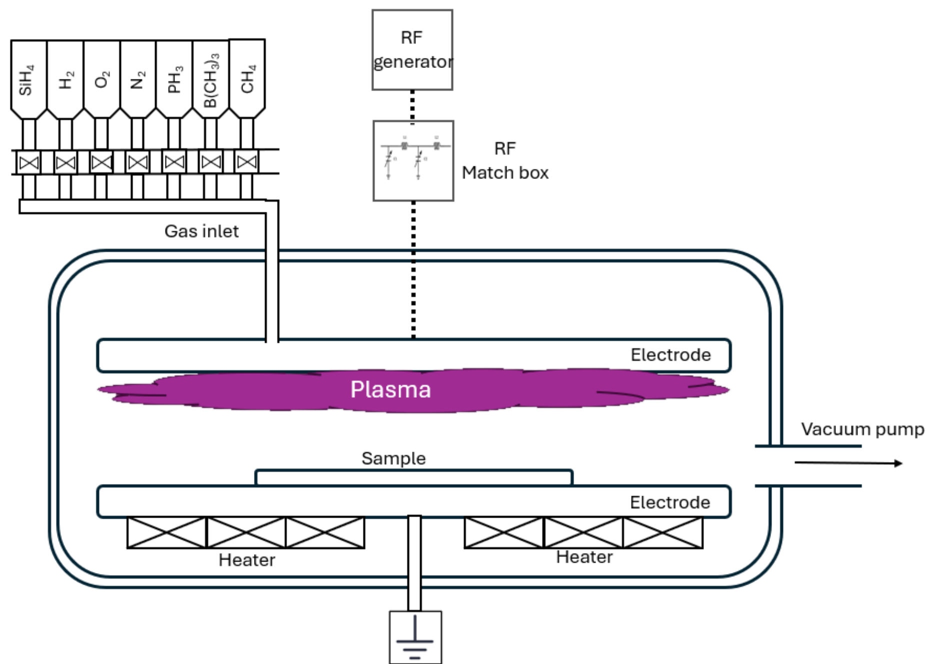

Figure 2-9 Schematic of a PECVD with parallel-plate configuration.

2.8 Photolithography

Photolithography is a crucial microfabrication technique used in semiconductor manufacturing to define intricate patterns on a substrate. The process involves depositing a light-sensitive material called photoresist on top of the substrate. The photoresist is selectively exposed to ultraviolet (UV) light through a mask that contains the desired pattern. Depending on the type of photoresist used (positive or negative), the exposed regions are either removed or retained. After this step, the patterned sample undergoes etching or material deposition to create the functional structures of semiconductor devices. Finally, a special chemical removes the remaining photoresist (lift-off process).

An important aspect of photolithography is the system's resolution since it defines the minimum size that can be accurately resolved. The resolution is determined by the Rayleigh criterion, which is expressed as follows.

$$CD = K_1 \frac{\lambda}{NA} \tag{2.5}$$

Where *CD* is the critical dimension, K_1 is a coefficient that depends on the system (typically in the range of 0.25 to 0.8 [21]), λ is the wavelength of the exposure light, and *NA* is the numerical aperture of the optical system.

During the development of the this thesis, an UV photolithography system *Karl-Suss MJB3 mask aligner*, which incorporates an Hg lamp with emission lines at 405 nm and 365 nm, was used. This system allows a maximum resolution of 0.8 µm. The Hg lamp is regulated by a *SUSSMicroTec* brand *CIC1200* constant intensity controller to radiate in a stable and controlled manner in one of the two emission lines. The photoresists are homogenized by a *PWM101 Headway Research spinner*, and heat treatments are performed on an *Isotemp RT Advanced ceramic hot plate* from *Fisherbrand*. For the negative photolithography, the *AZ NLOF* photoresist was used; in the case of positive photolithography, the *AZ 4533* photoresist and *TI primer* adhesion promoter were used. The *AZ 826 MIF* was employed as a developer both processes. Finally, the lift-off process was done using *TechniStrip Micro D350*. The entire system belongs to the *CAI* and is located in the clean room of the UCM.

For the contact resistivity of TiO_x/SiO_x/c-Si(n) and TiO_x/a-Si:H(i)/c-Si(n), a Cox & Strack (C&S) mask was employed, Figure 2-10 a). This mask consisted of four groups with eight circular contacts. The diameter of the contacts ranged between 5000 and 98 µm, and the defined area for all the patterns is

1.5 x 1.5 cm^2. Additionally, a TLM mask was patterned to determine the contact resistivity of the metal stack/Si(n^{++}), which was the rear part for the C&S samples, Figure 2-10 b).

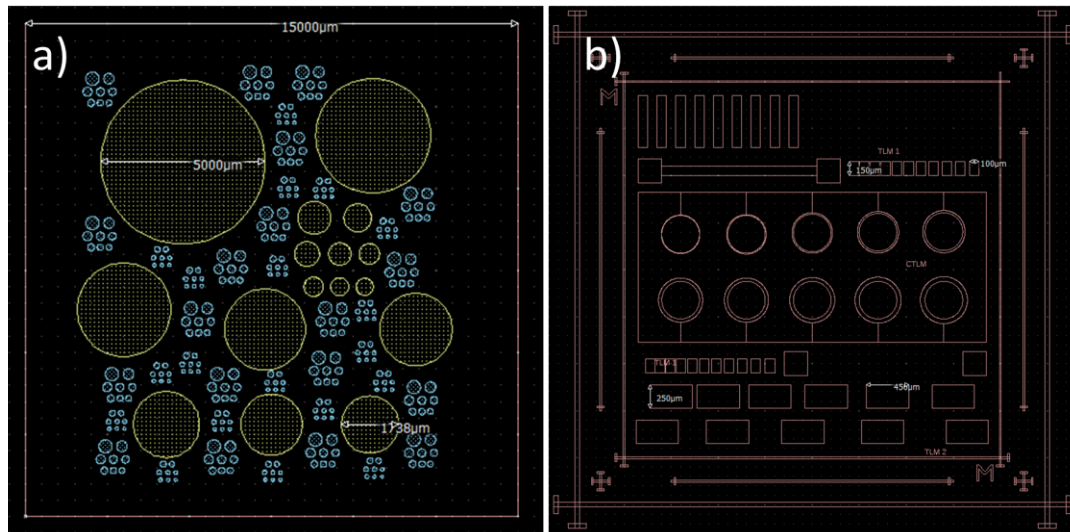

Figure 2-10 Photolithography masks: a) Cox & Strack mask and b) Transfer length method (TLM) mask. Both masks were used to measure the specific contact resistivity of the analysed materials.

Finally, another mask was used to define the frontal contact of the solar cell. This is shown in Fig. 2-3. It has five fingers of 60 µm in an active area of 1x1 cm^2 and has an external busbar of 500 µm. The function of the external busbar is to minimize the shading of the active area and thus improve carrier collection of the device. The shading that the fingers produce represents 0.30% of the active area.

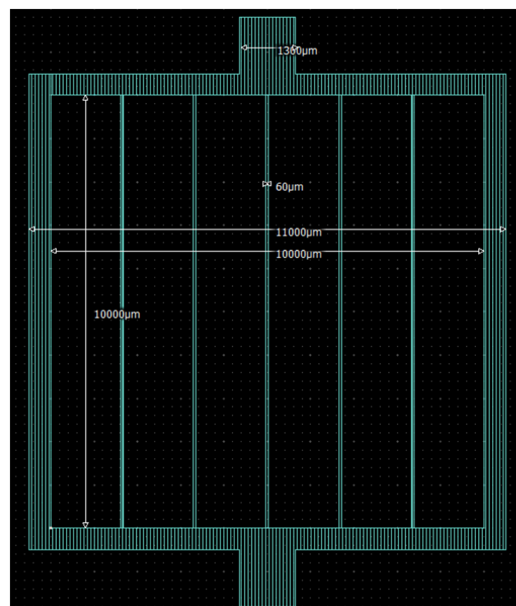

Figure 2-11 Photolithography mask for the frontal contact of the heterojunction solar cell fabricated.

2.9 Flash Lamp Annealing

Flash Lamp Annealing (FLA) is an annealing technique that works in the millisecond range. This makes it an intermediate option between RTA annealing (min) and laser annealing (LA) (ns). On the one hand, it reduces the thermal budget by working shorter times than RTA but achieving similar temperatures. On the other hand, unlike LA, where the heated area is a single spot, FLA can process a complete wafer since the Xe lamps illuminate the whole sample. Additionally, it has the advantage that only the illuminated area is modified, i.e., the bulk remains intact. This allows the minimization of the diffusion of impurities by making sharper dopant profiles [22] and making out-of-equilibrium processes. For instance, FLA allows obtaining hyperdoped materials [23], which is another topic under study in our research group.

Energy density must be absorbed to achieve a certain target temperature. The sample's reflectance must be considered to adjust the correct energy density. This is expressed in the following expression.

$$E_{abs} = E_0(1 - R) \qquad 2.6$$

Where E_{abs} is the energy density to be absorbed in Jcm^{-2}, E_0 is the energy density applied by the FLA system in Jcm^{-2}, and R is the reflectance of the samples at the wavelength of the maximum emission of the lamp (500 nm for the Xe lamps). As an example, the temperature profile of the surface of a c-Si substrate as a function of time and energy density is depicted in Figure 2-12.

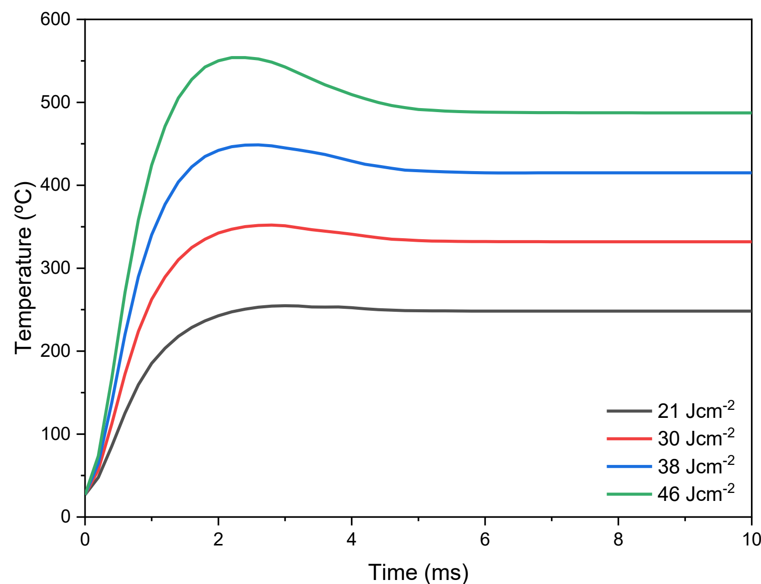

Figure 2-12 Temperature profile for a 300 µm Si wafer with several absorbed energy density.

During this thesis, an FLA system fabricated by *Helmholtz Zentrum Dresden Rossendorf* (HZDR) was used. A traditional setup of an FLA system is depicted in Figure 2-13. The processes were also done in HZDR, and it was used to anneal TiO_x/a-Si:H(i) samples to study the effect of FLA on the minority carrier lifetime. This system can work with a pulse duration range of 0.65 – 20 ms and an energy density of up to 200 Jcm^{-2}. The maximum substrate size that can be introduced is 15x15 cm, and the annealing process can be performed under N_2, Ar, O_2, or forming gas.

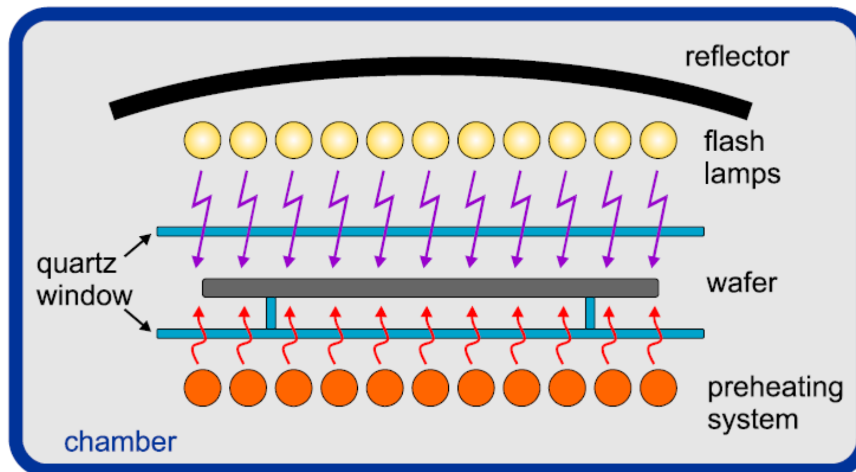

Figure 2-13 Scheme of a traditional FLA system for semiconductor processing. Scheme taken from [22].

2.10 Reference

[1] R. French and R. Abou-Rahme, “Absorption Edge and Band Gap of SiO~ 2 Fused Silica Glass,” *Ceramic Transactions*, vol. 28. pp. 63–81, 1992, [Online]. Available: http://csegroups.case.edu/vuv/files/9203absedgebandgapfusedsilicaceramtrans.pdf.

[2] B. Nagamani and C. Srinivasu, “Optical Band Gap of glass - Various Techniques,” no. 10, pp. 4–6, 2018.

[3] K. C. Lee and M. Weis, “Charge Traps in Wide-Bandgap Semiconductors for Power Electronics Applications,” *Inorganics*, vol. 12, no. 10, 2024, doi: 10.3390/inorganics12100257.

[4] W. Kern, “Evolution of silicon wafer cleaning technology,” *Proc. - Electrochem. Soc.*, vol. 90, no. 9, pp. 3–19, 1990, doi: 10.1149/1.2086825.

[5] S. Wolf, *Silicon Processing for the VLSI Era, Volume 1: Process Technology*, 2nd ed. Sunset Beach, CA, USA: Lattice Press, 2004.

[6] E. A. I. Ellis, M. Chmielus, S. Han, and S. P. Baker, “Effect of sputter pressure on microstructure and properties of β-Ta thin films,” *Acta Mater.*, vol. 183, pp. 504–513, 2020,

doi: 10.1016/j.actamat.2019.10.056.

[7] F. J. P. Zenteno *et al.*, "High Pressure Sputtering of Mo Targets in Mixed Ar/O2/H2Atmospheres for Hole Selective Contacts in Photovoltaic Cells," *14th Spanish Conf. Electron Devices, CDE 2023 - Proc.*, pp. 7–10, 2023, doi: 10.1109/CDE58627.2023.10339461.

[8] L. Tutsch, F. Feldmann, B. MacCo, M. Bivour, E. Kessels, and M. Hermle, "Improved Passivation of n-Type Poly-Si Based Passivating Contacts by the Application of Hydrogen-Rich Transparent Conductive Oxides," *IEEE J. Photovoltaics*, vol. 10, no. 4, pp. 986–991, 2020, doi: 10.1109/JPHOTOV.2020.2992348.

[9] M. Arif and C. Eisenmenger-Sittner, "In situ assessment of target poisoning evolution in magnetron sputtering," *Surf. Coatings Technol.*, vol. 324, pp. 345–352, 2017, doi: 10.1016/j.surfcoat.2017.05.047.

[10] D. Briggs, "X-ray photoelectron spectroscopy (XPS)," *Handb. Adhes. Second Ed.*, pp. 621–622, 2005, doi: 10.1002/0470014229.ch22.

[11] X. Wei *et al.*, "Preparation and characteristics of vanadium oxide thin films by controlling the sputtering voltage," *Opt. Mater. (Amst).*, vol. 36, no. 8, pp. 1419–1423, 2014, doi: 10.1016/j.optmat.2014.02.021.

[12] Y. Wang, M. H. Chi, J. J. C. Lou, and C. Z. Chen, *Handbook of Integrated Circuit Industry*. 2023.

[13] D. Halliday, R. Resnick, and J. Walker, *Fundamentals of Physics*, 10th ed. Hoboken, NJ, USA: Wiley, 2014.

[14] K. ichi Mori, K. Kobayashi, K. Takayanagi, K. Yagi, and G. Honjo, "Electron beam evaporator for in situ deposition studies of refractory metal thin films in UHV electron microscope," *Jpn. J. Appl. Phys.*, vol. 19, no. 1, pp. 183–189, 1980, doi: 10.1143/JJAP.19.183.

[15] V. Matkivskyi, Y. Lee, H. S. Seo, D. K. Lee, J. K. Park, and I. Kim, "Electronic-beam evaporation processed titanium oxide as an electron selective contact for silicon solar cells," *Curr. Appl. Phys.*, vol. 32, no. September, pp. 98–105, 2021, doi: 10.1016/j.cap.2021.10.005.

[16] J. Zheng, L. Ye, Y. Hu, Y. Huang, J. Yu, and T. Chen, "Effect of substrate temperature and annealing on the structure and opto-electrical properties of silicon carbide thin films prepared by e-beam evaporation," *Vacuum*, vol. 211, no. August 2022, 2023, doi: 10.1016/j.vacuum.2023.111979.

[17] A. M. Mahajan, L. S. Patil, J. P. Bange, and D. K. Gautam, "Growth of SiO2 films by TEOS-PECVD system for microelectronics applications," *Surf. Coatings Technol.*, vol. 183, no. 2–3, pp. 295–300, 2004, doi: 10.1016/j.surfcoat.2003.09.056.

[18] Y. Wan, K. R. McIntosh, and A. F. Thomson, "Characterisation and optimisation of PECVD SiNx as an antireflection coating and passivation layer for silicon solar cells," *AIP Adv.*, vol. 3,

no. 3, 2013, doi: 10.1063/1.4795108.

[19] S. Bau, S. Janz, T. Kieliba, C. Schetter, S. Reber, and F. Lutz, "Application of PECVD-SIC as intermediate layer in crystalline silicon thin-film solar cells," *Proc. 3rd World Conf. Photovolt. Energy Convers.*, vol. B, pp. 1178–1181, 2003.

[20] J. Ramanujam and A. Verma, "Photovoltaic properties of a-Si:H films grown by plasma enhanced chemical vapor deposition: A review," *Mater. Express*, vol. 2, no. 3, pp. 177–196, 2012, doi: 10.1166/mex.2012.1073.

[21] J. T. Azpiroz, "Analysis and modeling of photomask near-fields in sub-wavelength deep ultraviolet lithography with optical proximity corrections," *Thesis*, 2004, [Online]. Available: http://proquest.umi.com.turing.library.northwestern.edu/pqdweb?did=813784081&Fmt=7&clientId=30032&RQT=309&VName=PQD.

[22] L. Rebohle, S. Prucnal, and W. Skorupa, "A review of thermal processing in the subsecond range: Semiconductors and beyond," *Semicond. Sci. Technol.*, vol. 31, no. 10, pp. 1–38, 2016, doi: 10.1088/0268-1242/31/10/103001.

[23] S. Prucnal, L. Rebohle, and W. Skorupa, "Doping by flash lamp annealing," *Mater. Sci. Semicond. Process.*, vol. 62, no. October 2016, pp. 115–127, 2017, doi: 10.1016/j.mssp.2016.10.040.

CHAPTER III: CHARACTERIZATION TECHNIQUES

3.1 Plasma characterization

3.1.1 Optical Emission Spectroscopy (OES)

In a plasma process, numerous collisions occur among ions, electrons, and atoms, causing the plasma species to gain energy. When these atoms return to their ground state, they release part of this energy as photons. The wavelength of the emitted photons depends on the excitation level of the atoms and their ground state. This energy difference is characteristic of each atom, so by measuring the energy of the emitted photons, the plasma composition can be identified. Therefore, optical emission spectroscopy (OES) is a helpful characterization technique to monitor plasma composition in real time.

The HPS system is equipped with a *StellarNet BlueWave* spectrometer with three detectors for different wavelength ranges. Combining the three of them, we can detect photons in the 200–850 nm range with a resolution of 0.25 nm. This is achieved using a charge-coupled device (CCD) sensor with 2048 elements. Figure 3-1 shows the schematic of the HPS system with the OES tool as it is implemented. It features three optical fibers that observe the plasma through a sapphire window. These optical fibers are resistant to UV overexposure, and they are connected to the spectrometer, which is linked to a PC via USB. The plasma can be monitored on the PC using the *SpectraWiz* software, which saves spectra at intervals $\geq$ 1 s. Further analysis, such as species determination or integration of a specific wavelength range, was performed using *Spectragryph*, a free software developed by Dr. Friedrich Menges [1].

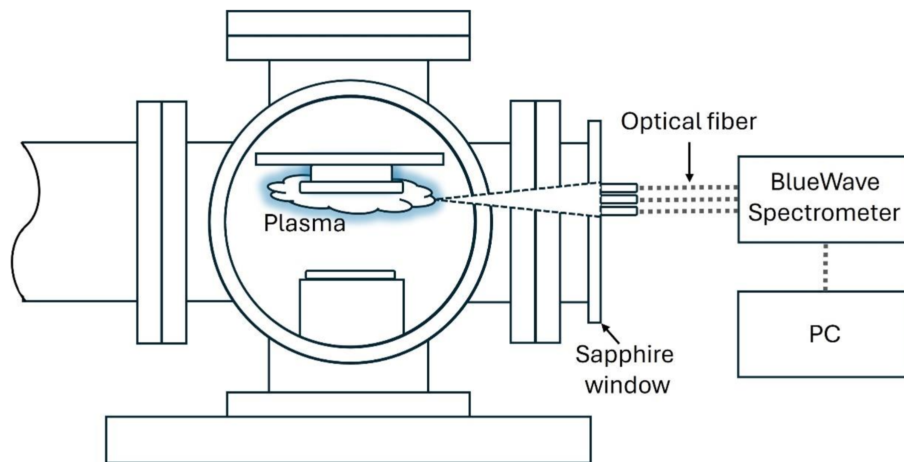

Figure 3-1 HPS system with an optical emission spectroscopy tool to monitor the species in the plasma.

3.2 Structural characterization

3.2.1 Profilometer

A profilometer is a technique used to measure changes in the film's topography. It utilizes a stylus to trace the sample's height change; the variations are then converted into an electrical signal, which is processed to generate a surface profile. The stylus tip typically features capacitive sensors to enhance the measurement's sensitivity. The system used in this thesis was the *Sloan Dektak 900050*, which was digitalized using LabVIEW and a *DAQ NI USB-6009* board to control and acquire data through a PC. The resolution of the equipment is in the order of a few tens of nanometers. This tool was used to determine the thickness of the ITO and Ti films and thus obtain the deposition rate of such materials under different deposition conditions.

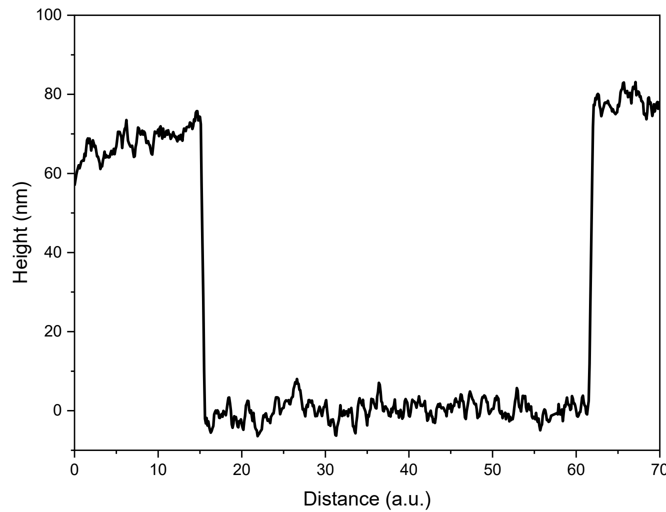

Figure 3-2 Example of an ITO film (~80 nm) measured by the Dektak profilometer.

3.2.2 X-ray photoemission spectroscopy (XPS)

X-ray photoemission spectroscopy is a surface-sensitive technique for analyzing the chemical composition and bonding of thin films. It was developed by the Swedish physicist Siegbahn in the 1960s. It is based on the photoelectric effect, where an X-ray beam irradiates a sample, causing the ejection of the core-level electrons from the sample atoms. The kinetic energy of these electrons is related to their binding energy, which is characteristic of each element. An electron energy analyzer detects the kinetic energy, allowing the calculation of their binding energy and thus revealing the sample's chemical composition and oxidation states. According to the photoelectric effect explained by Einstein in 1905 [2], the relationship between the kinetic energy of the electrons (E_k) and their binding energy (BE) is given by the following expression:

$$E_k = h\nu - BE - q\Phi_{sp} \qquad 3.1$$

Where $q\Phi_{sp}$ is the work function of the spectrometer (to consider the energy losses in the system), and $h\nu$ is the incident X-ray beam energy. Al K_α (1486.6 eV) and Mg K_α (1253.6 eV) are the most used X-ray sources. Due to their relatively low X-ray energy, XPS has a depth sensitivity of ~10 nm [3]. A basic schematic of an XPS system is depicted in the following figure.

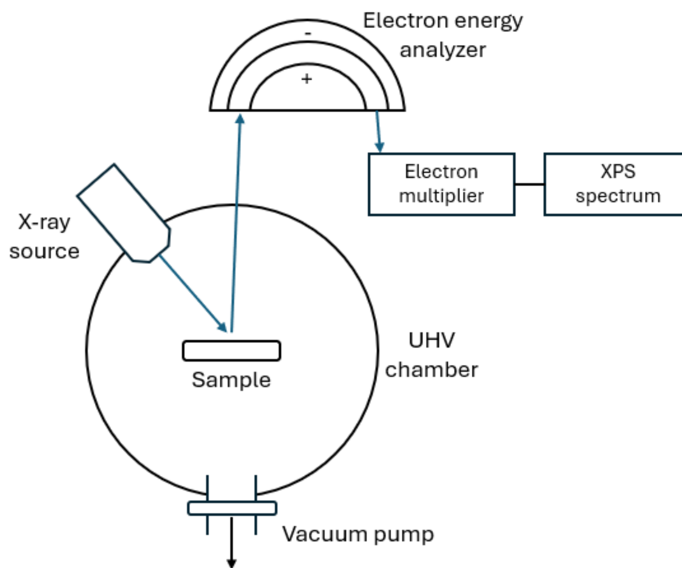

Figure 3-3 Basic scheme of an XPS system

It is worth mentioning that XPS detects not only photoelectrons but also Auger-emitted electrons. Unlike photoelectrons, which are directly ejected by the X-ray beam, Auger electrons result from the relaxation of an excited electron to an inner shell vacancy, transferring the excess energy to another electron that is then emitted. This process generates Auger peaks that are independent of the X-ray source, enabling us to compare the results across different XPS systems [4].

In this thesis, XPS was employed to determine the stoichiometry of TiO_x films deposited by HPS. The measurements and analyses were performed at *Centro Nacional de Investigaciones Metalúrgica* (CENIM). The XPS system was a *Fisons MT500* spectrometer equipped with a hemispherical electron analyzer (CLAM2) and a non-monochromatic Mg K_α X-ray source operated at 300 W. The samples were fixed on small flat discs supported on an XYZ manipulator placed in the analysis chamber. During data acquisition, the residual pressure in this ion-pumped analysis chamber was maintained at an ultra-high vacuum (UHV) level of 10^{-9} mbar. The spectra were collected at a pass energy of 20 eV, typical of high-resolution conditions. Spectra were analyzed using *CasaXPS* software. The intensities were estimated by calculating the area under each peak after subtracting the S-shaped background and fitting the experimental curve to combine Lorentzian and Gaussian lines of variable proportions. Although specimen charging was observed, it was possible to determine accurate binding energies (*BEs*) by referencing to the adventitious C1s peak at 285.0 eV. The maximum allowed variation in the binding energy was ±0.2 eV relative to the value specified for the peak center. The atomic ratios were computed from the peak intensity ratios and the reported atomic sensitivity factors [5].

3.2.3 Grazing Incidence X-ray diffraction (GIXRD)

X-ray diffraction (XRD) is a non-destructive technique for determining the crystal structure of materials. This technique involves directing an X-ray beam to analyze the sample. Once the beam reaches the sample, its crystalline planes give rise to the diffraction of the photons, which originate constructive and destructive interference peaks. This is due to the wavelength of the X-ray source, which is of the same order of magnitude as the interatomic distances in the crystals (0.15 – 0.5 nm) [6]. The most common X-ray source is the Cu, which has its K_α and K_β characteristics emission lines at 0.154 nm and 0.139 nm, respectively [7]. The Bragg equation explains the relationship between the diffracted X-ray and the lattice spacing.

$$n\lambda = 2d_{hkl}sin\theta_B \quad 3.2$$

Where d_{hkl} is the interplanar distance of a crystallographic plane with *hkl* Miller indices, λ is the wavelength of the incident beam, n is an integer referring to the order of the diffraction peak, and θ_B is the Bragg angle.

Depending on the XRD system configuration and accessories, many measurement methods can be performed. The most common methods are the 2θ/ω scan, the grazing-incidence XRD (GIXRD), rocking curves, and pole figures [6]. Nevertheless, in this thesis, only GIXRD was used to analyze the crystalline structure of the TiO_x, ITO, and ITO:H thin films. The GIXRD method enables surface analysis of samples at the nanometer scale. This contrasts with traditional 2θ/ω scans, which have a penetration depth of 1–100 µm, and thus thin films do not provide enough diffracted signal to be detected. In GIXRD, the incidence angle ω is fixed to small angles (0.5 – 1º), and the detector is moved in a 2θ angle to obtain the data. This is done to enhance the intensity of the film's peaks while reducing the contribution of the substrate. A schematic diagram of the GIXRD configuration is shown in the following figure.

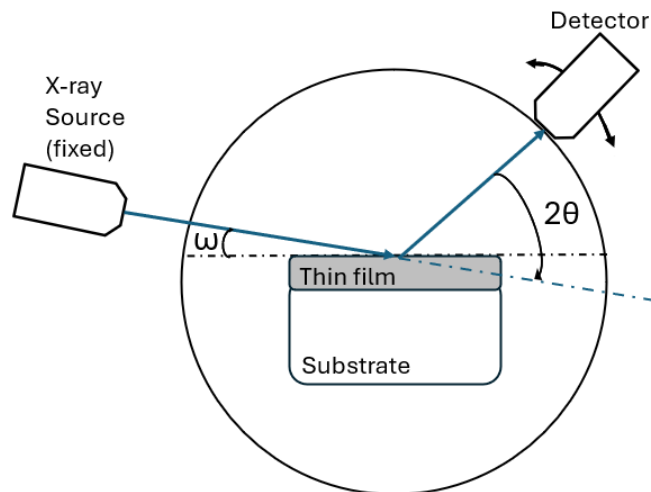

Figure 3-4 Schematic of GIXRD setup used to analyze thin film samples.

The diffraction patterns were obtained at CAI *de difracción de rayos-X* at UCM using a *Philips Xpert PRO MRD*. A copper tube (using K_α emission line, 0.154nm) with 45 kV and 40 mA power was used. In the incident optics, a parabolic mirror was used to obtain a parallel beam. A parallel plate collimator was used for the grazing incidence measurements in the diffracted beam optics. The measurement was performed in a 2θ range of 20° to 90°, with a 2θ step of 0.05°, and the measuring time was 3 seconds per step. To mitigate the contribution of the Si substrate, the incident angle (ω) was kept constant at 0.5º for all the samples.

3.2.4 Transmission Electron Microscopy (TEM)

Transmission Electron Microscopy (TEM) is an analytical technique in which high-energy electrons are transmitted through a sample to form an image. Typically, the electrons are accelerated to 80 – 300 keV. The sample to be analyzed must have a thickness of less than 200 nm to allow for the transmission of electrons [8]. In that sense, the sample needs to be thinned to create a lamella. This can be achieved through mechanical polishing or by using a Focused Ion Beam (FIB) [9]. FIB is a relatively expensive but very accurate technique for creating lamellae; it involves the gradual thinning of the sample by a focused beam (usually Ga^+ ions) until the desired thickness is achieved. During this process, it is necessary to deposit a Pt layer to manipulate and dissipate the electric charges induced to the sample. The entire process is visualized using Scanning Electron Microscopy (SEM). An example of a lamella attached to a FIB lift-out grid is depicted in the following image.

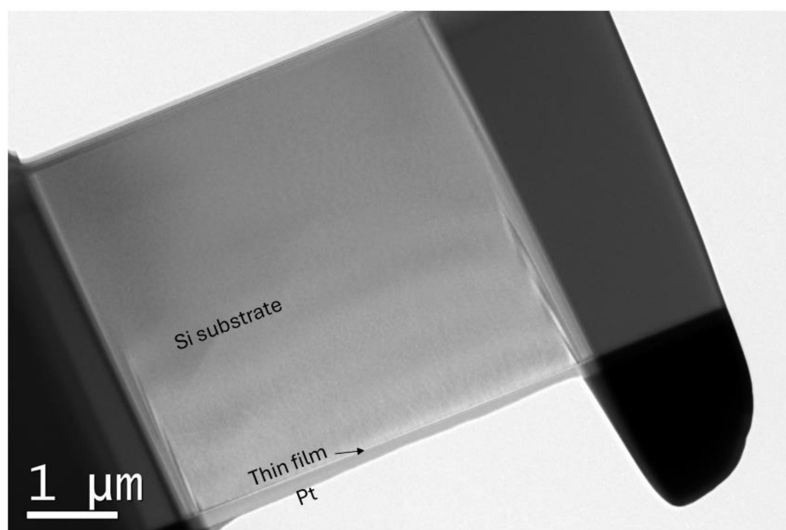

Figure 3-5 TEM image of a lamella attached to a FIB lift-out grid.

Additionally, some TEM systems incorporate chemical analysis of the sample through X-ray Energy Dispersive Spectroscopy (XEDS). This technique is based on the interaction of high-energy TEM electrons with the atoms of the sample. When the electrons of these excited atoms relax to lower energy states, they release photons (X-rays) that allow their identification.

During this thesis, the *JEOL 2100 HT* system from *Centro Nacional de Microscopía Electrónica* (CNME) was used to characterize the oxidation process of Ti using HPS. It has a resolution of 0.25 nm and operates at a voltage of 200 kV. A double-tilt sample holder was used to orient the lamella, and XEDS analysis was done using the *Oxford Instruments INCA* microanalysis system. The lamellae were fabricated in *Laboratorio de Microscopía Avanzada* (LMA) at the University of Zaragoza using a *Helios Nanolab 650* system.

3.3 Electrical characterization

3.3.1 Four-point probe

The four-point probe is a technique widely used to measure the sheet resistance of thin films. When the thickness is known, the resistivity can be also determined. In comparison to the two-point probe, this technique eliminates the contact resistance errors since the voltage and current are measured by

different probes. For thin film characterization, the probes are aligned in a straight line with equal spacing (collinear four-point probe). The outer probes are used for current injection, while the inner probes measure the voltage.

The most general expression for obtaining resistivity with a collinear four-point probe is given by the following equation.

$$\rho = 2\pi sF\frac{V}{I} \qquad 3.3$$

Where *s* is the probe spacing, and *F* is the correction factor that considers sample thickness, diameter, and probe placement [10]. For samples that fulfill the requirement that their thickness is less than two times the probe spacing, the expression is simplified and thus the resistivity and sheet resistance can be calculated with the following expressions

$$\rho = \frac{\pi}{\ln(2)} t \frac{V}{I} \qquad 3.4$$

$$R_{sh} = \frac{\rho}{t} = \frac{\pi}{\ln(2)}\frac{V}{I} \qquad 3.5$$

Where ρ is the resistivity, R_{sh} is the sheet resistance, *t* is the thickness of the layer, *V* is the voltage measured, and *I* is the current applied. The sheet resistance is an important parameter for characterizing semiconductors, as it measures the lateral resistance per unit area of a film with uniform thickness [11]. In the case of materials for photovoltaic applications, some materials need a low sheet resistance to achieve the lateral transport of the photogenerated carriers, for instance ITO films [12], or the highly doped emitter of photovoltaic cells.

During this thesis, we used an automated four-point probe CMT-SR2000PV system. It has a probe separation of 1 mm; therefore, the previous expression was used to determine the sheet resistance of the thin films. It allows us to measure the sample with an injected current range from 100 nA to 100 mA. Additionally, the system can measure in different locations of the sample to create sheet resistance maps. This equipment was used to characterize the Si (n^{++}) implanted layers, and the TiO_x, and ITO films deposited by HPS.

3.3.2 Hall effect and the van der Pauw configuration

Hall effect measurement is a powerful characterization technique to determine the resistivity, carrier concentration, and mobility of semiconductors. This effect was discovered by Edwin Hall in 1879 while he was investigating the impact of applying a magnetic field to a conductor carrying an electric current [13]. The carriers are affected in their trajectory due to the presence of the magnetic field, as described by Lorentz's law. This causes an accumulation of charges at the edges, leading to the formation of the Hall voltage (V_{Hall}), which is expressed in the following expression.

$$V_{Hall} = \frac{IB}{qnt} \qquad 3.6$$

Where I is the applied current, B is the magnetic field, q is the elementary charge, n is the carrier concentration, and t is the thickness of the sample. With this parameter, the mobility (μ) and carrier concentration (n) can be obtained as follows.

$$\mu = \frac{\Delta V_{Hall}}{IBR_{sh}} \qquad 3.7$$

$$n = \frac{1}{q\mu R_{sh}t} = \frac{IB}{q\Delta V_{Hall}t} \qquad 3.8$$

Where R_{sh} is the sheet resistance of the layer and ΔV_{Hall} is the average Hall voltage which is obtained by measuring eight different configurations as the one depicted in Figure 3-6. Those include the change in direction of the magnetic field.

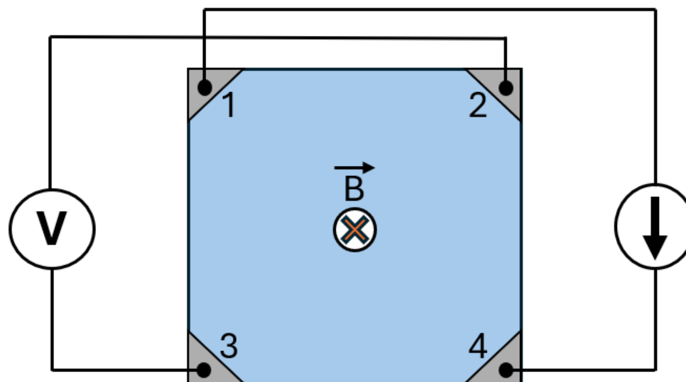

Figure 3-6 Configuration to measure a sample with Hall effect.

To measure the R_{sh} of the sample, it is common to use a special configuration of the four-point probe where the contacts are in the corners of the sample (van der Pauw configuration). The current is injected into two adjacent contacts, while the voltage is measured on the other two. Since there are four contacts on the edges, for compensate measuring errors and inhomogeneities it is possible to obtain up to eight possible configurations to make the measurement. Four configurations are obtained by rotating 90º the probes plus another four by changing the direction of the current (Figure 3-7).

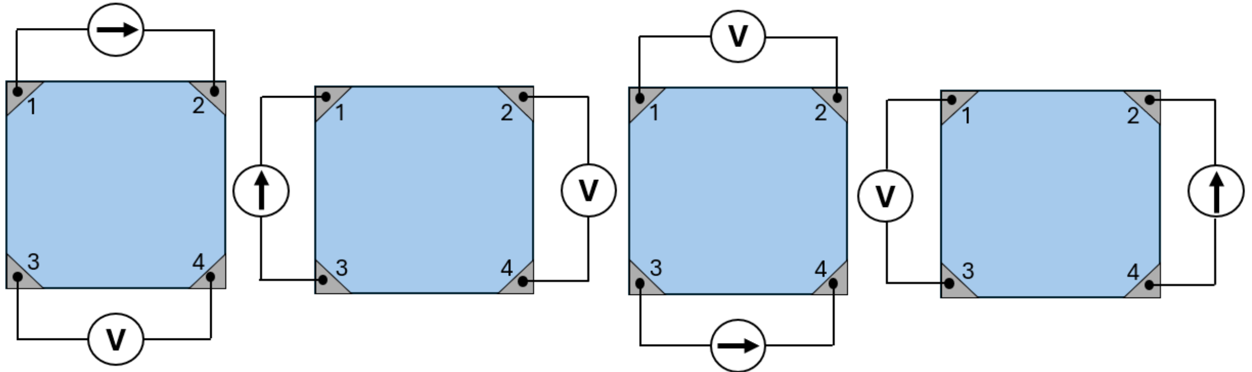

Figure 3-7 Four different configurations to obtain sheet resistance (R_{sh}) with van der Pauw configuration.

With those configurations, the R_{sh} value is obtained with the following expression

$$R_{sh} = \frac{\pi}{\ln(2)} \frac{R_A + R_B}{2} f(Q) \qquad 3.9$$

$$Q = \frac{R_A}{R_B}; Q \leq 1 \qquad 3.10$$

Where Q is the geometric factor defined in Equation 3.10, *f(Q)* is the van der Pauw function [14][10] which strongly depends on the geometry of the sample (for square samples, *f(Q)* is typically 1), and R_A and R_B are the average measured resistances in two different configurations i.e., R_A is the average resistance for the configurations depicted in Figure 3-7 and R_B is the average for the same configurations but changing the current direction. All these corrections are done to consider the non-uniformities of the sample. Finally, the resistivity of the sample can be calculated by the following expression:

$$\rho = \frac{1}{q(n\mu)} \qquad 3.11$$

Where q is the elementary charge, n is the carrier concentration, and μ is the mobility. This expression is only true when the layer shows a dominant carrier type, and the measurement is done when the semiconductor is in the extrinsic zone

During this work, the Hall effect measurements were done with a Keithley SCS 4200 system. A brief description of the system is explained as follows: the sample is connected by means of four metal probes in the corners; these probes are connected by means of low noise triaxial cables to four SMUs incorporated in the Keithley SCS 4200. The measurement is controlled by the special digital software *Keithley Interactive Test Environment (KITE),* which controls all the van der Pauw and Hall effect configurations. The electromagnet is the Alpha 7500 model with a KEPCO BOP 50-20 current source to achieve up to 0.95 T. The system is cooled by a water system which is controlled by an Arduino Nano microcontroller integrated into a Printed Circuit Board (PCB) depicted in Figure 3-8, this was designed during this thesis with *KiCAD IDE* software. The magnetic field is measured by a *Lakeshore 455 DSP* gaussmeter. This system is also capable of measuring at various temperatures (from 15 to 450 K) using a *Janis CSC-450 ST* cryostat. Nevertheless, all the samples were analyzed at room temperature as this is the typical operation condition for solar cells. To measure, silver was evaporated on the corner of the samples and then it was connected to the sample holder wires with silver paint. The samples characterized by this system were the HPS-deposited ITO. The TiO_x samples were measured as well, but the low thickness and high R_{sh} made it impossible to obtain accurate results.

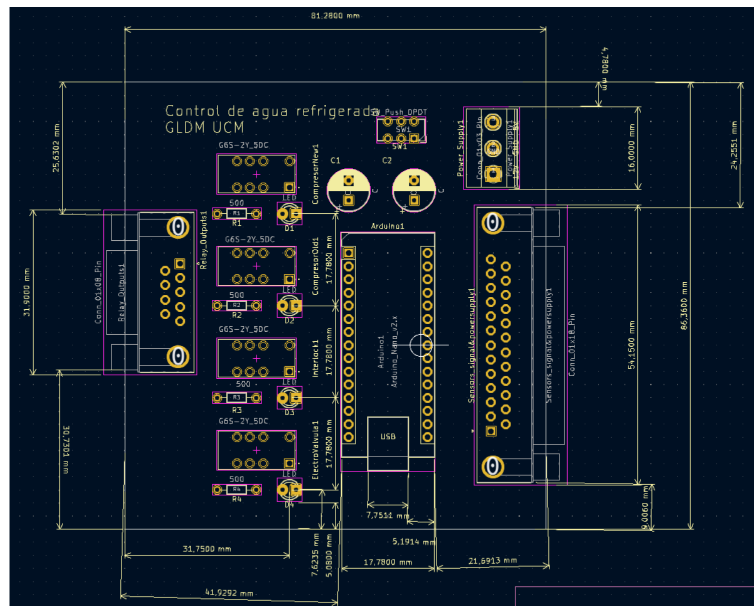

Figure 3-8 PCB layout for the water control system implemented in the Hall effect measurement system.

3.3.3 Transfer Length Method (TLM)

One of the most important parameters for solar cell design is the specific contact resistivity (ρ_c). This is the resistance that the carriers observe when passing from one material to another. This value should be as low as possible to extract the highest current. Besides, high values of ρ_c lead to higher values of series resistance, which leads to a reduction of the fill factor, and, therefore, the efficiency of the cell would decrease [15]. For instance, high-efficiency heterojunction solar cell shows ρ_c values in the 0.1 - 100 mΩcm^2 range for the a-Si:H(i)/a-Si:H(n) and a-Si:H(i)/a-Si:H(p) contacts [16].

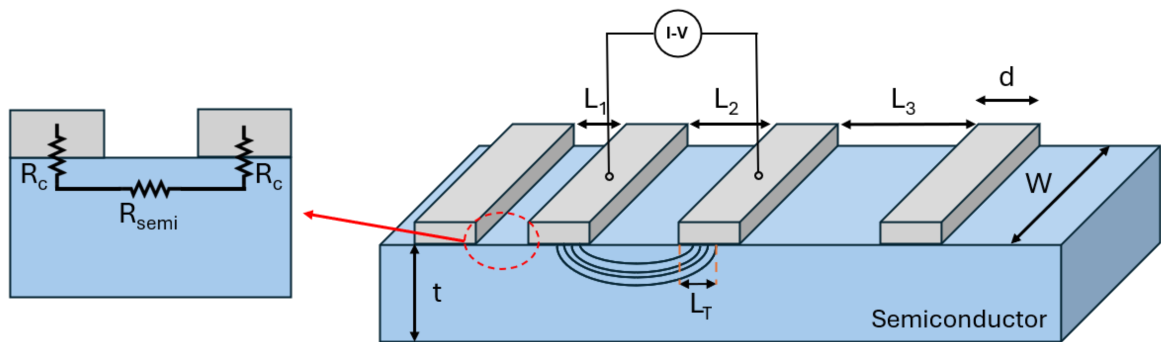

Figure 3-9 Scheme of a sample with TLM patterns with the most relevant dimension and parameters.

In that sense, the transfer length method (TLM) is one of the most used techniques to obtain the ρ_c for different stacks in solar cell devices. Figure 3-9 shows a sample for TLM measurements. To use this method, it is necessary to create a pattern of contacts along a substrate. These patterns are separated at intervals (L) defined by lithography or by mechanical shadowing. To ensure accurate measurement, it is necessary that the length (W) of the patterns is the same or similar to that of the semiconductor (substrate) to avoid current spreading. Thus, when a current is applied between two contiguous pads, it must pass through the resistance of the pad/substrate contact and the resistance of the substrate itself, which is the way that TLM models the current flux, and it is expressed with the following expression.

$$R_T = 2R_c + R_{semi} = \frac{2\rho_c}{L_T W} + \frac{R_{sh}}{W} L_x \qquad 3.12$$

Where R_c and R_{semi} are the contact resistance and semiconductor resistance, respectively, R_{sh} is the sheet resistance of the semiconductor, L_x is the distance between pads, and L_T is defined as current crowding.

The L_T is the average distance the current flows when entering into the pad, and this depends on the relationship between the R_{sh} and ρ_c [10]. This is defined with the following expression.

$$L_T = \sqrt{\frac{\rho_c}{R_{sh}}} \quad 3.13$$

Although the current crowding is normally expressed as a function of the length of the pads (W) and the resistance of the contact (R_c) as follows.

$$L_T = \frac{R_c W}{R_{sh}} \quad 3.14$$

Finally, a linear regression is done in the R_T versus L_x curve from which $2R_c$ is obtained from the y-intercept, R_{sh}/W is the slope, and from the x-intercept $2L_T$ is obtained. In that sense with TLM not only the ρ_c can be obtained but also the R_{sh} of the semiconductor. To accurately obtain these parameters, it is important that only one layer conducts laterally; for that reason, if the substrate is not the same as the semiconductor being analyzed, it must not conduct. This can be achieved by using a substrate with a very high R_{sh}, such as quartz, or by depositing the semiconductor on another semiconductor of the opposite type to create a depletion region and isolate the top layers.

The measurement of TLM samples was done in a Everbeing probe station located inside a Faraday box. This system includes micropositioners to achieve precise contact with the sample and a chuck stage where the sample is fixed by vacuum. Triaxial cables connect by needles to the Keithley 2636A SMU. A LabView program controls all the I-V measurements. This system, housed in the Electrical and Optoelectrical Thin Film Characterization Lab at UCM, was used to measure the contact resistivity of the metal/Si(n^{++}) stack. A similar system was also used during the stay at EPFL PV-Lab to obtain the ρ_c of the Ag/ITO:H/poly-Si(n) stack.

3.3.4 Cox & Strack Method (CSM)

Another technique used to determine the contact resistivity (ρ_c) was the Cox & Strack method (CSM). Unlike TLM, where the current flows laterally, CSM is based on vertical conduction. It was first implemented in 1967 by Robert Cox and Hans Strack to determine the contact resistance in GaAs devices [17]. This method consists of depositing circular contacts of different diameters as the front

contact. In contrast, the back contact is a common metal layer for the whole sample, as depicted in Figure 3-10. This method models the current flow with the following expression.

$$R_T = R_c + R_s + R_0 \tag{3.15}$$

Where R_c is the contact resistance, R_s is the resistance to the current spreading through the semiconductor, and R_0 is the residual resistance at the back contact. These parameters are traditionally defined as follows.

$$R_c = \frac{\rho_c}{\frac{1}{4}\pi d^2} \tag{3.16}$$

$$R_s \approx \frac{\rho_w}{\pi d} \arctan\left(\frac{4t}{d}\right) \tag{3.17}$$

Where ρ_c is the contact resistivity, ρ_w is the wafer resistivity, d is the diameter of the top contact, and t is the thickness of the semiconductor. The previous expression of the spreading resistance (R_s) is the original expression defined by Cox & Strack in the 60s. Nevertheless, recent works have solved the problem using finite element simulation to obtain a more accurate expression for the spreading resistance [18]. During this thesis, the following approximation by van Rijnbach et al. was used [19].

$$R_S \approx \frac{2\rho_w}{\pi d}\left(\frac{d}{2t} + \frac{4}{\pi} + \left(1 - \frac{4}{\pi}\right)\arctan\left(\frac{2d}{3t}\right)\right)^{-1} \tag{3.18}$$

This final expression only depends on the diameter of the top contacts and the wafer parameters; thus, it will be a constant for each contact. In that sense, the following expression can be plotted to obtain the ρ_c.

$$R_T - R_s = \frac{\rho_c}{\frac{1}{4}\pi d^2} + R_0 \tag{3.19}$$

When the $R_T - R_s$ versus *1/area* is plotted from the slope, the contact resistivity ρ_c is obtained while the y-intercept gives the residual resistance R_0.

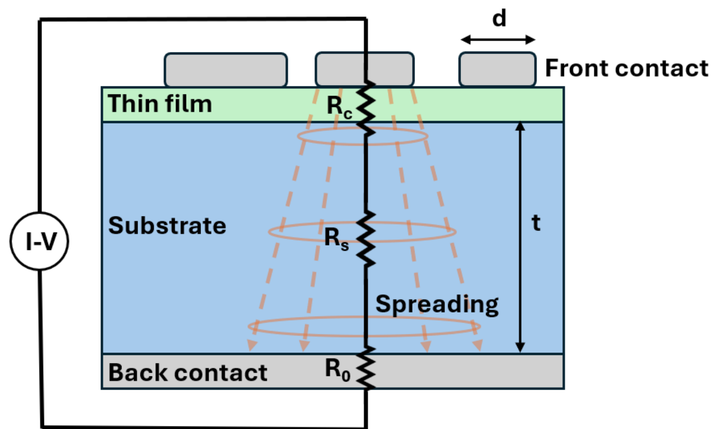

Figure 3-10 Scheme of a sample with Cox Strack patterns with the most relevant parameters.

The CSM is often used instead of TLM when the semiconductor to be analyzed has a high sheet resistance. Such materials would be difficult to measure with TLM as this method requires lateral transport. On the other hand, circular CSM patterns are easier to fabricate since the transport does not need to be confined to the pad width as in TLM. Therefore, smaller samples can be analyzed. However, certain conditions must be met for the measurement to be accurate:

1. **Measure the resistivity of the wafer**: Since the CSM model relies on the characteristics of the wafer substrate, it is crucial to measure the resistivity of each individual wafer used.

2. **Ensure no lateral condition**: The model does not account for lateral conduction in the thin film; low-sheet resistance films introduce additional spreading resistance, which can lead to errors in the results. When low-sheet resistance samples have to be measured, the film can be patterned with metal contacts through reactive ion etching (RIE) [20].

3. **Using small-diameter contacts:** To accurately distinguish the contact resistivity (ρc), it is essential to use the correct diameter dimension for the top contacts. Some studies have found that the diameter must be smaller than twice the wafer thickness ($d < 2t$) to clearly distinguish the contact resistivity [19]. For instance, Figure 3-11 shows the R_T versus d for various values of specific contact resistivity (ρc). In this graph, the total resistance remains similar when the contact diameters exceed 0.6 mm, and thus ρc becomes indistinguishable.

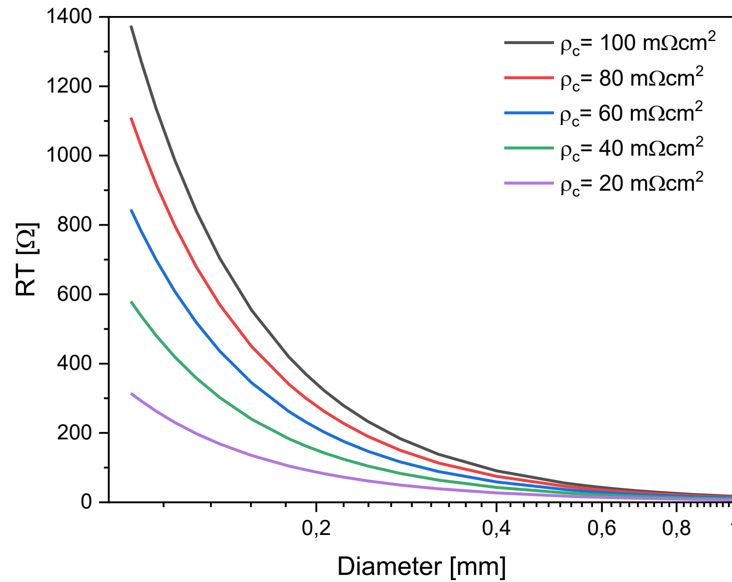

Figure 3-11 Total resistance (R_T) as a function of contact's diameter for different hypothetical contact resistivity (ρc). The R_T is calculated using Equations 3.15, 3.16, and 3.18, with the values ρw = 1 Ωcm, R_0 = 2 Ω, and t = 280 µm.

3.3.5 Photoconductance

One of the most crucial parameters for achieving high-efficiency solar cells is the minority carrier lifetime. As explained previously, the lifetime considers various recombination mechanisms that happen in the bulk and on the surface. To measure this crucial parameter, the most widely used technique is the photoconductance, originally developed by A. Sinton and A. Cuevas [21]. This is based on using a flash lamp to illuminate the sample and measuring the excess of minority carriers through a radio frequency circuit, which produces a voltage proportional to the conductivity of the wafer. In that sense, the conductivity of the wafer and the excess minority carriers can be related by the following expression.

$$\Delta\sigma(t) = qW(\mu_n + \mu_p)\Delta n(t) \qquad 3.20$$

Where $\Delta\sigma(t)$ is the change in conductivity, q is the elementary charge, W is the wafer thickness, μ_n, and μ_p are the electron and hole mobilities, and $\Delta n(t)$ is the of change minority carrier concentration. With the latter parameter, the lifetime value can be calculated using the continuity equation, which relates

the excess generation of photogenerated carriers (*Δn(t)*), the generation (*G*), and the recombination mechanisms.

$$\tau_{eff} = \frac{\Delta n(t)}{G - \frac{d\Delta n(t)}{dt}} \qquad 3.21$$

From this expression the two main methods of measuring lifetimes are derived. On the one hand, if the lifetime is obtained with a flash source that decays slowly enough to balance photogeneration and recombination (steady-state method), the above expression is simplified as follows.

$$\tau_{eff} = \frac{\Delta n(t)}{G} \qquad 3.22$$

On the other hand, if the lifetime is obtained using a short flash where the photogenerated carriers recombine without illumination (transient method), the expression is as follows.

$$\tau_{eff} = -\frac{\Delta n(t)}{\frac{d\Delta n(t)}{dt}} \qquad 3.23$$

There is a third method known as quasi-steady-state photoconductance (QSSPC), which combines the previous two methods. With the QSSPC method, the flash illumination gradually varies with time, allowing the production of different irradiation levels [22]. Thus, the lifetime expression can be obtained with the following expression.

$$\tau_{eff} = \frac{\Delta n(t) W}{N_{ph} f - W \frac{d\Delta n(t)}{dt}} \qquad 3.24$$

Where N_{ph} is the number of photons per second and cm^2 with energy greater than the Si bandgap, W is the wafer thickness, and f is the fraction of photons that are absorbed (optical constant). This value is typically ~0.7 for bare Si wafer, ~0.9 with antireflection coating, and ~1 with texturized wafer and antireflection coating [22][23].

Additionally, the implied open-circuit voltage (i-V_{oc}) can be calculated using the values of *Δn(t)* and the Shockley equation as follows.

$$iV_{oc} = \frac{kT}{q} \ln\left(\frac{\Delta n(t)(N + \Delta n(t))}{n_i^2} + 1\right) \qquad 3.25$$

Considering that $\Delta n = \Delta p$, N is the donor or acceptor concentration, kT/q is the thermal voltage, and n_i is the intrinsic carrier concentration. In this thesis, we used Sinton WCT-120 equipment to measure the lifetime of TiO_x, ITO, and ITO:H films on Si. Depending on the sample, either the transient (high lifetime values) or QSSPC (low lifetime values) method was employed. The method to be used can be determined by observing the temporal photoconductance response and the lamp illumination (Figure 3-12).

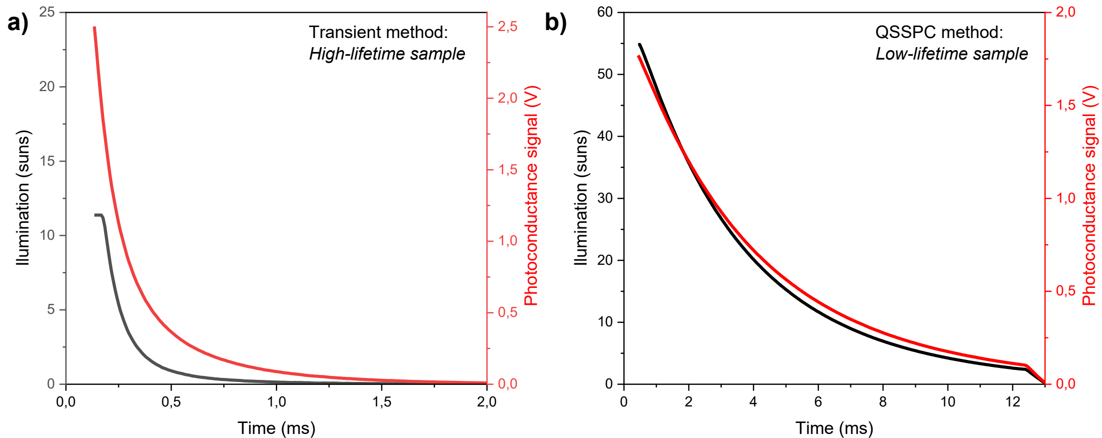

Figure 3-12 Photoconductance response and lamp illumination over time for a sample measured with a) transient method and b) QSSPC method.

3.3.6 Current-voltage characteristics of solar cell

For the solar cell protoypes, the current-voltage (I-V) curves were measured under standard test conditions (25 ºC, AM1.5G spectrum, 1000 W/m^2). From these measurements, the short circuit current *(I_{sc})*, open-circuit voltage *(V_{oc})*, and fill factor *(FF)* were obtained. A Sinus-70 solar simulator from Wavelabs was used to illuminate the sample, and a Keysight B2910BL SMU was used to sweep the voltage and record the current. The Sinus-70 simulates the solar spectrum through a number of LEDs with a spectral range from 350 to 1100 nm. The sample was vacuum-placed on a temperature-controlled chuck. To prevent the whole sample from being illuminated, a shadow mask with the shape of the active area is placed on top of the cell. The rear side is connected through the chuck itself. For the front contact, a probe contacts the busbars of the sample. Both contacts have a four-probe configuration to eliminate the influence of probe resistance. Finally, the I-V measurements are controlled by dedicated LabVIEW software, from which the data is obtained.

3.4 Optical characterization

3.4.1 Ellipsometry

This is a non-destructive technique that enables us to determine the thickness (t), refractive index (n), and extinction coefficient (k) of a sample. This technique measures the change in the polarization of the light due to interaction with the sample. Figure 3-13 shows a basic setup for ellipsometry measurement. In this case, a linearly polarized light reaches the sample at a specific angle. When the light is reflected, its polarization changes to an elliptical form due to the material's thickness and optical constants. The fundamental quantities measured are the change in amplitude (Ψ) and the change in phase (Δ), which are related to the reflection coefficients with the following expression

$$\rho = \frac{R_p}{R_s} = \tan(\Psi)\, e^{i\Delta} \qquad 3.26$$

Where ρ is the ratio of reflection coefficients, R_p and R_s are the reflection coefficients of the parallel and vertical components of the light, respectively. With the ellipsometry parameters Ψ and Δ, an optical that includes the Fresnel equation can be used to extract the complex refractive index ($n + ik$) and the thickness of the film.

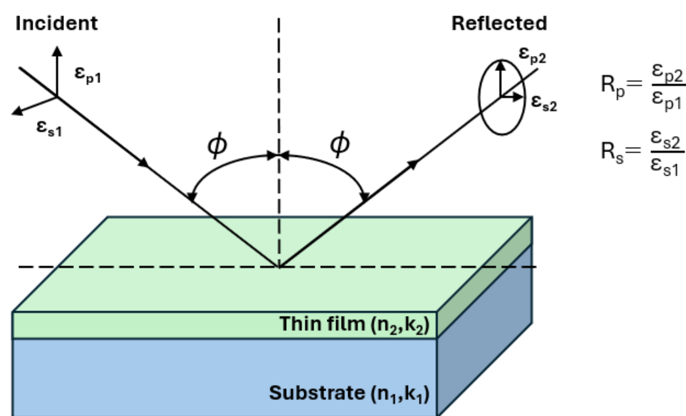

Figure 3-13 Basic scheme of ellipsometry technique.

This technique is typically used to determine the thickness of thin films in the 1–1000 nm range. The feasibility of the measurement will depend on the type of material measured. For example, semi-transparent semiconductors for the wavelength of the incident light will be able to measure larger thicknesses. In contrast, metallic samples absorb strongly at all wavelengths. However, metallic thin films can be measured when their thickness is in the range of a few nanometers [24].

During this thesis, the *LSE-WS Stokes WaferScan* system, equipped with a monochromatic red laser (He-Ne) at a wavelength of 633 nm and a fixed angle of 70º, was utilized. This system includes an automated platform that allows the measurement of maps with a resolution of 10 μm. This was used to measure the thickness of the Ti, TiO_x, and ITO samples.

3.4.2 UV-Vis-IR Spectrophotometry

UV-Vis-IR spectrophotometry is a widely used technique for the optical characterization of thin films in photovoltaics and microelectronics. This allows us to measure the transmittance and reflectance of the sample at different wavelengths. Knowing these parameters, the absorption can be estimated by subtracting the transmittance and reflectance to 100 % ($A = 1\text{-}T\text{-}R$). Understanding the optical behavior of the sample is crucial for optimizing materials for solar cell applications. For instance, transition metal oxides (TMOs) acting as selective contacts must have low absorption in the visible region to prevent parasitic absorption outside the Si absorber, which is detrimental to the solar cell's efficiency. In the case of transparent conductive oxides (TCOs), such as ITO, the transmittance must be as high as possible in the visible region to enhance the absorption of photons inside the Si. Additionally, this technique allows for the determination of other important parameters of the films. For instance, the optical band gap can be obtained by the Tauc plot fitting which is done with the following expression [25].

$$(\alpha h\nu)^n \propto (h\nu - E_{gap}) \qquad 3.27$$

Where α is the absorption coefficient, h is the Plank' constant, ν is the frequency of the incident light, n is the type of transition (2 for direct band gap and ½ for indirect band gap material), and E_{gap} is the band gap. The absorption coefficient determines how far the incoming light can penetrate before being absorbed, and this is typically obtained with the following expression [26].

$$\alpha(\lambda) = \frac{1}{t}\ln\left(\frac{(1 - R(\lambda))^2}{T(\lambda)}\right) \tag{3.28}$$

Where t is the thickness of the film, $T(\lambda)$ represents the transmittance at a specific wavelength, and $R(\lambda)$ denotes the reflectance at the same wavelength. The previous expression is transformed to the Beer-Lambert expression when the sample's reflectance is negligible. During this thesis, transmission, and reflectance measurements were performed using a *Lambda 1050+* from *PerkinElmer* house spectrophotometer, which features a 150 mm integration sphere. It includes two detectors, an R672 photomultiplier for the UV-Vis region and an InGaAs photodetector for the 800 – 2600 nm range. The samples were measured in the 250 – 2500 nm wavelength range with a measurement step of 4 nm. This system is located in the UCM, and it was used to characterize the TiO_x and ITO thin films fabricated. Additionally, during the stay at EPFL-PVlab a similar system (*Lambda 900* with an integration sphere) was used to measure the ITO:H samples.

3.4.3 Fourier Transform Infrared Spectroscopy (FTIR)

Fourier Transform Infrared Spectroscopy (FTIR) is a non-destructive optical technique that enables the study of the interaction between materials and infrared radiation. It is precisely in the infrared range that molecular bonds begin to absorb photons and start to vibrate. These oscillations occur only in molecules formed from atoms of different electronegativities, resulting in a dipole moment. Therefore, this technique enables us to understand the chemical bonds within materials that contain these types of molecules.

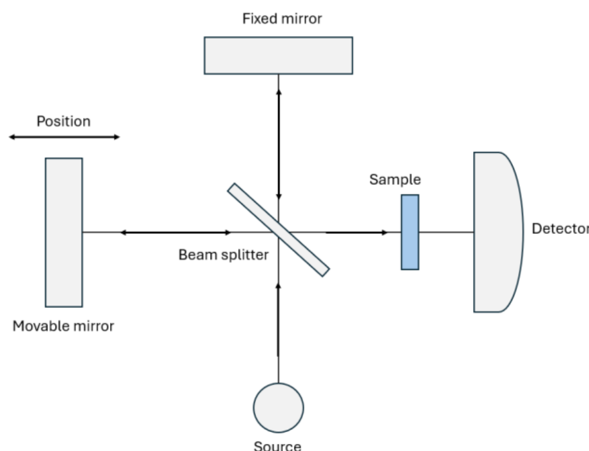

Figure 3-14 Schematic of a Michelson interferometer for a basic FTIR step-up.

This technique is based on the Michelson interferometer. A simplified scheme of this is shown in Figure 3-14. It works as follows: an infrared light source is collimated and directed into a beam splitter. This creates two optical paths where 50% of the light is transmitted, and the rest is reflected. In one of the optical paths, a fixed mirror is located, while in the other, a movable mirror is positioned. The beams are reflected and recombined in the beam splitter, creating interference phenomena that depend on the position of the movable mirror. Finally, the modulated light passes through the sample and reaches a detector, from which an interferogram is obtained. The information we have from the interferogram is the transmission as a function of the optical path difference. However, what is important is the spectral response of the transmission, for which the Fourier transform is performed [10].

$$T(f) = \int_{-\infty}^{\infty} I(x)\cos(2\pi x f)\,dx \tag{3.29}$$

Where *T(f)* is the transmittance response as a function of the frequency (*f*), and *I(x)* is the interferogram measured as a function of mirror displacement *(x).* Typically, in FTIR, the transmittance is given as a function of the wavenumber, which is the inverse of the wavelength or the ratio between the frequency and the speed of light ($v = f/c$).

In this thesis, an FTIR spectrophotometer (*Nicolet iS50*) was used, measuring in the 400 - 4000 cm^{-1} range, equipped with an EverGlo infrared light source, a KBr beam splitter, and a DTGS-KBr detector. The resolution of the measurements was 16 cm^{-1}, and each spectrum was averaged from 70 scans. The samples were measured in transmission. This system is located at CAI *de espectroscopía y correlación* from UCM. To obtain the final graphs, the c-Si(n) reference absorbance spectrum was subtracted from the total TiO_x/c-Si(n) spectrum, thereby eliminating the contribution of the Si substrate.

3.4.4 Photoluminescence (PL)

Photoluminescence (PL) imaging is a contactless and non-destructive characterization technique employed for the spatial analysis of semiconductor materials in photovoltaic applications. When a semiconductor is optically excited with radiation above its bandgap, electron-hole pairs are generated; their subsequent radiative recombination results in the emission of photons, which can be captured to form a PL image. The intensity of this emission is directly related to the excess carrier density, which is governed by the minority carrier lifetime and the recombination activity within the material [27]. PL imaging thus provides information about passivation quality, enabling rapid mapping of carrier

lifetime. Calibration methods, typically involving quasi-steady-state photoconductance (QSSPC), are necessary to extract quantitative lifetime values from PL intensity [28]. However, qualitative information is still available for non-calibrated setups.

This technique was used during the short stay at EPFL-PVlab to spatially characterize the passivation with ITO:H deposition on top of the poly-Si(n)/SiO_x/c-Si stack. Additionally, for some representative annealing steps, PL images were also captured. The system used was an in-house-built setup with an Ostech laser featuring a wavelength of 808 nm and an intensity of 1.2 Suns. A silicon-based camera, Pixis from Princeton Instruments, was used to record the PL image.

3.5 References

[1] F. Menges, "Spectragryph - optical spectroscopy software." [Online]. Available: http://www.effemm2.de/spectragryph/.

[2] A. Einstein, "Concerning an Heuristic Point of View Toward the Emission and Transformation of Light," *Transl. into English Am. J. Phys.*, vol. 17, no. 5.

[3] F. A. Stevie and C. L. Donley, "Introduction to x-ray photoelectron spectroscopy," *J. Vac. Sci. Technol. A Vacuum, Surfaces, Film.*, vol. 38, no. 6, 2020, doi: 10.1116/6.0000412.

[4] D. Harvey, "Intrumental analysis," *Open Educ. Resour. Libr.*, p. 199, 2022, [Online]. Available: https://libretexts.org.

[5] C. D. Wagner, L. E. Davis, M. V. Zeller, J. A. Taylor, R. H. Raymond, and L. H. Gale, "Empirical atomic sensitivity factors for quantitative analysis by electron spectroscopy for chemical analysis," *Surf. Interface Anal.*, vol. 3, no. 5, pp. 211–225, 1981, doi: 10.1002/sia.740030506.

[6] G. F. Harrington and J. Santiso, "Back-to-Basics tutorial: X-ray diffraction of thin films," *J. Electroceramics*, vol. 47, no. 4, pp. 141–163, 2021, doi: 10.1007/s10832-021-00263-6.

[7] G. Hölzer, M. Fritsch, M. Deutsch, J. Härtwig, and E. Förster, "Kα1,2 and Kβ1,3 x-ray emission lines of the 3d transition metals," *Phys. Rev. A - At. Mol. Opt. Phys.*, vol. 56, no. 6, pp. 4554–4568, 1997, doi: 10.1103/PhysRevA.56.4554.

[8] S. Trépout, M. L. Sgarra, S. Marco, and G. Ramm, "An introduction to scanning transmission electron microscopy for the study of protozoans," *Mol. Microbiol.*, vol. 121, no. 4, pp. 659–670, 2024, doi: 10.1111/mmi.15213.

[9] J. Mayer, L. A. Giannuzzi, T. Kamino, and J. Michael, "TEM sample preparation and FIB-induced damage," *MRS Bull.*, vol. 32, no. 5, pp. 400–407, 2007, doi: 10.1557/mrs2007.63.

[10] Dieter K. Schroder, *Semiconductor material and device characterization*, Third edit. Hoboken,

New Jersey: John Wiley and Sons Inc, 2006.

[11] M. Naftaly *et al.*, “Sheet resistance measurements of conductive thin films: A comparison of techniques,” *Electron.*, vol. 10, no. 8, 2021, doi: 10.3390/electronics10080960.

[12] D. Caudevilla *et al.*, “Indium tin oxide obtained by high pressure sputtering for emerging selective contacts in photovoltaic cells,” *Mater. Sci. Semicond. Process.*, vol. 137, 2022, doi: 10.1016/j.mssp.2021.106189.

[13] D. Birch, “A great Hall of science | Hub,” 2020. https://hub.jhu.edu/2020/01/07/hall-effect-2501-em1-art1-rea/ (accessed Apr. 02, 2025).

[14] L. J. van der Pauw, “A method of measuring specific resistivity and Hall effect of discs of arbitrary shape,” *Philips Res. Reports*, vol. 13, 1958.

[15] S. Bowden and A. Rohatgi., “Rapid and Accurate Determination of Series Resistance and Fill Factor Losses in Industrial Silicon Solar Cells,” *Proc. 17th Eur. Photovolt. Sol. Energy Conf.*, pp. 1802–1806, 2001, [Online]. Available: http://hdl.handle.net/1853/26165.

[16] W. Long *et al.*, “On the limiting efficiency for silicon heterojunction solar cells,” *Sol. Energy Mater. Sol. Cells*, vol. 231, no. June, p. 111291, 2021, doi: 10.1016/j.solmat.2021.111291.

[17] R. H. Cox and H. Strack, “Ohmic contacts for GaAs devices,” *Solid State Electron.*, vol. 10, no. 12, pp. 1213–1218, 1967, doi: 10.1016/0038-1101(67)90063-9.

[18] D. Turkay, K. Tsoi, E. Dönerçark, R. Turan, and S. Yerci, “Spreading Resistance Modeling for Contact Resistivity Extraction in Ohmic Multilayer Structures With Circular Electrodes,” *IEEE Trans. Electron Devices*, vol. 68, NO. 12, pp. 6344–6351, 2021.

[19] M. Van Rijnbach, R. J. E. E. Hueting, M. Stodolny, G. Janssen, J. Melskens, and J. Schmitz, “On the Accuracy of the Cox-Strack Equation and Method for Contact Resistivity Determination,” *IEEE Trans. Electron Devices*, vol. 67, no. 4, pp. 1757–1763, 2020, doi: 10.1109/TED.2020.2974194.

[20] N. Folchert and R. Brendel, “Extended Cox & Strack analysis for the contact resistance of planar samples with carrier-selective junctions on both sides,” *Sol. Energy Mater. Sol. Cells*, vol. 231, Oct. 2021, doi: 10.1016/J.SOLMAT.2021.111304.

[21] R. Sinton, A. Cuevas, and M. Stuckings, “Quasi-Steady-State photoconductance, a new method for solar cell material and device characterization,” *Conf. Rec. Twenty Fifth IEEE Photovolt. Spec. Conf.*, pp. 457–460, 1996.

[22] A. Cuevas and D. Macdonald, “Measuring and interpreting the lifetime of silicon wafers,” *Sol. Energy*, vol. 76, no. 1–3, pp. 255–262, 2004, doi: 10.1016/j.solener.2003.07.033.

[23] T. Roth, P. Rosenits, W. Warta, and S. W. Glunz, “Photoconductance-based excess carrier lifetime measurements on unpassivated silicon samples,” *24th Eur. PV Sol. Energy Conf. Exhib.*, no. September, pp. 2–5, 2009.

[24] H. G. Tompkins, S. Tasic, J. Baker, and D. Convey, "Spectroscopic ellipsometry measurements of thin metal films," *Surf. Interface Anal.*, vol. 29, no. 3, pp. 179–187, 2000, doi: 10.1002/(SICI)1096-9918(200003)29:3<179::AID-SIA701>3.0.CO;2-O.

[25] J. Klein, L. Kampermann, B. Mockenhaupt, M. Behrens, J. Strunk, and G. Bacher, "Limitations of the Tauc Plot Method," *Adv. Funct. Mater.*, vol. 33, no. 47, pp. 1–19, 2023, doi: 10.1002/adfm.202304523.

[26] M. Cesaria, A. P. Caricato, and M. Martino, "Realistic absorption coefficient of ultrathin films," *J. Opt. (United Kingdom)*, vol. 14, no. 10, 2012, doi: 10.1088/2040-8978/14/10/105701.

[27] R. K. Ahrenkiel, B. M. Keyes, and D. J. Dunlavy, "Intensity-dependent minority-carrier lifetime in III-V semiconductors due to saturation of recombination centers," *J. Appl. Phys.*, vol. 70, no. 1, pp. 225–231, 1991, doi: 10.1063/1.350315.

[28] T. Trupke, B. Mitchell, J. W. Weber, W. McMillan, R. A. Bardos, and R. Kroeze, "Photoluminescence imaging for photovoltaic applications," *Energy Procedia*, vol. 15, no. 2011, pp. 135–146, 2012, doi: 10.1016/j.egypro.2012.02.016.

CHAPTER IV: ITO DEPOSITED BY HIGH-PRESSURE SPUTTERING

Indium tin oxide (ITO) is widely used as a transparent conductive oxide (TCO) in optoelectronic devices, including flat-panel displays, light-emitting diodes, and photovoltaic cells, due to its high electrical conductivity and optical transparency in the visible spectrum. In the context of silicon-based solar cells, optimizing the deposition and properties of ITO is essential to ensure both low resistivity and minimal parasitic absorption. This chapter focuses on the deposition of ITO films by high-pressure sputtering (HPS), a technique that offers potential advantages in terms of film uniformity and reduced damage to underlying layers, particularly relevant for delicate structures such as amorphous silicon (a-Si:H). We have studied the influence of deposition parameters (argon pressure and power density) on the structural, electrical and optical properties of ITO films. Characterization techniques such as four-point probe for sheet resistance measurement, X-ray photoelectron spectroscopy (XPS), grazing incidence X-ray diffraction (GIXRD), and Hall effect measurements are employed to evaluate the film quality. Finally, the application of these HPS-deposited ITO layers in silicon heterojunction solar cells is also investigated to assess their compatibility and performance within a real solar device.

4.1 Structural and electrical characterization of ITO deposited by high-pressure sputtering

To characterize the deposition of ITO by HPS the resistivity of films deposited with several conditions was measured. ITO was deposited on 2.2 x 2.2 cm^2 glass substrates, and the sheet resistance was measured by four-point probes system while the thickness was measured by profilometry. The thickness of the samples was in the 100 - 200 nm range. Different pressures (0.5 - 1.5 mbar) and power densities (1.5 - 2.5 W/cm^2) were studied. For all the deposition processes only Ar was used as working gas, i.e., no reactive sputtering took place.

The resistivity results are depicted in Figure 4-1. The first thing to note is that Ar pressure affects resistivity more than power density. For example, considering a power density of 2.2 W/cm^2 (45 W), ITO deposited at 0.5 mbar shows a resistivity of $2.9x10^{-2}$ Ωcm while ITO deposited at 1.5 mbar has a resistivity of $4x10^{-4}$ Ωcm. Second, varying the power density does not significantly affect the resistivity of the samples. One possible explanation for the change in resistivity as a function of deposition pressure is that the deposition rate is different for each of them. The deposition rate varies from 3 nm/min (0.5 mbar) to 0.82 nm/min (1.5 mbar). This variation in deposition rate can affect film

morphology, particularly porosity, which in turn influences electrical resistivity [1]. In any case, the ITO films deposited at 1.5 mbar show resistivity values typically achieved for solar cells applications (10^{-4} Ωcm) [2], which demonstrate the feasibility of depositing solar cell quality ITO with HPS.

Resistivity is determined by carrier concentration and mobility. The literature shows that in polycrystalline ITO the Sn content has a big impact on its resistivity: crystalline In_2O_3 is an electrical insulator, and the Sn atoms that get incorporated into the film introduce an excess of electrons that converts ITO in a degenerate n-type semiconductor. There are works showing that the resistivity strongly depends on the Sn content and its activation , with an optimal Sn/In atomic ratio around 0.1 [3]. This is the reason why the typical ITO target composition is 90% In_2O_3/10% SnO_2 in weight, which translates to an Sn/In atomic ratio of 0.102. On the other hand, in amorphous ITO the role of Sn is not so straightforward. Some works [4][5] found that in this amorphous material the oxygen vacancies determine the free carrier concentration, and that Sn is mainly inactive. Concerning the mobility, typically amorphous metals present lower values than their crystalline counterparts [6] because in the electronic cloud the electron mean free path is similar to the atomic distance [7]. However, this is not the case in amorphous ITO, where the main free path is in the order of 10 nm [8], so the scattering due to collisions with the lattice is negligible. Thus, amorphous ITO can present resistivity values comparable to polycrystalline ITO [8].

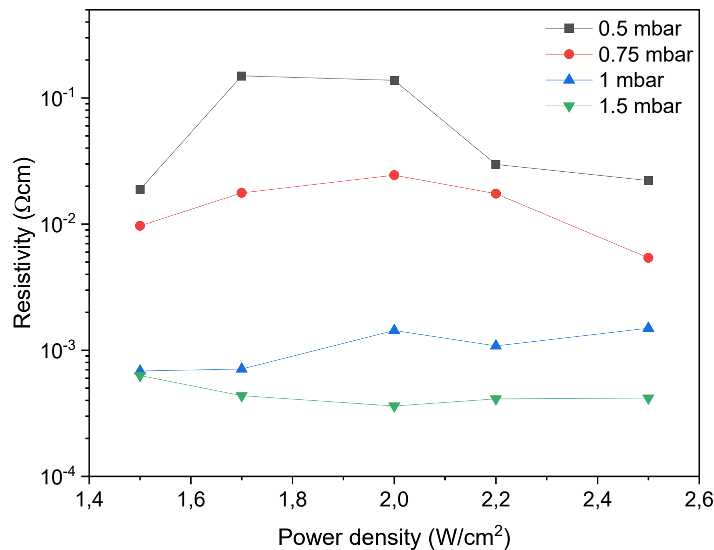

Figure 4-1 Resistivity of ITO films deposited by high-pressure sputtering varying the Ar pressure and power density of the deposition process. The ITO thickness is in the 100 – 200 nm range.

For all the deposition processes, the plasma was characterized by Optical Emission Spectroscopy (OES). The purpose was to determine the presence of sputtered species through their emission peaks. Figure 4-2 depicts de OES spectra of three processes with different Ar pressures (0.75, 1, and 1.5 mbar). It is noticeable that the spectra do not significantly change with the Ar pressure as the same

atomic emissions were found for the three processes. All the atomic peak emissions were catalogued using the *Handbook of Basic Atomic Spectroscopy Data* by Sansonetti and Martin [9]. The presence of In was detected for all the spectra at 203, 255, 328, 410, and 451 nm, while the presence of Sn was observed at 283 and 295 nm. Due to coincidence of emissions, the peak around 304 nm can be due either to In, Sn, or a superposition of both. Regarding all the peaks between 700 to 850 nm, they can be catalogued as Ar and ionized Ar. Additionally, some emission bands were also observed which can be related to molecular emissions. The band in the 309 – 315 nm range indicates some presence of OH^-, while the band located between 336 and 339 nm might indicate the NH emission [10]. There is not a clear tendency between the molecular emission and the deposition pressure. The presence of these species can be due to the contamination introduced when the deposition chamber is open to the atmosphere.

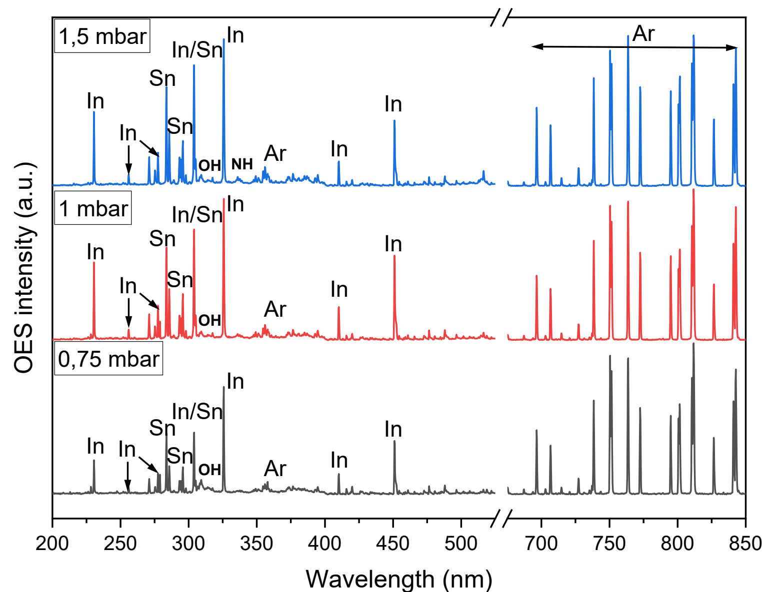

Figure 4-2 Optical Emission Spectroscopy (OES) spectra of HPS plasma during ITO deposition with different Ar pressures at a constant RF power of 2.2 W/cm².

To understand the difference in resistivity found between samples with different Ar pressures, XPS measurements were done with samples fabricated with the same conditions as Figure 4-2. No surface sputtering was performed during the XPS measurements; thus, the results come from the surface of the ITO samples. These samples have a thickness between 100 nm and 200 nm.

The results for the emissions of In-3d, Sn-3d and O 1s are shown in Figure 4-3. The Sn/In ratio was calculated with the relationship between the area of the Sn-3d and In-3d peaks. The results for the Sn/In ratio were 0.068 (0.75 mbar), 0.082 (1.0 mbar) and 0.070 (1.5 mbar). As a reference, in the target the atomic Sn/In ratio was 0.102. Considering the uncertainty of the fits, we can conclude from these results that in this pressure range there were no relevant differences in the Sn/In ratio.

In contrast, the deconvoluted O 1s emission peak exhibits a broad peak at 531 eV, commonly referred to as oxygen atoms with dangling bonds (i.e., unsaturated metal-oxygen bonds) or as oxygen vacancies (O_v) [11]. Another peak is also observed at 529 eV, and it is related to oxygen with saturated bonds which are related as lattice oxygen (O_L) [12]. There is a clear tendency between the pressure and the presence of O_v, as the Ar pressure is increased the percentage that represents O_v over O 1s peak is reduced. It goes from 89% (0.75 mbar) to 42% (1.5 mbar).

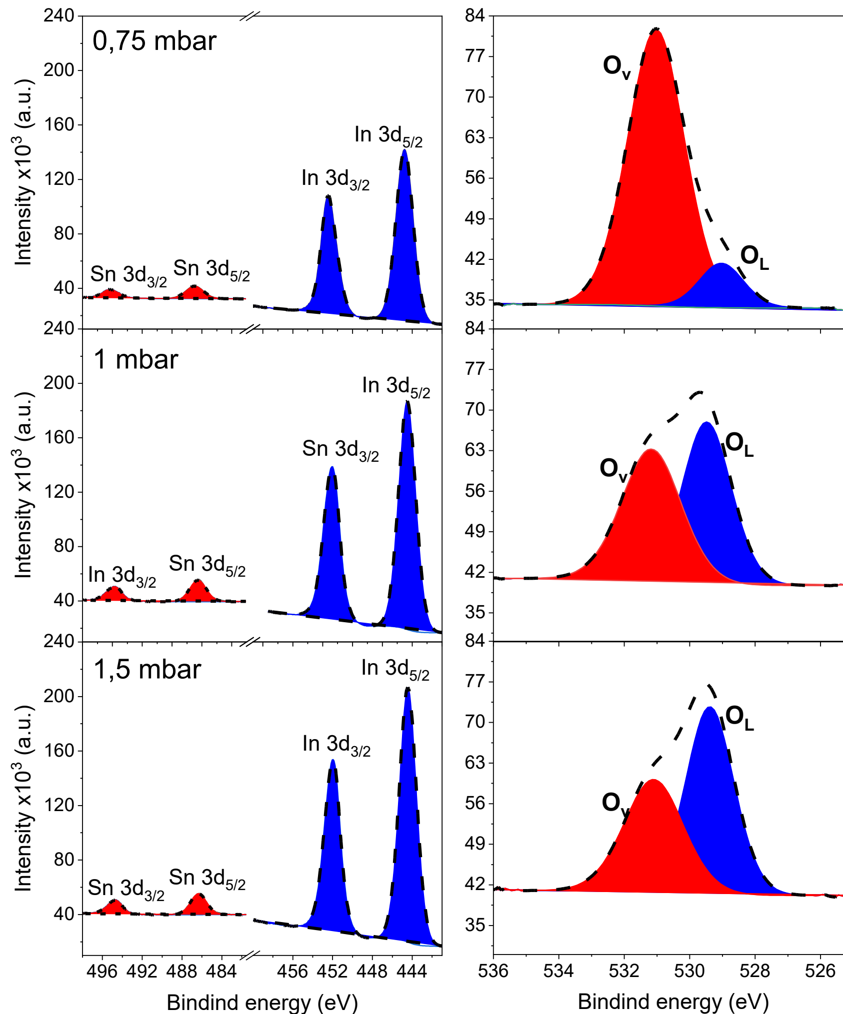

Figure 4-3 XPS spectra of In 3d, Sn 3d, and O 1s core levels for different ITO thin film samples fabricated with different Ar pressure at a constant power density of 2.2 W/cm².

The ITO sample deposited at 0.75 mbar exhibits the highest relative concentration of oxygen vacancies (O_v) typically associated with non-lattice oxygen. Although oxygen vacancies in ITO are known to act as donors, thereby contributing to free carrier generation, the film deposited at 0.75 mbar showed a higher resistivity compared to those deposited at 1.0 and 1.5 mbar. This apparent contradiction can be attributed to several factors. First, an excessive concentration of oxygen vacancies may lead to increased structural disorder which can create scattering, that in turn negatively impacts carrier

mobility. Second, low pressure deposition can create more porous films that can also modify the resistivity. Third, the surface-sensitive nature of XPS implies that the observed oxygen vacancy signal may not accurately reflect the bulk stoichiometry or electrical behavior. Considering all of this, since oxygen vacancies contribute to carrier concentration, an optimal balance between defect density and film microstructure is required to minimize resistivity in sputtered ITO films.

To explore whether the resistivity variation can be related to the crystallinity of the films, we performed GIXRD measurements. The results are shown in Figure 4-4. To ensure the maximum consistency between electrical and structural results, the samples characterized by GIXRD were the same square samples that were later used for Hall effect measurements using van der Pauw configuration. Thus, the samples had copper wires glued to the corners by silver paint. Because of this, in every diffractogram we found the main peaks of cubic Cu [13] from the cables and cubic Ag [14] from the Ag paste used to connect the cables to the corners of the sample. Some samples show a bump in the 15º - 20º region, likely due to the glass substrate. There is no signal of In_2O_3 planes for the ITO samples fabricated with pressure ≥ 0.75 mbar, indicating that these samples are amorphous. In contrast the 0.5 mbar sample exhibits some peaks at 30.6º, 35.5º, and 51º that correspond to the (222), (400), and (440) In_2O_3 planes respectively [15][16].

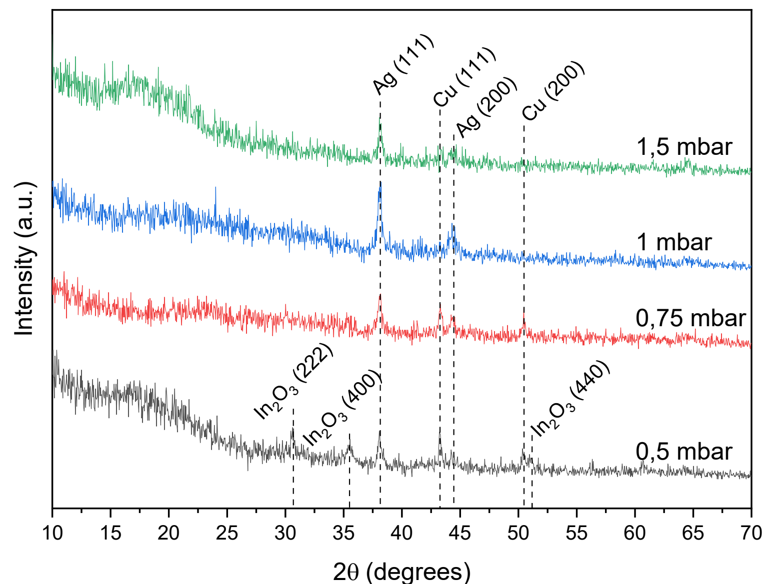

Figure 4-4 GIXRD patterns of ITO films deposited at different pressures with 2.2 W/cm².

Analyzing the GIXRD results together with the resistivity, we found that there is a correlation on the resistivity decrease with the polycrystalline/amorphous transition, being 0.75 mbar the turning point. In conventional magnetron sputtering systems the deposition pressure is much lower than 0.5 mbar (typically 10^{-2} – 10^{-3} mbar), and thus ITO films are typically polycrystalline, and the free carrier concentration is determined by Sn content and its activation [3]. On the other hand, in our samples

deposited at 1.0 mbar and above, the films are amorphous and therefore the carrier concentration is mainly due to the O vacancies [4].

The mobility and the carrier concentration of the ITO films deposited on glass substrate was obtained by Hall effect measurement. For this, the van der Pauw configuration was used. As mentioned, previously, in the cornets of the samples, Cu wires were glued with silver paint to ensure a good contact with the sample holder during Hall effect measurement. After each measurement, 30 min annealing steps in hotplate (in air) were performed for each sample and they were measured again. The results are depicted in Figure 4-5.

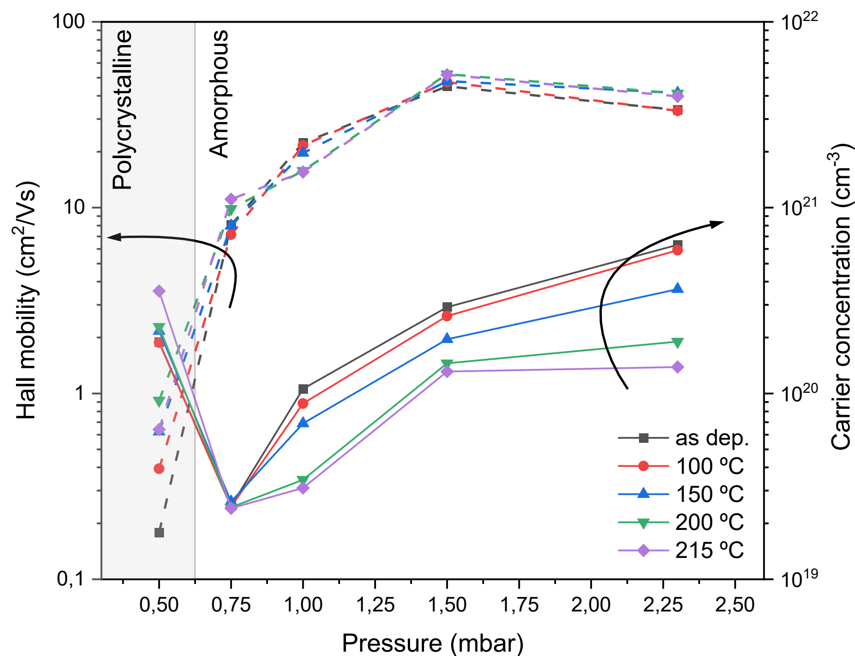

Figure 4-5 Mobility and carrier concentration of ITO films deposited with different pressures at 2.2 W/cm² as deposited and with different hotplate annealing steps for 30 min.

The first trend is that the carrier concentration increases with deposition pressure, with the only exception of the 0.5 mbar sample. This is the only one that shows polycrystalline nature, so it can justify this deviation from the trend. For pressures above 1.0 mbar the electron concentration is relatively high, in the 10^{20}-10^{21} cm^{-3} range. The maximum value is 6.3x10^{20} cm^{-3} for the 2.3 mbar sample, which is a very high value considering the amorphous character of the films. As it has been explained, in polycrystalline ITO Sn doping is the main origin of free carrier concentration, while in amorphous ITO, the origin is oxygen vacancy concentration [4][5]. The trend found for the carrier concentration agrees with this scenario: for low pressure we are detecting the Sn doping of polycrystalline ITO, while increasing the pressure produces films with more O_2 vacancies due to a reduced energy of the incoming species. Regarding the mobility, it increases with pressure up to a maximum of 45 cm^2/Vs at 1.5 mbar. There is a slightly decrease at 2.3 mbar. An unexpected result was

that the polycrystalline film presented the minimum mobility of the set, with a very low value of only 0.2 cm^2/Vs. This might indicate that for this sample, the electrons are dispersed by the grain boundaries, which is typically a limiting factor for the mobility [17]. On the other hand, the amorphous films present very high mobilities, with values comparable to optimized polycrystalline ITO films. In these films the limiting factor must be the ionized impurities (oxygen vacancies).

Taking into account the XPS results, there is an inverse trend between the oxygen vacancies (O_V) and the carrier concentration by Hall effect. XPS results show that by reducing the pressure (0.75 mbar), the percentage that represents the O_v over the total O 1s signal is higher, therefore a higher carrier concentration should be observed. This contradiction can be explained by the fact that XPS information primarily comes from the surface of the sample, thus it is possible that O_v presence comes from an oxide film that grew after the sample was removed from the sputtering chamber. Furthermore, the presence of C 1s (not shown) also confirms the unavoidable contamination of the sample during the extraction and XPS measurement. These results can be explained by a top oxide film that is different depending on deposition pressures. This is probably due to the difference in porosity caused by the difference in deposition rate.

Finally, the thermal stability of the films was studied with consecutive hotplate annealing processes, between 100 ºC - 215 ºC. The annealing duration was kept constant at 30 min. Annealing at 100 ºC in air with a hotplate for 30 min did not produce any relevant effect on the mobility and carrier concentration, indicating that the HPS ITO films were stable at typical cell operating conditions. On the other hand, annealing at higher temperatures affected mainly carrier concentration, with a small impact on mobility. The samples showed different trends depending on the crystal structure. The polycrystalline sample (0.5 mbar) was the only sample that improved both mobility and carrier concentration and, thus, resistivity. However, for the samples with lowest resistivity values before annealing (1.5 and 2.3 mbar), the carrier concentration strongly decreases while the mobility slightly improves. This is consistent with the fact that oxygen vacancies are in the origin of the carrier concentration: annealing in air produces the oxidation of the amorphous films, reducing the amount of oxygen vacancies and therefore reducing carrier concentration. After annealing at 215 ºC the best sample was the one deposited at 1.5 mbar with a mobility of 51.90 cm^2/Vs, carrier concentration of 1.3×10^{20} cm^{-3} and resistivity of 9×10^{-4} Ωcm.

4.2 Optical characterization of ITO deposited by high-pressure sputtering

To characterize the transparency, films with thickness ~100 nm were deposited on quartz substrates. The pressures analyzed were again 0.75, 1 or 1.5 mbar as these show a more pronounced change in

resistivity. The transmittance, reflectance (specular), and absorptance of these samples are shown in Figure 4-6 a). From the transparency standpoint there are no relevant differences between these samples: the films present a high transmittance value in the 70%–90% range in the visible region, with the typical oscillations due to interference. Focusing on the absorptance, it is negligible in the visible region as the three samples show values in the 1 – 2 % range. In the infrared region there is a small increase of the absorptance with pressure, which can be related to the increase of free carriers measured electrically. In any case, the absorptance is lower than 10% in the whole high wavelength region. The differences in resistivity do not have a relevant impact on the transmittance.

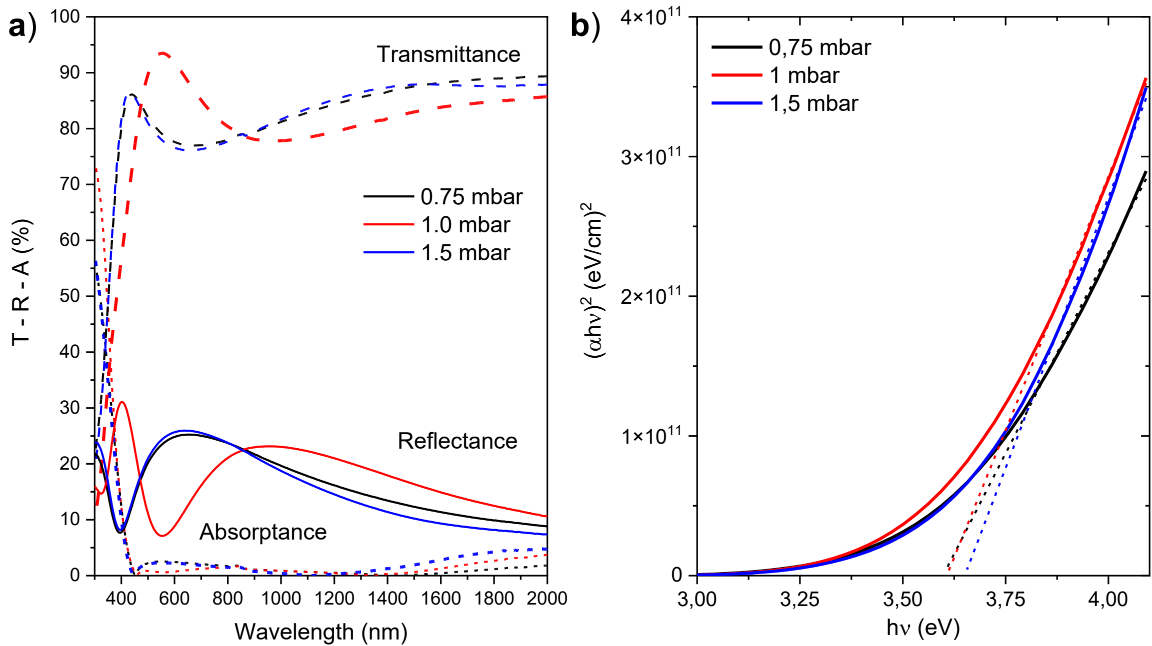

Figure 4-6 a) transmittance, reflectance and absorptance of ITO/quartz samples deposited with different pressures and 2.2 W/cm² and b) Tauc plot used to obtain the direct optical band gap of ITO.

The weighted transmittance was calculated to accurately compare the samples. The results of these calculations were very similar for the three films: 79.5% (0.75 mbar), 82.1% (1.0 mbar) and 79.1% (1.5 mbar). For this calculation, the following expression was used.

$$T_w = \frac{\int_{350}^{1100} T(\lambda) G_{AM1.5G}(\lambda) d\lambda}{\int_{350}^{1100} G_{AM1.5G}(\lambda) d\lambda} \quad 4.1$$

The optical band gap was also obtained by fitting the Tauc plot. For this, the absorption coefficient was calculated with the expression explained in Chapter III, (equation 3.28). As ITO has a direct transition between the valence and conduction band, an approximation of $(\alpha h\nu)^2 \propto (h\nu - E_{gap})$ was used. In the Tauc plot the intercept of the fit with the abscissa axis gives the gap energy. The bandgap is very similar in all three films: 3.60 eV (0.75 mbar), 3.61 eV (1.0 mbar), and 3.83 eV (1.5 mbar). These

values are within the variability of the Tauc representation and are in accordance with the results obtained in other works [18][19]. No clear Burstein-Moss displacement can be observed [20]. Thus, we can conclude that, although the ITO films deposited in this pressure range present different resistivities, there are no relevant differences in optical behavior. All the analyzed pressures give ITO films with high transparency which make them optically adequate for solar cell applications.

4.3 Electrical and optical characterization of a-Si:H(i)/ITO

With the aim to study the possible applications of the ITO deposited by HPS in Si heterojunction solar cells, ITO films were deposited on a-Si:H(i)/c-Si(n)/a-Si:H(i) substrate. It is known that hydrogen effusion from the a-Si:H(i) film at low temperatures can induce modifications on the film atomic arrangement, thus producing changes on the electrical behavior. Again, the mobility and carrier concentration were obtained by Hall effect measurement while resistivity was obtained by the van der Pauw configuration. The results are depicted in Figure 4-7 and Figure 4-8.

While the overall trend for this set of samples is similar to the samples deposited in glass, there are some differences. The as-deposited films present higher mobilities that decrease with the annealing at 100 ºC for the amorphous films, while for the 0.75 mbar ITO the mobility increases monotonically with annealing temperature. Also, this sample presents a higher electron concentration. The origin of the differences of the as-deposited films as compared with the glass substrate results is unclear, but it could be related to the difference on substrate temperature during deposition due to the different heat conductivity of Si and glass. Although the substrate holder reached roughly the same temperature, we do not have a direct measurement of the substrate surface. Besides, Si has higher heat conductivity than glass.

As with glass substrates, the carrier concentration decreases with the annealing temperature for all three samples, but with these c-Si substrates the decrease is more pronounced than for the glass substrate samples. This can be due to a reduction in the oxygen vacancies because of the effusion of hydrogen from a-Si:H(i). Regarding the resistivity, after the 215 ºC anneal, the resistivity of the 1.5 mbar sample degraded to $3x10^{-3}$ Ωcm, which again indicate that H effusion from the a-Si:H(i) plays a role in the ITO carrier concentration. Thus, to ensure that this effect is limited, a pre-deposition annealing step would be needed to promote lightly-bonded H effusion from the a-Si:H.

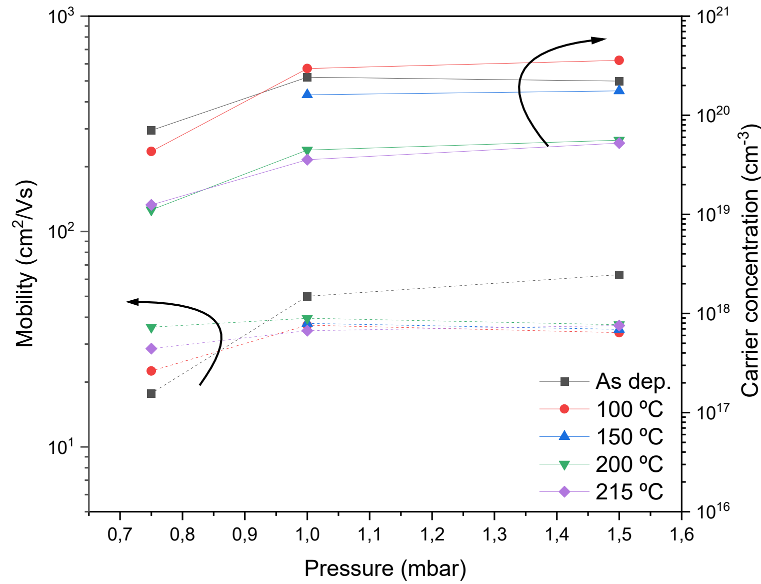

Figure 4-7 Mobility and carrier concentration of ITO films deposited on a-Si:H(i)/c-Si(n)/a-Si:H(i) substrates with different pressures at 2.2 W/cm² as deposited and with different hotplate annealing steps for 30 min.

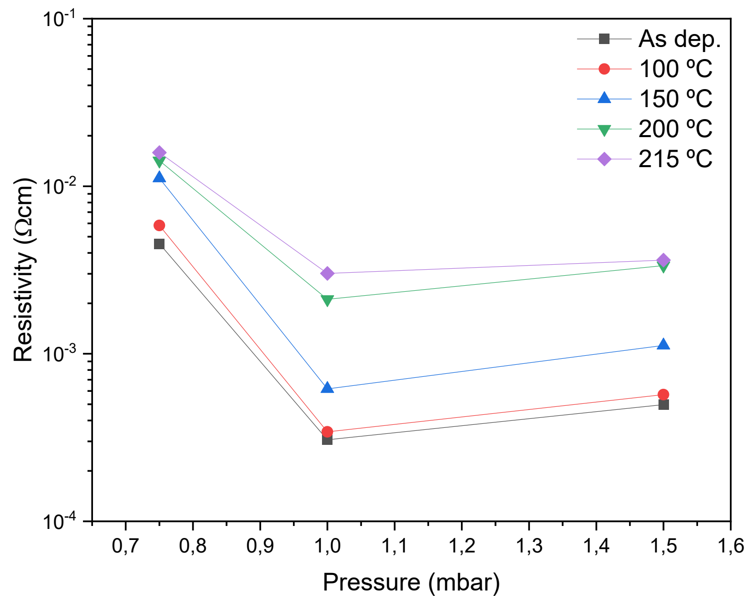

Figure 4-8 Resistivity of ITO films deposited on a-Si:H(i)/c-Si(n)/a-Si:H(i) substrates with different pressures at 2.2 W/cm2 as deposited and with different hotplate annealing steps for 30 min.

The minority carrier lifetime (τ_{eff}) and implied open circuit voltage (i-V_{oc}) of ITO deposited on a-Si:H(i)/c-Si(n)/a-Si:H(i) stack was also measured with the Sinton WCT-120 system. For this measurement the ITO was deposited following the conditions that showed minimal resistivity, this is: 1.5 mbar (Ar pressure) and 2.2 W/cm^2. After each step, i.e., ITO deposition and annealing steps, the τ_{eff} was measured. The results are depicted in Figure 4-9. Before the deposition of ITO, the sample shows a τ_{eff} (at 10^{15} cm^{-3}) of 1.8 ms and i-V_{oc} (at 1 sun) of 731 mV. After the ITO is deposited, the τ_{eff}

goes down to 14 µs. This is due to the well-known a-Si:H degradation when it is exposed to UV radiation [21]. This damage is not permanent and can be recovered by low temperature annealing in air. The origin of the degradation is the Si–H bond breakage by UV radiation of the plasma that takes place without atomic displacement. Low temperature annealing can heal most of these broken bonds. With the hotplate annealing steps, the τ_{eff} is recovered to the same order of magnitude as it was before the ITO deposition. With the 215 ºC annealing process, the τ_{eff} is 1.1 ms and i-V_{oc} 719 mV

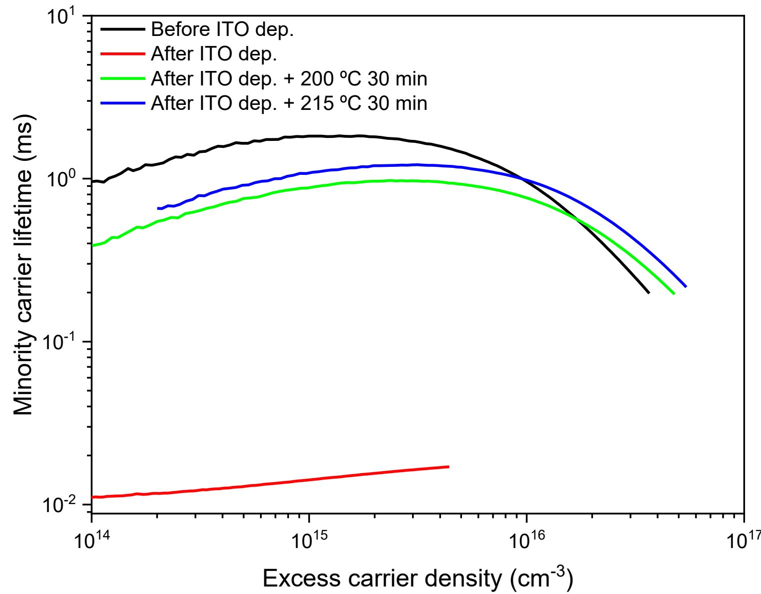

Figure 4-9 Minority carrier lifetime of ITO/a-Si:H(i)/c-Si(n)/a-Si:H(i) structure before and after the ITO deposition and annealing steps.

Finally, to study the antireflective properties of the optimized HPS ITO film after the anneals, the reflectance of the same sample as Figure 4-9 was measured in the 300–2500 nm wavelength range, and the results are shown in Figure 4-10. It is observed the typical characteristics of an antireflective coating on polished Si, with a reflectance minimum of only 0.8% at a wavelength of 656 nm. Additionally, the weighted reflectance in the 350–1100 wavelength range was calculated by the following expression.

$$R_w = \frac{\int_{350}^{1100} R(\lambda) G_{AM1.5G}(\lambda) d\lambda}{\int_{350}^{1100} G_{AM1.5G}(\lambda) d\lambda} \qquad 4.2$$

As a reference, while a polished Si wafer has a weighted reflectance of around 45%, in this case the weighed value was 16.4%. This is a satisfactory value for untextured Si solar cells with ITO films with ~80 nm thickness.

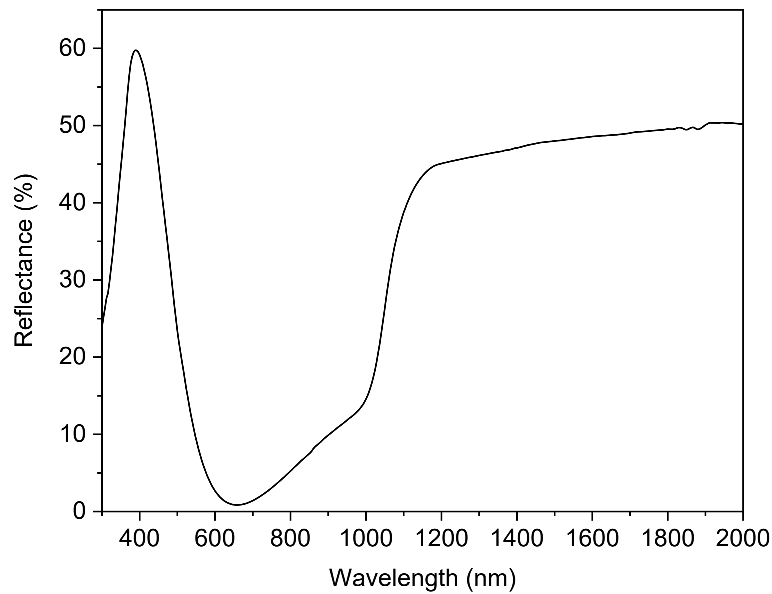

Figure 4-10 Reflectance of ITO/a-Si:H(i)/c-Si(n) sample after the 215 ºC 30 min annealing.

4.4 Si heterojunction solar cell with ITO deposited by high-pressure sputtering

Finally, a Si heterojunction solar cell prototype including ITO deposited by HPS was fabricated. For this cell, the deposition of a-Si:H(i), a-Si:H(n), and a-Si:H(p) were done at *CIEMAT*. A photograph as well as a schematic of the device are depicted in Figure 4-11. Before the deposition of ITO, the sample was measured with the Sinton WCT-120 to obtain the τ_{eff} and $i\text{-}V_{oc}$. The values were 1.6 ms at 10^{15} cm^{-3} and 710 mV at 1 sun, respectively. This represents an excellent starting point in terms of passivation to fabrication a solar cell.

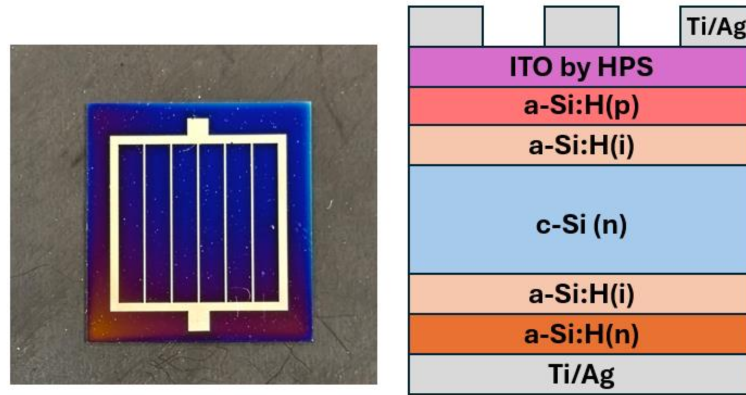

Figure 4-11 Photograph (left) and schematic diagram (right) of a Si heterojunction solar cell incorporating ITO deposited by high-pressure sputtering.

Once the ITO (~80 nm) and the Ti/Ag (20/500 nm) metal stack at the front and rear side are deposited. The IV curve of the solar cells was obtained by a Sinus-70 solar simulator with the AM1.5G spectrum. Subsequent annealing steps on hotplate were done to recover the sputtering damage caused by the ITO deposition. After each annealing, the IV curve of the sample was measured. The curves are depicted in Figure 4-12. The unannealed cell shows an IV curve that exhibits a "S-shape" which can be originated due to barriers in the charge transport [22]. These barriers primarily come from defects in the selective contacts, in this case a-Si:H(n) or a-Si:H(p), or even TCOs such as ITO that hinder the charge transport [23]. The S-shape in this case might be originated from the damage caused on the a-Si:H(i)/a-Si:H(p) by the ITO deposition that can create some defects on the interfaces that can create Fermi-level pinning.

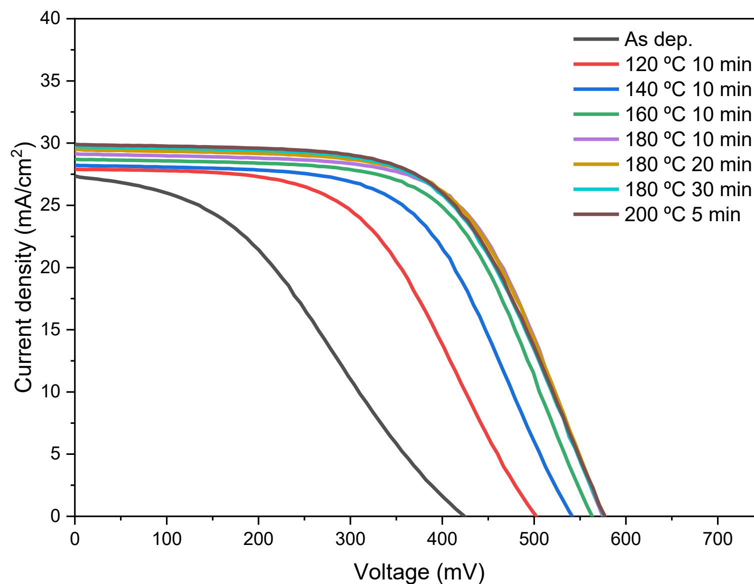

Figure 4-12 Evolution of IV curve of the Si heterojunction with ITO deposited by HPS with different hotplate annealing steps.

When the annealing processes are performed, the S-shape disappears until a more conventional IV curve is achieved at 160 ºC. Further annealing steps increase the short circuit current density (J_{sc}) and the open circuit voltage (V_{oc}) up to 29.9 mA/cm^2 and 577 mV (200 ºC 5 min annealing). The evolution on the J_{sc}, V_{oc}, and FF with the annealing steps are depicted in Figure 4-13. These three parameters improve with the annealing, which indicates that the sample recovers the passivation

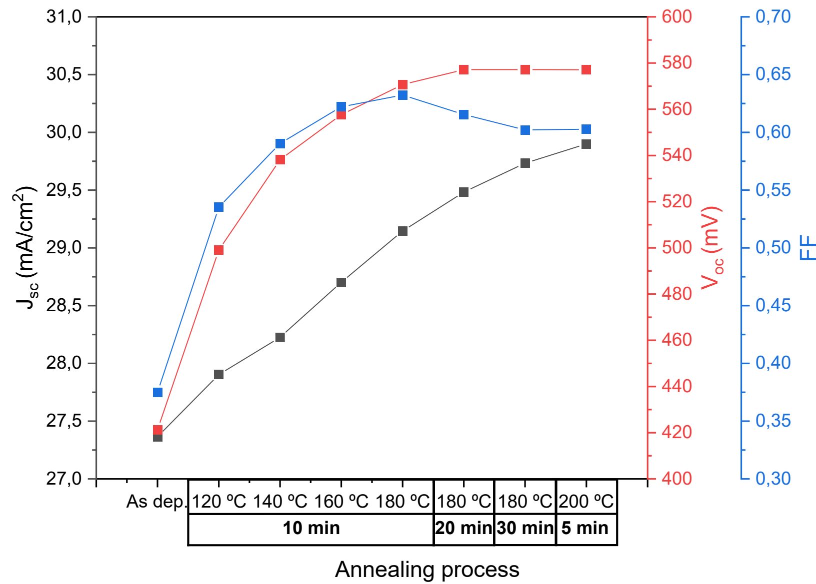

Figure 4-13 Evolution of Jsc, Voc, and FF of Si heterojunction solar cell with ITO deposited by HPS with subsequent annealing process performed with a hotplate.

The solar simulator can also extract the parallel resistance (R_p), and series resistance (R_s) for each IV curve. The evolution of these parameters as well as the efficiency of the cell is depicted in Figure 4-14. As it was observed in the IV curves, the estimated R_p is low, 66 Ω. This suggest that the ITO deposition is creating defects (pinholes) in the underlying a-Si:H(p) film that acts as shunting paths bypassing the a-Si:H(p)/c-Si(n) junction. Regarding the R_s, the as-deposited value is 6.48 Ω, which is considered high for solar cells. A high R_s indicates resistive losses in some parts of the device such as poor lateral conductivity of ITO, poor contact between ITO and metal grid, or even due to grid design [24]. In this case, the most likely reason is the contact between ITO and Ti/Ag metal stack as the resistivity of the ITO deposited at 1.5 mbar is ~5x10^{-4} Ωcm (Figure 4-8), which is in the same range as typical ITO for solar cells applications [25]. This leads to a low FF as it is observed in Figure 4-13 which is translated to an efficiency of 4.32 %.

With the annealing processes, the R_p immediately increases to 821 Ω and stays around this value for the rest of annealing steps. The R_s also improves with the first annealing step as this decreases to 4.6 Ω. The decrease of R_s continues until the 180 ºC 10 min annealing step when the minimum R_s value is obtained 3.2 Ω. After this temperature the R_s slightly increases to 4 Ω. All of this indicates that low

temperature anneals in air can recover the sputtering damage and improve the contact resistivity between ITO and the metal grid. Extended annealing process at 180 ºC or 200 ºC beging to degrade the R_s probably due to an increase in the resistivity of the ITO/a-Si:H as it was observed in Figure 4-8. The efficiency also plateaued with the 180 ºC 10 min annealing process, achieving a value of ~10 %

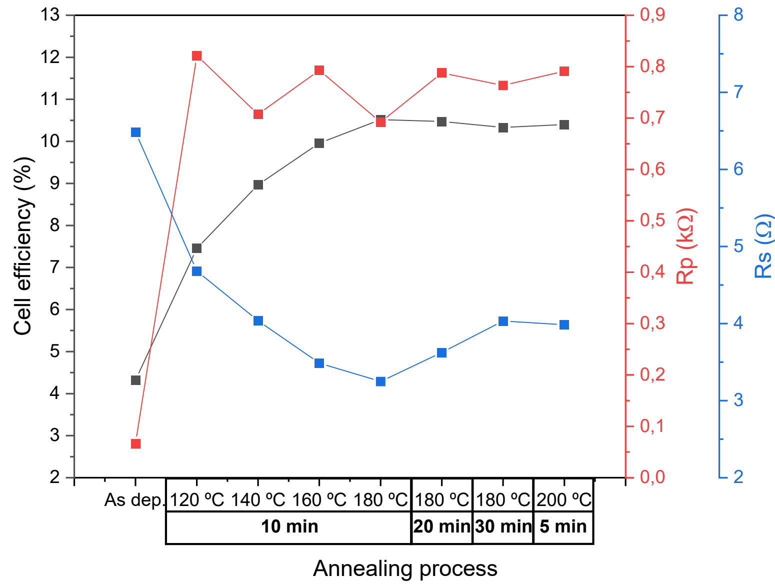

Figure 4-14 Evolution of efficiency, R_p, and R_s of Si heterojunction solar cell with ITO deposited by HPS with subsequent annealing process performed with a hotplate.

Finally, the external quantum efficiency (EQE) of the solar cell was measured, as shown in Figure 4-15. The spectral response exhibits a shape that closely resembles that of conventional silicon heterojunction solar cells [26], indicating similar absorption and collection mechanisms. In the short-wavelength region (below 500 nm), a pronounced drop in EQE is observed, which is attributed to blue parasitic absorption in the hydrogenated amorphous silicon (a-Si:H) layers on the front side of the device. For instance, at 400 nm the EQE reaches only 15%, highlighting the optical losses due to the front contact stack. In the intermediate wavelength range, from approximately 600 to 950 nm, the EQE attains its peak values around 80%, consistent with the strong absorption coefficient and efficient carrier collection in the crystalline silicon bulk. Beyond 950 nm, the EQE gradually declines with increasing wavelength, which can be due to reduced photon absorption near the Si band edge and increased recombination losses at the rear interface.

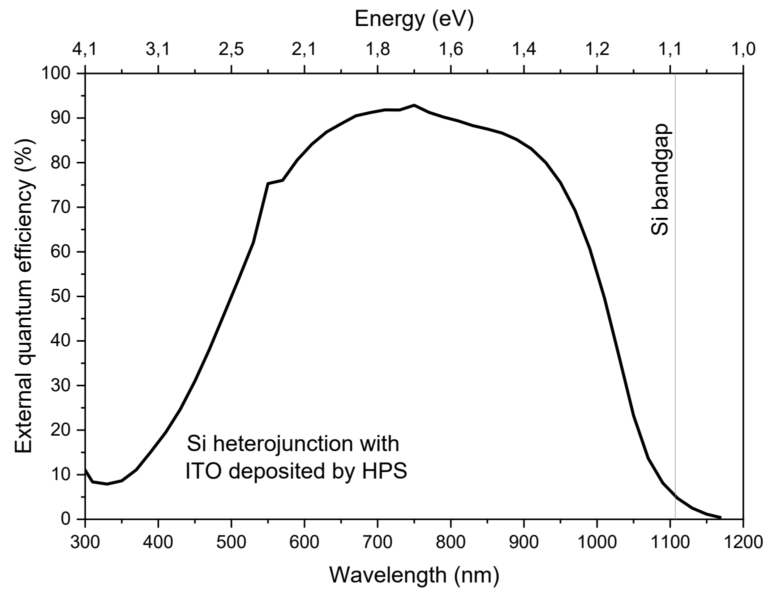

Figure 4-15 External quantum efficiency for the solar cell fabricated with ITO deposited by HPS after the 200 ℃ 5 min annealing process.

4.5 Summary and conclusions

In this chapter, the deposition and characterization of indium tin oxide (ITO) thin films fabricated by high-pressure sputtering (HPS) were comprehensively analyzed with the aim of evaluating their applicability in silicon heterojunction solar cells. The study explored the effect of varying argon working pressures (0.5–2.3 mbar) and power densities (1.5–2.5 W/cm²) on the structural, electrical, and optical properties of ITO films.

Electrical resistivity was found to be strongly influenced by the argon pressure, with higher pressures (≥ 1.0 mbar) leading to low-resistivity films in the range of 10^{-4} Ωcm, which is suitable for photovoltaic applications. Hall effect measurements showed that carrier concentration increased with pressure, mainly due to the formation of oxygen vacancies in amorphous films, while the highest electron mobility (~45 cm²/V·s) was achieved at 1.5 mbar. X-ray photoelectron spectroscopy (XPS) shows a higher density of oxygen vacancies at lower deposition pressures, although the correlation between surface vacancies and bulk carrier concentration was limited by surface oxidation and porosity effects. GIXRD analysis revealed a transition from polycrystalline to amorphous structure as pressure increased, with the amorphous regime offering better electrical performance.

Optical measurements confirmed high transmittance (70–90%) in the visible range and low absorptance (~1–2%), with negligible impact from resistivity variations. Tauc plot analysis revealed direct optical bandgaps of 3.6–3.8 eV with no clear Burstein-Moss shift, indicating minimal band filling effects despite high carrier concentrations.

When integrated into a-Si:H(i)/c-Si(n)/a-Si:H(i) heterostructures, the ITO films exhibited electrical properties similar to those deposited on glass, although slight differences suggested substrate-dependent effects, likely related to thermal conductivity and hydrogen effusion. Post-deposition annealing was shown to recover the passivation properties of a-Si:H(i) and improve the ITO/metal stack interface. The final heterojunction solar cell incorporating HPS-ITO achieved an efficiency of ~10% after mild thermal treatment, with improved series and shunt resistance values.

In conclusion, ITO films deposited by HPS exhibit excellent electrical and optical characteristics for photovoltaic applications, particularly when deposited at pressures around 1.5 mbar. The results demonstrate that HPS is a viable deposition method for producing high-quality TCOs compatible with silicon heterojunction solar cells, offering an alternative to conventional low-pressure sputtering processes.

4.6 References

[1] M. H. Ahn, E. S. Cho, and S. J. Kwon, "Effect of the duty ratio on the indium tin oxide (ITO) film deposited by in-line pulsed DC magnetron sputtering method for resistive touch panel," *Appl. Surf. Sci.*, vol. 258, no. 3, pp. 1242–1248, 2011, doi: 10.1016/j.apsusc.2011.09.081.

[2] O. Tuna, Y. Selamet, G. Aygun, and L. Ozyuzer, "High quality ITO thin films grown by dc and RF sputtering without oxygen," *J. Phys. D. Appl. Phys.*, vol. 43, no. 5, 2010, doi: 10.1088/0022-3727/43/5/055402.

[3] Y. Shigesato and D. C. Paine, "Study of the effect of Sn doping on the electronic transport properties of thin film indium oxide," *Appl. Phys. Lett.*, vol. 62, no. 11, pp. 1268–1270, 1993, doi: 10.1063/1.108703.

[4] K. Okada *et al.*, "Correlation between resistivity and oxygen vacancy of hydrogen-doped indium tin oxide thin films," *Thin Solid Films*, vol. 519, no. 11, pp. 3557–3561, 2011, doi: 10.1016/j.tsf.2011.01.249.

[5] H. Morikawa and M. Fujita, "Crystallization and electrical property change on the annealing of amorphous indium-oxide and indium-tin-oxide thin films," *Thin Solid Films*, vol. 359, no. 1, pp. 61–67, 2000, doi: 10.1016/S0040-6090(99)00749-X.

[6] S. Patwardhan and B. Kavaipatti, "Effect of ITO capping and its deposition parameters on

electrical properties of MoO3/Si carrier-selective contact solar cell," *Ina. Lett.*, vol. 4, no. 3, pp. 139–145, 2019, doi: 10.1007/s41403-018-0053-0.

[7] J. R. Bellingham, W. A. Phillips, and C. J. Adkins, "Amorphous indium oxide," *Thin Solid Films*, vol. 195, no. 1–2, pp. 23–32, Jan. 1991, doi: 10.1016/0040-6090(91)90255-V.

[8] N. Ito, Y. Sato, P. K. Song, A. Kaijio, K. Inoue, and Y. Shigesato, "Electrical and optical properties of amorphous indium zinc oxide films," *Thin Solid Films*, vol. 496, no. 1, pp. 99–103, 2006, doi: 10.1016/j.tsf.2005.08.257.

[9] J. E. Sansonetti and W. C. Martin, "Handbook of basic atomic spectroscopic data," *J. Phys. Chem. Ref. Data*, vol. 34, no. 4, pp. 1559–2259, 2005, doi: 10.1063/1.1800011.

[10] W. R. ANGUS, "The Identification of Molecular Spectra," *Nature*, vol. 148, no. 3748. pp. 240–240, 1941, doi: 10.1038/148240a0.

[11] B. Bharti, S. Kumar, H.-N. Lee, and R. Kumar, "Formation of oxygen vacancies and Ti 3+ state in TiO 2 thin film and enhanced optical properties by air plasma treatment," 2016, doi: 10.1038/srep32355.

[12] S. Guan, L. Hao, M. Murayama, X. Xie, S. Komuro, and X. Zhao, "Influence of anneal temperature in air on surface morphology and photoluminescence of ZnO thin films," *IOP Conf. Ser. Mater. Sci. Eng.*, vol. 522, no. 1, 2019, doi: 10.1088/1757-899X/522/1/012004.

[13] Y. Kobayashi, T. Shirochi, Y. Yasuda, and T. Morita, "Synthesis of silver/copper nanoparticles and their metal-metal bonding property," *J. Min. Metall. Sect. B Metall.*, vol. 49, no. 1, pp. 65–70, 2013, doi: 10.2298/JMMB120927025K.

[14] J. Zemann, "Crystal structures," *Acta Crystallogr.*, vol. 2, no. 1, pp. 7–83, 1965, doi: 10.1107/s0365110x65000361.

[15] J. Gwamuri, M. Marikkannan, J. Mayandi, P. K. Bowen, and J. M. Pearce, "Influence of oxygen concentration on the performance of ultra-thin RF magnetron sputter deposited indium tin oxide films as a top electrode for photovoltaic devices," *Materials (Basel).*, vol. 9, no. 1, 2016, doi: 10.3390/ma9010063.

[16] Z. Chen, W. Li, R. Li, Y. Zhang, G. Xu, and H. Cheng, "Fabrication of highly transparent and conductive indium-tin oxide thin films with a high figure of merit via solution processing," *Langmuir*, vol. 29, no. 45, pp. 13836–13842, 2013, doi: 10.1021/la4033282.

[17] A. Valla, P. Carroy, F. Ozanne, and D. Muñoz, "Understanding the role of mobility of ITO films for silicon heterojunction solar cell applications," *Sol. Energy Mater. Sol. Cells*, vol. 157, pp. 874–880, 2016, doi: 10.1016/j.solmat.2016.08.002.

[18] M. Marikkannan, M. Subramanian, J. Mayandi, M. Tanemura, V. Vishnukanthan, and J. M. Pearce, "Effect of ambient combinations of argon, oxygen, and hydrogen on the properties of DC magnetron sputtered indium tin oxide films," *AIP Adv.*, vol. 5, no. 1, 2015, doi: 10.1063/1.4906566.

[19] A. Tumbul, F. Aslan, A. Göktaş, and I. H. Mutlu, "All solution processed superstrate type

Cu2ZnSnS4 (CZTS) thin film solar cell: Effect of absorber layer thickness," *J. Alloys Compd.*, vol. 781, pp. 280–288, 2019, doi: 10.1016/j.jallcom.2018.12.012.

[20] I. Hamberg, C. G. Granqvist, K. F. Berggren, B. E. Sernelius, and L. Engström, "Band-gap widening in heavily Sn-doped In2O3," *Phys. Rev. B*, vol. 30, no. 6, pp. 3240–3249, 1984, doi: 10.1103/PhysRevB.30.3240.

[21] B. Demaurex, S. De Wolf, A. Descoeudres, Z. Charles Holman, and C. Ballif, "Damage at hydrogenated amorphous/crystalline silicon interfaces by indium tin oxide overlayer sputtering," *Appl. Phys. Lett.*, vol. 101, no. 17, 2012, doi: 10.1063/1.4764529.

[22] R. Saive, "S-Shaped Current-Voltage Characteristics in Solar Cells: A Review," *IEEE J. PHOTOVOLTAICS*, vol. 9, no. 6, pp. 1477–1484, 2019, doi: 10.1109/JPHOTOV.2019.2930409.

[23] Z. C. Holman *et al.*, "Current losses at the front of silicon heterojunction solar cells," *IEEE J. Photovoltaics*, vol. 2, no. 1, pp. 7–15, 2012, doi: 10.1109/JPHOTOV.2011.2174967.

[24] M. Wolf and H. Rauschenbach, "Series resistance effects on solar cell measurements," *Adv. Energy Convers.*, vol. 3, no. 2, pp. 455–479, 1963, doi: 10.1016/0365-1789(63)90063-8.

[25] C. G. Granqvist and A. Hultåker, "Transparent and conducting ITO films: New developments and applications," *Thin Solid Films*, vol. 411, no. 1, pp. 1–5, 2002, doi: 10.1016/S0040-6090(02)00163-3.

[26] A. Descoeudres, Z. C. Holman, L. Barraud, S. Morel, S. De Wolf, and C. Ballif, ">21% Efficient Silicon Heterojunction Solar Cells on N-and P-Type Wafers Compared," *IEEE J. Photovoltaics*, vol. 3, no. 1, pp. 83–89, 2013, doi: 10.1109/JPHOTOV.2012.2209407.

CHAPTER V: ITO:H DEPOSITED BY RF SPUTTERING

This chapter is based on the research conducted during an international stay at the Photovoltaics and Thin Film Electronics Laboratory (PV-Lab) at EPFL working with the High-Temperature Passivating Contacts group, led by Dr. Franz-Josef Haug. The work was focused on the characterization of ITO films deposited by RF sputtering with H_2 atmosphere to fabricate hydrogen saturated ITO films (ITO:H). The final objective was to reduce the fabrication steps for Tunnel Oxide Passivated Contact (TOPCon) solar cells as ITO:H can have a double function: acting as a transparent conducting layer and as a hydrogen reservoir to induce passivation on the underlying films. Additionally, ITO:H can also be integrated into perovskite/silicon (PK/Si) tandem as a recombination layer.

First, a brief section is presented to motivate the potential use of ITO:H in TOPCon technologies. This is followed by a section where results of this research are shown.

5.1 Motivation

This research seeks to reduce the number of fabrication steps of TOPCon solar cells as bottom cells for Si/PK tandem devices. In the manufacturing process of such tandem devices, a hydrogenation step is necessary to passivate defects resulting from the formation of the poly-Si passivating layer. Typically, this is achieved by depositing a hydrogen-rich silicon nitride (SiN_x:H) layer followed by a firing step carried out at high temperature. After hydrogenation, the SiN_x:H, layer should be removed by a chemical etching with diluted HF before the deposition of a TCO, which, in Si/PK tandem devices act as a recombination junction. In that sense, an ITO:H could hit two targets with one shot since the hydrogen contained inside the ITO could passivate the defects at the interfaces while the ITO layer acts as the recombination junction.

5.2 Experimental results

To obtain an ITO:H layer, a commercial *Univex* RF sputtering from *Leybold* was used. This system was adapted to supply three gasses: pure Ar, mixed Ar/O_2 (95 %/5 %), and mixed Ar/H_2 (95 %/5 %).

The ITO target composition was 90 % In_2O_3 + 10 % SnO_2 with a purity of 99.99 %. More details about the sputtering system can be found in Chapter II. Three main experiments were conducted: electrical and optical characterization of ITO deposition varying the power density with Ar atmosphere, electrical and optical characterization of ITO deposition with constant power density and $Ar/O_2/H_2$ atmosphere and testing passivation of poly-Si(n)/ITO:H with different annealing processes.

To determine the content of each gas inside the chamber during the ITO deposition, the following formulas where MFC_x stands for the MFC percentage for each gas line.

$$Ar_{content}\,(\%) = \frac{50 * MFC_{Ar}(\%) + 9.5 * MFC_{Ar-O_2}(\%) + 9.5 * MFC_{Ar-H_2}(\%)}{50 * MFC_{Ar}(\%) + 10 * MFC_{Ar-O_2}(\%) + 10 * MFC_{Ar-H_2}(\%)} * 100$$

$$O_{2content}\,(\%) = \frac{0.5 * MFC_{Ar-O_2}(\%)}{50 * MFC_{Ar}(\%) + 10 * MFC_{Ar-O_2}(\%) + 10 * MFC_{Ar-H_2}(\%)} * 100 \qquad 5.1$$

$$H_{2content}(\%) = \frac{0.5 * MFC_{Ar-H_2}(\%)}{50 * MFC_{Ar}(\%) + 10 * MFC_{Ar-O_2}(\%) + 10 * MFC_{Ar-H_2}(\%)} * 100$$

For testing the passivation effect of ITO:H films, ~18 nm of a-Si(n) layer was deposited by PEVCD and annealed at 850 ºC to obtain poly-Si(n) on top of a n-type Si wafer. During a-Si(n) deposition, methane was introduced to form a-SiC(n) to avoid blistering effects [1]. Nevertheless, the carbon quantity is so low that the material is essentially poly-Si(n). This layer was deposited on both sides of the wafer. Between the Si wafer and the poly-Si(n), a chemical SiO_x was grown to improve the passivation of the wafer. Finally, ~80 nm ITO:H was deposited on both sides following the best conditions obtained in the first experiment batch. Additionally, the specific contact resistivity of poly-Si(n)/ITO:H/Ag stack was also extracted by TLM. Those structures are depicted in the following figure:

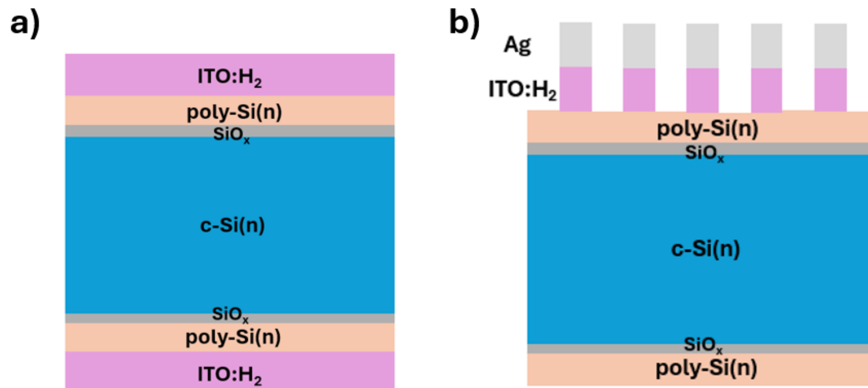

Figure 5-1 a) sample for measuring the minority carrier lifetime after the ITO deposition, and b) TLM sample for obtaining the contact resistivity of poly-Si(n)/ITO:H/Ag

5.2.1 Characterization of ITO deposited with Ar atmosphere

First, the deposition rate of ITO was characterized, considering a power density of 0.4 Wcm^{-2} to 2.4 Wcm^{-2}. For this, the working gas was only Ar, 16 sccm. This represented a working pressure of about 2.2 $x10^{-3}$ mbar. The ITO deposit was performed on 8 x 4 cm^2 glass substrate. Figure 5-2 shows the deposition rate for each of the power densities. As expected, the lower the power density, the smaller the deposition rate. For example, in the case of 0.4 Wcm^{-2}, the deposition rate is 0.24 nm/min, while for 2.4 Wcm^{-2}, it increases to 4.41 nm/min. The deposition rate may be important since it has been observed that at higher power densities, the ITO films may present a poly crystalline structure. In contrast, at lower power densities, the films could be amorphous [2].

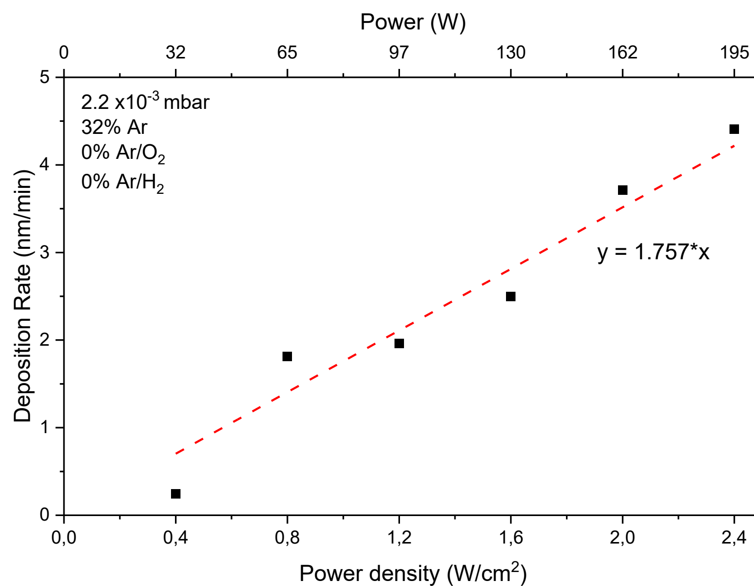

Figure 5-2 Deposition rate of ITO as a function of the power density of RF sputtering with pure Ar atmosphere.

The mobility, carrier concentration, and resistivity of these samples were measure and the results are depicted in Figure 5-3. Those fabricated at 0.4 Wcm^{-2} or 0.8 Wcm^{-2} show considerably low mobility values (between 6 and 9 cm^2/Vs). Those samples also show a lower carrier concentration of $\sim 10^{20}$ cm^{-3}. This can be explained by the deposition rate for these power densities (0.2 nm/min for 0.4 Wcm^{-2} and 1.8 nm/min for 0.8 Wcm^{-2}), which are smaller than the rest of the samples, for instance, 2.5 nm/min for 1.6 Wcm^{-2}. The effect of depositing at a low deposition rate, i.e., low power density, is a lower carrier concentration due to fewer O vacancies and lower mobility [3]. These results lead to an increase in the resistivity of the ITO layers. For the case of the samples fabricated at 1.2 Wcm^{-2} or higher power density, they present similar values of mobility (~17 cm^2/Vs), carrier concentration (~$2.5x10^{20}$ cm^{-3}), and resistivity (~$2x10^{-3}$ Ωcm). For all the samples, an interesting behavior was found, as the carrier concentration increased the mobility also increased. Although this is contrary to the normal trend in

crystalline semiconductor, this has been found for polycrystalline semiconductors such as poly-Si [4] and ITO [5]. The total mobility depends on various mechanisms (phonons scattering, ionized impurities, grain boundaries, etc.) where the more relevant dominates the concentration-mobility trend. The grain boundary mechanism typically shows this trend (as carrier concentration increases, mobility also increases). A higher concentration of carriers can modify the energy barrier between grains, sort of passivation, reducing such barriers and thus improving the mobility of the carriers.

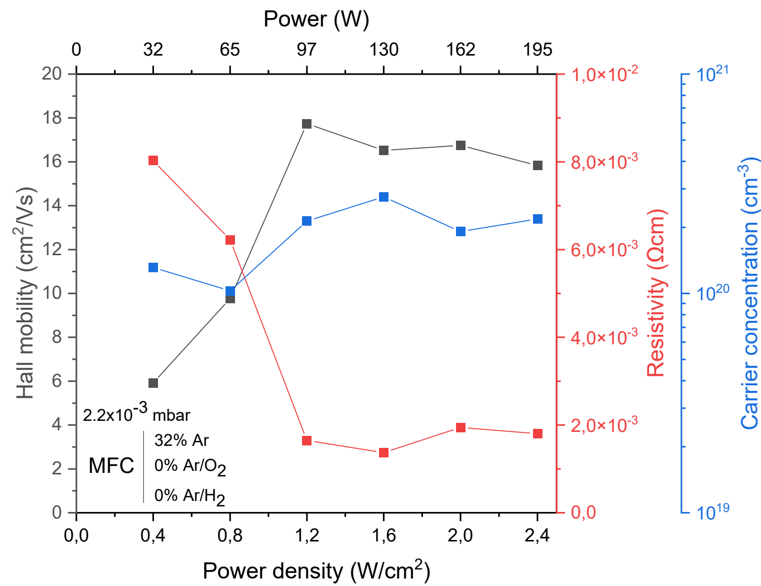

Figure 5-3 Hall mobility, carrier concentration, and resistivity of ITO thin films (~80 nm) deposited at different RF sputtering power densities.

The optical parameters (transmittance, reflectance, and absorption) were obtained by a *PerkinElmer Lambda 900* spectrophotometer with an integration sphere, measuring from 250 nm to 2500 nm with a step of 10 nm. Figure 5-4 shows the results for the power density variation experiment.

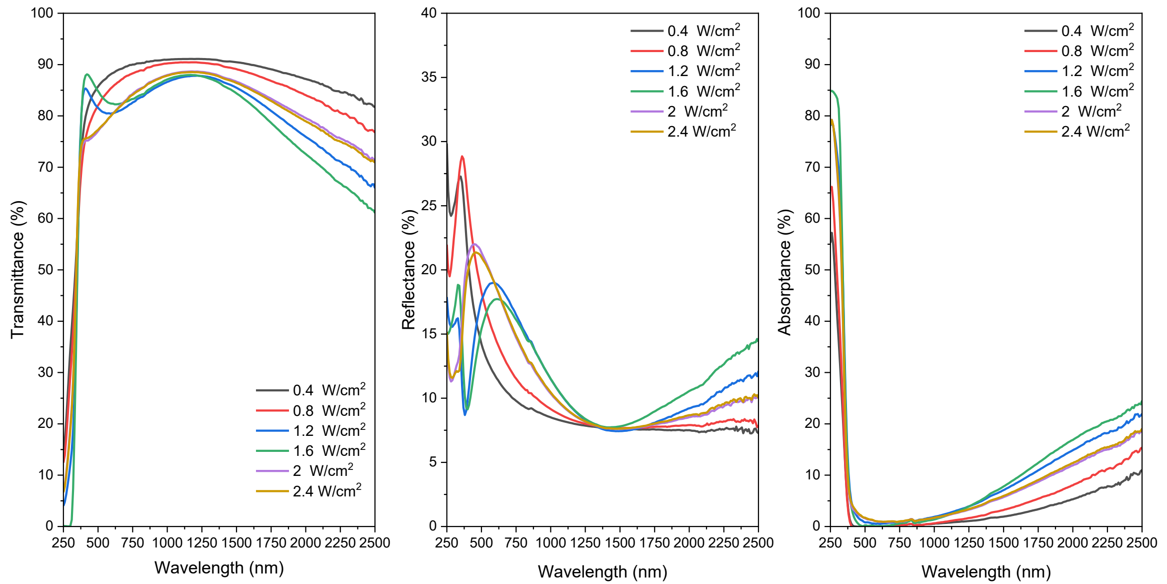

Figure 5-4 Transmittance, reflectance, and absorptance of the ITO samples fabricated at different sputtering power densities. Only Ar atmosphere.

We can observe that the samples fabricated with the lower power density (0.4 Wcm^{-2} and 0.8 Wcm^{-2}) show higher transmittances for all the wavelength ranges. This translates that these samples have the lowest absorption, which is clearly observable in the near-infrared range (NIR). This behavior is congruent to the mobility results obtained by the Hall effect, since those samples presented the lowest values of mobility and carrier concentration (~10^{20} cm^{-3}). This might be caused by fewer O vacancies in these films, which act as electron donors in ITO films [6]. In contrast, the moderate power density samples (1.2 Wcm^{-2} and 1.6 Wcm^{-2}) show a higher absorptance in the NIR. Additionally, just before the bandgap absorptance edge, some peaks appear that could be related to the difference in the thickness of the layer or the grain size [7] due to the power density change. The samples with the higher power density (2 Wcm^{-2} and 2.4 Wcm^{-2}) show a transmittance >88% in the visible range, like the samples of 1.2 Wcm^{-2} and 1.6 Wcm^{-2}. However, the transmittance in the NIR (at 2000 nm) of these samples is ~79 % in contrast to the ~75 % (1.2 W/cm^2) and ~72 % (1.6 W/cm^2). As the electrical characteristics of these samples are similar, the difference could be related to changes in the crystalline structure of the samples.

Moreover, the absorptance was normalized to the AM1.5G spectrum to compare all the samples with the following expression.

$$A_w = \frac{\int_{350}^{1100} A(\lambda) G_{AM1.5G}(\lambda) d\lambda}{\int_{350}^{1100} G_{AM1.5G}(\lambda) d\lambda} \qquad 5.2$$

Figure 5-5 shows the weighted absorptance for 300 to 1000 nm and 300 to 2500 nm ranges. As previously mentioned, the samples fabricated at lower power densities show lower absorption; nevertheless, their electrical values are not the best of the batch. Thus, we decided to continue the experiments with the power density balances the low weighted absorptance with low resistivity, i.e., the 1.6 Wcm^{-2} power density.

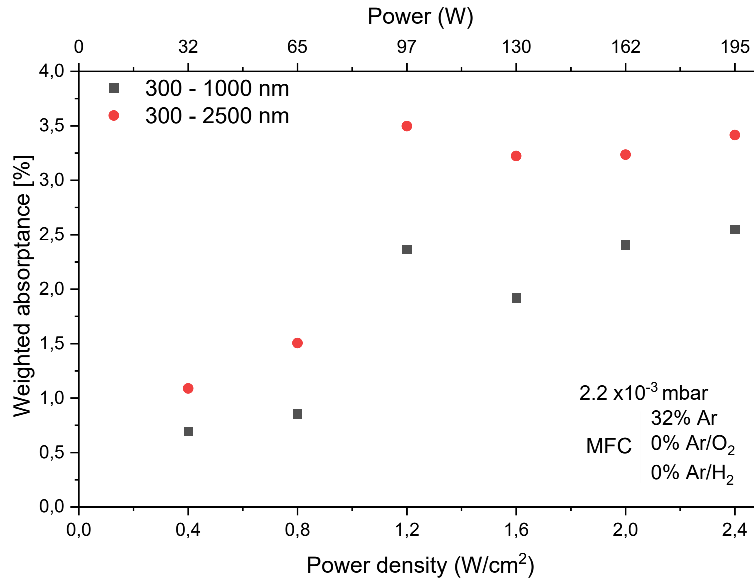

Figure 5-5 Weighted absorptance of different ITO samples fabricated at different power densities.

Figure 5-6 a) depicts the diffractogram of different samples fabricated at different power densities. As a reference, a glass substrate was measured under the same condition to confirm that the peaks were unrelated to the substrate. As expected, the glass substrate showed no peak, indicating its amorphous structure. With respect to the glass/ITO samples, some diffraction peaks appear. The most predominant peak appears around $2\theta = 34^o$; this is related to the reflection associated with the (114) In_2O_3 plane [8]. Additional peaks appear as the power density increases; for instance, the 2.4 W/cm^2 sample shows some relevant peaks at 36º and 62º, which correspond to the (200) and (331) planes of SnO_2, respectively [9]. To determine the crystallinity of the samples, the crystalline fraction (X_c) was calculated using the following equation.

$$X_c = \frac{A_c}{A_c + A_a} \tag{5.3}$$

Where A_c is the area of the diffraction peaks, A_a is the area of the amorphous component, and thus $A_a + A_c$ is the total area of the diffractogram. As a result, Figure 5-6 b) shows that increasing the power density from 0.4 W/cm^2 to 1.2 W/cm^2 leads to more crystalline samples. Nevertheless, more than 1.2 W/cm^2 does not increase the crystalline fraction any further, indicating that the crystallinity of the

samples stabilizes, most probably due to partial amorphization [3]. This is consistent with the electrical properties since the mobility follows the same tendency as the crystalline fraction, as depicted in Figure 5-3. Increasing the temperature of the substrate holder during the deposition might promote a higher crystalline fraction and potentially higher mobilities [10]. This possibility was not explored in this project.

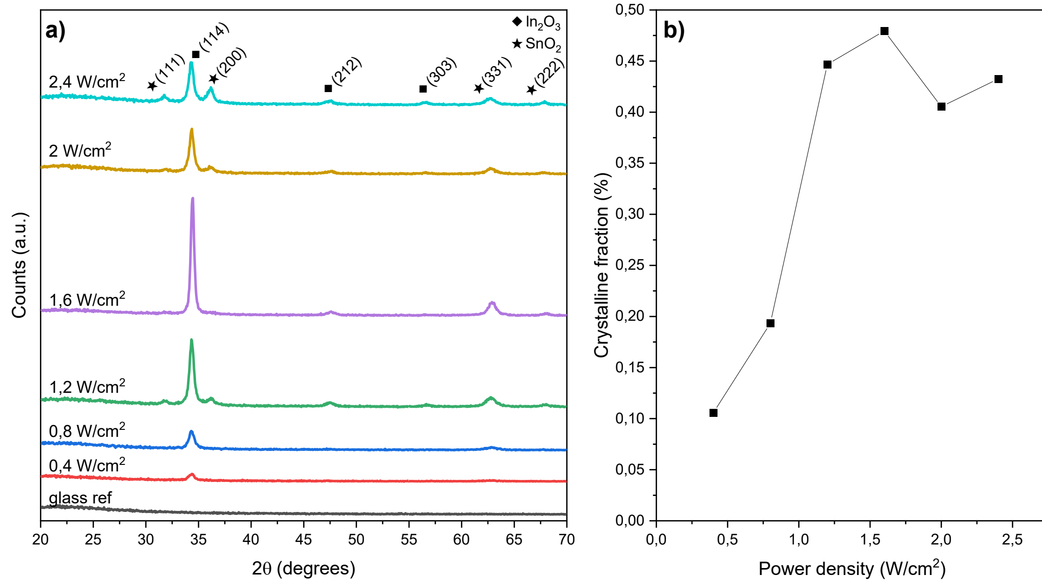

Figure 5-6 a) diffractograms of glass/ITO samples deposited with different power densities, b) crystalline fraction of the same samples.

5.2.2 Characterization of ITO deposited with Ar/O_2 atmosphere

In a second experiment, we decided to analyze the effect of including an O_2 flux during the deposition of ITO films. As mentioned above, all the following experiments were done with a power density of 1.6 Wcm^{-2}. The reason for introducing O_2 in the deposition chamber is to ameliorate the transmittance in the visible range. The free carrier absorption due to oxygen vacancies tend to decrease when O_2 flux is introduced in sputtering process. Figure 5-7 depicts the mobility, carrier concentration, and resistivity of ITO samples fabricated with different O_2 fluxes. Other groups have observed [11], that increasing the oxygen in the chamber during the deposition process produces a reduction in the mobility and an increase in the resistivity. For the samples fabricated with no O_2, we obtained values of 16 cm^2/Vs, $1.3x10^{-3}$ Ωcm, and 2.7 $x10^{20}$ cm^{-3}. In contrast, in the sample with 1% O_2, the values were 1 cm^2/Vs, 3.6 Ωcm, and $1.7x10^{18}$ cm^{-3}. This shows that introducing small quantities of oxygen can drastically alter the electrical properties of the ITO films.

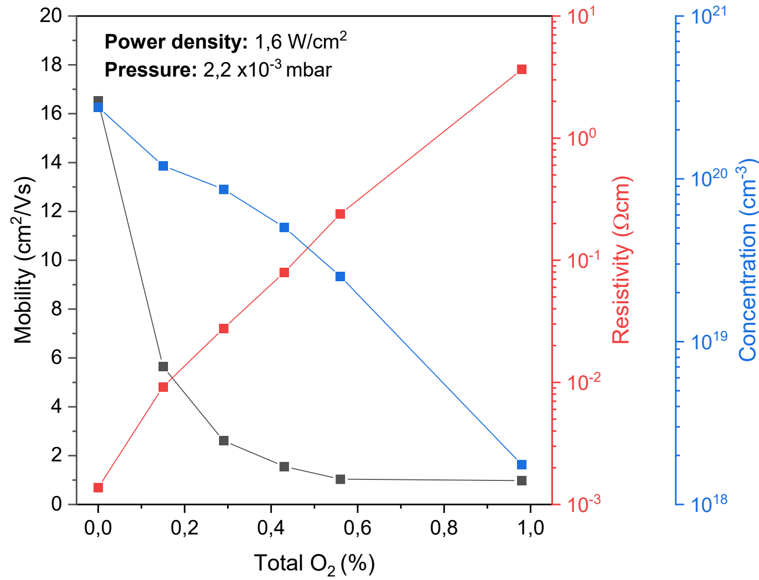

Figure 5-7 Hall mobility, carrier concentration, and resistivity of ITO thin films (~80 nm) deposited with different fluxes of O_2 with a power density of 1.6 W/cm²

Once again, the transmittance, reflectance, and absorptance were measured, as it is shown in Figure 5-8. In this case, a clear tendency is observed in the transmittance and absorptance; as the oxygen flux increases, the transmittance increases, and the absorptance decreases. The Drude effect can explain this; as the O_2 content increases, more oxygen atoms could fill the vacancies in the ITO film, reducing the electron concentration and, thus, the free carrier absorptance[12].

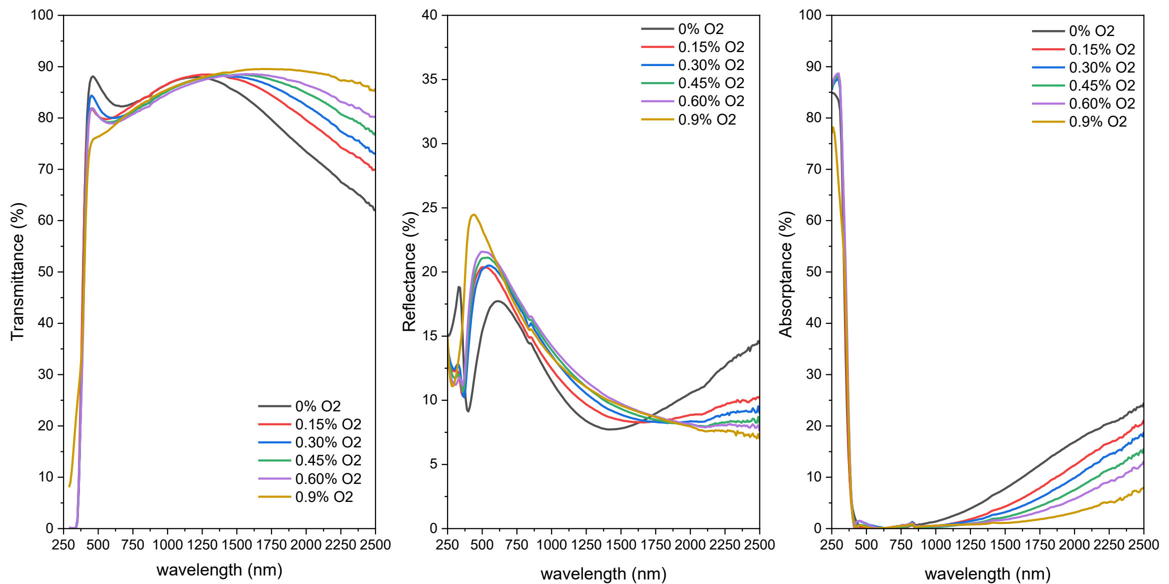

Figure 5-8 Transmittance, reflectance, and absorptance of the ITO samples fabricated with different fluxes of O_2. With a power density of 1.6 W/cm²

Figure 5-9 depicts the weighted absorptance for each of the samples. Considering the 300 – 1000 nm range, the lowest value (1.6 %) is found with the sample 0.15 % O_2. In contrast, the sample fabricated with 0% O_2 shows a value of 1.8%. This shows that a minimal quantity is necessary for obtaining the lowest absorptance value. Even though the electrical properties of this sample are not the best of the batch (i.e., the sample with no O_2), it is expected that the inclusion of H in the deposition process could increase the carrier density and, thus, the mobility in the layer. Besides, annealing of the samples can induce the formation of crystal structures, which can also increase mobility [13].

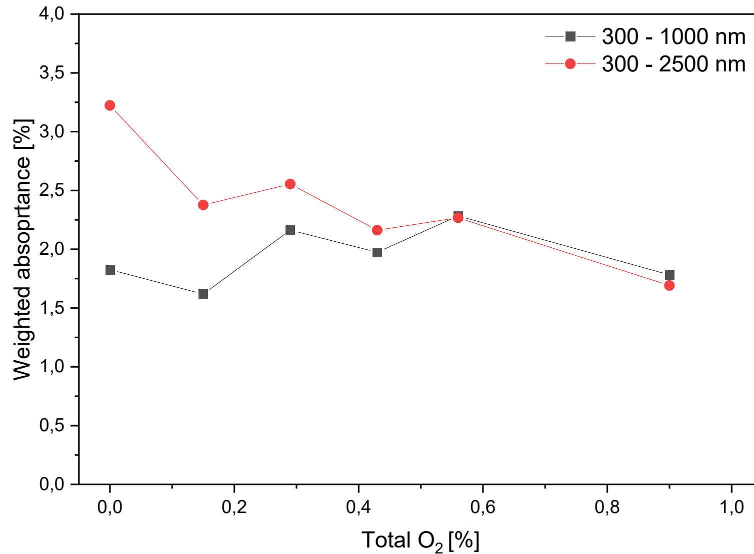

Figure 5-9 Weighted absorptance of different ITO samples fabricated with different fluxes of O_2.

5.2.2.1 Hotplate annealing effect on ITO films

To investigate the change in the electrical and optical parameters of the ITO films with the annealing process, we performed an annealing with a hotplate in air (uncontrolled) atmosphere. We decided to anneal these samples at 210 ºC for 30 minutes since this is the standard annealing process for curing the Ag-grid paste used for the frontal contact of heterojunction and TOPCon solar cells in PVlab [14].

Figure 5-10 depicts the mobility, carrier concentration, and resistivity of the samples as deposited and after the annealing process (210 ºC 30 min). In the case of the carrier concentration, there is an increment for all the samples. This could be explained as follows: the oxygen inside the films seems to diffuse, leaving oxygen vacancies that increase the carrier concentration. This increment leads to an important reduction in mobility due to increased scattering between carriers, as observed. For the

resistivity, the samples fabricated with less than 0.6 % oxygen remain similar; however, for the samples with 0.6% or higher percentage of oxygen, the resistivity decreases after the annealing.

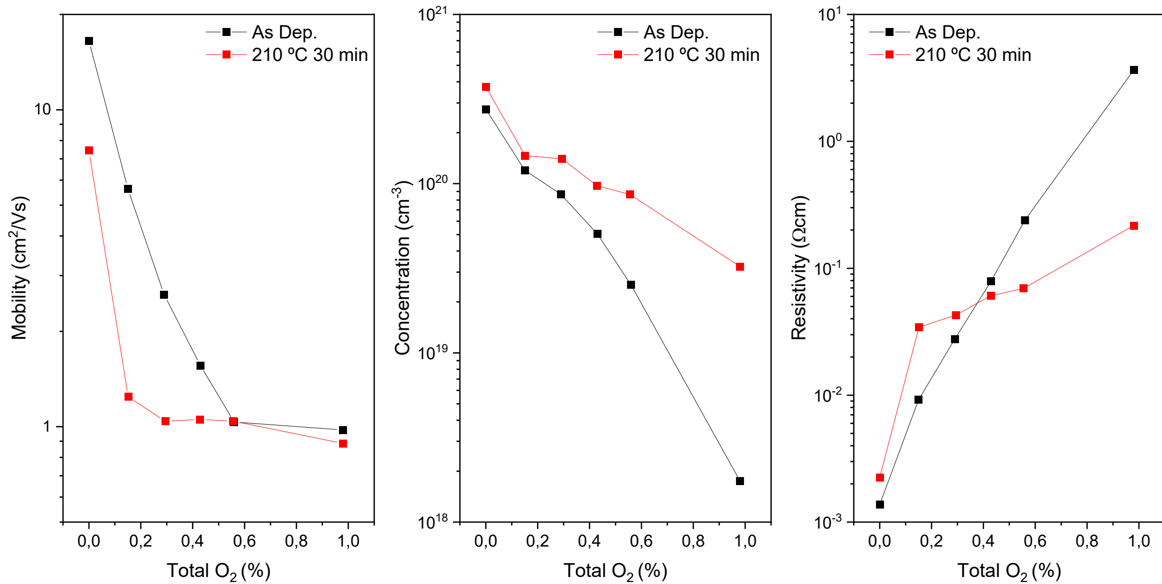

Figure 5-10 Mobility, carrier concentration, and resistivity of ITO samples fabricated with different oxygen content. The black line is the samples as deposited, the red one after the 210 ºC 30 min annealing.

Regarding the optical results (Figure 5-11), the samples show the biggest change in the infrared range. Except for the sample without oxygen, the rest show an increment in the transmittance and a reduction in the absorption. Considering the results of the Hall effect, this could be counterintuitive since the increase in the free carrier concentration normally leads to an increase in the IR absorption. However, this could be related to the shift in the plasma frequency (ω_p) according to the following expression [15].

$$\omega_p = \sqrt{\frac{nq^2}{\epsilon_0 m^*}} \quad 5.4$$

Where n is the carrier concentration, q is the elementary charge, ϵ_0 is the permittivity in free space, and m^* is the effective mass. The plasma frequency will increase as the carrier concentration increases, blue-shifting the plasma wavelength. However, the effective mass can be altered with the crystalline structure formed with the annealing process, translating the plasma wavelength to the infrared range. This could explain the results after the annealing process.

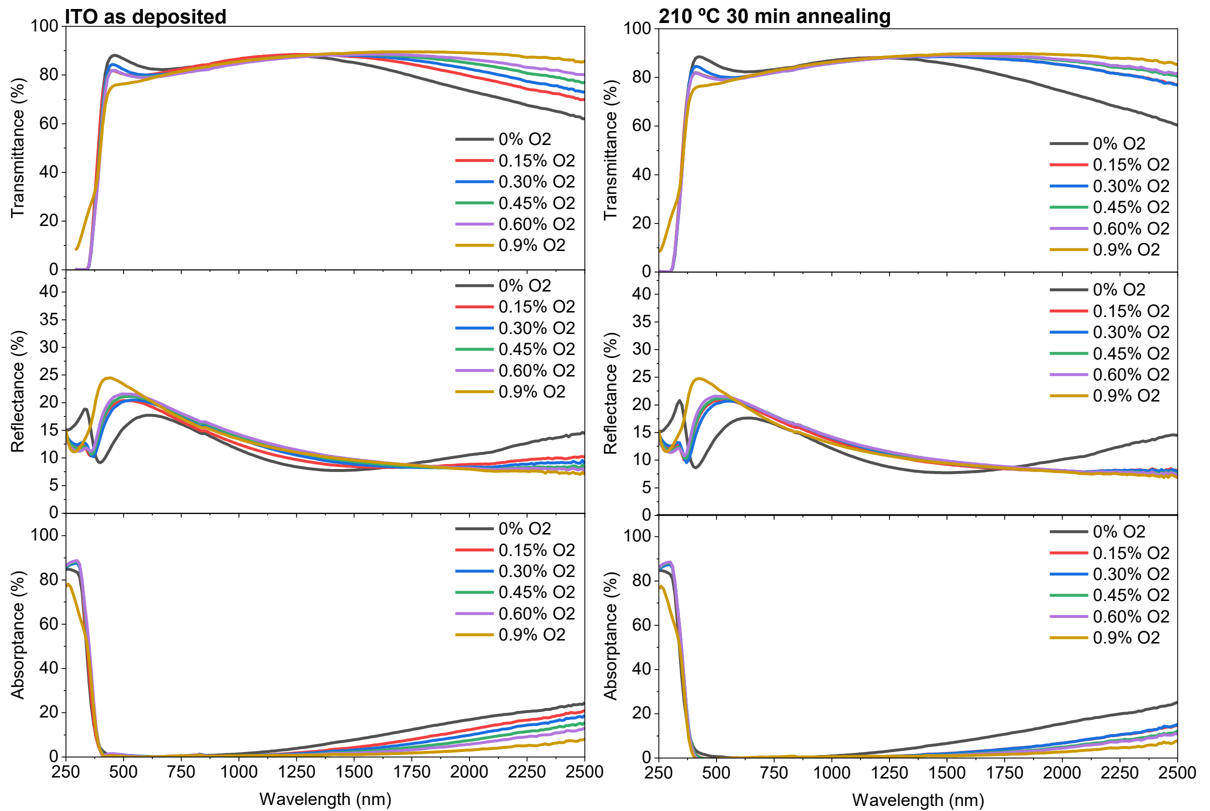

Figure 5-11 Transmittance, reflectance, and absorptance of the ITO samples fabricated with different oxygen content. Before the annealing (curves on the left) and after the annealing process (curves on the right).

It is worth noting that the sample fabricated with no oxygen flux did not present any change in the transmittance, reflectance, and absorptance after the annealing process. This suggests that the oxygen introduced during the sputtering process effuses during the annealing, and the interaction with the atmosphere's oxygen does not take an important role. Nevertheless, the reduction in mobility could be related to a change in the grain size of the film, an increment of the oxygen vacancies, or a combination of both.

Figure 5-12 shows that the absorptance in the visible range did not change meaningfully, unlike the complete range, while the reduction in the infrared range becomes relevant after annealing. As previously mentioned, the plasma frequency shifting of the samples might be the origin of this result.

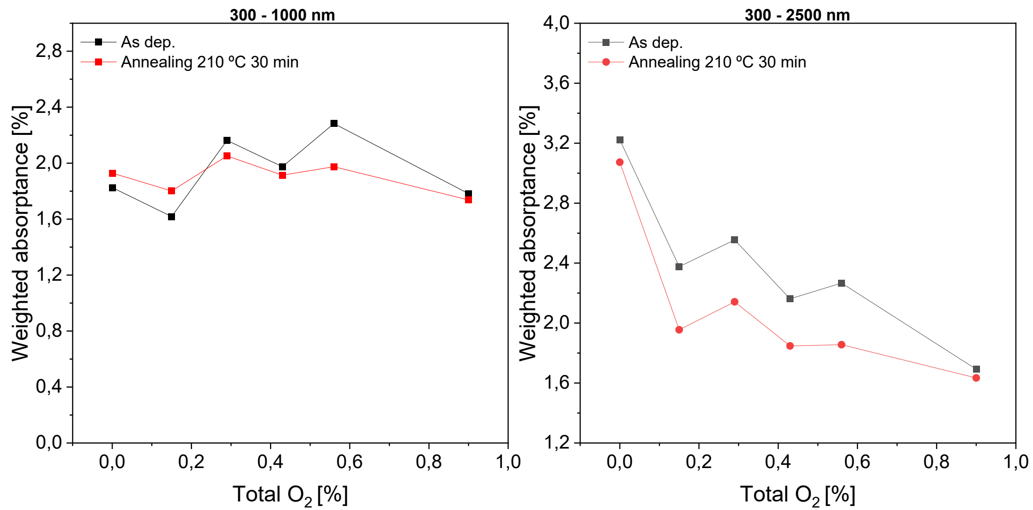

Figure 5-12 Weighted absorptance of the ITO samples fabricated with different oxygen content.

5.2.3 Characterization of ITO deposited with Ar/O2/H2 atmosphere

Once the effect of introducing O_2 was studied, hydrogen was also introduced into the chamber to deposit ITO:H. The hydrogen content was varied from 0 % to 0.9 %. Two main experiments were conducted: varying the H_2 content with constant 0.1% O_2 and varying the H_2 content with constant 0.8% O_2. The latter showed extremely low mobility values (~1 cm^2/Vs) thus these results are not presented here. In contrast, the 0.1% O_2 plus variation of H_2 content showed better results and will be discussed here. With this approach, the minimum O_2 flux is introduced with the goal to increase the mobility of the samples while maintaining a low absorptance and high transmittance in the visible range

Figure 5-13 shows the mobility, carrier concentration, and resistivity found by the Hall effect. In this case, the reference samples (i.e., the sample fabricated with 0.1 % O_2 and 0 % H_2) show better values than its counterpart with 0.8% O_2. The values were mobility 7.5 cm^2/Vs, carrier concentration $2x10^{20}$ cm^{-3}, and resistivity $4x10^{-3}$ Ωcm. The increase in the hydrogen content increases the carrier concentration up to $4.4x10^{20}$ $cm^{-3,}$ and the mobility increases slightly to 13 cm^2/Vs. Meanwhile, the resistivity decreases to $1x10^{-3}$ Ωcm. The better results (compared to the 0.8 % O_2) can be explained by a higher amount of free carrier donors (oxygen vacancies) caused by the reduced oxygen content in the deposition chamber.

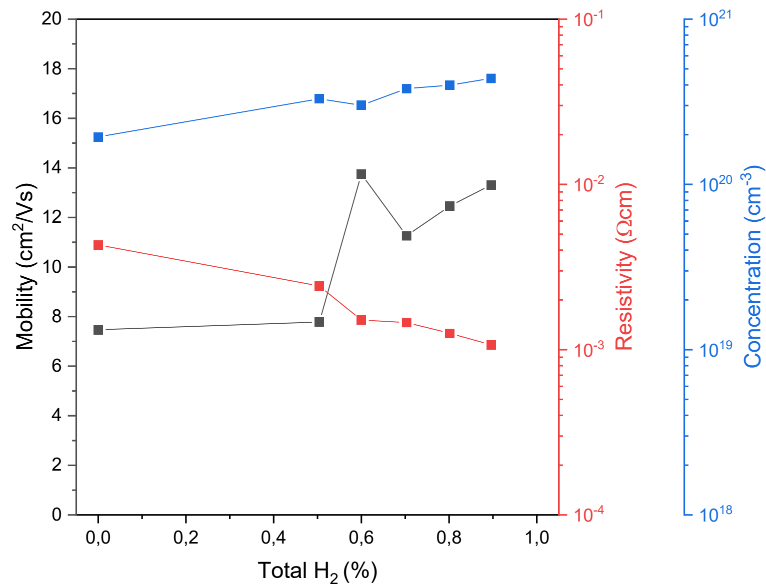

Figure 5-13 Hall mobility, carrier concentration, and resistivity of ITO thin films (~80 nm) deposited with different percentages of H_2, with a constant 0.1% O_2, and a power density of 1.6 W/cm^2

Figure 5-14 shows the transmittance, reflectance, and absorptance of these samples. The ITO:H sample deposited with 0% H_2 (and 0.1% O_2) shows practically the same behavior as the samples fabricated in the previous experiment of varying oxygen flux, as depicted in Figure 5-8. The samples with a H_2 content $\geq$ 0.6% show a similar behaviour among each other, suggesting that the content of hydrogen reach a saturation level in the ITO film. We observed a reduction in the transmittance at 2000 nm, it goes from 78 % (0 % H_2) to 66 % (0.9% H_2), and increase in the reflectance from 8.6 % (0 % H_2) to 14.5% (0.9% H_2) and thus an increase in the absorptance which goes from 13.4% (0 % H_2) to 19 % (0.9% H_2). This suggests an increase in the free carrier absorption in the infrared region most likely due to an increase of oxygen vacancies inside ITO films. The Hall effect results also confirm this trend. Regarding the sample fabricated with 0.5 % H_2, it shows an intermediate trend between the 0% H_2 samples and those with $H_2 \geq 0.6\%$. Despite these results, the transmittance in the visible range is around 85 % for all the samples. All of this might indicate that the hydrogen is being introduced into the ITO films which leads to an increase in the absorptance in the infrared region due to an increase of the free carrier density.

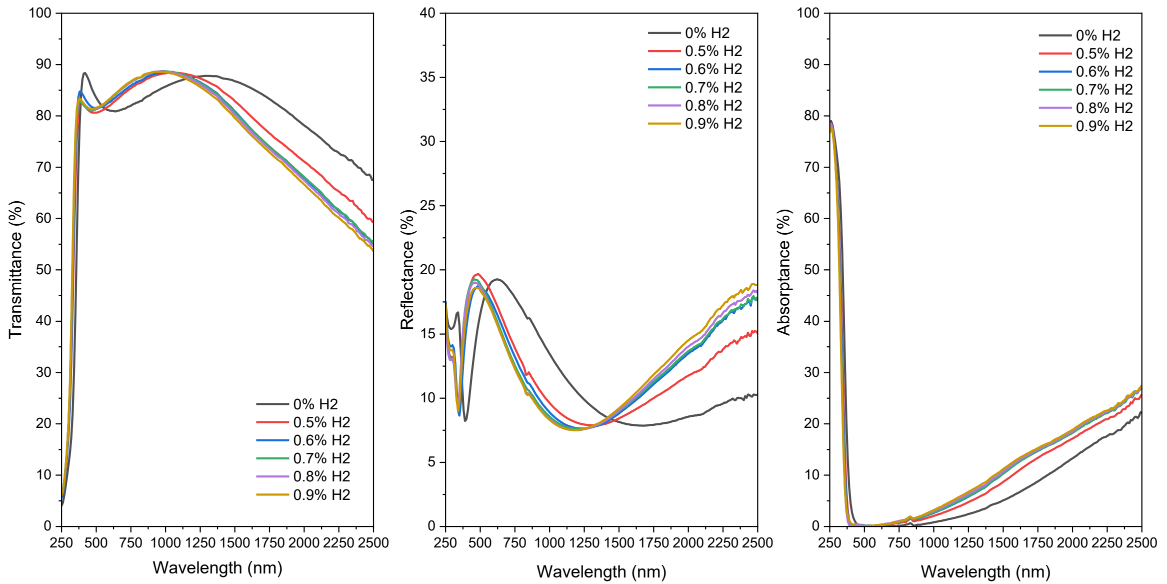

Figure 5-14 Transmittance, reflectance, and absorptance of the ITO samples fabricated with different content of H_2 and constant 0.1 % O_2. Power density of 1.6 W/cm^2

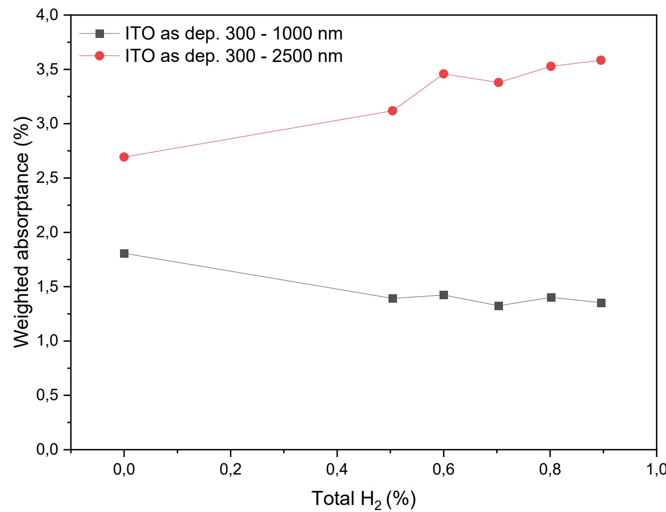

Figure 5-15 Weighted absorptance of different ITO samples fabricated with different content of H_2 and constant 0.1% O_2.

Figure 5-16 a) shows the diffractograms of glass/ITO:H samples. The increase of hydrogen during ITO deposition does not produce the appearance of new diffraction peaks. As mentioned earlier, the peaks at ~34º and ~62º are again observed, corresponding to the (114) plane of In_2O_3 and the (331) plane of SnO_3. However, a shift towards lower angles of these peaks is observed as the hydrogen content increases. For example, in the case of the sample with 0 % H_2, the peak is found to be 34.47º. In comparison, for the sample with 1.2% H_2, it is found to be 33.97º, Figure 5-16 b). This shift to lower angles is usually attributed to tensile compression, as interstitial defects (H_2) and oxygen vacancies are introduced into the lattice, the interplanar spacing tends to increase, and thus micro strain appears [16].

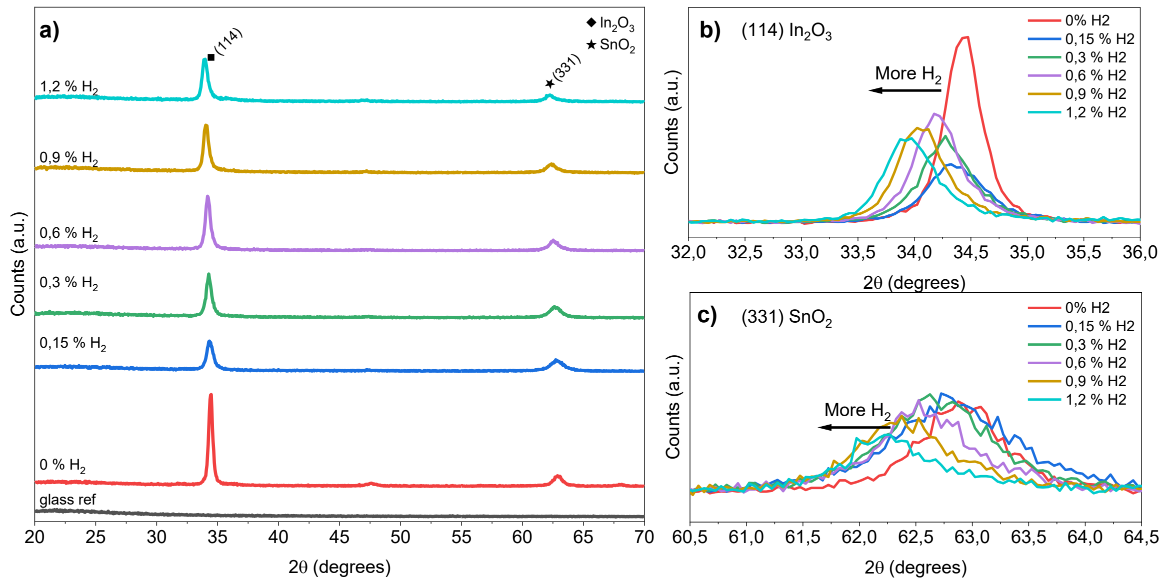

Figure 5-16 a) Diffractogram of ITO:H samples deposited at 1.6 W/cm² varying the H_2 content (0.1% of O_2). b) Diffraction peak around 34° and c) diffraction peak around 62.5° of the ITO:H samples

Using the Sherrer approximation, the micro-strain of the samples can be calculated. The most relevant diffraction peak at ~ 34º representing the (114) plane of In_2O_3 was used to determine the micro-strain (ϵ).

$$\epsilon = \frac{FWHM}{4tan\theta} \quad 5.5$$

FWHM is the full width at half maximum, and θ is the Bragg angle. Figure 5-17 a) depicts the results of using this approximation. It is observed that the micro-strain increases with a higher percentage of hydrogen, going from 4.1×10^{-3} (0 % H_2) to 6.3×10^{-3} (1.2 % H_2). This corroborates the observations of the Hall effect and optical measurements that showed that the hydrogen introduced during the sputtering deposition process is being incorporated into the ITO films, causing interstitial defects and/or oxygen vacancies. Additionally, the crystallite size (D) was calculated using the Sherrer equation.

$$D = \frac{K\lambda}{FWHMcos\theta} \quad 5.6$$

Where K stands for the Sherrer constant (~0.94), and λ is the X-ray wavelength (for Cu Kα λ = 0.15406 nm). Figure 5-17 b) depicts the crystallite sizes estimated using the diffraction peak at ~ 34º. A decrease in the crystallite size is observed as the hydrogen content is increased. For instance, the estimated crystallite size for the 0% H_2 sample is 29.42 nm, while the sample with 1.2%

H_2 reduces that value to 19.59 nm. This behaviour suggests that the hydrogen incorporation disrupts the grain growth by introducing a higher density of structural defects, which hinder the crystallite expansion. This could also explain the absence of other diffraction peaks like those observed in the ITO without H_2 samples.

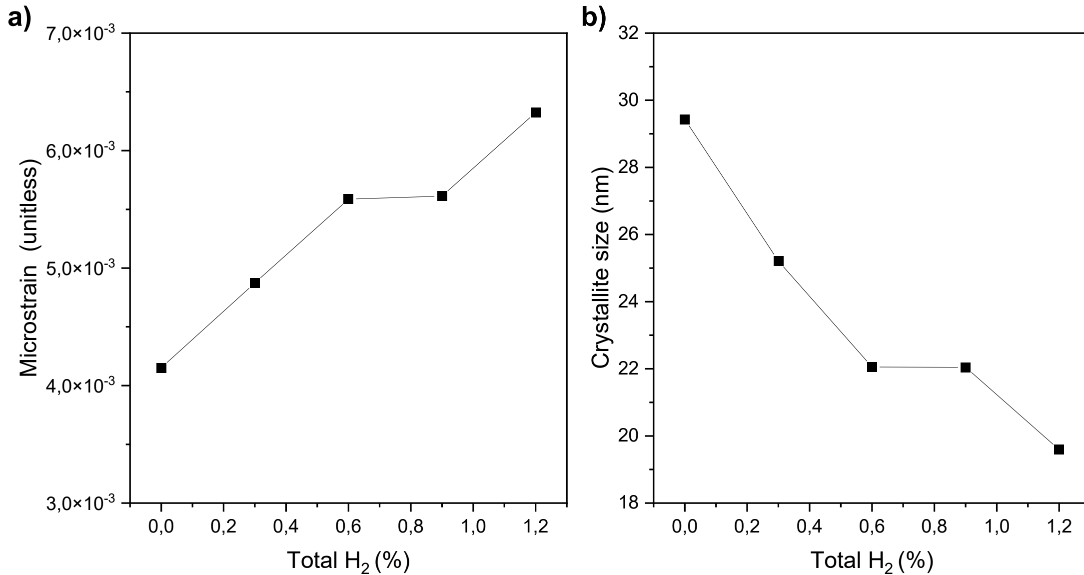

Figure 5-17 a) Micro-strain of different ITO:H samples deposited at 1.6W/cm2 with constant O2 (0.1 %). b) crystallite size of the same ITO:H samples.

With this approach (0.1% O_2 and varying H_2), we obtained better properties in comparison with the previous experiment using O_2 and Ar. The increase in hydrogen content from 0% to 0.9% led to a systematic shift toward smaller angles, indicating lattice expansion due to the formation of oxygen vacancies and interstitial hydrogen incorporation. This structural modification was further confirmed by the increase in micro-strain, which rose from 4.1×10^{-3} to 6.3×10^{-3}, suggesting enhanced defect-induced internal stress. Simultaneously, the crystallite size decreased from 29.42 nm to 19.59 nm, indicating that hydrogen inhibited grain growth by introducing structural disorder. Regarding electrical properties, the free carrier concentration doubled from $2\text{x}10^{20}$ cm^{-3} to $4.4\text{x}10^{20}$ cm^{-3}, improving mobility from 7.5 cm^2/Vs to 13 cm^2/Vs. These increases produced a reduction on resistivity to 10^{-3} Ωcm, making the films highly conductive. Additionally, as it was expected, optical characterization revealed increased infrared absorption, attributed to free carrier effects, while maintaining high transmittance in the visible range.

5.2.3.1 Hotplate annealing effect on ITO:H films

The original samples were cleaved into four 1x1 cm^2 samples to explore different annealing processes: 210 ºC (10 min and 30 min) and 300 ºC (5 min and 10 min). Again, the annealing process was done with a hotplate in an uncontrolled atmosphere (air). The results are depicted in Figure 5-18. First, the annealing processes at 210 ºC 10 min and 30 min show a similar reduction in the carrier concentration from ~$3x10^{20}$ cm^{-3} to ~$1x10^{20}$ cm^{-3} and a similar decrease in the mobility to ~1 cm^2/Vs. In consequence, the resistivity increases by one order of magnitude to ~ $2x10^{-2}$ Ωcm. Second, for the annealing processes at 300 ºC 5 min and 10 min, there is an even higher reduction in the carrier concentration, most likely due to the higher incorporation of hydrogen or oxygen atoms in the vacancies, reducing the defects of the samples. Nevertheless, reducing free carriers is insufficient to increase mobility since all the samples show a decrease in mobility to values around 1 cm^2/Vs.

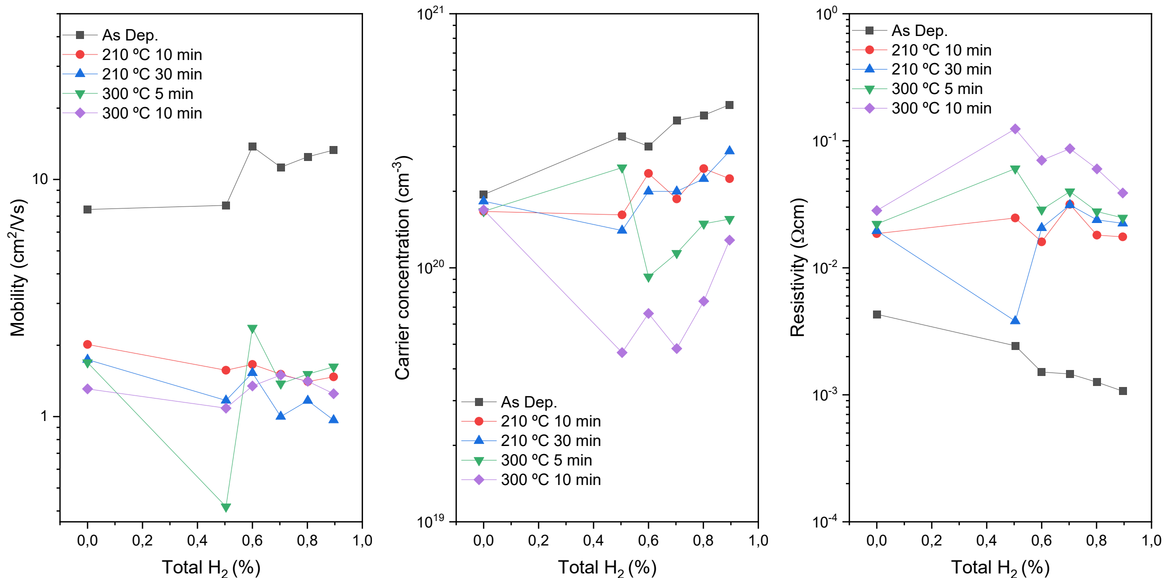

Figure 5-18 Mobility, concentration, and resistivity of ITO samples fabricated with different hydrogen content with constant 0.1% oxygen before and after the annealing

Taking into consideration previous results, we found the following trend with hotplate annealing processes: ITO samples deposited with Ar/O_2 atmosphere showed a decrease in mobility after the annealing (210 ºC 30 min) probably due to the increment of the free carrier concentration. The excess oxygen in the film diffuses, leaving more oxygen vacancies, and thus, there is an increase in the carrier scattering. ITO sample deposited with Ar/O_2/H_2 atmosphere also showed a decrease in mobility but also in carrier concentration. The hydrogen might be passivating the defects in the samples, leaving fewer free carrier donors. However, the hydrogen might also interact with the components of the atmosphere, such as the O_2 or H_2O, forming hydroxyl groups. This kind of layer can act as an electron trap and thus reduce mobility. [17]

Figure 5-19 a) shows the diffractograms of ITO:H samples deposited in the same process, that is, 1.6 W/cm^2 with an H_2 content of 0.7 % and O_2 content of 0.1 %. The thickness is around 80 nm. At the end of the deposition, the glass sample was cut into four pieces to perform different hotplate annealing processes. This figure shows that the annealing processes do not affect the crystallisation of the samples, as shown by the crystalline fraction in Figure 5-19 b). Again, the micro-strain was calculated, and it is shown in Figure 5-19 c). These values are similar to the micro-strain found for the samples between 0.6 % and 0.8 % hydrogen from the previous experiment. This may indicate that the hydrogen within the samples does not effuse with this annealing process. All of this indicates that the annealing process at 210 ºC might not be enough to increase the crystallinity of the samples or even modify the hydrogen inside the samples. A longer annealing process or higher temperatures might be necessary to observe changes in the samples.

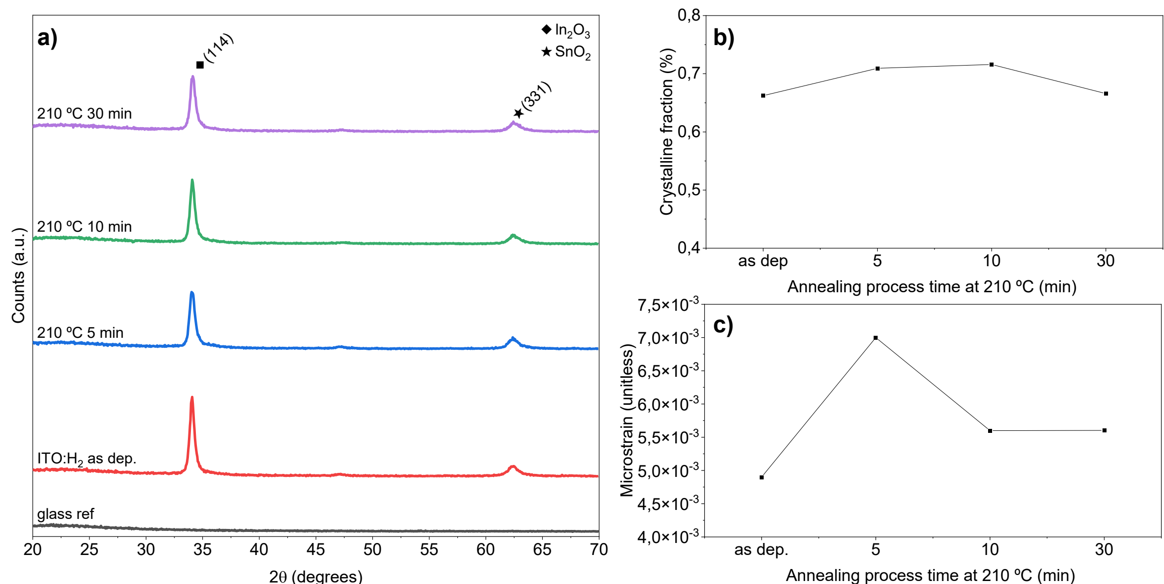

Figure 5-19 a) Diffractogram of ITO:H samples fabricated with 1.6 W/cm^2, 0.7 % H_2 and 0.1 % O_2, b) crystalline fraction of the same samples and c) microstrain of samples calculated with the FWHM of 34° diffraction peak.

5.2.3.2 Hotplate annealing effect on ITO:H films in N_2 atmosphere

Once it was observed that the cause or mobility reduction could be originated from the interaction of the sample with the atmosphere, we fabricated on 1x1 cm^2 glass substrate a set of samples with the following deposition parameters: 1.6 W/cm^2, 0.1% of O_2 and H_2 from 0 % to 0.9 %. The thickness of the layer was approximately 80 nm. For each deposition process, three samples were fabricated. The control sample (as dep.), a sample for air annealing and a sample for N_2 annealing. The annealing

process was done at 300 ºC for 10 min this time. Figure 5-20 depicts the results on mobility, carrier concentration and resistivity of the samples mentioned above.

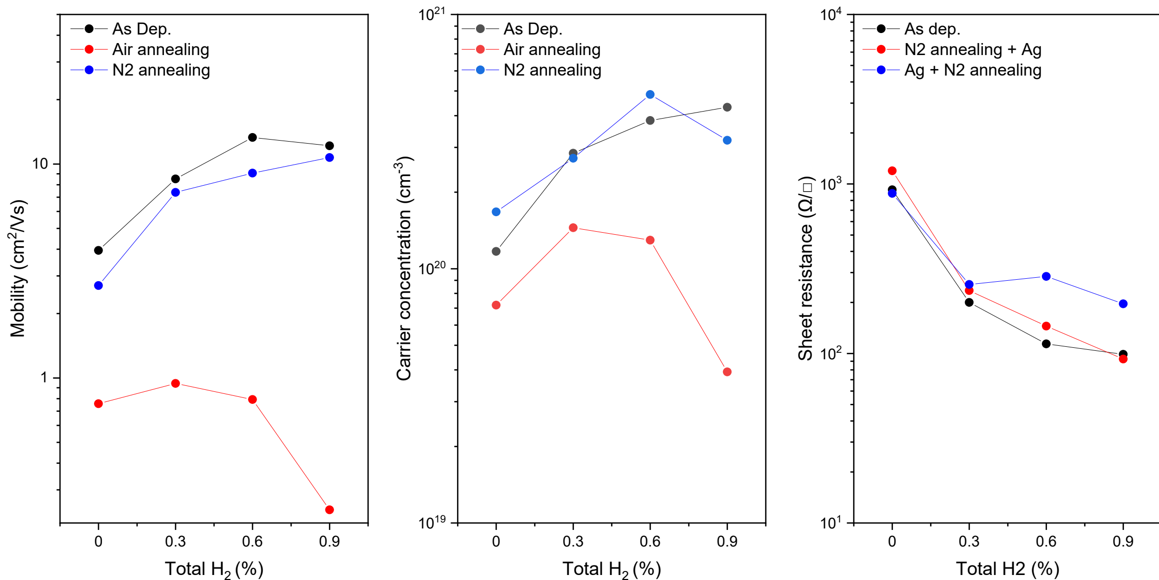

Figure 5-20 Mobility, concentration, and resistivity of ITO samples fabricated with different hydrogen content with constant 0.1% oxygen before and after the annealing on air and N_2.

There is a difference between the samples annealed with air and N_2. For instance, with N_2 annealing, the carrier concentration remains the same as the deposited samples. Meanwhile, the carrier concentration for air annealing samples decreases below 10^{20} cm^{-3}. This might be caused by the interaction of the vacancies and H_2 in the sample with the O_2 or H_2O of the atmosphere, thus reducing the free carrier donors. Similarly, the mobility for the as-deposited and N_2-annealed samples remains similar, but the values for the air-annealed samples decrease to ~ 1 cm^2/Vs. The same behaviour was observed in the previous experiments. Again, this can be justified due to the formation of a hydroxyl-based layer in the surface of the samples that drastically reduces mobility. For that reason, the resistivity of the air-annealed samples increases by more than one order of magnitude, going from 10^{-3} Ωcm to $6\text{x}10^{-2}$ Ωcm (for the 0.9% H_2 samples). Regarding the effect of increasing the H_2 content, there is an increment in the carrier concentration and the mobility while the resistivity is reduced. Although this is a positive result, higher temperatures or longer annealing time could be necessary to improve the crystallinity of the samples and potentially further increase the mobility.

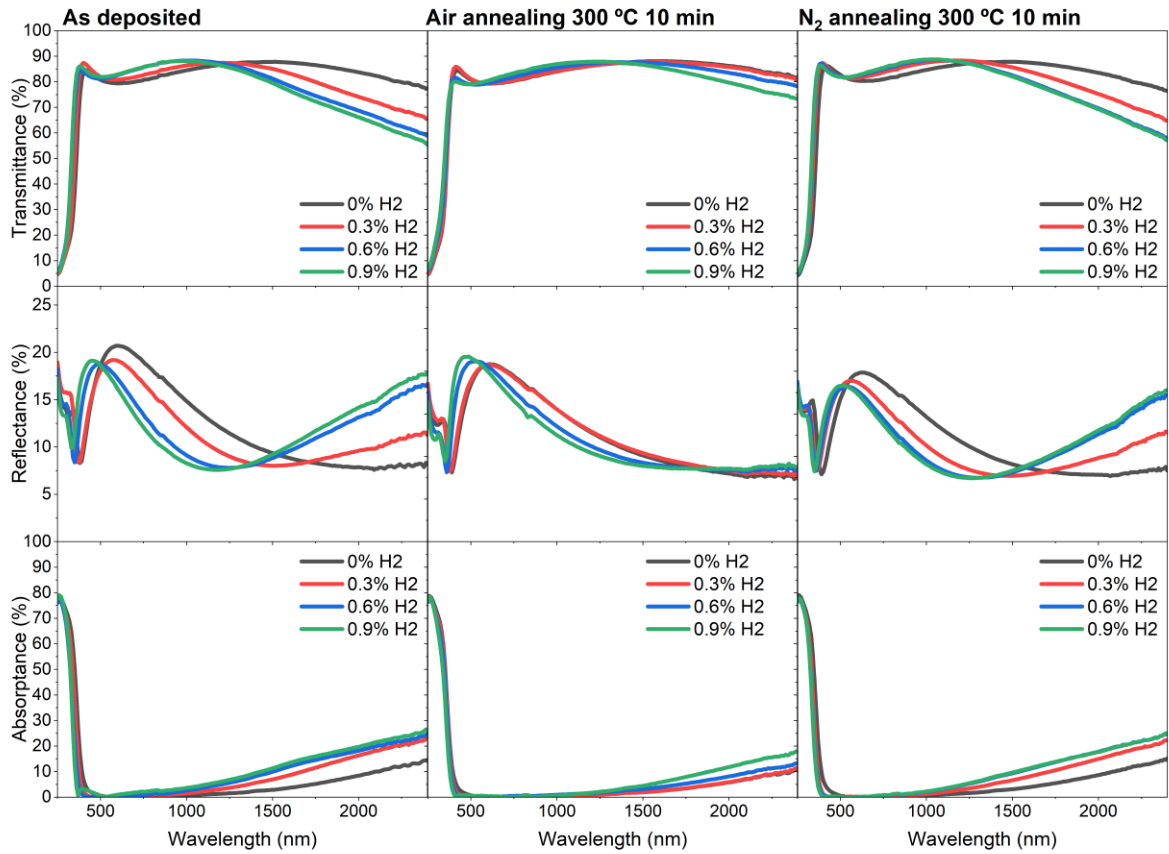

Figure 5-21 Transmittance, reflectance, and absorptance of the ITO samples fabricated with different content of H_2 and constant 0.1 % O_2. Left column as deposited, middle column air annealing, right column N_2 annealing. Power density of 1.6 W/cm^2

Figure 5-21 depicts this batch of samples' transmittance, reflectance and absorptance. With the air annealing process, a reduction in the absorptance (in the infrared range) and an increase in transmittance (in the visible range) is observed. This is the same behaviour observed in the previous experiment i.e., 0.1 % O_2 experiment. However, the N_2-annealed samples remain like the as-deposited samples. However, two important facts occurred for these samples. First, the 0.6 % and 0.9 % H_2 show almost identical characteristics after the annealing process, which can reveal a saturation in the interaction of the H_2 with the defects of the sample. Second, there is a slight increase in the transmittance in the visible range for all the samples with hydrogen after the N_2 annealing process. To quantify the change in absorptance, the AM1.5G-normalized absorptance was calculated. This is shown in Fig. 25. With this figure, it is confirmed that there is a slight reduction in the absorptance in the visible and infrared range for the N_2-annealed samples. Even though the carrier concentration remains constant, the reduction in absorptance can be caused by the change in the grain size, which has been shown to affect the optical parameters of ITO samples [13].

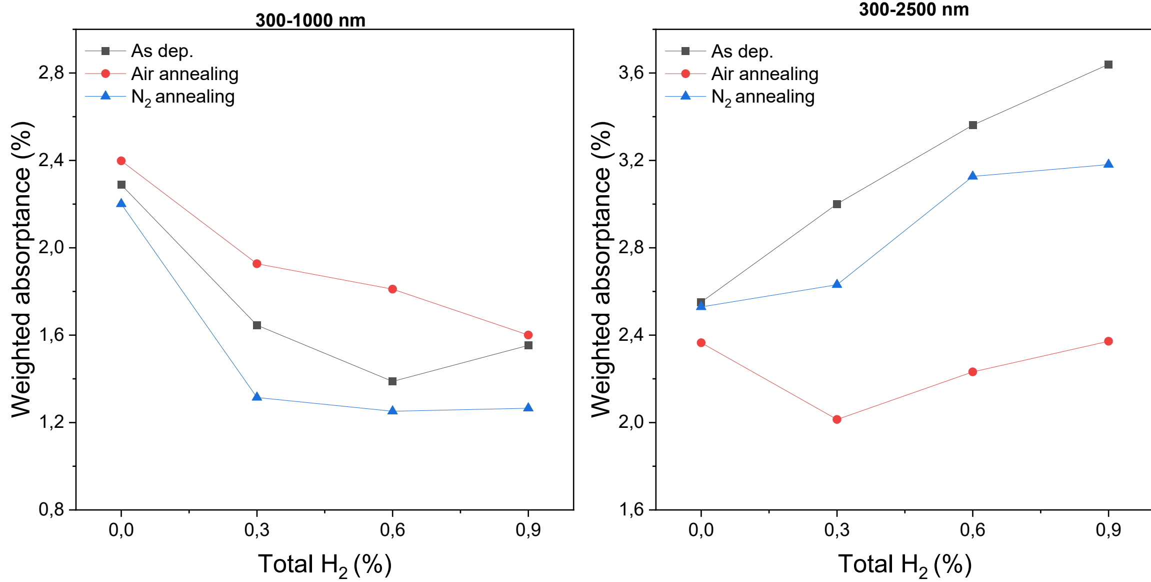

Figure 5-22 Weighted absorptance of the ITO samples fabricated with different hydrogen content with a constant 0.1% oxygen. Black squares are the as-deposited samples, red circles are the air-annealed samples, and blue triangles are the N_2-annealed samples.

Finally, the specific contact resistivity (ρ_c) ITO:H/Ag was measured by TLM. For this measurement, glass samples with approximately 1x5 cm^2 were used. Again, three different samples were fabricated per each deposition process: the as-deposited, the air-annealed, and the N_2-annealed sample. Figure 5-23 depicts the results of contact resistivity and sheet resistance (R_{sh}) obtained by TLM. Firstly, for the as-deposited films the increment in the hydrogen of the samples reduces the ρ_c; this could be related to hydrogen passivation of the defects in the ITO/Ag junction and/or better band alignment. We found in the previous experiments that mobility increases as the hydrogen content increases and this can positively affect the contact resistivity between ITO/Ag and the ITO sheet resistance.

The air-annealed samples showed rectifying behaviour, and the extraction of the ρ_c and R_{sh} by TLM was impossible. When the annealing process was performed in nitrogen (300 ºC 10 min), the ρ_c was reduced by two orders of magnitude for the 0 % H_2 sample and one order of magnitude for the rest of the samples. For instance, the contact resistivity of the 0.6 % H_2 sample goes from 10^{-1} Ωcm^2 to 10^{-2} Ωcm^2. Although the effect on ρ_c of hydrogen-saturated TCO/metals has not been extensively studied, some works have shown that H_2 annealing can reduce the ρ_c of this kind of junction [18].

The Figure 5-23 b) shows that effect on the R_{sh} with the N_2 annealing is marginal (~150 Ω/□ for the 0.6% H_2 samples). This is consistent with the resistivity values obtained previously, which did not change after the N_2 annealing process.

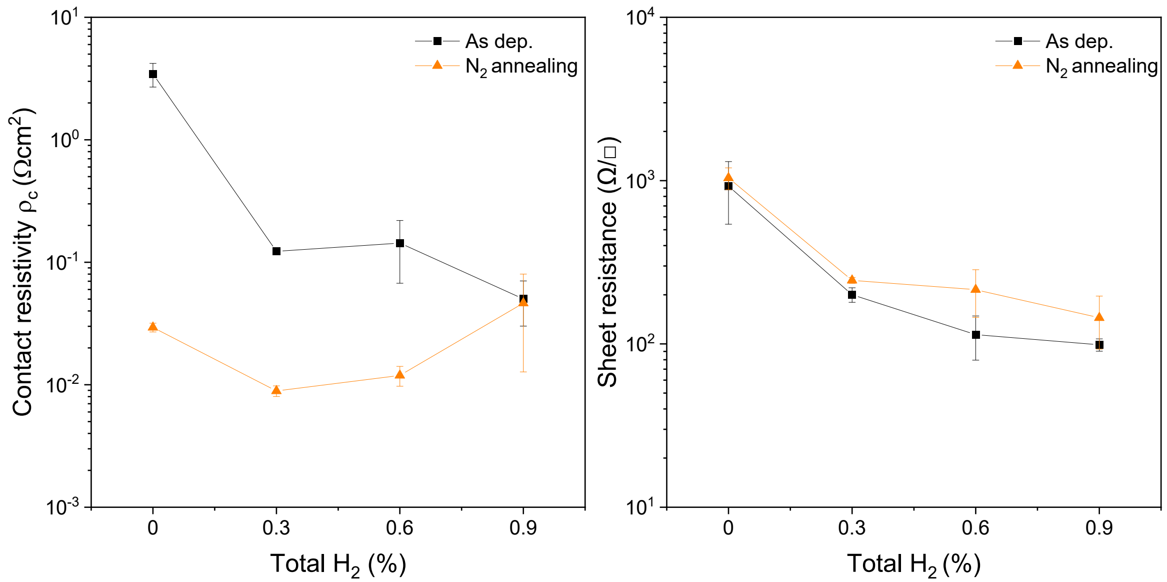

Figure 5-23 ITO:H/Ag contact resistivity and ITO sheet resistance for different H_2 content samples. As deposited samples (black squares) and N_2 annealed samples (orange triangles).

5.2.4 ITO:H films (~80 nm) on poly-Si(n)/c-Si(n) junctions

As previously mentioned, the idea of using ITO:H on c-Si(n)/SiO_x/poly-Si(n) stack is to passivate the defects resulting from the formation of the poly-Si(n) layer. Usually, this is achieved by depositing hydrogen-rich silicon nitride (SiN_x:H) followed by a firing step at high temperatures [19]. After hydrogen diffusion, the SiN_x must be removed using a diluted HF solution. This etching step has to be carefully optimized to avoid the degradation of the poly-Si(n) layer. Finally, the ITO is deposited on the poly-Si(n). In that sense, ITO:H might be used for two purposes (passivating the defects and as a traditional transparent conducted layer). Also, it is worth mentioning that the HF etch process would be avoided. For that, we decided to deposit ITO (Ar, 0.1% O_2, varying the H_2 flux) on c-Si(n)/poly-Si(n) samples to assess the possibility to introduce ITO:H layer into the TOPCon fabrication route. For that, the specific contact resistivity and the minority carrier lifetime was measured.

Figure 5-24 depicts the result of the ρ_c of these samples obtained by TLM. The black squares represent the values of the samples with the c-Si/poly-Si(n)/ITO/Ag sample, while the red circles represent the values of only glass/ITO/Ag. First, it is noticed that the contact resistivity of c-Si/poly-Si(n)/ITO/Ag is approximately one order of magnitude higher than the glass/ITO/Ag samples. For instance, for the samples with 0.6% H_2, the ρ_c for the c-Si/poly-Si(n)/ITO/Ag structure is 1.26 Ωcm^2 while the glass/ITO/Ag structure shows a ρ_c of 0.14 Ωcm^2. This clearly indicates that the ρ_c increment is due to the poly-Si(n)/ITO junction. One possible reason for this increment is the sputtering damage suffered

by the poly-Si(n) layer that might increase the defects in the junction. This effect has been observed with the deposition of ZnO:Al on poly-Si/SiO_x stacks [20]. Additionally, the variation in the H_2 content does not show an important change in the ρ_c. The sample deposited with no H_2 shows the lowest value of the set (~ $2x10^{-1}$ Ωcm^2).

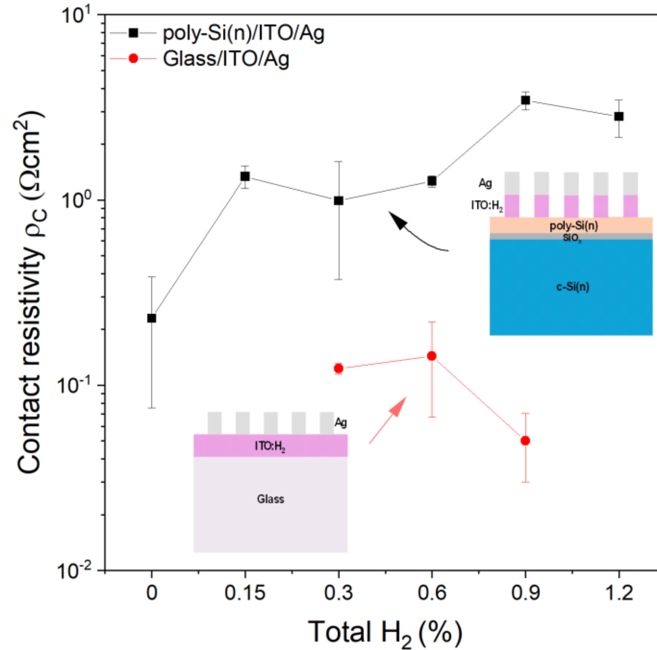

Figure 5-24 Contact resistivity of poly-Si(n)/ITO:H/Ag and ITO:H/Ag obtained by TLM. The thickness of the ITO:H films was ~80 nm.

5.2.4.1 Passivation effect of ITO:H films (~80 nm) on poly-Si(n)/c-Si(n) junctions

To investigate the possibility of passivation, the c-Si(n)/poly-Si(n) samples were measured before and after the deposition of ITO:H. Besides, after the ITO:H deposition, subsequent annealing processes were performed with hotplate (in air). After each step, the lifetime was measured. The results of these measurements are depicted in Figure 5-25. With this experiment, we explored the increment of annealing temperature going from 200 ºC to 400 ºC for 5 min. The graph on the left represents the exact lifetime values, while the graph on the right represents the normalized lifetime change for each sample. First, the original lifetime values for each of the seven samples are shown in the black bar. Even though all the poly-Si(n) were deposited and annealed simultaneously, the lifetime varied between 0.5 and 2.25 ms. This can originate from the inhomogeneity in the a-Si(n) deposition in the PECVD chamber or from differences in the temperature profile during the formation of the poly-Si(n). Second, the lifetime after the ITO deposition is shown by the red bar. Noticeably, after the deposition

process, the lifetime decreases for all the samples, and this decrease is more noticeable as the hydrogen in the deposition process increases. For instance, for the 1.2% H_2 sample, the lifetime decreases from 0.78 ms to 0.25 ms; this represents a reduction of 68%, as is depicted in the graph on the right. Third, the samples containing $H_2 \geq 0.3\%$ show an increase in the lifetime after the subsequent annealing steps. For instance, the 0.6% H_2 sample goes from 1 ms (after ITO:H deposition) to 1.75 ms (400 ºC 5 min); however, the annealing process was not enough to recover to the original value (2 ms). Finally, for the sample with 0% H_2, there is no significant reduction in the lifetime after the ITO deposition, and the annealing process does not show a clear improvement.

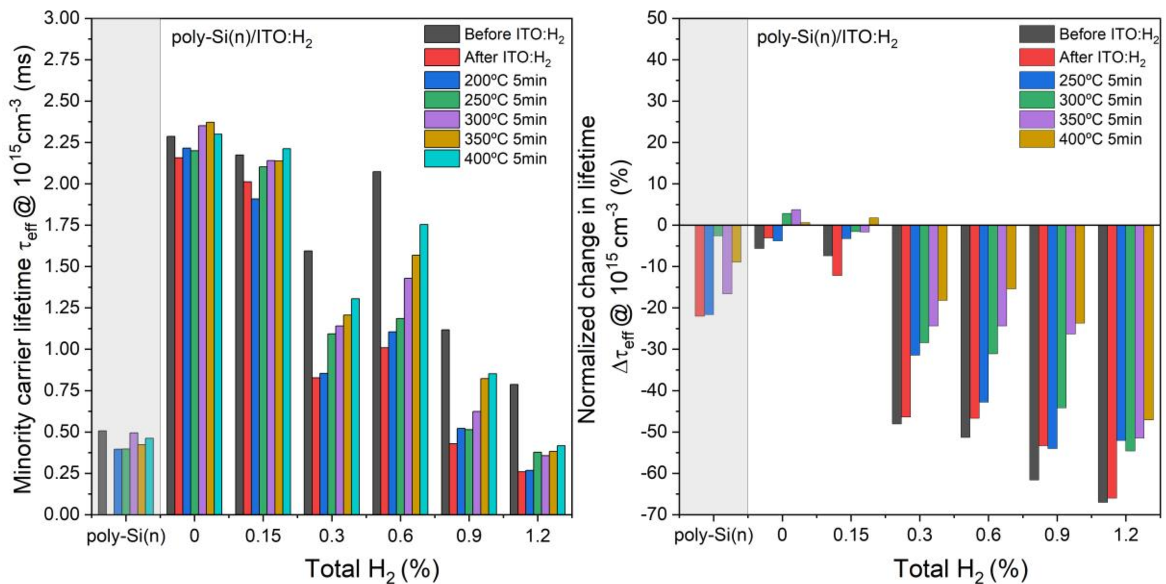

Figure 5-25 Left curve, minority carrier lifetime at 10^{15} cm^{-3} of different ITO:H samples. Right curve, normalized change in the lifetime of the same samples. Subsequent annealing processes on hotplate were performed from 200 ℃ to 400 ℃ for 5 min.

Figure 5-26 depicts the results of the intrinsic open voltage (i-V_{oc}) at one sun. Before the ITO:H deposition, all samples show values between 673 mV and 705 mV. After the ITO deposition, all the samples with hydrogen content ≤ 0.15 %, show a slight increment of around 1 %. In contrast, the tendency for the rest of the samples is similar to the lifetime; as the hydrogen content increases, the i-Voc decreases more. For instance, the i-V_{oc} value for the 1.2% H_2 sample decreases from 683 mV to 662 mV; this represents a reduction of 3 %. After annealing, the samples with hydrogen content ≥ 0.3% recover their i-V_{oc} . Even for the samples with 0.3% and 0.6% hydrogen, there is an improvement of ~0.5%. Even though the deposition process caused damage, the samples with hydrogen content show a slight recovery, which may indicate that hydrogen is diffusing into the junctions and is starting to passivate the junction defects.

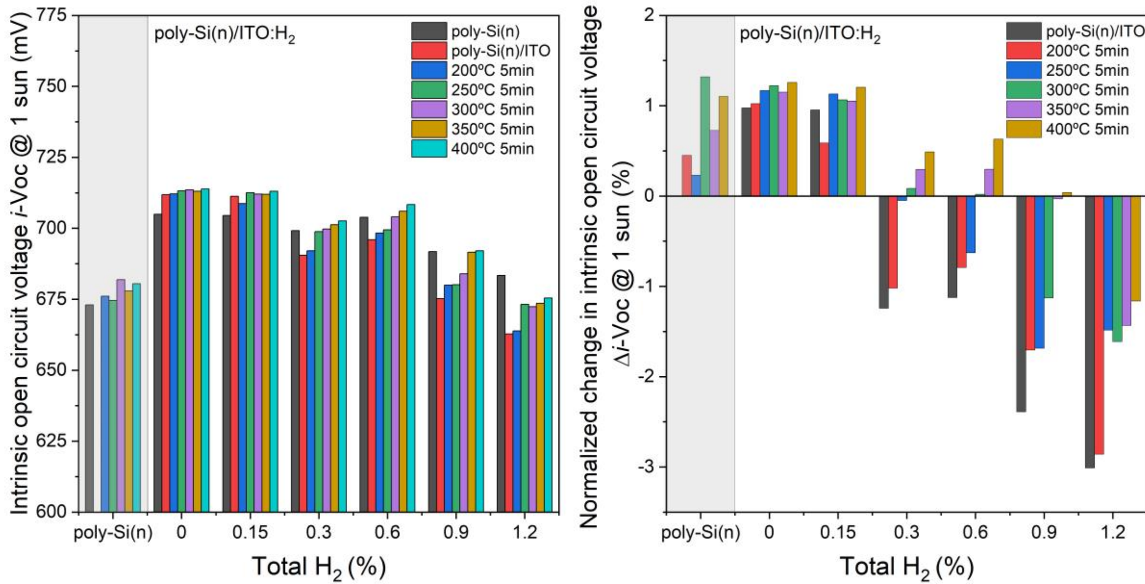

Figure 5-26 Left curve, i-V_{oc} at one sun of different ITO:H samples. Right curve, normalized change in the i-V_{oc} of the same samples. Subsequent annealing processes on air (hotplate) were performed from 200 ºC to 400 ºC for 5 min.

Since these annealing processes did not improve the lifetime, we decided to investigate only the hotplate (in air) annealing at 400 ºC but increasing the annealing duration (from 5 to 90 min). This was performed with the same samples. Figure 5-27 shows the lifetime results; it can be observed that the ref (poly-Si(n)) sample, the sample without hydrogen, and the samples with 0.15% and 0.3% hydrogen show the same values for all annealing times. This shows that the poly-Si(n) or ITO alone is not responsible for improving the lifetime. On the other hand, samples with a higher hydrogen content ≥ 0.6% show a considerable improvement in the lifetimes after the annealing process. For annealing times longer than 20 min, the lifetimes of such samples exceed the original values, i.e. the lifetimes just after the poly-Si(n) deposition. For example, for the sample with 0.9% hydrogen, the reference value was 1.11 ms; after ITO:H deposition was 0.42 ms, and after 20 min of annealing at 400°C it was 1.57 ms. Finally, with 90 min, a value of 5.87 ms was obtained. This represents a 425% improvement over the reference value. All this indicates that the excess hydrogen contained in these samples has been able not only to recover the reference values but also to passivate the defects and increase the lifetimes effectively.

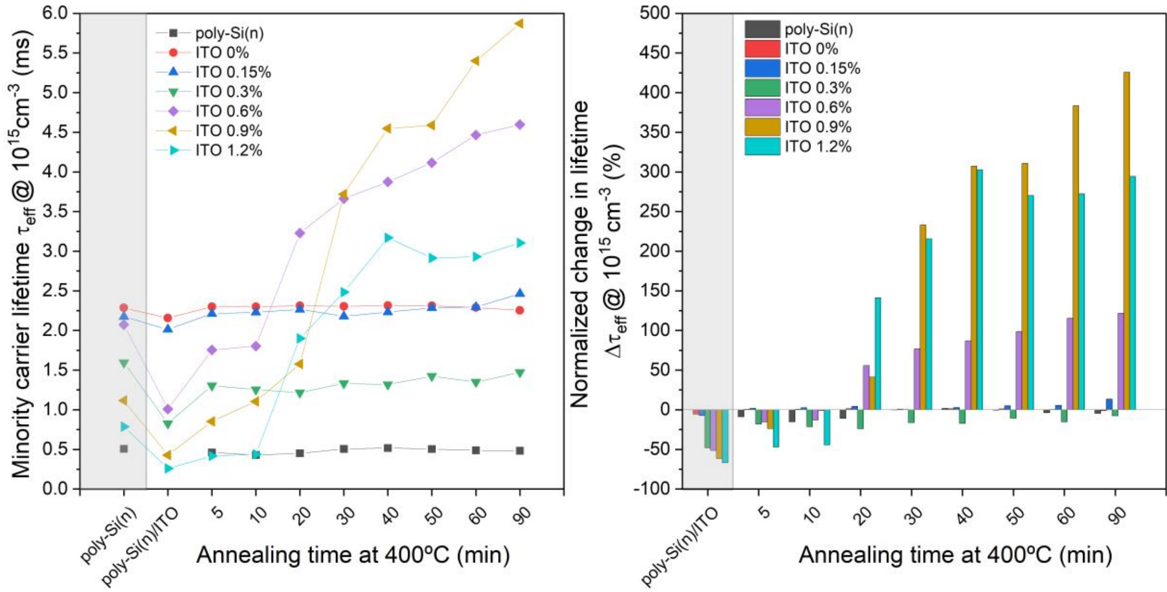

Figure 5-27 Left curve, minority carrier lifetime at 10^{15} cm^{-3} for the samples annealed with 400 ºC from 5 min to 90 min. Right curve, normalized change in lifetime for the same samples

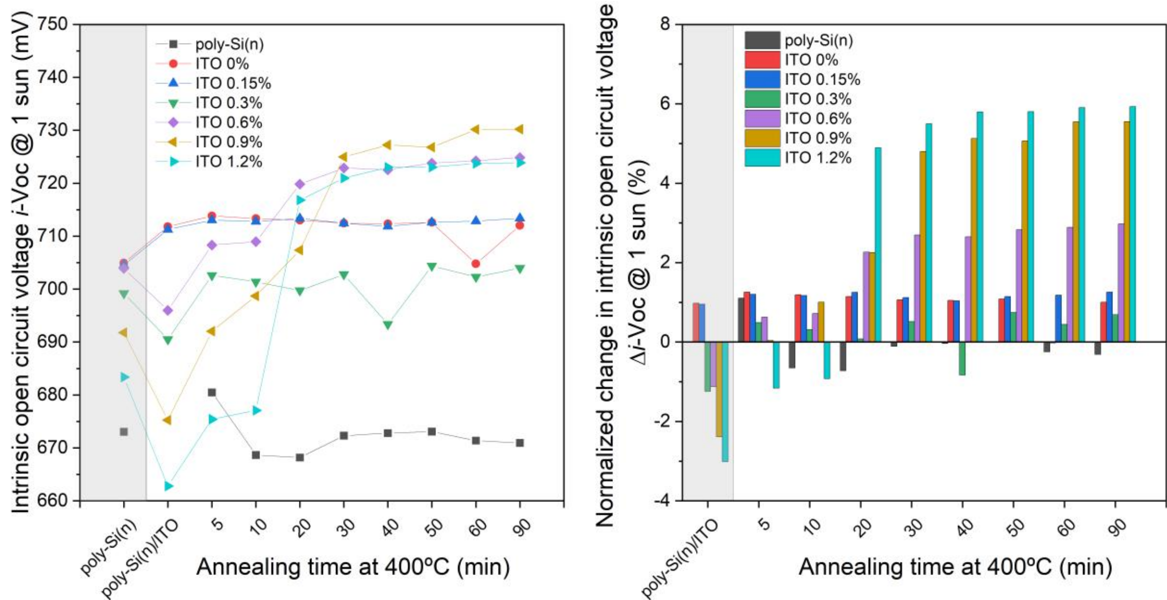

Figure 5-28 Left curve, i-V_{oc} at one sun for the samples annealed with 400 ºC from 5 min to 90 min. Right curve, normalized change in i-V_{oc} for the same samples.

Figure 5-28 shows the *i*-V_{oc} results for annealing processes at 400ºC. Again, the same behavior as the lifetimes is observed. The samples with only poly-Si(n) show no improvement, as do those with 0%, 0.15%, and 0.3% hydrogen. On the other hand, the samples with 0.6%, 0.9%, and 1.2% hydrogen show considerable improvement over their reference values. These had an increase in *i*-V_{oc} of 2.95%, 5.55%, and 5.97%, respectively. For example, for the 1.2% hydrogen sample, the *i*-V_{oc} values increased from

683 mV to 723 mV. This shows that an ITO:H with at least 0.6% hydrogen is necessary to notice the passivation of defects caused by hydrogen diffusion.

Finally, the same trend is observed with the recombination current density (*J_0*), as depicted in Figure 5-29. The samples with poly-Si(n) and those with 0%, 0.15%, and 0.3% hydrogen show no change with the annealing process. On the other hand, the samples with a hydrogen content ≥ 0.6% show a reduction in the recombination current of about 55% with a 90 min process. For example, the sample with 1.2% hydrogen went from having a J_0 of 11 fAcm^{-2} to 4 fAcm^2. This shows that the ITO:H layer with an annealing process at 400°C for at least 20 min can contribute to the passivate the SiO_x/poly-Si(n)/ITO stack defects.

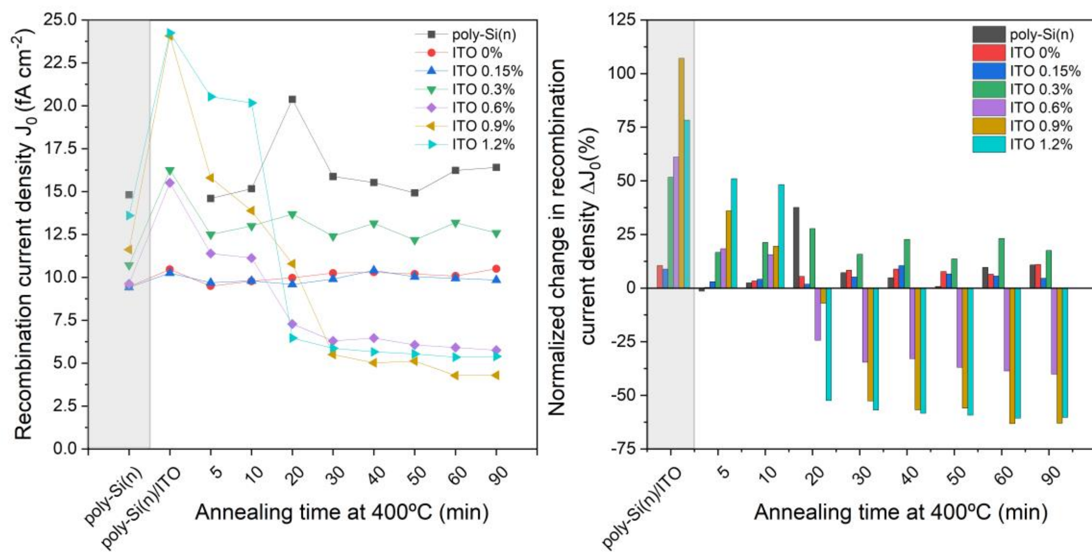

Figure 5-29 Left curve, recombination current for the samples annealed with 400 ºC from 5 min to 90 min. Right curve, normalized change in recombination current for the same samples

To confirm the uniformity of the ITO:H deposition and the spatial effect of the 400 ºC annealing process, photoluminescence (PL) images were taken for some of the samples. Figure 5-30 illustrate the passivation effect of ITO:H on poly-Si(n) with varying hydrogen content and subsequent annealing at 400°C in air. The initial poly-Si(n) samples show relatively low PL intensity, indicating significant surface recombination. Upon deposition of ITO:H, the PL intensity remains similar for the 0.15%, 0.3%, and 0.6% samples; meanwhile, the 1.2% samples show a decrease in the PL intensity. The most significant changes occur after annealing. The 5-minute air annealing step further enhances PL intensity, implying activation of hydrogen passivation and potential improvement in defect passivation. Extending the annealing duration to 90 minutes results in a strong enhancement of PL, particularly for higher hydrogen contents (≥0.30%), suggesting a more effective reduction of interface recombination. The trend indicates that the passivation effect of ITO:H is strongly dependent on both hydrogen content

and annealing time, where prolonged annealing maximizes the passivation benefits, leading to higher PL intensities and, thus, lower recombination losses.

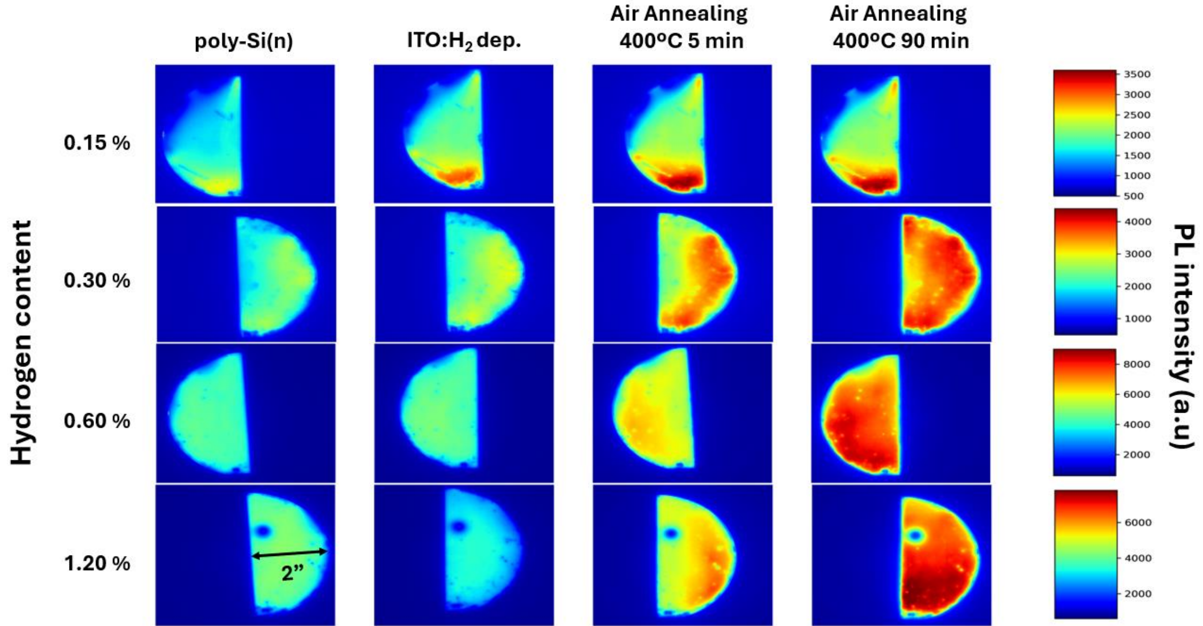

Figure 5-30 Photoluminescence images before and after the deposit of ITO:H, and after 5 min and 90 min annealing process at 400 ºC.

5.2.5 *Summary and conclusions*

The effectiveness of ITO:H in the passivation of defects in the c-Si(n)/SiO_x/poly-Si(n) structure has been tested for ITO:H thicknesses of 80 nm. However, annealing processes in air negatively affect the electrical properties of the films. For that reason, similar annealing experiments in an N_2 atmosphere would be interesting to maintain the electrical properties while increasing the structure's lifetime. On the other hand, the ITO:H samples, as deposited, show relatively low mobility values. Therefore, the characterization of ITO:H deposited without including any oxygen could increase the mobility of the films, although the absorptance could be affected.

The main results can be summarized as follows:

1. **Optimization of Sputtering Conditions for ITO:H:** The best power density for depositing ITO:H was determined to be 1.6 W/cm², balancing low absorptance, resistivity, and high mobility. Introducing oxygen (O_2) during deposition significantly impacts the electrical properties. An optimal 0.15% O_2 was found to provide low absorption while maintaining reasonable conductivity. Adding hydrogen (H_2) during deposition increases carrier

concentration and mobility, but excessive H_2 increases free carrier absorption in the infrared (IR) range. The best results were obtained with 0.15 % O_2 and 0.9 % H_2 with 13.31 cm^2/Vs mobility, $4.38x10^{20}$ cm^{-3} carrier concentration, $1x10^{-3}$ Ωcm resistivity, and 1.35 % normalized absorptance (300-1000 nm).

2. **Annealing Effects on Optical and Electrical Properties:** Air annealing process (210 ºC 30 min or 300 ºC 10 min) drastically reduces mobility and carrier concentration. Thus, the resistivity increases to ~0.2 Ωcm for all samples. The normalized absorptance (300-1000 nm) slightly increase to ~1.8 %. This effect is similar for all the samples with H_2; however, for the samples with O_2 and no H_2, the carrier concentration increases after the annealing process, showing a different reason for the mobility decrease. Although it is still unclear, the H_2 excess in the samples might interact differently with the constituent of the atmosphere (O_2 or H_2O), negatively affecting the electrical properties of the samples. In contrast, N_2 annealing (300 ºC 10 min) shows minimal effect on the electrical properties of the films, but the normalized absorptance (300-1000 nm) is reduced to ~1.2 %.

3. **Contact Resistivity and Sheet Resistance Trends:** The addition of H_2 reduced the contact resistivity (ρ_c) between ITO:H and Ag (glass/ITO:H samples), improving the junction's electrical performance. The annealing process in N_2 further reduced contact resistivity (~ 10^{-2} Ωcm^2), while air annealing resulted in a rectifying behavior, indicating unwanted chemical reactions. The sheet resistance decreases with the H_2 content, the best result was obtained with the 0.9 % H_2 sample with 98 Ω/□. The N_2 annealing process does not reduce the sheet resistance any further. The ρ_c of poly-Si(n)/ITO:H was higher (~1 Ωcm^2) than for ITO:H/Ag, possibly due to sputtering damage to the poly-Si layer. Annealing with hotplate in air (200 ºC 10 min) increases dramatically the contact resistivity, making it impossible to measure.

4. **Passivation of Poly-Si(n)/c-Si(n) via ITO:H:** ITO:H showed potential as a passivating layer in TOPCon structures, acting as both a passivation and conductive layer. The best passivation performance was obtained with 400 ºC air annealing process. The 80 nm ITO:H samples require at least 20 min to overcome their lifetime reference value. The best result was obtained with 0.9 % H_2, lifetime at 10^{15} cm^{-3}: 5.87 ms, $i\text{-}V_{oc}$: 730 mV, and J_0: 4.29 $fAcm^{-2}$ after 90 min air annealing process (400 ºC).

5.3 References

[1] J. Zheng *et al.*, "Blistering-free polycrystalline silicon carbide films for double-sided passivating contact solar cells," *Sol. Energy Mater. Sol. Cells*, vol. 238, no. September 2021, p. 111586, 2022, doi: 10.1016/j.solmat.2022.111586.

[2] E. Terzini, G. Nobile, T. Polichetti, and P. Thilakan, "Development and application of low temperature RF magnetron sputtered ITO thin films for a-Si:H based p/i/n junction solar cells," *Conf. Rec. IEEE Photovolt. Spec. Conf.*, pp. 667–670, 1997, doi: 10.1109/pvsc.1997.654177.

[3] A. Tchenka *et al.*, "Effect of RF Sputtering Power and Deposition Time on Optical and Electrical Properties of Indium Tin Oxide Thin Film," 2021, doi: 10.1155/2021/5556305.

[4] N. C. C. Lu, L. Gerzberg, C. Y. Lu, and J. D. Meindl, "Modeling and Optimization of Monolithic Polycrystalline Silicon Resistors," *IEEE Trans. Electron Devices*, vol. 28, no. 7, pp. 818–830, 1981, doi: 10.1109/T-ED.1981.20437.

[5] H. C. Lee, "Electron scattering mechanisms in indium-tin-oxide thin films prepared at the various process conditions," *Appl. Surf. Sci.*, vol. 252, no. 10, pp. 3428–3435, 2006, doi: 10.1016/j.apsusc.2005.03.203.

[6] S. Xian *et al.*, "Effect of oxygen stoichiometry on the structure, optical and epsilon-near-zero properties of indium tin oxide films," *Opt. Express*, vol. 27, no. 20, p. 28618, 2019, doi: 10.1364/oe.27.028618.

[7] N. M. Ahmed, F. A. Sabah, H. I. Abdulgafour, A. Alsadig, A. Sulieman, and M. Alkhoaryef, "The effect of post annealing temperature on grain size of indium-tin-oxide for optical and electrical properties improvement," *Results Phys.*, vol. 13, no. March, p. 102159, 2019, doi: 10.1016/j.rinp.2019.102159.

[8] B. García-Domene *et al.*, "Synthesis and High-Pressure Study of Corundum-Type In2O3," *J. Phys. Chem. C*, vol. 119, no. 52, pp. 29076–29087, 2015, doi: 10.1021/acs.jpcc.5b06939.

[9] J. Haines and J. Léger, "X-ray diffraction study of the phase transitions and structural evolution of tin dioxide at high pressure:ffRelationships between structure types and implications for other rutile-type dioxides," *Phys. Rev. B - Condens. Matter Mater. Phys.*, vol. 55, no. 17, pp. 11144–11154, 1997, doi: 10.1103/PhysRevB.55.11144.

[10] C. Diletto *et al.*, "Influence of Process Parameters on Properties of Non-Reactive RF Magnetron-Sputtered Indium Tin Oxide Thin Films Used as Electrodes for Organic Light-Emitting Diodes," *Crystals*, vol. 14, no. 9, p. 776, 2024, doi: 10.3390/cryst14090776.

[11] S. I. Jun, T. E. McKnight, M. L. Simpson, and P. D. Rack, "A statistical parameter study of indium tin oxide thin films deposited by radio-frequency sputtering," *Thin Solid Films*, vol. 476, no. 1, pp. 59–64, 2005, doi: 10.1016/j.tsf.2004.09.011.

[12] X. Zhang, G. Shi, J. A. Leveillee, F. Giustino, and E. Kioupakis, "Ab initio theory of free-carrier absorption in semiconductors," *Phys. Rev. B*, vol. 106, no. 20, pp. 1–8, 2022, doi:

10.1103/PhysRevB.106.205203.

[13] N. M. Khusayfan and M. M. El-Nahass, "Study of structure and electro-optical characteristics of indium tin oxide thin films," *Advances in Condensed Matter Physics*, vol. 2013. 2013, doi: 10.1155/2013/408182.

[14] F. Meyer *et al.*, "Optimization of front SiNx/ITO stacks for high-efficiency two-side contacted c-Si solar cells with co-annealed front and rear passivating contacts," *Sol. Energy Mater. Sol. Cells*, vol. 219, 2021, doi: 10.1016/j.solmat.2020.110815.

[15] Y. Wang *et al.*, "Tunability of indium tin oxide materials for mid-infrared plasmonics applications," *Opt. Mater. Express*, vol. 7, no. 8, p. 2727, 2017, doi: 10.1364/ome.7.002727.

[16] B. Yang *et al.*, "Strain effects on halide perovskite solar cells," *Chem. Soc. Rev.*, vol. 51, no. 17, pp. 7509–7530, 2022, doi: 10.1039/d2cs00278g.

[17] H. Jiang, Z. Huang, G. Xue, H. Chen, and H. Li, "Electron transport at the interface of organic semiconductors and hydroxyl-containing dielectrics," *J. Mater. Chem. C*, vol. 6, no. 44, pp. 12001–12005, 2018, doi: 10.1039/c8tc01343h.

[18] M. Zhang *et al.*, "Ohmic Contact of Pt / Au on Hydrogen-Terminated," *Coatings*, vol. 9, p. 539, 2019.

[19] T. N. Truong *et al.*, "Hydrogenation Mechanisms of Poly-Si/SiOx Passivating Contacts by Different Capping Layers," *Sol. RRL*, vol. 4, no. 3, pp. 1–6, 2020, doi: 10.1002/solr.201900476.

[20] C. Seron *et al.*, "Hydrogenation of sputtered ZnO:Al layers for double side poly-Si/SiOxsolar cells," *EPJ Photovoltaics*, vol. 13, 2022, doi: 10.1051/epjpv/2022005.

CHAPTER VI: TiO_X DEPOSITED BY HIGH-PRESSURE SPUTTERING USING LOW-TEMPERATURE OXYGEN PLASMA

Titanium oxide (TiO_x) has emerged as a promising material for electron-selective contacts in crystalline silicon (c-Si) solar cells due to its favourable band alignment, chemical stability, and compatibility with low-temperature processes [1]. This chapter explores the synthesis of ultra-thin TiO_x films via a two-step oxidation process by high-pressure sputtering (HPS). This process includes Ti deposition followed by thermal-plasma oxidation using low-temperature oxygen plasma (150 ºC - 200 ºC). The primary objective is to develop an oxidation process which allows the Ti film oxidation while minimizing the growth of SiO_x on the Si substrate surface. In a previous work of the research group [2], the deposition of TiO_x film by a TiO_x target showed a relevant growth of SiO_x at the Si surface, thus a single step deposition was not investigated in this thesis.

The structural, chemical, and optical properties of TiO_x films were systematically investigated as a function of deposition parameters, oxidation conditions, and post-deposition treatments. A comprehensive characterization approach was employed, including X-ray photoelectron spectroscopy (XPS), Fourier-transform infrared spectroscopy (FTIR), transmission electron microscopy (TEM), grazing incidence X-ray diffraction (GIXRD), UV-VIS-IR spectroscopy and ellipsometry. In addition, the potential of TiO_x as an electron-selective contact was evaluated by extracting the specific contact resistivity (ρ_c) using the Cox and Strack method, and by assessing the minority carrier lifetime (τ_{eff}) through quasi-steady-state photoconductance (QSSPC) measurements.

6.1 Characterization of Ti deposition with high-pressure sputtering

The first step in obtaining the TiO_x layer was the characterization of the Ti deposition with different power densities and pressures. For that, a glass substrate was used to measure the thickness of the Ti layer fabricated under various conditions. In this experiment, the deposition time was kept constant at three hours. A small piece of glass was used as a shadow mask to leave an area without Ti deposition. After removing the sample from the chamber, the thickness was measured with a profilometer as the difference in heights left by the glass mask. Figure 6-1 depicts the deposition rates under different chamber pressures and power densities. As commonly seen in sputtering, increasing the chamber pressure decreases the deposition rate since there are more particles in the vicinity of the plasma, which causes the reduction of the mean free path. This translates into a decrease in the rate at which the sputtered atoms arrive at the substrate [3].

As the power density increases, the deposition rate also increases. At higher power, the ionized particles in the plasma will have greater kinetic energy, enabling them to extract more atoms from the target. However, caution must be taken as the power increases, since the target can be damaged by the high temperatures reached with high power densities.

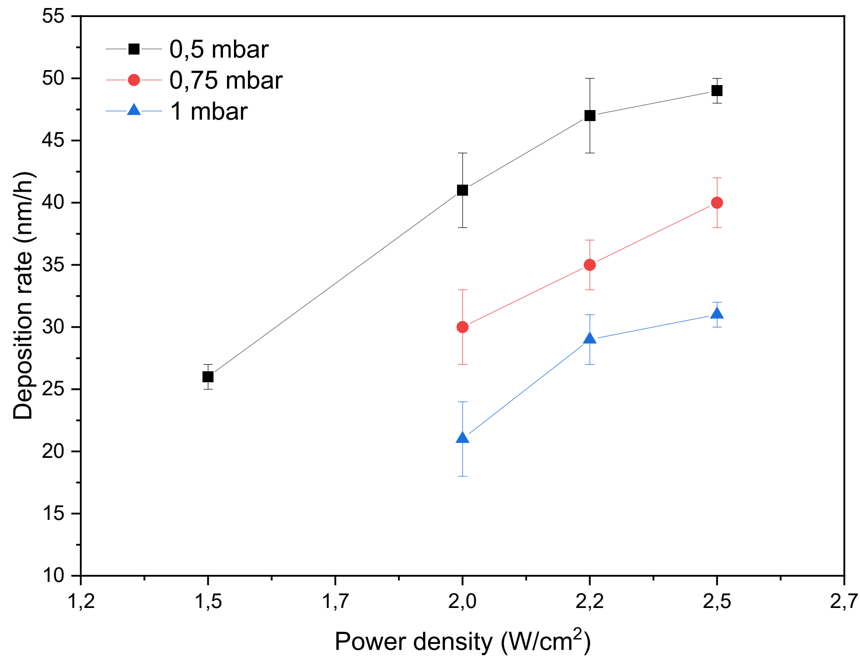

Figure 6-1 Ti deposition rate under different pressures as a function of power densities.

One of the main objectives of this thesis is the research on high-pressure to reduce the damage to the substrate. However, a compromise must be made between a realistic deposition rate and the pressure/power density. Therefore, it was decided to continue the rest of the thesis with a power density of 2.2 W/cm^2 (power of 45 W) and a pressure of 0.5 mbar. With these conditions, a 47 nm/h deposition rate was expected.

With the deposition conditions of 2.2 W/cm^2 and 0.5 mbar, several Ti layers were deposited on glass and then measured with the aligned four-point probe method to determine the sheet resistance ($R_{\square}$). These results are depicted in Figure 6-2. As the deposition time increases, the sheet resistance of the Ti films decreases. Although different deposition times (i.e., different Ti thicknesses) were considered, the objective is to obtain a Ti layer around 5 nm and then oxidize it. This is the typical thickness used for TiO_x as a selective contact in solar cells [4]. With a deposition time of 0.1 h (6 min), the expected thickness is ~5 nm. The $R_{\square}$ obtained was 854 Ω/□, which gives a Ti resistivity of 4.27 x10^{-4} Ωcm. This resistivity is congruent with extremely thin Ti layers deposited by sputtering, as found by others groups [5].

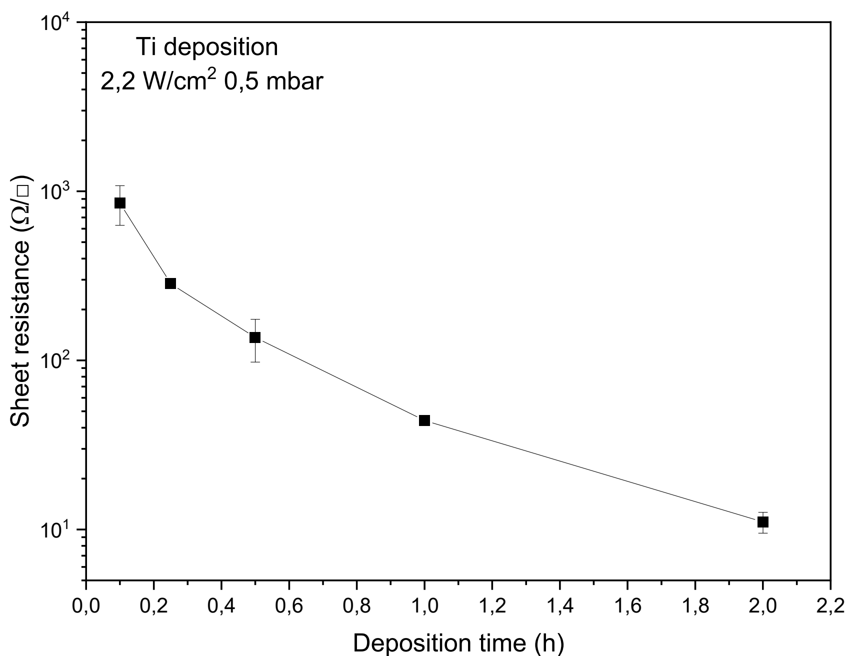

Figure 6-2 Sheet resistance of Ti layers with different deposition times

6.2 Oxidation of Ti thin film through low-temperature O_2 plasma

Once the Ti layer was characterized, the second step to obtain the TiO_x layer was to perform an oxidation process. For this, a change in the $R_{\square}$ was sought as an indication for Ti oxidation. It is well known that transition metal oxides, such as TiO_x, has higher $R_{\square}$ that metallic thin films (Ti). Different approaches were considered to oxidize the Ti layer, such as increasing the substrate temperature and introducing O_2 into the chamber (thermal oxidation), or using the Ti target to create an O_2 plasma and place it on top of the substrate (plasma oxidation). However, none of these options significantly changed the measured $R_{\square}$. The option with which we finally managed to obtain an increase in $R_{\square}$ and thus clear indications of Ti oxidation was a combination of both, i.e., increasing the substrate temperature while a mixed Ar/O_2 plasma is placed on top of the sample (thermal-plasma oxidation). Two different substrate temperatures were used, either 150 ºC or 200 ºC. Those relatively low temperatures were used since the aim of these TiO_x layers is to be compatible with HIT solar cell technology. The a-Si:H and doped a-Si:H films are sensitive to moderate temperatures, and start to degrade at ~250 ºC [6]. Thus, the oxidation temperature was limited to 200 ºC Also, the O_2 concentration inside the chamber was kept at 5 % because this is the lowest flux that the O_2 mass flow controller can properly control; the remaining 95 % content in the chamber was Ar.

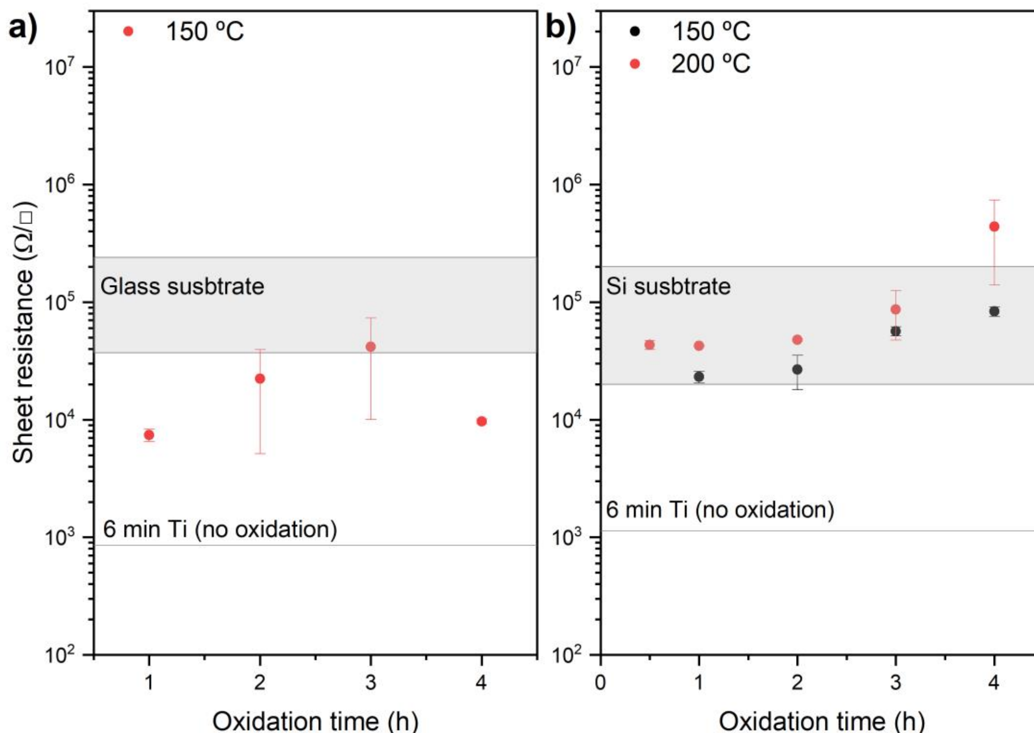

Figure 6-3 Sheet resistance as a function of oxidation time of TiO_x fabricated with the thermal-plasma oxidation process. a) TiO_x samples on glass substrate and b) TiO_x samples on high-resistivity Si substrate.

Figure 6-3 shows the sheet resistance of different oxidized samples, varying the oxidation time. The figure on the left side depicts the TiO_x samples on glass substrates. The sheet resistance of the Ti layer deposited during 6 min (~5 nm) is shown as a reference. Besides, the sheet resistance of different glass substrates was measured and depicted as a grey region. With a 150ºC oxidation process, the sheet resistance of the samples increases at least one order of magnitude compared to the Ti reference layer, reaching values between $7.4x10^3$ and $4.1x10^4$ Ω/□. This would represent resistivity values between $7.4x10^{-3}$ and $2x10^{-2}$ Ωcm. In the figure on the right side, samples on high-resistivity Si substrates are shown. Again, the grey area represents the substrate's sheet resistance according to the manufacturer's data ($2x10^4$ to $2x10^5$ Ω/□). In this case, two different oxidation temperatures were considered (150 ºC and 200 ºC). A clear trend is noticeable as the samples processed at higher temperatures (200 ºC) show higher sheet resistance, reaching values as high as $4.4x10^5$ Ω/□ (resistivity of 0.2 Ωcm). The samples processed at 150 ºC show similar values in the $2.3x10^4$ to $8.3x10^4$ Ω/□ range. Since the TiO_x layers are very thin, a possible reason for these values is that the Si substrate is being measured; however, many samples with Ti layers (non-oxidized) were measured, and the four-probe system can measure such thin layers. In any case, those values show that the Ti layer has been successfully oxidized to reach a sheet resistance similar to or even higher than the Si substrate. Such resistivity values are congruent with sub-oxidized TiO_x films found by others [7].

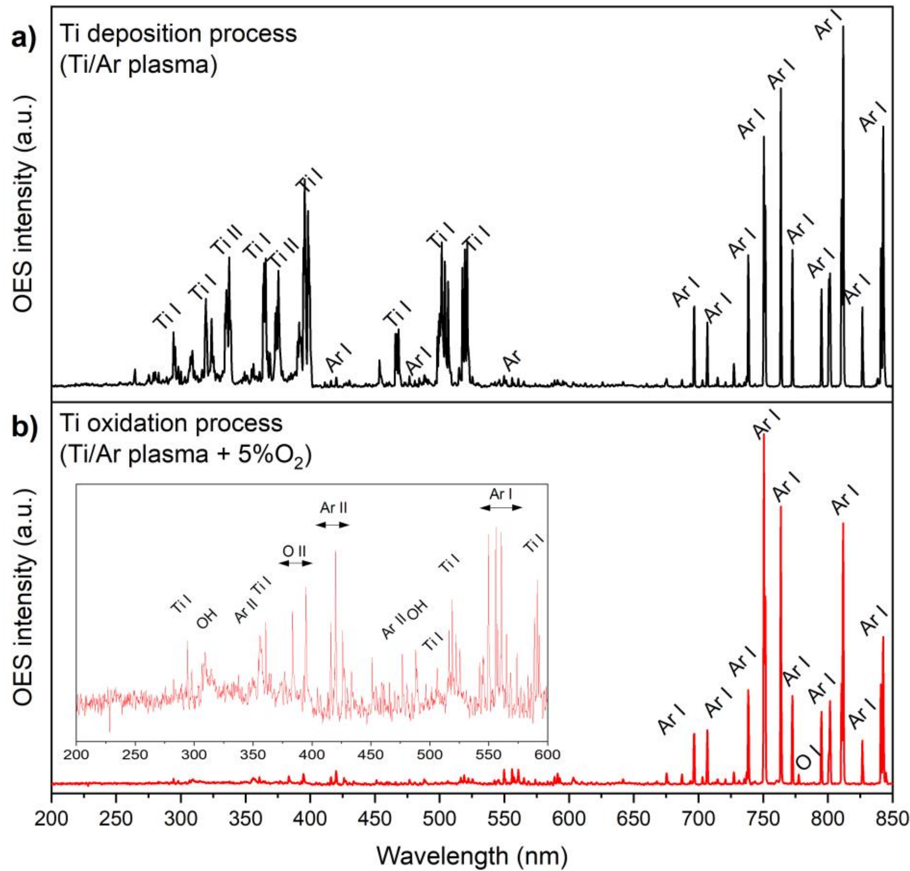

Figure 6-4 Optical Emission Spectroscopy (OES) spectra of HPS plasma for the TiO_x deposition steps 2.2 W/cm^2 and 0.5 mbar. a) plasma spectrum for the Ti deposition step and b) the plasma spectrum for the oxidation step.

Figure 6-4 shows the Optical Emission Spectroscopy (OES) spectra for the two steps used to fabricate the TiO_x film. First, the Ti deposition spectrum shows firm emission peaks in the 200 - 600 nm range related to the Ti extraction. For this deposition step, the strongest Ti emission lines are present at 395 nm, 504 nm, and 520 nm, representing the photons obtained from excited Ti atoms (Ti I). Additionally, photons from ionized Ti atoms (Ti II) are present at 337 nm and 375 nm. The 700 - 850 nm emission peaks represent the excited Ar species [8]. Second, the Ti emission peaks are drastically reduced in the oxidation step spectrum due to the introduction of O_2, but still, there are some small Ti peaks in the 200 – 600 nm range. Additionally, a broad peak is observed around 320 nm, which is commonly associated with OH emission [9]. The Ar emission peaks in the 700 – 850 nm range remain almost identical to the Ti deposition step. From this, it can be concluded that the O_2 introduction hinders most of the Ti extraction as the O_2 interacts with the surface of the Ti target, creating a TiO_x layer. In the reactive sputtering process, this is sometimes referred to as target poisoning [10].

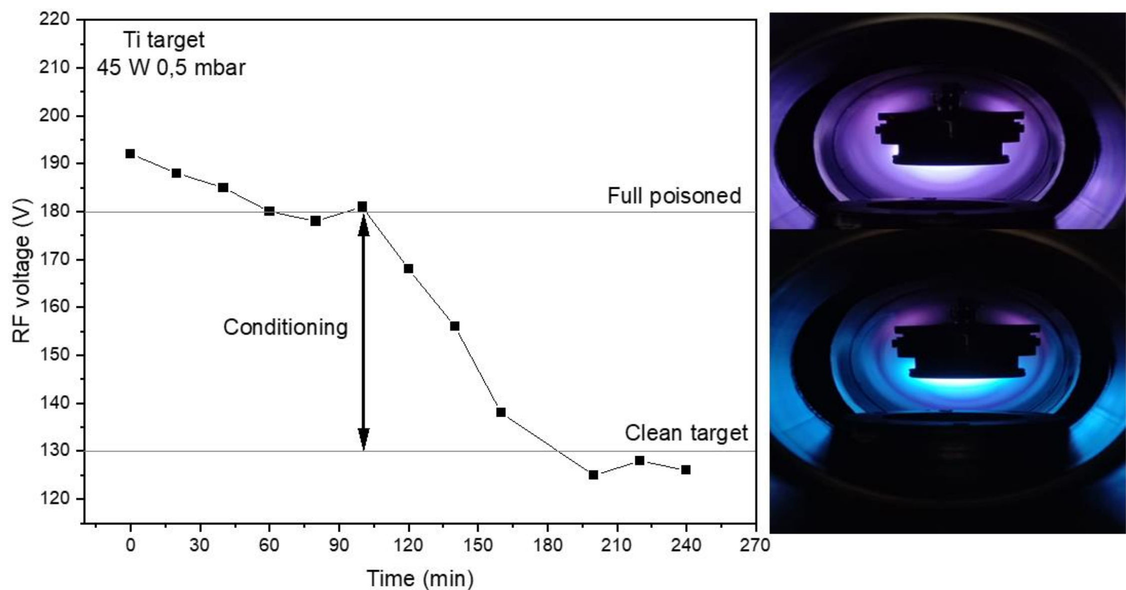

Figure 6-5 RF voltage as a function of conditioning time to determine the cleanliness of the Ti target. On the right side are images of the Ti target in poisoned (purple plasma) and clean regimes (blue plasma).

Cleaning the Ti target before another Ti deposition process is crucial to obtain reproducible samples with the two-step oxidation process. Therefore, a cleaning process (conditioning step) with a non-reactive gas such as Ar must remove the TiO_x layer created on the target surface during the previous oxidation step. Monitoring the RF voltage on the RF generator is a helpful way to determine whether the target is clean, since this value changes as a function of the sputtered material. As explained in the Fabrication Chapter, dielectric materials such as TiO_x need a higher voltage than metals to be sputtered. Figure 6-5 shows the RF voltage as a function of the conditioning time, going from a poisoned target to a clean target. This transition takes place around three hours with a power density of 2.2 W/cm^2 and 0.5 mbar. Once the RF voltage reaches ~130 V, the Ti target is completely clean and ready to deposit another Ti layer. The transition from clean to poisoned target is instantaneous, however, at least 30 min of conditioning is allowed to ensure that the Ar/O_2 plasma stabilizes.

6.3 Structural characterization of TiO_x fabricated by the two-step oxidation process

The first structural technique used to characterize the TiO_x films was XPS. The purpose was to confirm the oxidation of the samples and determine the O/Ti atomic ratio (stoichiometry of the TiO_x films). Samples fabricated at 150 ºC and 200 ºC with oxidation times between 1 h and 4 h were analyzed. Figure 6-6 depicts the deconvoluted O-1s electron emission peaks of the samples. All the samples

present a broad peak at 531 eV, commonly associated to oxygen vacancies (O_V), suggesting the presence of oxygen atoms with dangling bonds [11]. Another peak is observed at 529 eV and it is related to lattice oxygen (O_L) [12], which is the predominant peak observed for all the samples. A tendency is observed when the percentage representing the O_V peak over the O-1s peak is calculated, as this value decreases as the temperature or the oxidation time increases. For instance, for the 150 ºC samples, O_V goes from 27 % to 25 % as the oxidation time increases. At 200 ºC, the value goes from 26 % to 21 %. This represents that the oxygen atoms are forming bonds with the Ti lattice, leading to a stoichiometric TiO_x.

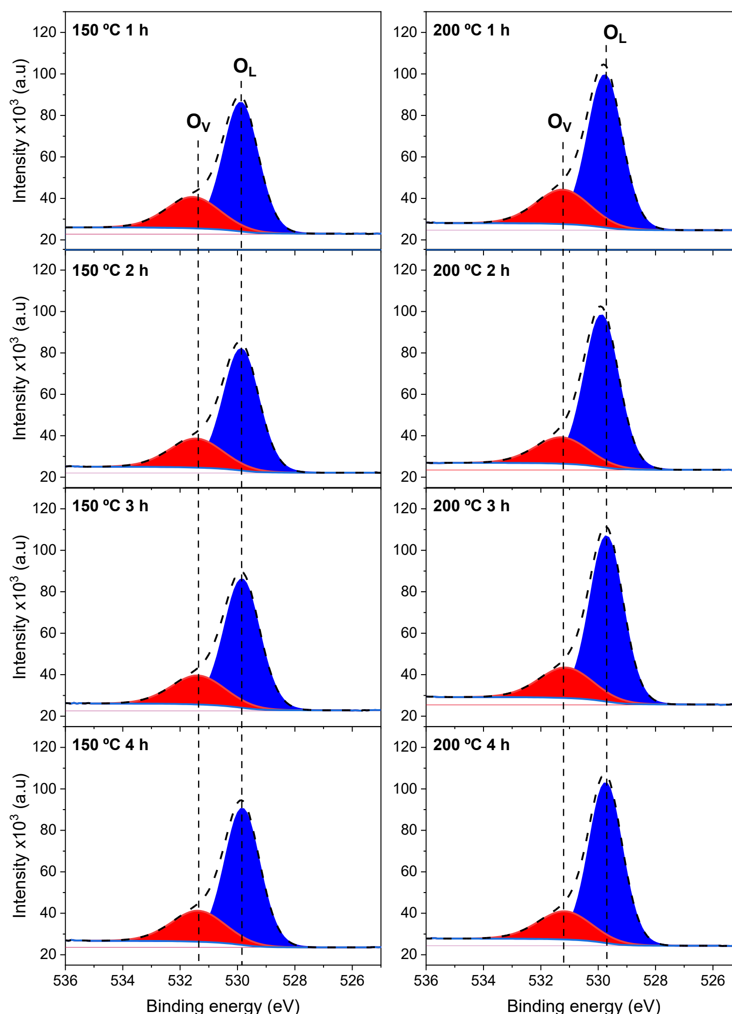

Figure 6-6 XPS spectrum of the O 1s emission peaks for samples fabricated at 150ºC and 200ºC with different oxidation times

Figure 6-7 shows the deconvoluted peaks for the Ti 2p electron emission. Some oxidation states are observed for the samples fabricated at 150 ºC and 200 ºC. The oxidation states represent the number of electrons donated to form bonds with the surrounding elements. In the case of TiO_2 film, the most relevant oxidation state is Ti(+4) as the Ti has lost four electrons to two O atoms to form the bonds. In

sub-stoichiometric TiO_x films, other oxidation states are present, such as Ti(+3) and Ti(+2). This indicates either oxygen vacancies or simply that Ti and O have not formed the bonds necessary to form TiO_2 . The oxidation states present in these samples do not change with the increment of the oxidation time, as the Ti(+4) represents 90 % of the Ti-2p peak for the 150 ºC 1 h and 150 ºC 4h samples. The temperature does not change this ratio either, since the 200 ºC 1 h sample shows a Ti(+4) percentage of 90.20% while 200 ºC 4 h sample shows 90.40%. Finally, the O/Ti ratio is obtained by considering the relative height of the Ti(+4) peak with respect to the rest of the oxidation states (i.e., Ti(+3) and Ti(+2)). For the 150 ºC samples O/Ti ratio goes from 1.93 (1 h oxidation) to 1.95 (4 h oxidation). In the case of 200 ºC sample the values stay the same (1.93) for all the oxidation times. The O/Ti ratio was also calculated based on the O 1s and Ti 2p peak areas. However, the resulting O/Ti ratio was greater than 2, which is physically unrealistic for titanium oxide. This discrepancy may be attributed to surface contamination, since the samples had to be transferred to another laboratory to be analyzed.

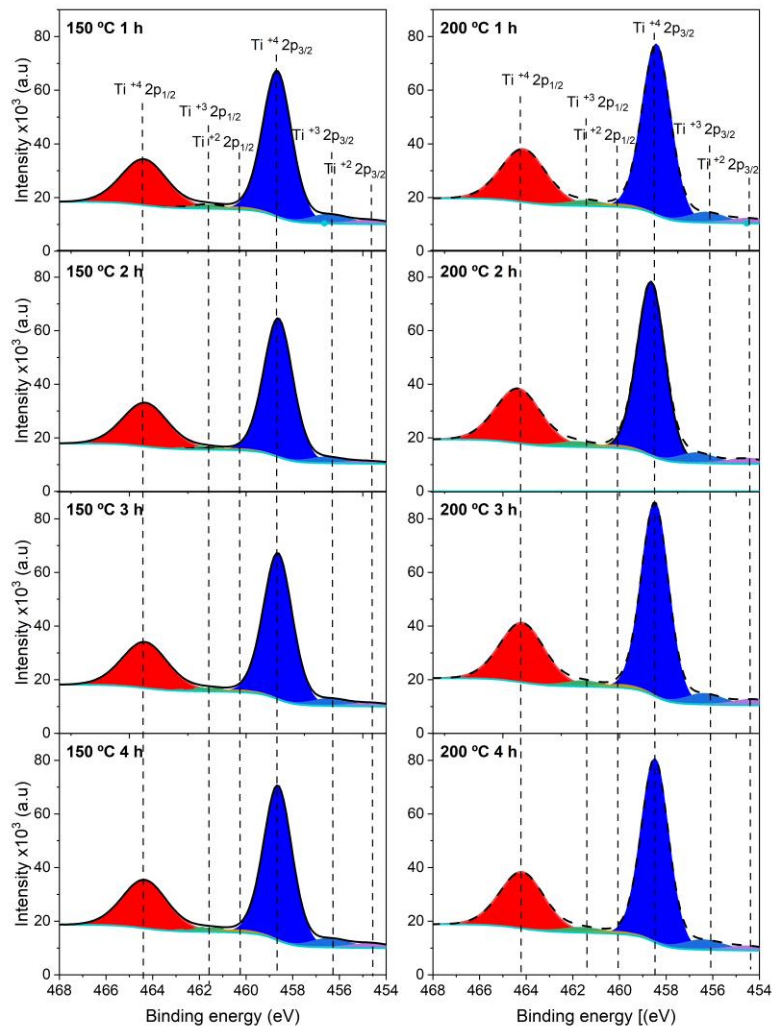

Figure 6-7 XPS spectrum of the Ti 2p emission peaks for samples fabricated at 150ºC and 200ºC with different oxidation times.

The XPS data confirm that the Ti samples have been successfully oxidized using the low-temperature plasma process, which yields sub-stoichiometric TiO_x films. Both temperatures (150 ºC and 200 ºC) seem to obtain the same kind of films. Besides, a one-hour oxidation process appears enough to reach such sub-stoichiometric TiO_x films, O/Ti ratio equal to ~1.9.

FTIR analysis was performed to gain insight on the chemical bonding of the TiO_x films fabricated by the two-step oxidation process. The Ti-O bond oscillations are typically observed at a lower wavenumber range (700 - 400 cm^{-1}) [13] . It was not easy to detect those absorbance peaks for these samples since the TiO_x films are very thin (~ 5 nm). However, some peaks appear between 500 and 400 cm^{-1}, which are related to Ti-O oscillations. Thus, the Si substrate signal was subtracted from the measured data to better observe their differences. The results are depicted in Figure 6-8. For the 150 ºC samples, two peaks located at 418 and 495 cm^{-1} start to appear after two hours of oxidation, which can be related to Ti-O stretching [14] and Ti-O bending [15] respectively. The same absorbance peaks are present in all the samples fabricated at 200 ºC. The absence of these peaks in the 150 ºC samples with an oxidation time of less than two hours can be explained by a broader peak at around 435 cm^{-1}, often related to anatase phase TiO_x [16]. This indicates that a minimum time and temperature are required to form the crystalline structure to observe Ti-O stretching and Ti-O bending vibrations. Additionally there is a relevant absorbance peak located at 615 cm^{-1} which represents the Si-Si stretching absorbance [17]. It is worth noting that no broad peak related to Si-O stretching at around 1060 cm^{-1} [18] is appreciable in these spectra**.** This is relevant since the plasma oxidation at low temperature could oxidize the Si substrate, creating a SiO_x layer in between the Si and the TiO_x.

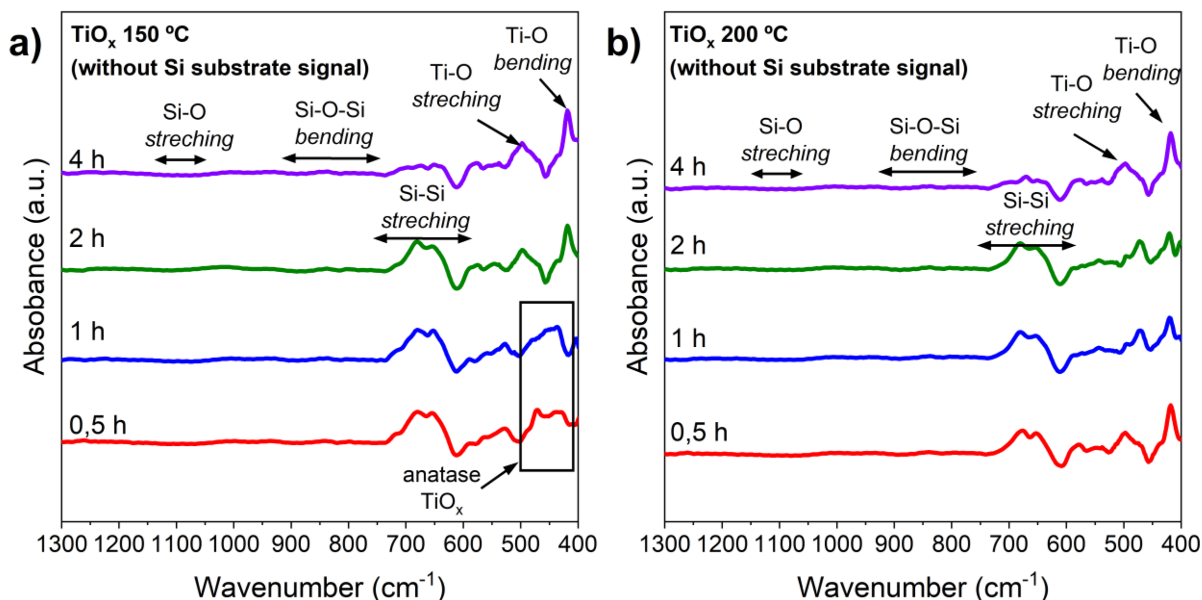

Figure 6-8 FTIR spectra for TiO_x samples fabricated with the two-step oxidation process without the Si substrate signal contribution. a) FTIR spectra for 150 ºC TiO_x samples and, b) FTIR spectra for 200 ºC TiO_x samples.

The plasma analysis (OES spectra) showed that Ti extraction is reduced during the oxidation step, but it is still detectable. For that, the role of the Ti layer as a capping layer during plasma oxidation was evaluated. This experiment was also carried out on Si substrates without the Ti layer. The spectra of these films after substrate correction is depicted in the Figure 6-9. For both temperatures (150 ºC and 200 ºC), without the Ti capping step, there is a strong presence of the Si-O stretching peak at 1050 cm^{-1} even for the shortest oxidation process of 0.25 h. In contrast, for the samples with Ti capping layer plus an 200 ºC 2 h oxidation process the presence of Si-O stretching is minimal, comparable to the Si substrate sample that was cleaned with HF previously for FTIR measurement. These results indicate that the first step (deposition of ~5 nm Ti layer) is crucial to mitigate the oxidation of the Si substrate. As the purpose of the TiO_x layer is to be used as an electron-selective contact, a thick intermediate SiO_x would drastically increase the contact resistivity and thus reduce the recombination of photogenerated carriers.

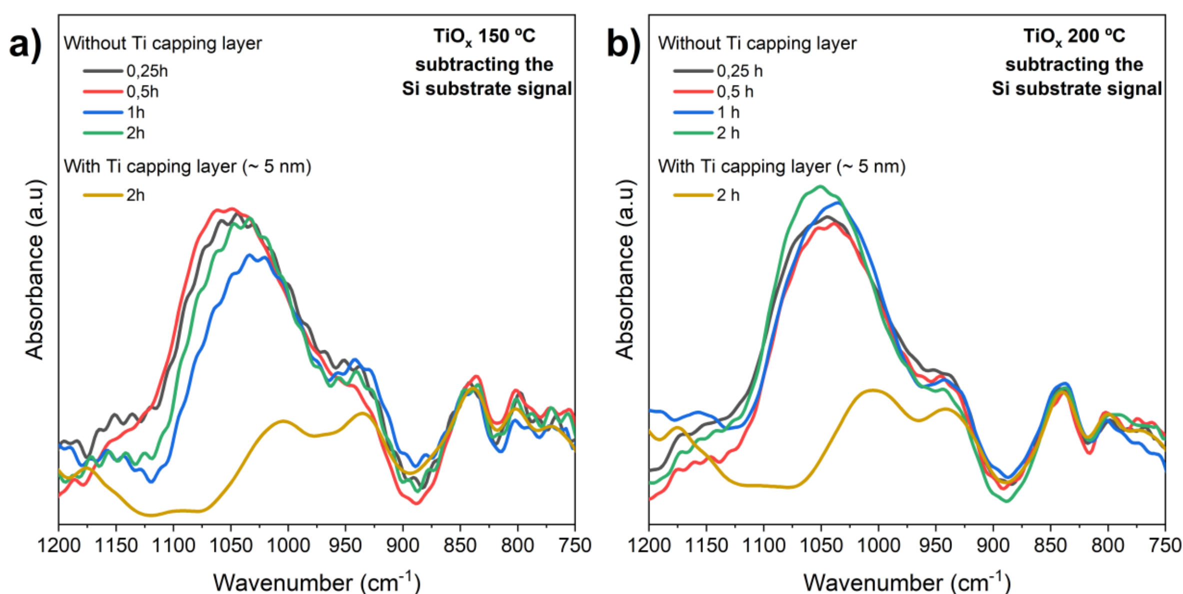

Figure 6-9 FTIR spectra comparing the action of the plasma oxidation step with and without Ti capping layer, a) samples with an oxidation temperature of 150 ºC, and b) samples with an oxidation temperature of 200 ºC

To determine whether the TiO_x samples present any degree of crystallinity, some samples fabricated at 150 ºC and 200 ºC were measured with GIXRD. The incidence angle was kept constant for all the samples at 0.5º to maximize the signal from the surface. The results are depicted in Figure 6-10. We can observe the presence of a broad peak around $2\theta = 55º$ for all the samples. At certain azimuth angles of the samples with respect to the detector, the (113) Si plane can be observed, corresponding to $2\theta = 56.4$, as it has been observed when Si (100) substrates are measured with GIXRD [9][19]. This broad peak is also present in the diffractogram of the bare Si sample, so we can confirm that it is partly due to the Si substrate, and will not be discussed further. The as-deposited Ti sample diffractogram is practically the same as the Si substrate, thus showing the amorphous nature of the sputtered Ti layer.

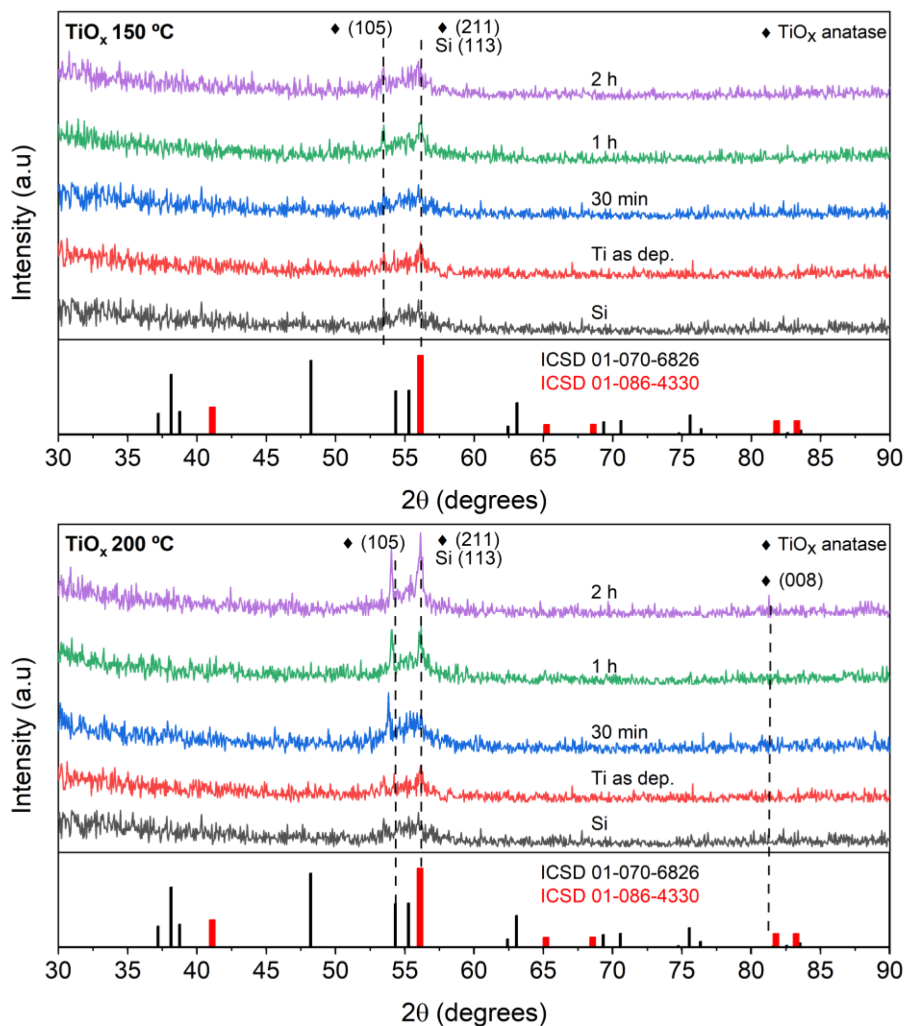

Figure 6-10 Diffractograms of TiO_x samples (~5 nm) fabricated at 150 ºC and 200 ºC measured with GIXRD configuration with an incidence angle of 0.5º. The Si substrate diffractogram and the reference anatase TiO_x (ICSD 01-070-6826 and ICSD 01-086-4330) are also included to compare.

Regarding the TiO_x samples fabricated at 150 ºC, there is a slight presence of peaks at $2\theta = 53.47$ and 56.10 which might indicate the presence of (105) and (211) anatase TiO_x planes according to the *Inorganic Crystal Structure Database* (ICSD) reference files, however such signals are almost at the noise level thus it is difficult to confirm. In contrast, the samples fabricated at 200 ºC show an increase in the intensity of the peaks located at $2\theta = 56º$ and $2\theta = 54º$, indicating a stronger presence of such crystalline planes of TiO_x. Furthermore, as the oxidation time increases, the intensity of those peaks also increases. This shows that increasing oxidation duration leads to the formation of more crystalline planes related to anatase TiO_x, which is congruent with the minimum temperature (~200 ºC) necessary to observe the anatase phase of TiO_x [20]. Nevertheless, as the intensity of those peaks is still very low, the TiO_x samples could be considered essentially amorphous.

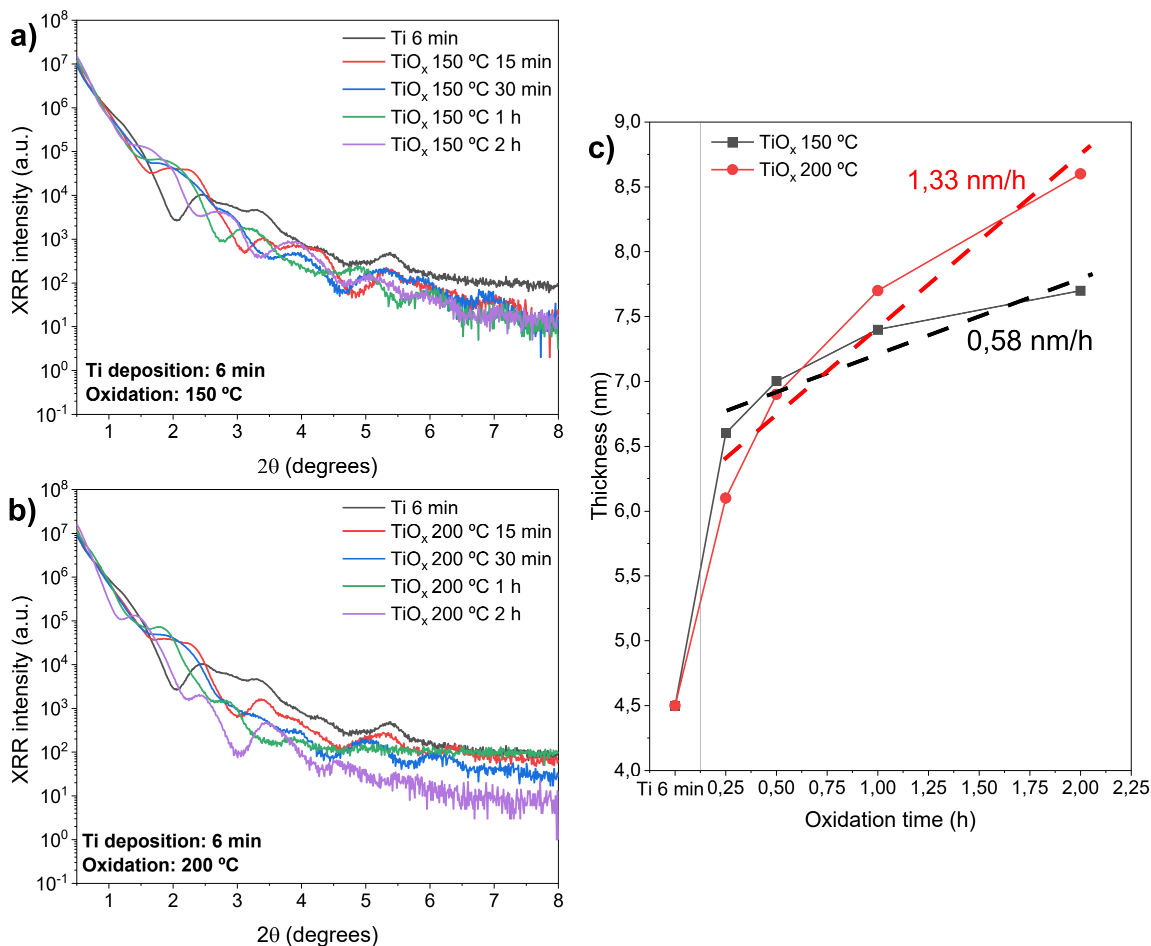

Figure 6-11 XRR measurements of different TiO_x samples fabricated at 150 ºC and 200 ºC. a) measurements for the 150 ºC samples, b) measurements for the 200 ºC samples, and c) estimated thickness (from linear fitting) for both oxidation temperatures.

In the OES spectra for the oxidation process (Figure 6-4(b)), it was observed that although the intensity of the Ti peaks drops drastically, some peaks still appear, which may imply that in step 2, not only the previously deposited Ti film is oxidized, but there is also a small TiO_x deposition. To corroborate this, the samples measured with GIXRD were also measured with X-ray reflectometry (XRR) to determine their thickness. The XRR measurement for the 150 ºC and 200 ºC, as well as the estimated thickness, are depicted in Figure 6-11. The FFT (Fast Fourier Transform) method from the AMASS-XRR software was used to determine the thickness. The XRR results show that the thickness of the TiO_x samples is higher than that of the Ti, which in this sample is 4.5 nm. Also, there is a thickness increase tendency as the oxidation time increases. For instance, for the 150 ºC samples, the thickness increases from 6.6 nm with 0.25 h oxidation time to 7.7 nm for 2 h oxidation time. Regarding the 200 ºC samples, there is even a higher increase as the thickness goes from 6.1 nm (0.25 h) to 8.6 nm (2 h). This confirms that the oxidation step deposits a small amount of TiO_x, depending on the process's duration and temperature.

Some TiO_x samples were selected to obtain lamellae and observe them by TEM, to accurately determine the thickness. Figure 6-12 depicts the TEM image for a TiO_x sample fabricated at 150 ºC and 0.5 h. As mentioned previously from XRR results, the oxidation step should slightly increase the final thickness of the sample. For this specific oxidation process, the thickness should be around 7 nm. TEM image confirms that the thickness of the TiO_x layer is around 6.6 nm. Additionally, the TEM image depicts a SiO_x layer with a thickness of around 1.5 nm, which indicates that the Ti layer is acting as a capping layer for this oxidation process, as the native SiO_x layer in Si wafers is between 1 – 2 nm [21]. The presence of the SiO_x layer may result from native oxide regrowth during sample transfer after HF cleaning, as it was performed outside the deposition chamber. Alternatively, the plasma oxidation could slightly oxidize the Si/Ti interface, forming a thin SiO_x layer. The XEDS analysis on the TiO_x layer shows Ti emission lines at 4.5 and 4.9 keV, which belong to Ti K_α and Ti K_β, respectively. A weak peak also appears at ~0.4 keV that corresponds to Ti L_a. Another significant peak is present at 0.5 keV, which corresponds to O K_α [22]. The presence of the Si peak (1.74 keV corresponding to Si K_α [23]) is due to the measurement spot dimension (~ 1 nm) that could have excited the SiO_x layer or even the Si substrate. Finally, the Cu peaks are presented due to the material of the FIB lift-out grid, and the Pt peaks due to its use as a protective layer during lamella fabrication with FIB.

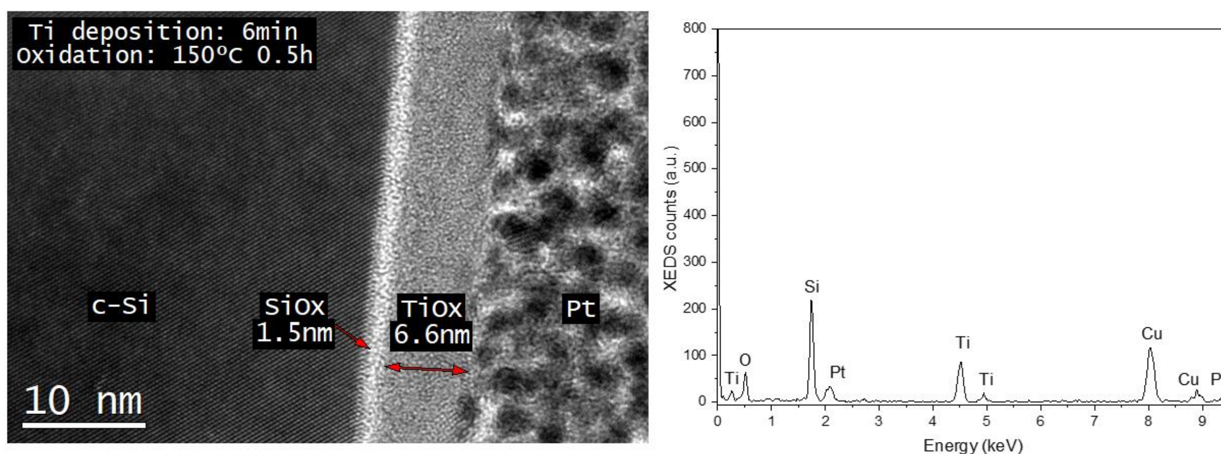

Figure 6-12 TEM image and XEDS spectrum for a TiO_x sample fabricated with a 150 ºC oxidation process during 0.5 h.

Considering the samples fabricated at 150 ºC for 4 h (Figure 6-13), the TEM image shows a TiO_x thickness of ~ 11 nm. No sample with this characteristic was measured with XRR, but considering the deposition rate at 150 ºC (0.58 nm/h) during the oxidation step, plus the ~5 nm of original Ti, would give a final thickness of ~7.3 nm. The difference between the two techniques would indicate that the TiO_x deposition during the oxidation step is even higher, or more oxygen is incorporated into the film, leading to a volume expansion. Additionally, the TiO_x layer shows some crystalline structure on the surface from which the reciprocal space is obtained by *Fast Fourier Transform* (FFT), inset on the TEM image. Since the distance of the spots in the reciprocal space is inversely related to the real space spacing of crystal planes, this was calculated, and an interplanar distance of 0.25 nm was obtained.

Comparing this value with the ICSD file used for GIXRD measurements, the anatase TiO_x plane that matches better with that interplanar distance is the (400) plane, which shows d = 0.24 nm. This plane, located at 2θ = 37.37º, was not found in the GIXRD diffractograms; however, the following reasons can explain this. As the GIXRD measurements are sensitive to different plane orientations, plane (400) can reflect the X-ray at an angle not observable by the detector, or plane (400) represents a low fraction of the crystalline structure, whose reflection is too low to be observed in the diffractograms. In any case, the oxidation process, which lasts four hours, leads to the formation of crystalline structures on the surface of the TiO_x layer, as the TEM image shows. This time, the XEDS analysis depicts the same peaks as the previous sample, but the intensity of the peaks is higher due to the increase of the TiO_x thickness.

Regarding the thickness of the SiO_x layer, this is ~1.3 nm. This indicates that even with the longest oxidation time at 150 ºC of four hours, the first deposited Ti layer acts as a capping layer, which minimizes the growth of SiO_x. The thickness of this layer can be critical for the performance of a solar cell since thick SiO_x leads to an increase in the contact resistivity that ultimately limits the photogenerated charge extraction. However, some SiO_x layers can also increase the minority carrier lifetime by reducing the amount of recombination defects at the surface, as some works have shown [24].

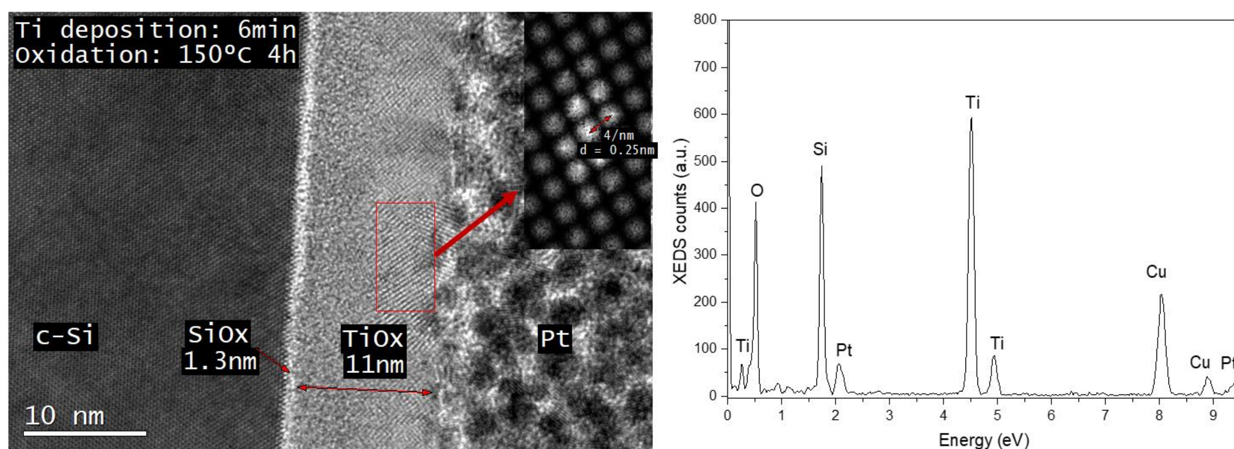

Figure 6-13 TEM image and XEDS spectrum for a TiO_x sample fabricated with a 150 ºC oxidation process during 4 h.

Finally, a TiO_x sample fabricated at 200 ºC and two hours was also observed by TEM. This is depicted in Figure 6-14. The TiO_x thickness for this sample is around 9 nm, similar to the thickness determined by XRR for this oxidation condition (~8.6 nm). Some crystalline structures appear on the surface like the previous sample (150 ºC 4 h). In this case, the interplanar distance is 0.19 nm. This could be related to the plane (211) of the TiO_x anatase, which has an interplanar distance of 0.16 nm. This plane appears in the GIXRD diffractogram for the 200ºC samples and becomes more intense as the oxidation duration process is increased. This time, the SiO_x thickness is ~ 2.2 nm, which, in comparison to the 150 ºC

samples, is thicker, but this is still in the thickness range for native SiO_x, which indicates that the oxidation process at 200 ºC does not severely oxidize the Si surface. This is congruent with the FTIR results, which do not show a relevant increase in the Si-O stretching peak at 1050 cm^{-1} with this oxidation condition (200 ºC, 2 h).

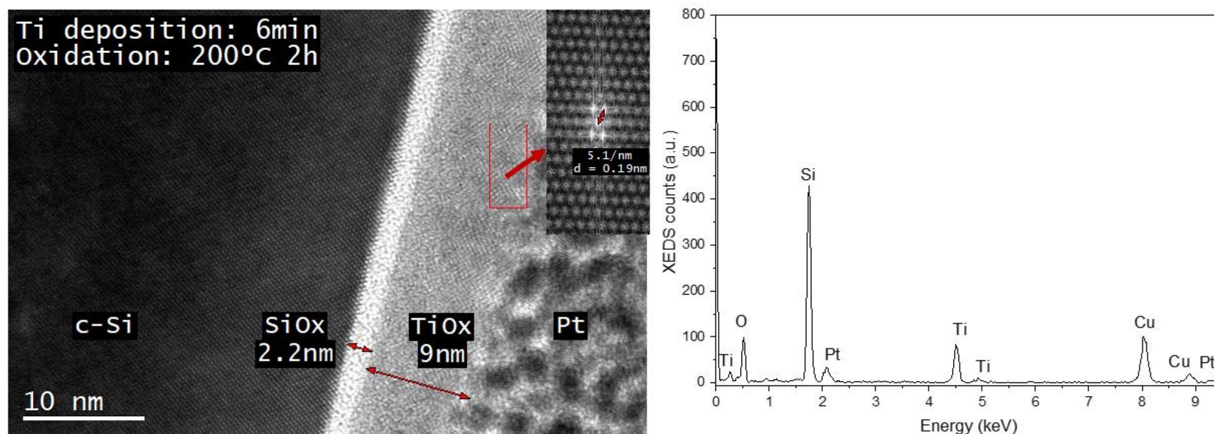

Figure 6-14 TEM image and XEDS spectrum for a TiOx sample fabricated with a 200 ºC oxidation process during 2 h.

The presence of crystalline structures only on the surface of TiO_x samples treated at 150 °C for 4 h and at 200 °C for 2 h can be attributed to a combination of factors, including surface interaction with reactive plasma species, thermal energy supplied, limited oxygen diffusion, and the formation of thermal gradients. These factors lead to crystallization at the surface of the material, while the bulk remains amorphous due to less favourable conditions for nucleation and crystalline growth. Some studies involving the crystallization of sputtering-deposited TiO_x via oxygen plasma have shown that lower temperatures, such as 150 ºC, are enough to crystallize the TiO_x sample if the oxygen pressure is high [25]. In this work, the oxygen inside the chamber was kept at 5% of the total gas flow.

6.4 Optical characterization of TiO_x fabricated by the two-step oxidation process

For all the TiO_x samples, ellipsometry measurements were done to obtain the thickness and refractive index of the layer. As discussed in the **Chapter III,** our ellipsometer uses a fixed incident angle (70º) and a single wavelength (632 nm) to measure the sample. This limits the refractive index to that specific wavelength. For the data fit, it was considered a simple two-layer structure: a Si substrate with fixed standard values (at 632.8 nm) of refractive index of 3.86 and extinction coefficient −0.0016 [26] and a

TiO_x layer (5 nm) with an initial refractive index of 2.41 and a fixed extinction coefficient of 0 at 632.8 nm [20]. The fitted parameters were the thickness and refractive index of this film.

These results are depicted in Figure 6-15 and show a difference between the oxidation temperature and process duration. In the case of the 150 ºC oxidation process, the refractive index varies from 1.9 with the shortest oxidation time duration (0.5 h) to 2.3 with the longest oxidation (4 h). In contrast, for the 200 ºC samples, the refractive index only varies from 2.23 to 2.3. There can be many reasons for this trend. For example, in suboxidized TiO_x, the density of the films can change due to oxygen vacancies and a higher quantity of Ti-Ti bonds; thus, the refractive index might change [27]. Generally, denser layers lead to higher values of refractive index. However, the XPS results showed that all the samples with oxidation durations longer than one hour show similar stoichiometry (~1.9), so the chemical composition should be comparable. Another reason for this can be the change in density due to the crystallization of the layers; some works have shown an increase in the density of TiO_x fabricated by ALD, going from 2.75 g/cm^3 (150 ºC) to 3.50 g/cm^3 (200 ºC) [20]. Besides, the refractive index of TiO_x can change depending on its structure. For instance, some studies have shown that the refractive index of TiO_x at 635 nm is between 2.10 and 2.45 for amorphous TiO_x, ~2.49 for anatase TiO_x [28], and ~2.8 for rutile TiO_x [29]. All of this is congruent with the TEM images for the 150 ºC 4 h (Figure 6-13) oxidation condition sample and 200 ºC 2 h (Figure 6-14) and the GIXRD results (Figure 6-10) which show the presence of crystalline structures of the surfaces than can be related to anatase TiO_x phase. Despite this, a more complex ellipsometer model which also includes a SiO_x film should be necessary to accurately obtain the refractive index of HPS-TiO_x. For solar cell applications such as ARC, the typically used TiO_x (anatase phase) has a refractive index of ~2.4 in the visible range due to its low absorption [30].

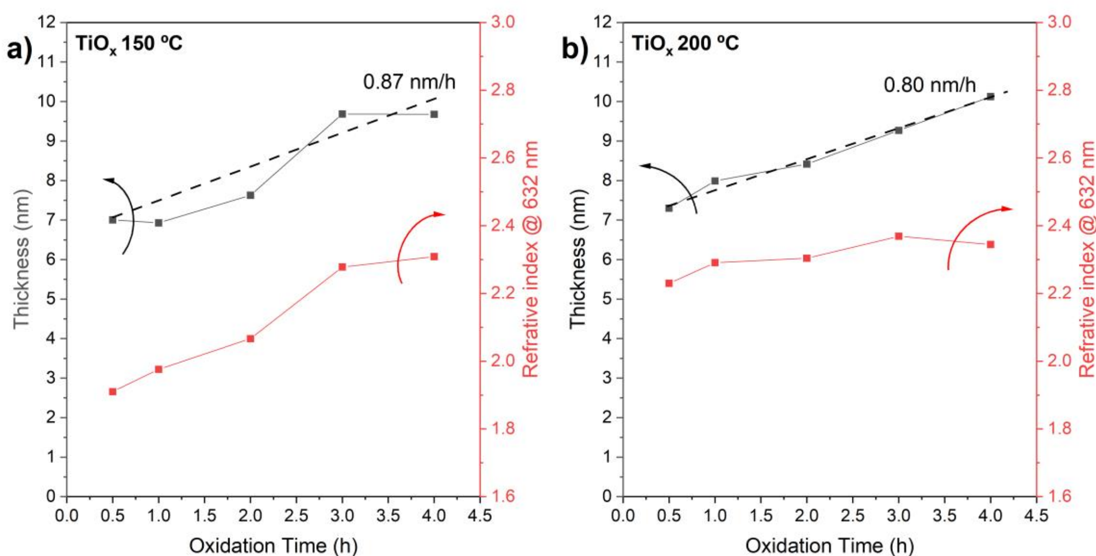

Figure 6-15 Refractive index at 632 nm and thickness obtained by ellipsometry for TiO_x samples fabricated at a) 150 ºC and b) 200 ºC for different oxidation times.

Another parameter obtained by ellipsometry was the thickness of the TiO_x films. As observed in XRR measurements and TEM images, the thickness of the layers increases as the oxidation time increases. The deposition rate during the oxidation step is ~0.8 nm/h for both temperature processes. In contrast, the XRR results give 0.58 nm/h and 1.33 nm/h for 150 ºC and 200 ºC, respectively. Considering the TEM images for the 150 ºC samples, the deposition rate is 1.26 nm/h. Meanwhile, for the 200 ºC samples, the thickness increases from 5 nm of Ti to 9 nm of TiO_x, giving a 2 nm/h deposition rate. The XRR and ellipsometry results can vary depending on the resolution method, and the TEM images of only three samples are not statistically enough to give an exact value due to possible variations in the sputtering process; despite this, the mean deposition rates are similar and are presented in the Table 6-1.

Table 6-1 Deposition rate of TiO_x during the oxidation step obtained by XRR, ellipsometry, and TEM images

Oxidation process temperature (ºC)	Deposition rate by XRR (nm/h)	Deposition rate by ellipsometry (nm/h)	Deposition rate by TEM images (nm/h)	Mean deposition rate (nm/h)
150	0.58	0.87	1.26	0.90
200	1.33	0.80	2	1.37

The transmittance and reflectance of TiO_x films on quartz substrates were measured with a PerkinElmer spectrophotometer that includes an integration sphere. The absorptance was also calculated considering that $100 = T + R + A$. These measurements are depicted in Figure 6-16. For the 150 ºC TiO_x samples, there is a clear tendency in the optical parameters as the oxidation time increases. Considering the values at 550 nm, the transmittance goes from 83% for the shortest oxidation time (0.5 h) to 89% for the longest (4 h), the reflectance stays at 9% for all the samples, and thus the absorptance varies from 8% for the 0.5 h TiO_x samples to 2 % for the 4 h sample. The reason for the reduction of absorptance as the oxidation time increases should be related to the proper oxidation of the Ti layer and the correct incorporation of oxygen into the layer and thus a reduction of free carrier absorption.

The XPS results shown in **section 4.3** could explain these optical results. For instance, for the 150 ºC samples, the deconvoluted O-1s peak which depicts the presence of oxygen vacancies (O_v), went from 27 % of the total O-1s peak (1 h) to 25 % (4 h). These O_v in TiO_x are known for introducing donor states that allow the transition from these states to the conduction band [31], thus increasing the absorption. Higher oxidation temperature leads to more stoichiometric films, which reduces the percentage of O_v, thus reducing the free carrier absorption. This is the observation for the 200 ºC

samples. In this case, the transmittance at 550 nm goes from 86 % to 89 %; the reflectance remains at ~9.5 % for all samples, and the absorption varies from 3.7 % to 1.2 %.

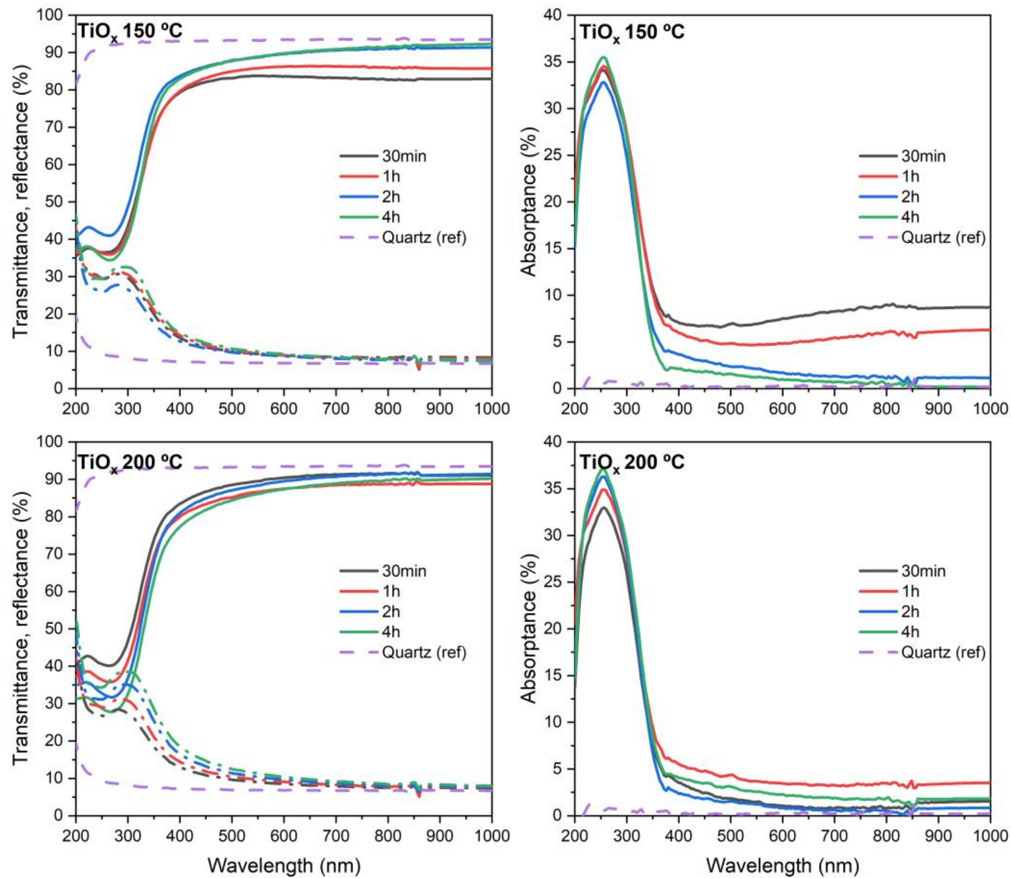

Figure 6-16 Transmittance, reflectance, and absorptance of TiO_x/Quartz samples fabricated with 150 ºC and 200 ºC oxidation temperatures. Quartz measurements are included as a reference.

To properly compare the absorption of the TiO_x samples, the weighted absorption to the AM1.5G spectrum was calculated using the following expression.

$$A_w = \frac{\int_{300}^{1000} A(\lambda) G_{AM1.5G}(\lambda)\, d\lambda}{\int_{300}^{1000} G_{AM1.5G}(\lambda)\, d\lambda} \qquad 6.1$$

Where A_W is the weighted absorption in the 300 – 1000 nm range, $A(\lambda)$ is the measured absorption, and $G_{AM1.5G}(\lambda)$ is the spectral irradiance of the AM1.5G standard solar spectrum. The weighted absorption is shown in Figure 6-17. For the 150 ºC samples, there is a reduction in the absorption as the oxidation time increases, going from 8% (0.5 h) to 1.2 % (4 h). In contrast, for 200 ºC samples, the weighted absorption remains similar for all the oxidation times at ~2.2 %. All of this corroborates the trend observed in the transmittance and XPS data, which indicates that for the 150 ºC oxidation process, it is necessary to have at least two hours to obtain similar results to 200 ºC samples.

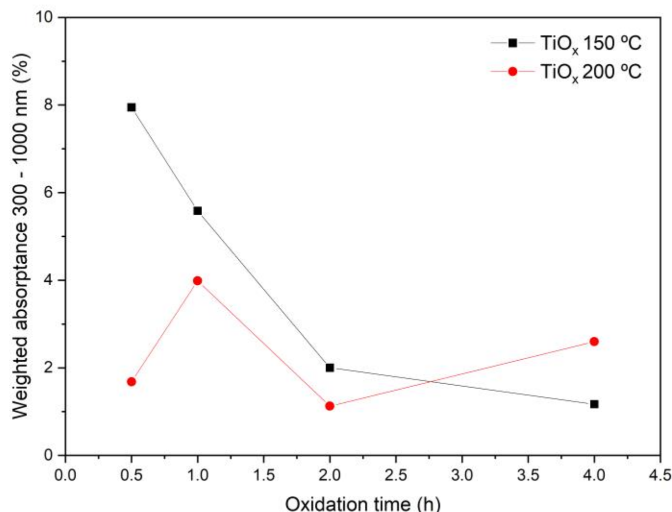

Figure 6-17 TiO_x/Quartz samples absorptance normalized to AM1.5G spectrum.

Strong peak absorption in the UV range has been observed in TiO_x films. This is related to the optical band gap of the TiO_x, which is typically 2.5 – 3.4, depending on the stoichiometry and the crystalline structure [10]. Some research has explored such absorption in UV-photocatalysis applications, such as air pollution cleaning and virus elimination [32]. For the TiO_x samples analyzed, their optical band gap was calculated through the Tauc's plot [33]. The Beer-Lambert expression was used to determine the absorption coefficient (α), which is generally used for thin films [34].

$$\alpha(\lambda) = \frac{1}{t}\ln\left(\frac{1}{T(\lambda)}\right) \qquad 6.2$$

Where t is the thickness of the film, $T(\lambda)$ are the transmittance values obtained by the spectrophotometer, and $\alpha(\lambda)$ is the absorption coefficient. With the values of absorption coefficients, the optical band gap was obtained by finding the x-intercept in the hv vs $(\alpha hv)^{1/2}$ graph (Tauc's plot). This is commonly used to determine the band gap of amorphous/polycrystalline semiconductors with indirect interband transitions [35]. The Tauc's plots and the obtained band gap values are depicted in Figure 6-18. The samples oxidized at 150 ºC show an increase in the band gap from 2.67 eV for the shortest (0.5 h) oxidation time to 2.92 eV for the longest (4 h). Meanwhile, the 200 ºC samples do not show a relevant change in the band gap, going from 2.83 eV to 2.90 eV.

The optical band gap for stoichiometric anatase TiO_2 (calculated by Tauc's plot) is reported to be ~3.2 eV [33]. Nevertheless, other works have shown that O_2 vacancies inside the TiO_2 can reduce the bandgap between 2.7 eV and 3.2 eV [36]. The estimated bandgap values are below the stoichiometric value for all the samples. For the 150 ºC, there is a trend as the bandgap increases with extended plasma oxidation time. This indicates that short oxidation time at this temperature leaves some oxygen vacancies, which reduces the band gap. In contrast, all the oxidation processes at 200 ºC lead to similar

bandgap values, which indicates a faster oxidation of the Ti films and thus a lower content of oxygen vacancies. According to the literature, the O_2 vacancies create donor levels, while the Ti vacancies create acceptor levels; these are responsible for modifying the value of the bandgap in TiO_x films [37].

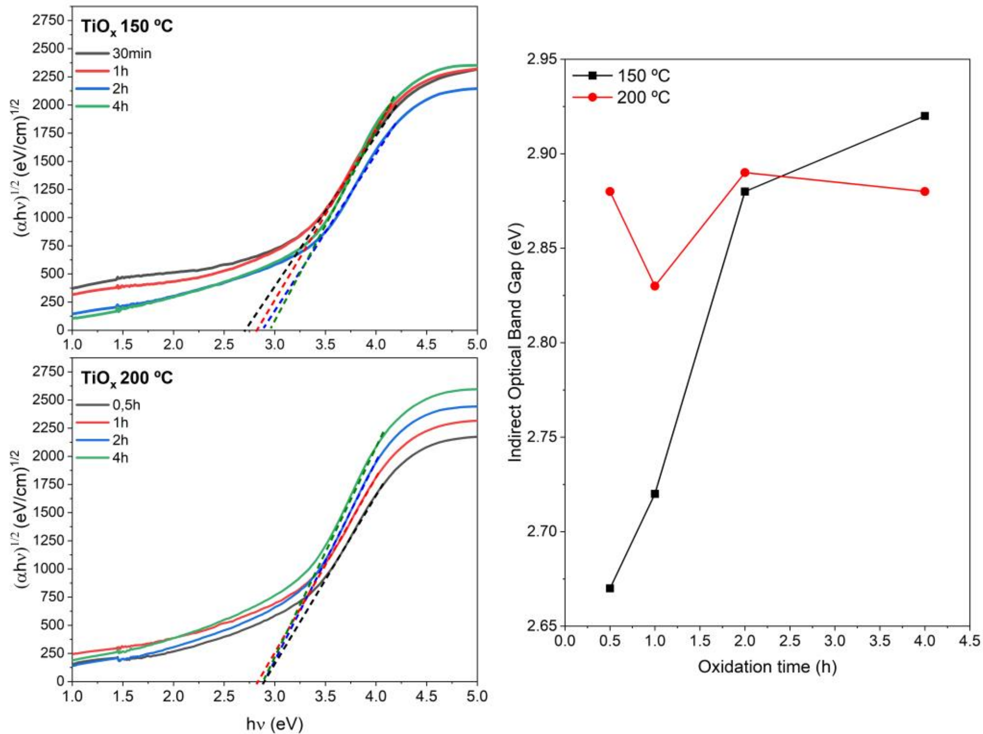

Figure 6-18 Tauc's plot for obtaining the indirect optical band gap of TiO_x samples fabricated at 150 ºC and 200 ºC

6.5 Minority carrier lifetime measurements of Si/TiO_x and $Si/SiO_x/TiO_x$ by quasi-steady state photoconductance

One of the most critical parameters for a material to work as a selective contact is that its deposition does not generate too many recombination centers at the interface. In fact, some materials can even increase the minority carrier lifetime (passivation). In the case of TiO_x deposited using HPS, the following structures (Figure 6-19) were fabricated to measure their lifetimes.

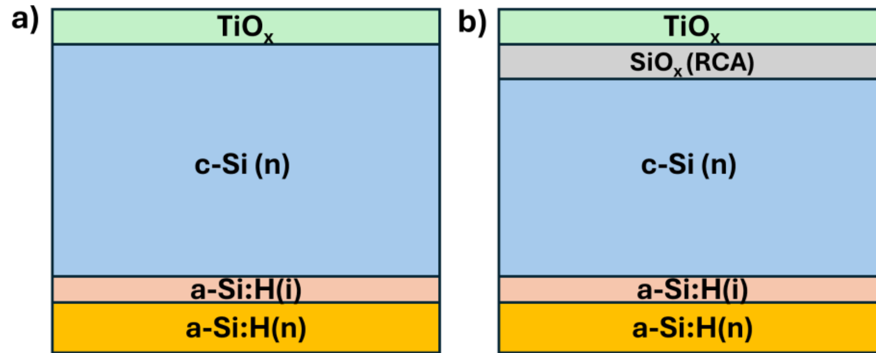

Figure 6-19 Structures to test the passivation of a) TiO_x film, and b) TiO_x/SiO_x stack. [1] is the SiO_x regrowth due to plasma oxidation

First, the rear side of the samples was deposited with the a-Si:H(i)/a-Si:H(n) stack by PECVD to ensure good passivation on the backside. The minority carrier lifetime (τ_{eff}) and implied open circuit voltage (i-V_{oc}) obtained for samples with such a stack on both sides is ~5 ms (at an injection level of 10^{15} cm^{-3}) and 715 mV (1 sun), respectively. The thickness of these layers is ~6 nm and ~18 nm for the a-Si:H(i) and a-Si:H(n) respectively. The deposition and optimization of such layers were done at *CIEMAT* by Dr. Ignacio Torres Almarza. A n-type float zone Si wafer with low resistivity (1 - 5 Ωcm) fabricated by *TOPSIL* was used as a substrate.

After the deposition of the a-Si:H(i)/a-Si:H(n) stack, the TiO_x films were deposited on the opposite side, considering the 150 ºC and 200 ºC oxidation temperatures and oxidation times of 0.5, 1, and 2 h. Six samples (3,5 x 3,5 cm^2) with different TiO_x layers were fabricated. However, those samples were cleaved from two 4’’ wafers where the a-Si:H(i)/a-Si:H(n) stack was deposited. Before the deposition of the TiO_x, such wafers were measured by the Sinton WCT-120 system using the QSSPC method as a reference. In this manner, the structure depicted in Figure 6-19 a) was finished. Such structures were fabricated because TiO_x, was expected to be the main limiting factor of the measured lifetimes and, therefore, indicate the quality of the c-Si(n)/TiO_x interface.

The results of τ_{eff} (10^{15} cm^{-3}) and i-V_{oc} (one sun) are shown in Figure 6-20. The mean τ_{eff} value for the wafers before the TiO_x deposition is ~40 µs, and the i-V_{oc} is 583 mV (references dashed lines). Such values are extremely low and indicate that the surface without any passivating layer acts as a strong recombination surface. Unfortunately, when the TiO_x layer is deposited, the τ_{eff} further decreases, reaching values ~8 µs for all the oxidation conditions. The i-V_{oc} also decreases to ~540 mV for all the samples. Rapid thermal annealing (RTA) process in forming gas (FG) atmosphere was performed to induce hydrogen diffusion into the defects and potentially increase the τ_{eff}. A process with 250 ºC for 10 min and 300 ºC for 5 min were tested. We did not study, RTA processes at higher temperature since it is well known that the a-Si:H starts to degrade at temperatures above 300 ºC [6].

For some of the samples, there was an increase in the τ_{eff} and $i\text{-}V_{oc}$. For instance, for the samples with TiO_x oxidized at 150 ºC 1 h, the lifetime increased from 7.8 to 15 µs while the $i\text{-}V_{oc}$ rose from 545 to 560 mV. Unfortunately, these results show that the TiO_x film deposited by HPS does not function as an effective passivation layer. This behavior of TiO_x has been reported even with deposition techniques known to create an optimal passivation layer, such as ALD. [38]

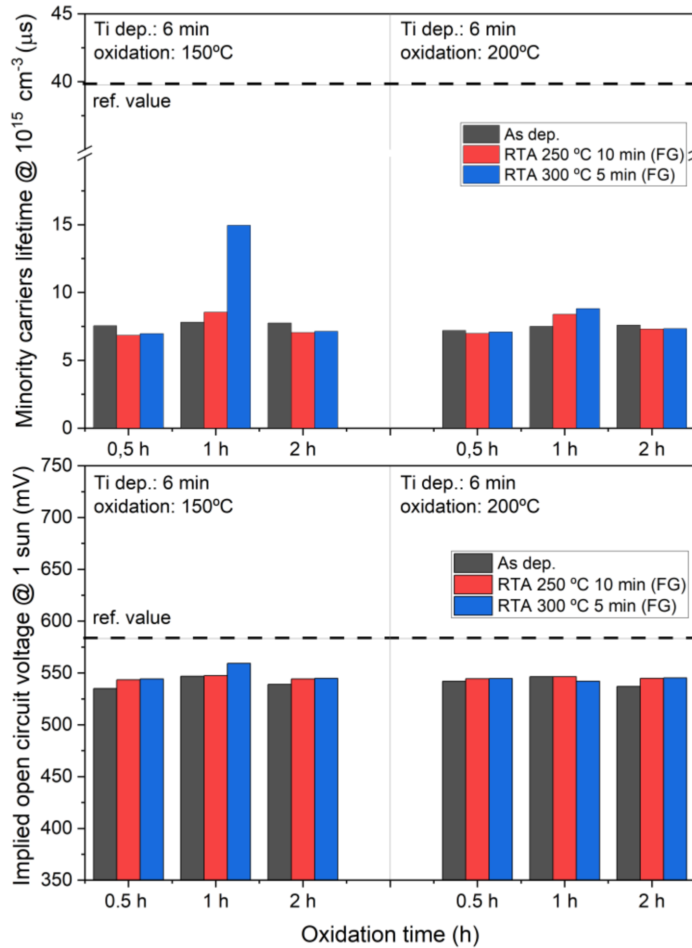

Figure 6-20 Minority carrier lifetime (10^{15} cm^{-3}) and implied open circuit voltage (1 sun) obtained by Sinton WCT-120 system for the a-Si:H(n)/a-Si:H(i)/c-Si (n)/TiO_x structure with Rapid Thermal Annealing (RTA) processes on forming gas

An alternative approach to enhance τ_{eff} and $i\text{-}V_{oc}$ involves increasing the RTA process temperature under a FG atmosphere. As the temperature rises, the hydrogen will diffuse further, and the probability of passivating the dangling bonds will be higher. As mentioned above, the a-Si:H layers tend to degrade at ~300 ºC; for that reason, another experiment was performed. In this, the TiO_x deposition process plus the RTA on forming gas was done before the deposition of the a-Si:H(n)/a-Si:H(i) to avoid the degradation. The TiO_x layer was deposited using the same oxidation condition: 200 ºC 1 h, only to compare the effect of different temperatures of RTA processes. The results of τ_{eff} and $i\text{-}V_{oc}$ are shown in Figure 6-21. The TiO_x + RTA processed samples exhibit a higher minority carrier lifetime compared

to the reference sample, i.e., only a-Si:H(n)/a-Si:H(i) on the rear side. The τ_{eff} at 10^{15} cm^{-3} increased from ~7 µs to 11 µs with the 450 ºC RTA process, while the $i\text{-}V_{oc}$ increased from a reference value of 532 mV to 545 mV. Although τ_{eff} and $i\text{-}V_{oc}$ increased relative to the reference, the values remained comparable to those observed in the initial experiment, where the RTA process was performed after the deposition of a-Si:H(n)/a-Si:H(i) stack. This indicates that the RTA process on the first experiment (300 ºC 5 min) is not degrading the a-Si:H(n)/a-Si:H(i) but that the RTA process with FG atmosphere has not been able to improve the c-Si(n)/TiO_x interface, even though the temperature increased to 450 ºC.

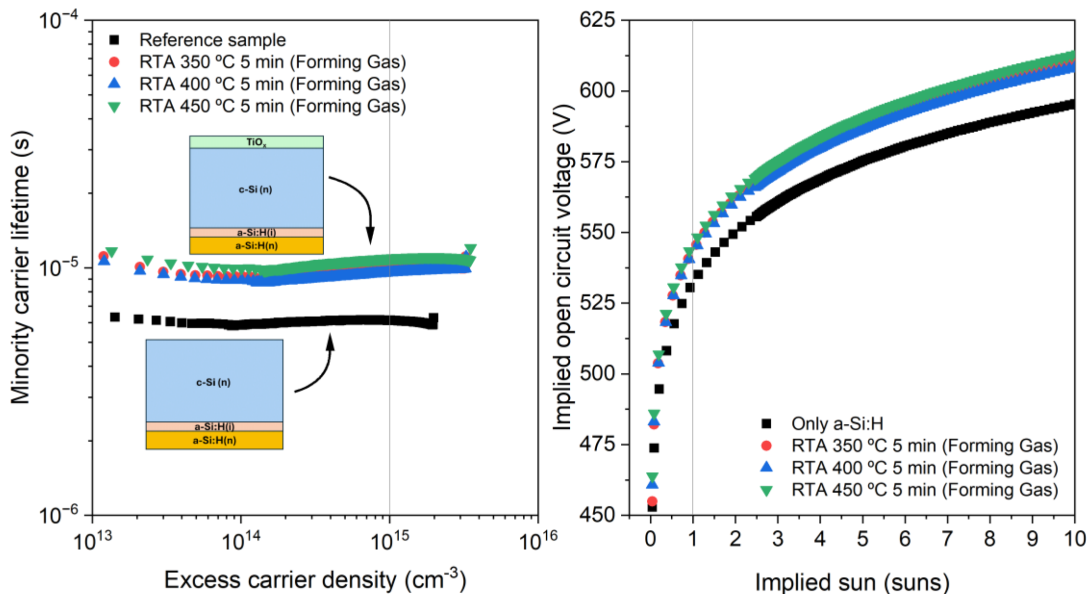

Figure 6-21 Minority carrier lifetime as a function of carrier density and iVoc as a function of injection level (implied sun) for TiO_x samples (200 ºC 1 h) with RTA in forming gas before the deposition of a-Si:H(n)/a-Si:H(i).

In most of the works where TiO_x shows relatively high lifetime values (> 500 µs), the analyzed film is not only TiO_x but SiO_x/TiO_x [39][40]. Some of them relied on the chemical process for the SiO_x growth, such as the SC2 solution (H_2O:HCl:H_2O_2) from the RCA cleaning process [41]. Thus, this strategy was also tested for the HPS TiO_x films. As the samples were always cleaned with the RCA process, all the samples should have a SiO_x (SC2) film; the only difference in this experiment was omission of the HF cleaning step before introducing the samples inside the HPS chamber. In that sense, the SiO_x (SC2)/TiO_x stack was created on the front side. Finally, on the rear side, the a-Si:H(n)/a-Si:H(i) stack was deposited by PECVD; the final structure is shown in Figure 6-19 b). For these samples, the Ti oxidation conditions were 150 ºC or 200 ºC for one or two hours.

The τ_{eff} and $i\text{-}V_{oc}$ results are depicted in Figure 6-22. As references, a a-Si:H(n)/a-Si:H(i)/c-Si(n)/SiO_x (SC2) sample and a-Si:H(n)/a-Si:H(i)/c-Si(n)/TiO_x (150 ºC 2h) sample were also fabricated. This time, along RTA process, hotplate annealing, i.e., without controlled atmosphere was also tested. The initial

observation is that the SiO_x only sample does not exhibit a significant improvement in τ_{eff} or $i\text{-}V_{oc}$. It remains at ~9 µs and 543 mV. The sample with only TiO_x (150 ºC 2 h oxidation), shows an increase in the τ_{eff} from 8 to 18 µs while the $i\text{-}V_{oc}$ increased from 543 to 552 mV. The TiO_x/SiO_x samples show low lifetime values of ~9 µs and $i\text{-}V_{oc}$ of ~545 mV. When the annealing processes are performed, all samples have increased τ_{eff} or $i\text{-}V_{oc}$. This trend becomes evident at temperatures starting from 250 ºC.

Additionally, it is observed that RTA in FG further increases the lifetime compared to hotplate annealing, which indicates that the hydrogen in the FG is passivating the dangling bonds. Among all the samples, the largest increase was observed with the TiO_x sample (150 ºC 2 h), which went from having lifetime values of 9.5 to 40.5 µs and 546 to 581 mV in the case of $i\text{-}V_{oc}$. This is an 120 % improvement in lifetime and 5.3% for the $i\text{-}V_{oc}$, compared to the sample with only TiO_x. These results show that the TiO_x/SiO_x is moderately better in terms of passivation as compared with only TiO_x and this can be due to a better quality of c-Si(n)/SiO_x/TiO_x interface.

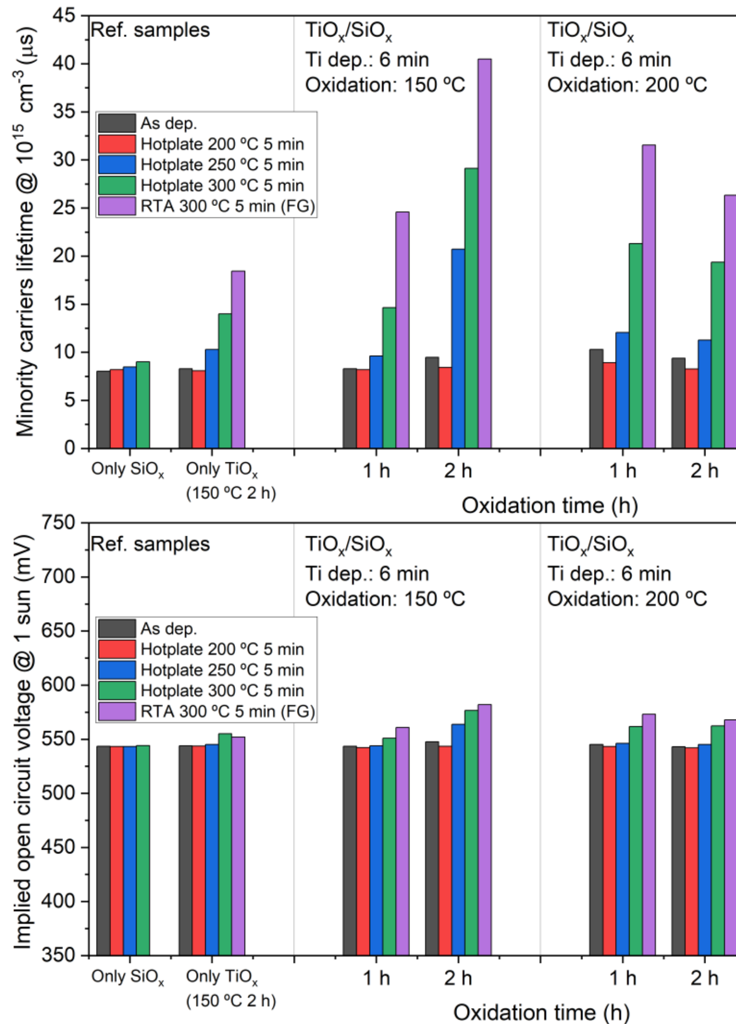

Figure 6-22 Minority carrier lifetime at 10^{15} cm^{-3} and iVoc at one sun for SiO_x/TiO_x samples.

6.6 Optimization of the rear contact for Cox & Strack samples for determining the contact resistivity of Si(n)/TiO_x junction.

A key parameter in evaluating the performance of a selective contact material for solar cells is the specific contact resistivity (ρ_c). As described in the **Chapter I**, this parameter quantifies the electrical resistance at the interface between the contact material and the Si substrate. Low ρc values are essential to ensure minimal series resistance and optimal fill factors [42], thus increasing the solar cell's efficiency.

During this work, the TiO_x/c-Si(n) contact resistivity was determined by the Cox & Strack (C&S) method. The structure fabricated for this purpose is depicted in Figure 6-23. To ensure the correct extraction of ρc, the first important step was to create a low-resistance ohmic contact on the rear side of the C&S device, which is shown in the figure as n^{++} layer. To obtain this contact, phosphorus was implanted with the following conditions: energy: 32 keV, dose: $4x10^{15}$ cm^{-3}. Subsequently, a thermal activation step was performed during 120 s RTA process in Ar at 1000 ºC. These conditions were selected to obtain a highly doped layer for narrowing the Schottky barrier between the metal and the semiconductor, increasing the probability of tunneling transport of the majority carriers (e^- in this case). This suppresses the typical rectifying behavior of metal-semiconductor contacts and ensures an ohmic contact.

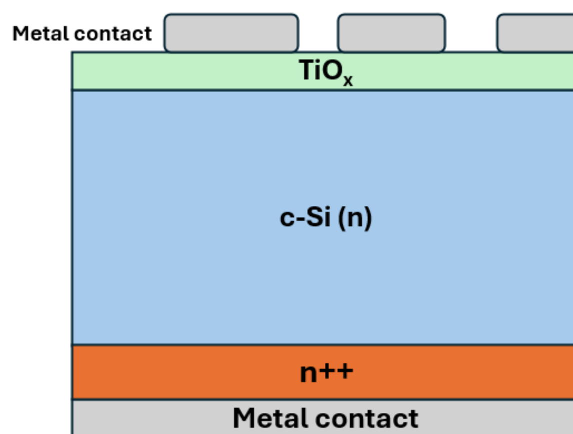

Figure 6-23 Cox & Strack structure that was fabricated to measure the contact resistivity between TiO_x and c-Si(n).

Figure 6-24 shows the simulation profile (Silvaco-Athena) for the implantation process. This shows the P profile in depth, as implanted and after the RTA process. The RTA process leads to a uniform concentration profile of ~ $2x10^{20}$ cm^{-3} up to ~200 nm, a concentration level in the range typically used for ohmic contacts in solar cells [43]. This uniformity is essential to achieve a low resistivity throughout the layer since gradients in the concentration might cause local electric fields opposing to the current

flow [44]. The simulation also extracts the sheet resistance of the P-doped layer and gives a value of 21.66 Ω/□. This value is within the range obtained by other groups for forming P-doped layers for Si solar cell applications [43]. Considering a rear contact of 1x1 cm^2, the contribution of the contact resistance to the total series resistance would be in the 10^{-9} Ω range, ensuring that the doped layer will not affect the extraction of TiO_x/c-Si(n) contact resistivity by the C&S method.

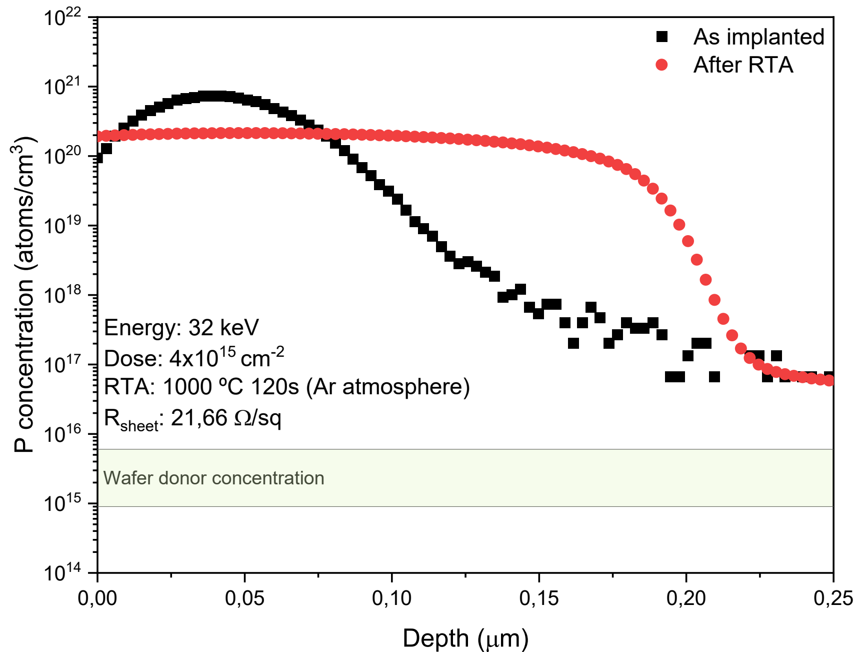

Figure 6-24 Phosphorus concentration profile for the implantation + RTA process used as rear contact in Cox & Strack samples simulated by Silvaco-Athena.

TLM devices were fabricated to decide which metal should be deposited on the Si(n^{++}) layer. To do this, the P-doped layer was deposited on c-Si(p) to create a depletion region and isolate the layer from the substrate. The implanted layer was etched by reactive ion etching (RIE) with SF_6 to form a mesa structure and avoid the lateral conduction; the final thickness for this step was ~2 µm. Finally, different metals were deposited on top to create the TLM pattern. Photolithography was used to define the patterns (see the fabrication chapter). Figure 6-25 a) shows an image of a final TLM sample where the TLM pattern on top of the mesa is depicted at the bottom of the image. Figure 6-25 b) presents the fitting of the total resistance as a function of the distance between TLM pads (length) of two samples from where the *ρc* is extracted.

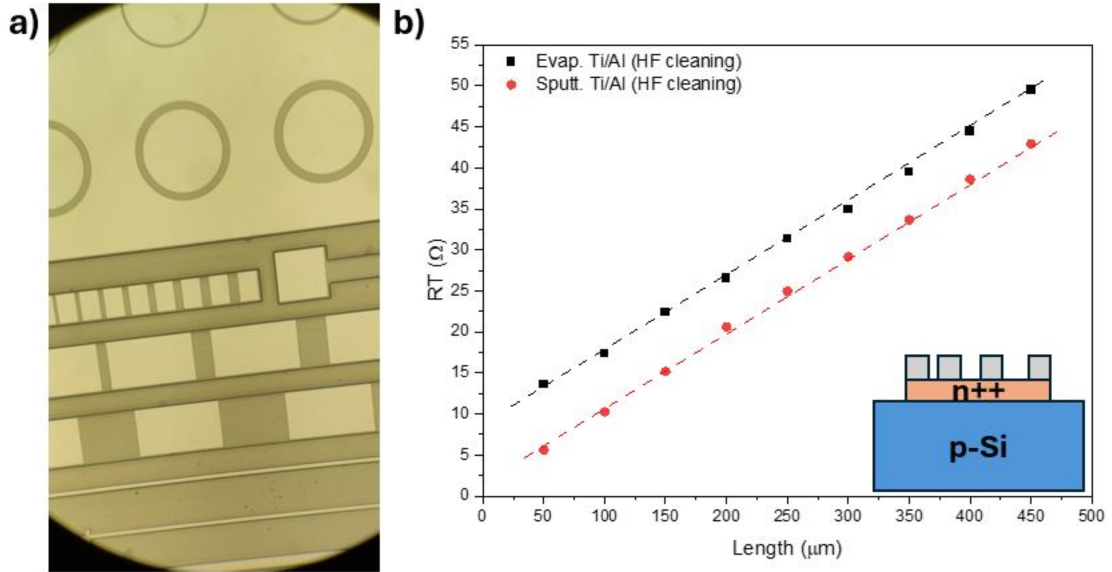

Figure 6-25 TLM samples to measure the contact resistivity of the P-implanted layer, a) microscopy image of TLM sample, b) TLM fitting to obtain the contact resistivity value for Si(n++)/Ti/Al samples.

The metals considered for contact with the Si(n^{++}) layer were Ti/Al (50/100 nm) and Al (150 nm). Two different deposition techniques were considered for both metal stacks, either evaporation or RF sputtering. Furthermore, before the metal deposition, some samples were cleaned with HF and rinsed with deionized water to remove the native SiO_x. The TLM results (contact resistivity and sheet resistance) are depicted in Figure 6-26. These results reveal that the metals deposited by conventional RF sputtering show lowest contact resistivity in comparison to evaporated metals. This is due to the higher adhesion of the sputtered metals in comparison to evaporated metals as it has been frequently cited [45]. The Ti/Al stack shows better ρc in comparison to the Al alone for all the cases. This can be due to the enhanced adhesion of the Ti with the Si(n^{++}) layer due to its interfacial scavenging properties [9] and also because Al acts as a p-type dopant in Si which can form a parasitic pn junction on the contact. Ti is commonly used as an adhesion layer for semiconductors substrates [46], and acts as a diffusion barrier, preventing Al atoms from diffusing into the Si(n^{++}) layer.

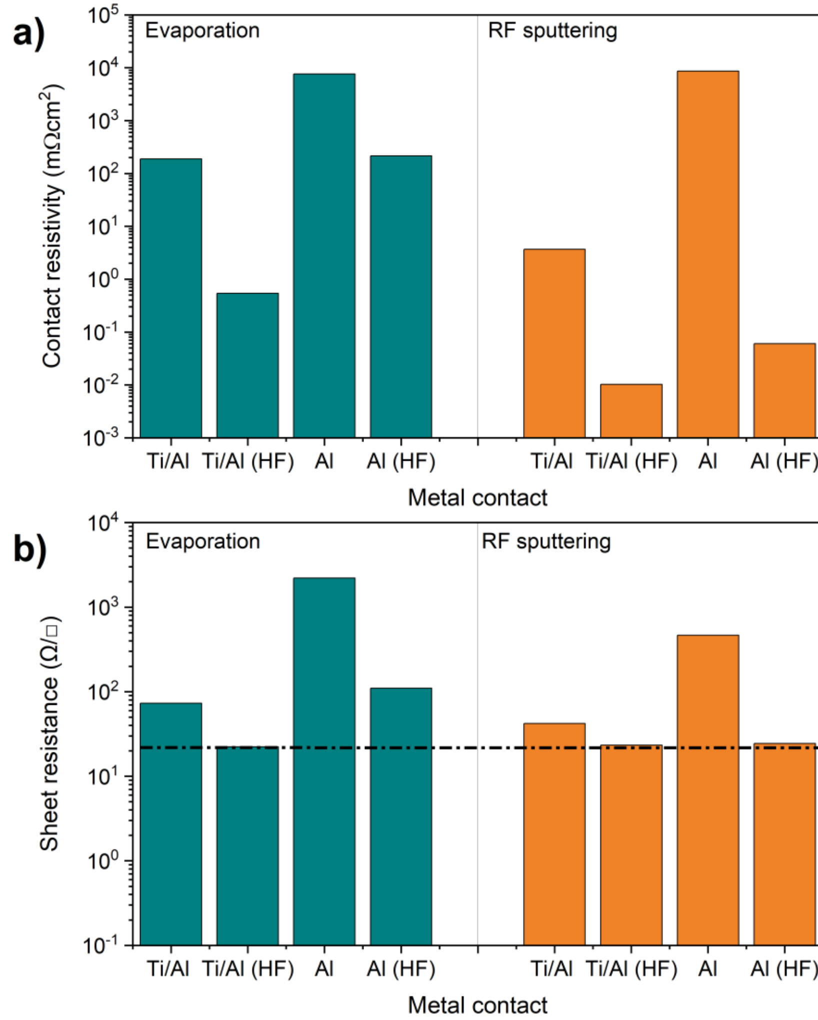

Figure 6-26 Contact resistivity and sheet resistance obtained by TLM for the Si(n)/metal samples as deposited. The dashed line in the sheet resistance graph represents the value obtained by Silvaco-Athena simulation.

Moreover, it has been observed that the HF cleaning process leads to lower ρ_c for both deposition techniques. This is an important finding during the development of this thesis as the rear contact with C&S samples is generally disregarded in literature. For instance, for the sputtered Ti/Al stack, the contact resistivity is reduced from 3.67 mΩcm^2 to 0.01 mΩcm^2 when the HF cleaning process is performed. This represents a reduction of more than two orders of magnitude. This shows that even with few nanometers, native SiO_x is acting as an insulation barrier, hindering the carrier transport between the metal and Si(n^{++}) layer, and can severely impact the contact resistivity determination.

Regarding the sheet resistance obtained by the TLM, for the Ti/Al with HF cleaning process, the value of ~23 Ω/□ is really similar to that obtained by the Silvaco-Athena simulation (21.66 Ω/□). In contrast, all the samples without the HF cleaning process show much higher values (up to 2200 Ω/□). As the Si(n^{++}) layer was implanted in the same process, its sheet resistance value should be the same for all the samples. The variations in extracted sheet resistance are most likely not due to real differences in

the Si(n^{++}) layer but are artifacts of poor current injection caused by native oxide, inhomogeneous metal interfaces, or high contact resistivity. It has been documented that TLM measurements can overestimate this value when the metal-semiconductor contact is poor [47].

Taking into account these results, it is concluded that the best metal to be deposited on the rear side for the C&S structure is Ti/Al with a HF cleaning before the deposition. The following section shows the extraction of the contact resistivity between TiO_x/Si(n), considering the fabrication of the rear contact under such conditions.

6.7 Extraction of contact resistivity of c-Si(n)/TiO_x and c-Si(n)/SiO_x/TiO_x by Cox & Strack method

For obtaining the contact resistivity between the Si(n) wafer and the TiO_x studied so far, C&S structures (Figure 6-23) were fabricated. The fabrication steps were the following:

1. Si wafer (4’’, float zone, double side polish, 1 – 5 Ωcm, <100>, 300 µm) fabricated by *TOPSIL* were implanted with phosphorus (32 keV, $4x10^{15}$ cm^{-3}), following a RTA process (1000 ºC 120 s) to create an ohmic contact on the rear side.

2. Using a diamond scribe, the wafer was cleaved into four pieces (3.5 x 3.5 cm^2).

3. The pieces were cleaned with the standard RCA cleaning process, and before the TiO_x deposition process, the samples were cleaned with diluted HF to remove the SiO_x grown by the RCA process.

4. Deposition of Ti layer with HPS on the front side of the samples. The deposition time varied from 2 to 6 min to obtain different Ti thickness between ~ 1.5 nm and 5 nm.

5. Plasma oxidation of the Ti layer at 150 ºC or 200 ºC with HPS. The oxidation time varied from 0.25 to 2 h. During steps 4 and 5, the HPS chamber was kept in vacuum.

6. Cox & Strack circular pads were patterned by negative photolithography. Before this process, the samples were cleaned with acetone and IPA to remove any organic contaminants. The exact photoresist products are mentioned in the fabrication technique chapter.

7. The rear side, i.e., the Si(n^{++}) layer, was cleaned using diluted HF. Extreme care was taken only to clean this side of the sample, leaving the TiO_x side untouched.

8. Deposition of the rear side metal contact. As previously mentioned, Ti/Al (50/100 nm) was used for all the samples.

9. Deposition of the front-side metal contact. In this case, a Ti/Ag (50/100 nm) stack was deposited.

10. Lift-off process to remove the remaining photoresist. For this purpose, *TechniStrip Micro D350* was used.

After these fabrication steps, the final C&S samples were measured using a Keithley 2636A SMU controlled by a LabVIEW program. With this, I-V curves of eight different circular pads were obtained. The diameters of the measured pads are between 400 and 180 µm. Figure 6-27 a) shows a picture of a final C&S device, with the circular pad group measured for all the samples encircled in red. These diameters were chosen to fulfill the conditions explained in the characterization chapter to clearly distinguish contact resistivity values (pad diameters must be less than two times the wafer thickness). Finally, the ρ_c value was obtained by fitting the total resistance minus the spreading resistance (R_T - R_s) vs the inverse of the area (*1/area*). As an example, Figure 6-27 b) depicts this fitting for two TiO_x samples fabricated with different oxidation conditions.

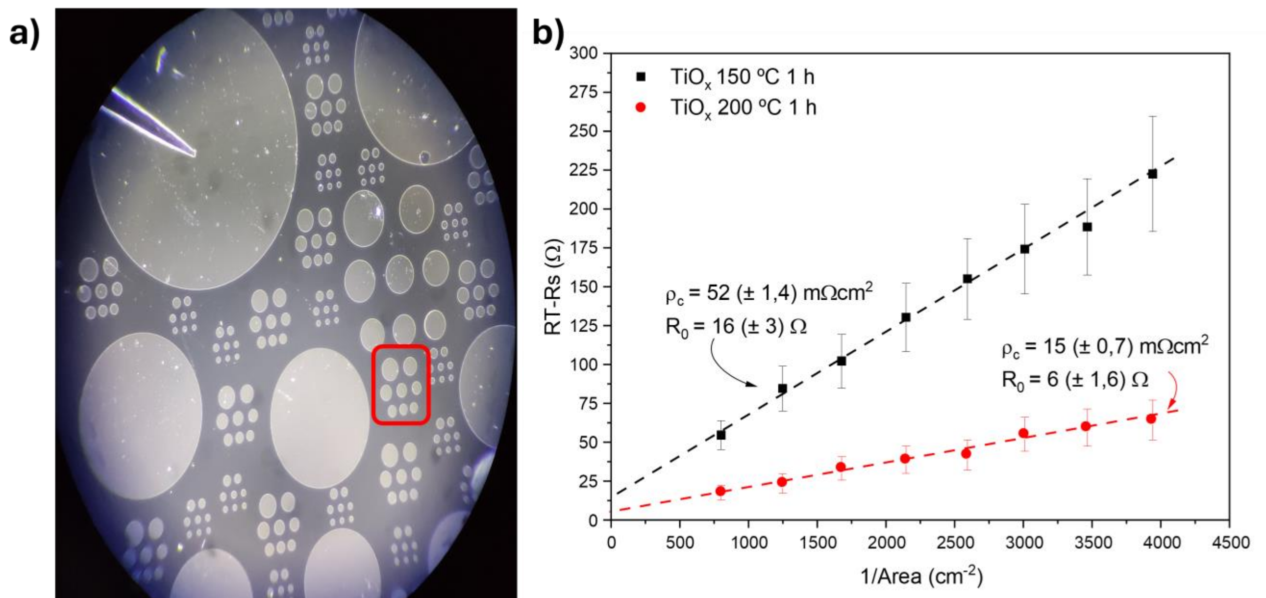

Figure 6-27 a) Microscope image of a C&S sample to extract the contact resistivity of c-Si(n)/TiO_x, the circular pad group measured for all samples is encircled in red. b) fitting examples using the C&S method for TiO_x samples fabricated at 150 ºC and 200 ºC.

Figure 6-28 shows the contact resistivity values for TiO_x samples fabricated at 150º C. For this experiment, three different Ti thickness were analyzed, i.e., Ti deposition for 2, 4 and 6 min. After the Ti deposition, the oxidation process was performed between 0.5 to 2 h. Also, a 0.25 h oxidation process

was tested but only for the 6 min (~ 5nm) Ti as capping layer. A clear tendency is observed; lower ρ_c values are obtained as the Ti capping layer becomes thicker (longer deposition time). For instance, for the samples with a Ti layer with only 2 min deposition shows very high contact resistivity, in the 10^4 - 10^6 mΩcm^2 range. The samples with 4 min of Ti deposition, the ρ_c is around 10^2 mΩcm^2 , and the samples with 6 min of Ti deposition shows really low ρ_c values between 13 and 63 mΩcm^2. The objective was to find the minimum Ti thickness that allows to protect the Si substrate from the plasma oxidation process. These results reveal that a minimum Ti thickness (6 min deposition, ~5 nm) is necessary to avoid the interaction between the O_2 plasma and the Si substrate.

All the samples with 6 min Ti deposition show similar ρ_c. However, considering the structural and optical characterization explained in previous sections, the samples with 1 h or 2 h oxidation process are considered the best options to integrate into a solar device. Finally, the c-Si(n)/SiO_x/TiO_x heterojunction was also studied. The SiO_x layer was grown by the RCA process and the objective was to improve the minority carrier lifetime as this layer is of better quality than native SiO_x. After this, the TiO_x was deposited at 150 ºC for 2 h oxidation conditions. The ρ_c obtained for this sample was ~10^5 mΩcm^2. Even when the thickness of SiO_x grown by RCA is expected around 1 nm, according to the literature [48], the stoichiometry is different to native SiO_x and can drastically change the probability of tunnelling [49]. This can explain why the ρ_c value increases from 18 to ~10^5 mΩcm^2.

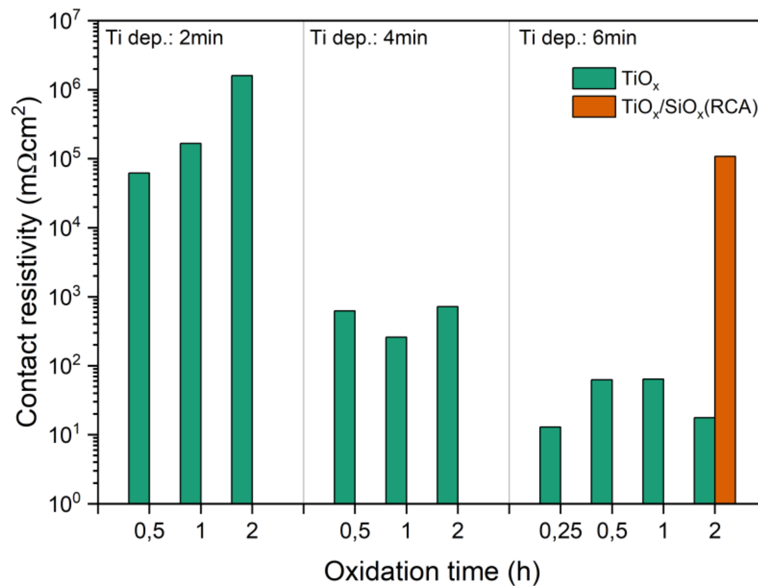

Figure 6-28 Contact resistivity of c-Si(n)/TiO_x and c-Si/SiO_x/TiO_x junctions. TiO_x samples fabricated with 150 ºC oxidation temperature and the Ti deposition time was varied (2 min, 4 min and 6 min.)

Figure 6-29 depicts the ρ_c for the samples oxidized at 200 ºC. Again, three different Ti deposition times were considered (2, 4, and 6 min). An identical trend to the 150 ºC samples was found, the ρ_c increases exponentially as the thickness of the Ti is reduced. For instance, for 2 min Ti deposition, the ρ_c is

between the 10^4 to 10^8 mΩcm^2 range and it increases with the duration of the oxidation process. For the 4 min Ti deposition, the ρ_c is around 10^4 mΩcm^2 for all the samples. And, for the 6 min Ti deposition samples, the contact resistivity is between 6 to 40 mΩcm^2 for oxidation times below 2 h. When this time is exceeded, the ρc increases again to 10^4 mΩcm^2. This behavior may be attributed to a thinner-than-expected initial Ti film or extended oxidation duration, allowing oxygen to diffuse through the TiO_x and initiate thicker oxidation of the underlying Si substrate.

Subsequently, using the conditions of the sample exhibiting the lowest contact resistivity (200 ºC 0.5 h), another sample was fabricated without removing the SiO_x grown during the RCA process. Similar to the sample fabricated at 150 °C, the ρ_c increases to a value around $4x10^4$ mΩcm^2. This indicates that the limiting factor in the case of the c-Si(n)/SiO_x/TiO_x structure is the SiO_x film since for both oxidation temperatures, the value of ρ_c is equally large. These results underscore that although RCA-grown SiO_x can enhance carrier lifetime, its thickness must be precisely controlled to prevent increased contact resistivity

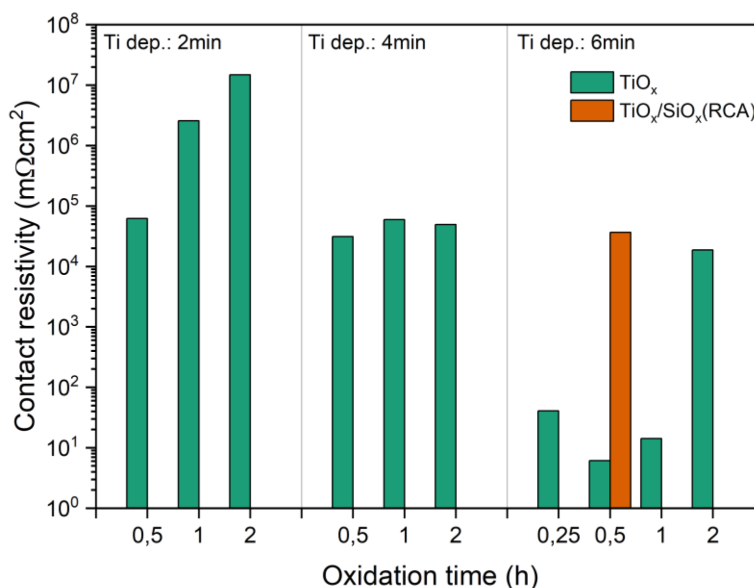

Figure 6-29 Contact resistivity of c-Si(n)/TiOx and c-Si/SiOx/TiOx junctions. TiOx samples fabricated with 200 ºC oxidation temperature and the Ti deposition time was varied (2 min, 4 min and 6 min).

6.8 Summary and conclusions

In this chapter, the fabrication and characterization of TiO_x thin films by low-temperature oxygen plasma oxidation via the high-pressure sputtering were systematically studied for their application as electron-selective contacts in silicon solar cells. The two-step process enabled the formation of

sub-stoichiometric TiO_x layers with controlled thicknesses (~6 - 11 nm) and tuneable optical and electronic properties, while maintaining compatibility with thermally sensitive materials such as a-Si:H. Structural and chemical analyses confirmed that low-temperature oxidation at 150 °C and 200 °C leads to mostly amorphous films, with partial surface crystallization into the anatase phase observed only after extended oxidation durations (150 ºC 4 h or 200 ºC 2 h). XPS revealed an O/Ti atomic ratio of ~1.9, indicating sub-stoichiometric TiO_x, with a decrease in oxygen vacancy content as oxidation progressed. The optical band gap, extracted from Tauc plots, increased with oxidation time from 2.67 eV to 2.92 eV at 150 °C and remained in the range of 2.83-2.90 eV at 200 °C, reflecting reduced sub-gap absorption due to improved Ti oxidation. While TiO_x alone did not provide effective surface passivation, resulting in minority carrier lifetimes (τ_{eff}) below 10 µs and implied open-circuit voltages ($i\text{-}V_{oc}$) around 540-550 mV, the inclusion of a thin RCA-grown SiO_x interlayer followed by forming gas annealing enhanced τ_{eff} up to ~40 µs and $i\text{-}V_{oc}$ up to ~581 mV. However, this interlayer significantly increased the contact resistivity (ρ_c), with values rising from ~18 mΩcm² (no interlayer) to ~10^4–10^5 mΩcm² due to the tunnelling barrier imposed by the SiO_x. The lowest ρ_c values (13 - 63 mΩ·cm²) were achieved with a minimum Ti thickness of ~5 nm and oxidation durations of 0.5 - 1 h, underlining the importance of controlling interfacial oxide layers. The optimized TiO_x layers demonstrate potential as electron-selective contacts, provided that the interface quality is carefully managed to balance passivation and conductivity requirements. However, the low lifetime values make it necessary to investigate other passivation layers to include TiO_x in a solar cell structure.

6.9 References

[1] M. Xue *et al.*, “Carrier-selective interlayer materials for silicon solar cell contacts,” *J. Appl. Phys.*, vol. 123, no. 14, 2018, doi: 10.1063/1.5020056.

[2] E. San Andrés, “Fabrication and characterization of high-k dielectrics for gate MIS devices applications,” Ph.D. dissertation, Universidad Complutense de Madrid, Madrid, Spain, 2004.

[3] D. M. Mattox, *Handbook of physical vapor deposition (PVD) processing*. Albuquerque, New Mexico: Noyes Publications, 1998.

[4] X. Yang, P. Zheng, Q. Bi, and K. Weber, “Silicon heterojunction solar cells with electron selective TiOx contact,” *Sol. Energy Mater. Sol. Cells*, vol. 150, pp. 32–38, Jun. 2016, doi: 10.1016/J.SOLMAT.2016.01.020.

[5] Y. L. Jeyachandran, B. Karunagaran, S. K. Narayandass, D. Mangalaraj, T. E. Jenkins, and P. J. Martin, “Properties of titanium thin films deposited by dc magnetron sputtering,” *Mater. Sci. Eng. A*, vol. 431, no. 1–2, pp. 277–284, 2006, doi: 10.1016/j.msea.2006.06.020.

[6] J. Shi, M. Boccard, and Z. Holman, “Plasma-initiated rehydrogenation of amorphous silicon to

increase the temperature processing window of silicon heterojunction solar cells," *Appl. Phys. Lett.*, vol. 109, no. 3, 2016, doi: 10.1063/1.4958831.

[7] Y. Ju, M. Wang, Y. Wang, S. Wang, and C. Fu, "Electrical properties of amorphous titanium oxide thin films for bolometric application," *Adv. Condens. Matter Phys.*, vol. 2013, no. 100, pp. 1–5, 2013, doi: 10.1155/2013/365475.

[8] J. E. Sansonetti and W. C. Martin, "Handbook of basic atomic spectroscopic data," *J. Phys. Chem. Ref. Data*, vol. 34, no. 4, pp. 1559–2259, 2005, doi: 10.1063/1.1800011.

[9] M. Á. Pampillón Arce, "Growth of High Permittivity Dielectrics by High Pressure Sputtering from Metallic Targets," PhD thesis, Universidad Complutense de Madrid, Madrid, Spain, 2016.

[10] M. Arif and C. Eisenmenger-Sittner, "In situ assessment of target poisoning evolution in magnetron sputtering," *Surf. Coatings Technol.*, vol. 324, pp. 345–352, 2017, doi: 10.1016/j.surfcoat.2017.05.047.

[11] B. Bharti, S. Kumar, H.-N. Lee, and R. Kumar, "Formation of oxygen vacancies and Ti 3+ state in TiO 2 thin film and enhanced optical properties by air plasma treatment," 2016, doi: 10.1038/srep32355.

[12] S. Guan, L. Hao, M. Murayama, X. Xie, S. Komuro, and X. Zhao, "Influence of anneal temperature in air on surface morphology and photoluminescence of ZnO thin films," *IOP Conf. Ser. Mater. Sci. Eng.*, vol. 522, no. 1, 2019, doi: 10.1088/1757-899X/522/1/012004.

[13] A. El Mragui, O. Zegaoui, I. Daou, and J. C. G. Esteves da Silva, "Preparation, characterization, and photocatalytic activity under UV and visible light of Co, Mn, and Ni mono-doped and (P,Mo) and (P,W) co-doped TiO2 nanoparticles: a comparative study," *Environ. Sci. Pollut. Res.*, vol. 28, no. 20, pp. 25130–25145, 2021, doi: 10.1007/s11356-019-04754-6.

[14] M. C. Marchi, S. A. Bilmes, C. T. M. M. Ribeiro, E. A. Ochoa, M. Kleinke, and F. Alvarez, "A comprehensive study of the influence of the stoichiometry on the physical properties of TiOx films prepared by ion beam deposition," *J. Appl. Phys.*, vol. 108, no. 6, p. 64912, 2010, doi: 10.1063/1.3481442.

[15] C. B. Samantaray, A. Dhar, D. Bhattacharya, M. L. Mukherjee, and S. K. Ray, "Effect of post-deposition annealing on microstructural and optical properties of barium strontium titanate thin films deposited by r.f. magnetron sputtering," *J. Mater. Sci. Mater. Electron.*, vol. 12, no. 7, pp. 365–370, 2001, doi: 10.1023/A:1011222312230.

[16] S. Duẽas *et al.*, "A comparative study of the electrical properties of TiO2 films grown by high-pressure reactive sputtering and atomic layer deposition," *Semicond. Sci. Technol.*, vol. 20, no. 10, pp. 1044–1051, 2005, doi: 10.1088/0268-1242/20/10/011.

[17] S. Hava, J. Ivri, and M. Auslender, "Wavenumber-modulated patterns of transmission through one- and two-dimensional gratings on a silicon substrate," *J. Opt. A Pure Appl. Opt.*, vol. 3, no. 6, 2001, doi: 10.1088/1464-4258/3/6/370.

[18] J. O. Carneiro *et al.*, "Compositional, optical and electrical characteristics of SiOx thin films

deposited by reactive pulsed DC magnetron sputtering," *Coatings*, vol. 9, no. 8, 2019, doi: 10.3390/coatings9080468.

[19] M. Schnabel, C. Weiss, P. Löper, P. R. Wilshaw, and S. Janz, "Self-assembled silicon nanocrystal arrays for photovoltaics," *Physica Status Solidi (A) Applications and Materials Science*, vol. 212, no. 8. pp. 1649–1661, 2015, doi: 10.1002/pssa.201431764.

[20] A. Jolivet *et al.*, "Structural, optical, and electrical properties of TiO2 thin films deposited by ALD: Impact of the substrate, the deposited thickness and the deposition temperature," *Appl. Surf. Sci.*, vol. 608, no. July 2022, 2023, doi: 10.1016/j.apsusc.2022.155214.

[21] E. Mello Ceresa and F. Garbassi, "AES/XPS thickness measurement of the native oxide on single crystal Si wafers," *Mater. Chem. Phys.*, vol. 9, pp. 371–385, 1983.

[22] D. Augustowski, P. Kwaśnicki, J. Dziedzic, and J. Rysz, "Magnetron sputtered electron blocking layer as an efficient method to improve dye-sensitized solar cell performance," *Energies*, vol. 13, no. 11, 2020, doi: 10.3390/en13112690.

[23] P. D. Ngo, "Energy Dispersive Spectroscopy," *Fail. Anal. Integr. Circuits*, pp. 205–215, 1999, doi: 10.1007/978-1-4615-4919-2_12.

[24] S. P. Muduli and P. Kale, "State-of-the-art passivation strategies of c-Si for photovoltaic applications: A review," *Mater. Sci. Semicond. Process.*, vol. 154, no. October 2022, p. 107202, 2023, doi: 10.1016/j.mssp.2022.107202.

[25] H. Ohsaki, Y. Shibayama, A. Nakajim, A. Kinbara, and T. Watanabe, "Plasma treatment for crystallization of amorphous thin films," *Thin Solid Films*, vol. 502, no. 1–2, pp. 63–66, 2006, doi: 10.1016/j.tsf.2005.07.244.

[26] C. Schinke *et al.*, "Uncertainty analysis for the coefficient of band-to-band absorption of crystalline silicon," *AIP Adv.*, vol. 5, no. 6, pp. 1–22, 2015, doi: 10.1063/1.4923379.

[27] F. T. Geldasa and F. B. Dejene, "Effects of S Doping and Oxygen Vacancy on the Physical Properties of Rutile TiO2 for Photocatalysis Applications Based on Density Functional Theory Study," *Materials (Basel).*, vol. 18, no. 8, 2025, doi: 10.3390/ma18081688.

[28] J. D. B. Bradley *et al.*, "Submicrometer-wide amorphous and polycrystalline anatase TiO_2 waveguides for microphotonic devices," *Opt. Express*, vol. 20, no. 21, p. 23821, 2012, doi: 10.1364/oe.20.023821.

[29] B. Agnarsson *et al.*, "Rutile TiO2 thin films grown by reactive high power impulse magnetron sputtering," *Thin Solid Films*, vol. 545, pp. 445–450, 2013, doi: 10.1016/j.tsf.2013.07.058.

[30] B. Liao, B. Hoex, A. G. Aberle, D. Chi, and C. S. Bhatia, "Excellent c-Si surface passivation by low- Temperature atomic layer deposited titanium oxide," *Appl. Phys. Lett.*, vol. 104, no. 25, p. 253903, Jun. 2014, doi: 10.1063/1.4885096/940823.

[31] A. El Mesoudy *et al.*, "Band gap narrowing induced by oxygen vacancies in reactively sputtered TiO2 thin films," *Thin Solid Films*, vol. 769, no. February, p. 139737, 2023, doi: 10.1016/j.tsf.2023.139737.

[32] S. Prucnal *et al.*, “TiO2 Phase Engineering by Millisecond Range Annealing for Highly Efficient Photocatalysis,” *J. Phys. Chem. C*, vol. 127, no. 26, pp. 12686–12694, Jul. 2023, doi: 10.1021/ACS.JPCC.3C01165.

[33] Y. Doubi *et al.*, “Experimental study of properties of TiO2 thin films deposited by spray pyrolysis for future sensory applications,” *Appl. Phys. A Mater. Sci. Process.*, vol. 127, no. 6, pp. 1–11, 2021, doi: 10.1007/s00339-021-04629-z.

[34] S. Fernández, I. Torres, and J. J. Gandía, “Sputtered Ultrathin TiO2 as Electron Transport Layer in Silicon Heterojunction Solar Cell Technology,” *Nanomaterials*, vol. 12, no. 14, p. 2441, Jul. 2022, doi: 10.3390/nano12142441.

[35] J. Klein, L. Kampermann, B. Mockenhaupt, M. Behrens, J. Strunk, and G. Bacher, “Limitations of the Tauc Plot Method,” *Adv. Funct. Mater.*, vol. 33, no. 47, pp. 1–19, 2023, doi: 10.1002/adfm.202304523.

[36] B. Zhou, X. Jiang, Z. Liu, R. Shen, and A. V. Rogachev, “Preparation and characterization of TiO2 thin film by thermal oxidation of sputtered Ti film,” *Mater. Sci. Semicond. Process.*, vol. 16, no. 2, pp. 513–519, Apr. 2013, doi: 10.1016/j.mssp.2012.05.001.

[37] R. V. Nair, P. K. Gayathri, V. S. Gummaluri, P. M. G. Nambissan, and C. Vijayan, “Large bandgap narrowing in rutile TiO2 aimed towards visible light applications and its correlation with vacancy-type defects history and transformation,” *J. Phys. D. Appl. Phys.*, vol. 51, no. 4, 2018, doi: 10.1088/1361-6463/aaa187.

[38] I. S. Yu, Y. W. Wang, H. E. Cheng, Z. P. Yang, and C. T. Lin, “Surface passivation and antireflection behavior of ALD TiO2 on n-type silicon for solar cells,” *Int. J. Photoenergy*, vol. 2013, 2013, doi: 10.1155/2013/431614.

[39] K. Gotoh, H. Miura, A. Shimizu, Y. Kurokawa, and N. Usami, “Passivation mechanism of the high-performance titanium oxide carrier-selective contacts on crystalline silicon studied by spectroscopic ellipsometry,” *Jpn. J. Appl. Phys.*, vol. 60, no. SB, 2021, doi: 10.35848/1347-4065/abd6dd.

[40] V. Titova, B. Veith-Wolf, D. Startsev, and J. Schmidt, “Effective passivation of crystalline silicon surfaces by ultrathin atomic-layer-deposited TiOx layers,” *Energy Procedia*, vol. 124, pp. 441–447, Sep. 2017, doi: 10.1016/J.EGYPRO.2017.09.272.

[41] S. Miyagawa, K. Gotoh, K. Kutsukake, Y. Kurokawa, and N. Usami, “Application of Bayesian optimization for high-performance TiOx/SiOy/c-Si passivating contact,” *Sol. Energy Mater. Sol. Cells*, vol. 230, no. June, p. 111251, 2021, doi: 10.1016/j.solmat.2021.111251.

[42] A. Onno, C. Chen, P. Koswatta, M. Boccard, and Z. C. Holman, “Passivation, conductivity, and selectivity in solar cell contacts: Concepts and simulations based on a unified partial-resistances framework,” *J. Appl. Phys.*, vol. 126, no. 18, 2019, doi: 10.1063/1.5117201.

[43] H. Boo *et al.*, “Effect of high-temperature annealing on ion-implanted silicon solar cells,” *Int. J. Photoenergy*, vol. 2012, no. March 2016, 2012, doi: 10.1155/2012/921908.

[44] N. Shibata *et al.*, “Imaging of built-in electric field at a p-n junction by scanning transmission electron microscopy,” *Sci. Rep.*, vol. 5, pp. 2–4, 2015, doi: 10.1038/srep10040.

[45] W. Li, X. Yan, A. G. Aberle, and S. Venkataraj, “Adhesion Improvement and Characterization of Magnetron Sputter Deposited Bilayer Molybdenum Thin Films for Rear Contact Application in CIGS Solar Cells,” *Int. J. Photoenergy*, vol. 2016, no. 4, 2016, doi: 10.1155/2016/2124087.

[46] M. Todeschini, A. Bastos Da Silva Fanta, F. Jensen, J. B. Wagner, and A. Han, “Influence of Ti and Cr Adhesion Layers on Ultrathin Au Films,” *ACS Appl. Mater. Interfaces*, vol. 9, no. 42, pp. 37374–37385, 2017, doi: 10.1021/acsami.7b10136.

[47] T. Fiducia and Z. Holman, “Correcting Overestimates in TLM-Based Contact Resistivity Measurements,” *Conf. Rec. IEEE Photovolt. Spec. Conf.*, pp. 817–819, 2024, doi: 10.1109/PVSC57443.2024.10749054.

[48] H. Yousuf *et al.*, “Tunnel Oxide Deposition Techniques and Their Parametric Influence on Nano-Scaled SiOx Layer of TOPCon Solar Cell: A Review,” *Energies*, vol. 15, no. 15, 2022, doi: 10.3390/en15155753.

[49] M. Köhler, M. Pomaska, F. Lentz, F. Finger, U. Rau, and K. Ding, “Wet-Chemical Preparation of Silicon Tunnel Oxides for Transparent Passivated Contacts in Crystalline Silicon Solar Cells,” *ACS Appl. Mater. Interfaces*, vol. 10, no. 17, pp. 14259–14263, 2018, doi: 10.1021/acsami.8b02002.

CHAPTER VII: TiO_X/A-SI:H(I) AS ELECTRON SELECTIVE CONTACT FOR SI HETEROJUNCTION SOLAR CELL

This chapter presents a comprehensive study on the structural, electrical, and passivation properties of TiO_x/a-Si:H(i) stacks where the TiO_x layer is fabricated by high-pressure sputtering (HPS) and low-temperature thermal oxidation. The contact resistivity (ρ_c), minority carrier lifetime (τ_{eff}), and implied open-circuit voltage (i-V_{oc}) was measured with various TiO_x layers fabricated with different temperature and duration of the oxidation step. The inclusion of the a-Si:H(i) layer between the TiO_x and the n-type crystalline silicon aims to enhance surface passivation by reducing the density of dangling bonds. As discussed in the previous chapter, the deposition of TiO_x alone was insufficient to achieve adequate passivation. Importantly, even with the addition of a-Si:H(i) to improve interface quality, the approach remains consistent with the objective of fabricating doping-free solar cells.

Initially, the performance of stacks incorporating (~10 nm) of a-Si:H(i) was investigated through Cox & Strack contact resistivity measurements and transient photoconductance decay (TPCD) lifetime techniques. Subsequent thermal treatments, including conventional hotplate annealing and Flash Lamp Annealing (FLA), were employed to evaluate their impact on the interfacial properties and carrier transport behavior. Additionally, transmission electron microscopy (TEM) was used to correlate structural features with electrical performance. Finally, the viability of using TiO_x/a-Si:H(i) as a rear electron selective contact (ESC) was tested in complete heterojunction solar cell devices. Moreover, a direct comparison with a reference HIT cell was carried out.

7.1 Minority carrier lifetime and contact resistivity measurements of TiO_x/a-Si:H(i) (~ 10 nm)

The first approach to be explored was the deposition of ~10 nm of a-Si:H(i) in between the Si substrate and the TiO_x layer. For the Cox & Strack structures, the following steps were followed:

1. A 4'' n-type Si wafer (FZ, double side polish, <100>, 1-5 Ωcm, 300 μm) from *TOPSIL* was used as a substrate.

2. On the rear side, phosphorus was implanted following the same conditions mentioned in the previous chapter (32 keV, $4x10^{15}$ cm^{-3} + 1000 ºC 120 s RTA in Ar).

3. On the front side, the a-Si:H(i) was deposited by PECVD. It is worth mentioning that the a-Si:H(i) is a stack of two different layers, the first one to avoid the Si epitaxy, and another for the proper passivation of the surface. The combined thickness of both layers is approximately 10 nm. For the sake of simplicity such layers will be referred only as a-Si:H(i).

4. The wafer was cleaved in 1x1 cm^2 samples and the TiO_x layer was deposited on top of the a-Si:H(i). The TiO_x layer was deposited by HPS using the 2-steps oxidation process explained in the previous chapter. The Ti layer was deposited for 6 min, which gives a thickness of approximately 5 nm. Again, two temperatures were explored for the oxidation step (150 ºC and 200 ºC) and the oxidation duration was either 0.5, 1 or 2 h.

5. Finally, metal electrodes were evaporated on the front side (Ti/Ag - 50/100 nm) and on the rear side (Ti/Al – 50/100 nm). For the rear side electrode, the Si surface was carefully cleaned with HF before the deposition of the Ti/Al stack.

Figure 7-1 depicts the contact resistivity (ρ_c) of Ag/Ti/TiO_x/a-Si:H(i)/c-Si(n) stack obtained by the Cox & Stack method using circle contacts with diameters between 400 and 180 µm. As a reference, a sample without TiO_x was also measured to obtain the contact resistivity of Ag/Ti/a-Si:H(i)/c-Si(n) stack. This sample exhibited a ρ_c of 574 $m\Omega cm^2$, a value which is similar to those obtained by others [1].

Regarding the samples with TiO_x a trend is observed with the temperature and the oxidation time duration. For the samples oxidized at 150 ºC, the ρ_c increases from 271 $m\Omega cm^2$ (0.5 h) to 986 $m\Omega cm^2$ (2 h). In contrast, the 200 ºC processed samples show extremely high ρ_c values, going from 63 Ωcm^2 for an oxidation duration of 0.5 h to 62 $k\Omega cm^2$ for 2 h oxidation process. These results show a similar trend to those observed in the previous chapter, as the temperature increases, the contact resistivity also increases most probably due to the oxidation of the underlying layer, in this case the a-Si:H. Extended oxidation process exacerbates even further this trend. In the case of the samples oxidized at 150 ºC, the temperature seems to be not enough to produce oxygen diffusion that could react with the a-Si:H(i).

In the work of M. Leilaeioun et al, the a-Si:H(doped) oxidation effect on the contact resistivity has been investigated increasing the O_2 partial pressure during TCO sputtering deposition [2]. This study shows that increasing the O_2 partial pressure from 0.1 mTorr to 0.9 mTorr leads to an increase in the ρ_c of more than 1 order of magnitude, most likely due to the a-Si:H oxidation. Our results show a similar trend for the samples oxidized at 200 ºC as there is a ρ_c increase of two of more orders of magnitude in comparison to the only a-Si:H(i) sample. This can be due to the partial oxidation of the underlying a-Si:H(i) film due to the extended oxidation process. Interestingly, the 150 ºC did not show a relevant increase in the ρ_c which could be explained by the limited oxygen diffusion that takes place at that temperature.

Another possibility for the increase in the contact resistivity is the thickening of the TiO_x layer as the oxidation process at 200 ºC is extended. A thicker TiO_x might cause a reduction in the extraction of photogenerated carrier due to its high resistivity and thus the measured current would be lower. The increase in the contact resistivity as a function of TiO_x thickness has been shown in other works [3].

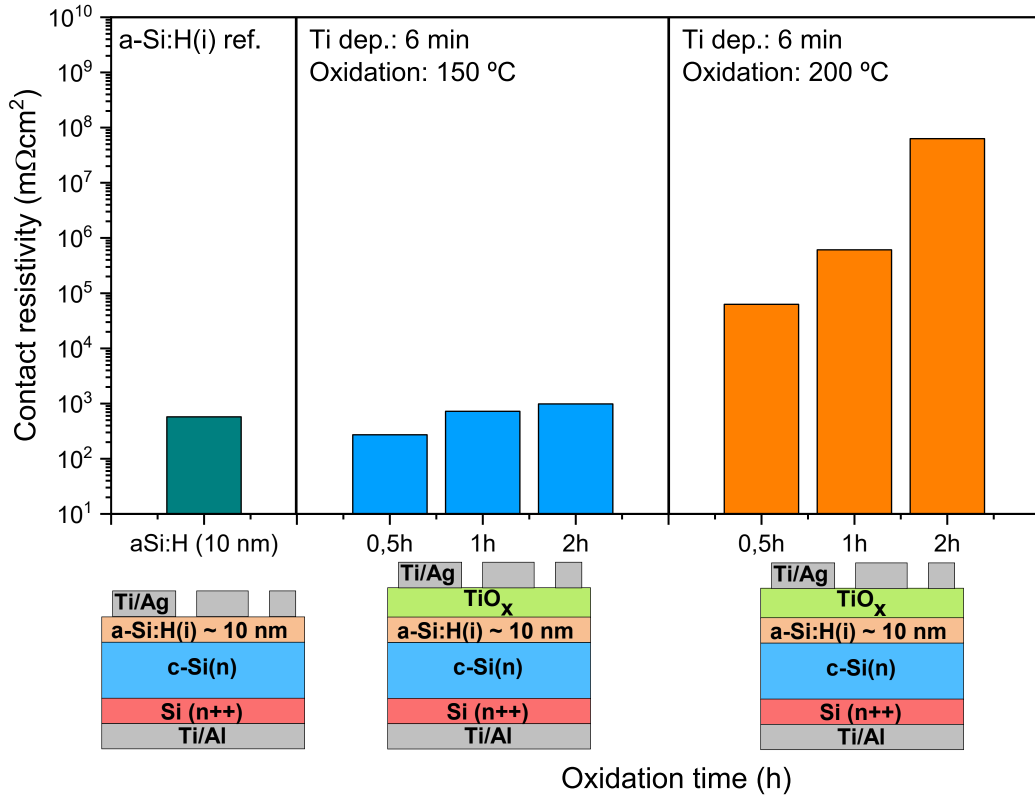

Figure 7-1 Contact resistivity of Ti/Ag/TiOx/a-Si:H (~10 nm) stack considering a Ti layer deposited for 6 min by HPS with different oxidations condition.

The minority carrier lifetime of the TiO_x/a-Si:H(i) on c-S(n) substrate was also measured using the transient method with the Sinton WCT-120 system. For this, a-Si:H(n)/a-Si:H(i)/c-Si(n)/a-Si:H(i)/TiO_x structures were fabricated. In this case, on the rear side an intrinsic and a doped a-Si:H was deposited to ensure an optimal passivation through chemical and electrical passivation respectively. The thickness for such layers is ~10 nm for the a-Si:H(i) and ~10 nm for the a-Si:H(n). On the front side, i.e., the TiO_x side, the same a-Si:H(i) layer as the Cox & Strack sample was deposited.

Figure 7-2 depicts the minority carrier lifetime (τ_{eff}) at 10^{15} cm^{-3} and the implied open circuit voltage (i-V_{oc}) at 1 sun of samples with different oxidation conditions. As a reference value, the original wafer was measured before the cleavage and the subsequent TiO_x deposition. The wafer exhibits a τ_{eff} of 9.27 ms and i-V_{oc} of 737 mV. After the deposition of the TiO_x by HPS, the τ_{eff} decreases to values between 283 and 636 µs depending on the oxidation process. Subsequent annealing steps on hotplate increase these values to the range of 1 to 1.6 ms. This increment seems to reach a plateau when the

first annealing process at 200 ºC for 5 min is performed. Regarding the i-V_{oc}, the samples show a similar trend as with τ_{eff}, when the TiO_x is deposited the i-V_{oc} decreases to a range of 640 to 702 mV (depending on the oxidation process). The hotplate annealing steps also help to recover to some extent the original value, reaching values between 680 and 700 mV.

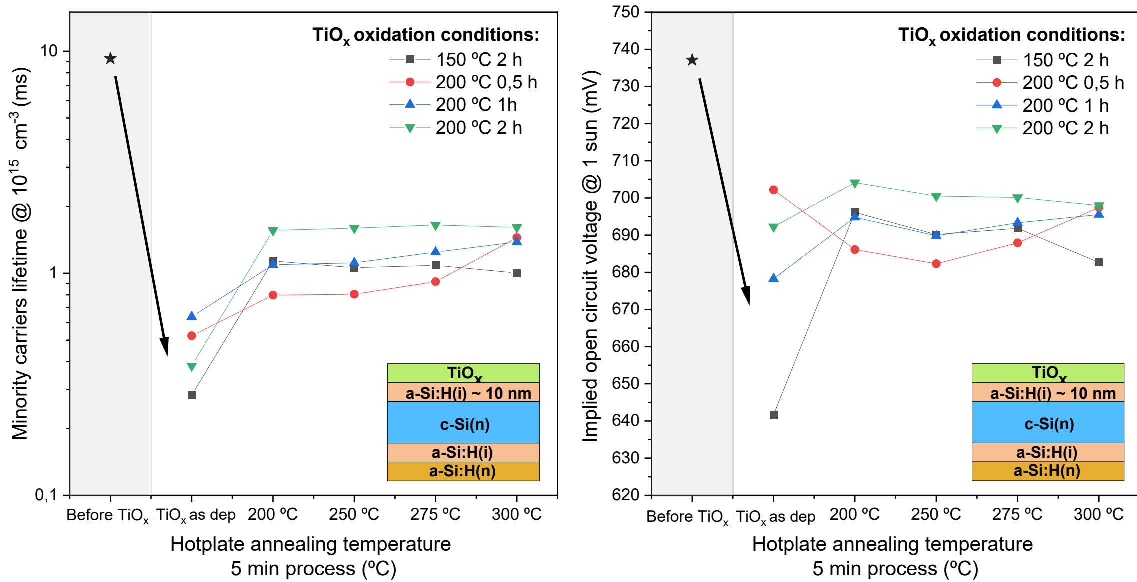

Figure 7-2 Minority carrier lifetime (τ_{eff}) and implied open circuit voltage (i-V_{oc}) for TiO_x/a-Si:H (~10 nm) samples with subsequent hotplate annealing processes.

Although XPS of TiO_x samples (see Chapter IV) analysis revealed no significant difference in the Ti^{4+}/Ti total ratio among the TiO_x layers oxidized at 150 °C and 200 °C (oxidation time ≥ 1 h) indicating similar chemical stoichiometry, the samples treated at 200 °C exhibited higher τ_{eff} and i-V_{oc}. This enhancement can be due to structural differences rather than compositional changes. Specifically, the TiO_x layer oxidized at 200 °C showed signal of crystallinity structures, as opposed to the predominantly amorphous structure observed at 150 °C. A combination of amorphous and anatase phase TiO_x has proved better passivation properties than amorphous alone or rutile phase [4].

The TiO_x/a-Si:H(i) stack with a a-Si:H(i) thickness of ~10 nm shows minority carrier lifetime and implied open circuit voltage appropriate for solar cells devices, in the range of 1 to 1.6 ms and 640 to 702 mV. The contact resistivity is relatively high for solar cell structures; the best results were found for the 150 ºC oxidized samples with 271 mΩcm^2 (0.5 h oxidation process). However, as the TiO_x/a-Si:H(i) stack will be deposited on the whole backside area, its contribution to the final series resistance can be limited according to $R_s = \rho_c/A$. In contrast, the samples oxidized at 200 ºC shows extremely high contact resistivity values (63 Ωcm^2 to 62 kΩcm^2) which precludes its use as electron selective contact. A possible solution to overcome this is to decrease the thickness of the a-Si:H(i) to

enhance the tunnel transport through the TiO_x/a-Si:H(i) stack while being thick enough to act as a passivating layer.

7.2 Minority carrier lifetime measurements of TiO_x/a-Si:H(i) (~ 7 nm)

The effect on the minority carrier lifetime with a-Si:H(i) layer with ~7 nm was investigated. For this batch two 4'' wafers were used to deposit to create the a-Si:H(n)/a-Si:H(i)/c-Si(n)/a-Si:H(i) structure. The whole wafer was measured with the Sinton WCT-120 system using the transient method. The value of τ_{eff} and i-V_{oc} for such wafers was 0.98 ms and 693 mV for the first wafer and 1.25 ms and 697 mV for the second wafer. After that, the wafers were cleaved to obtain eight samples with dimensions of 3.5 x 3.5 cm^2 and the TiO_x was deposited following the 2-step oxidation process. The oxidation processes were the same as in the previous experiment, i.e., 150 ºC or 200 ºC with a duration of 0.5 h, 1 h or 2 h. With the final sample, subsequent annealing steps on hotplate were performed to improve the passivation.

The results of τ_{eff} are depicted in Figure 7-4. The reference sample with only a-Si:H(i) shows an increase in the τ_{eff} when the annealing process is performed up to 250 ºC for 5 min. Going from the original value of 1.25 to 6.69 ms. However, when the temperature reaches 300 ºC there is a reduction to 5.24 ms. An extra annealing step with the same temperature (300 ºC) shows even a higher reduction to 3.79 ms. This is expected as the a-Si:H(i) is known to degrade with temperatures > 250 ºC, according to some works [5]. Regarding the samples with TiO_x, all of them exhibit a reduction in the τ_{eff} after the deposition of the TiO_x layer. The duration of the oxidation step does not show a clear trend for this degradation. However, the samples oxidized at 150 ºC show lower τ_{eff} than 200 ºC samples. The mean value for the 150 ºC samples is 170 µs while the mean value for the 200 ºC is 253 µs. A possible reason for the behavior is the formation of some crystalline structure within the 200 ºC samples as it was described in the previous experiment using 10 nm of a-Si:H(i). When the hotplate annealing steps are performed, the τ_{eff} for the 150 ºC samples increases up to the 300 ºC 5 min annealing step, when similar values around 730 µs are reached for all the samples. This effect is different from the sample which only a-Si:H(i) which shows a degradation with the 300 ºC 5 min annealing step. This indicates that even when the a-Si:H(i) degrades for such temperature the improvement in the TiO_x layer is overcoming this effect which is translated to a total increase in τ_{eff}. In contrast, the 200 ºC oxidized samples show an improvement up to 250 ºC, reaching values in the 338 to 504 µs range. When the temperature increases to 300 ºC, the τ_{eff} worsens to a mean value of 297 µs.

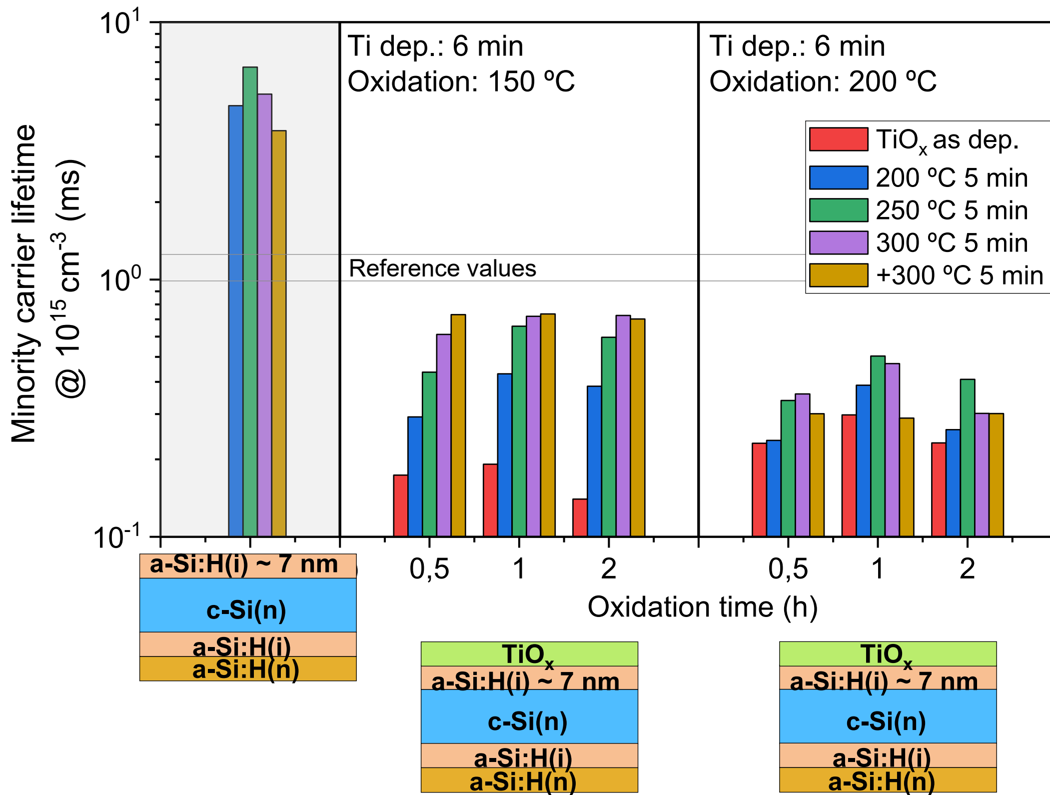

Figure 7-3 Minority carrier lifetime of TiO_x/a-Si:H (~7 nm) samples with subsequent hotplate annealing processes.

Figure 7-4 depicts the $i\text{-}V_{oc}$ for the same samples. The tendency is identical to the τ_{eff}. This is expected as the $i\text{-}V_{oc}$ depends on the excess carrier density (Δn) which in turn is a parameter that is affected by the degree of passivation (carrier lifetime). Regarding the reference sample, it goes from 723 to 732 mV with the 250 ºC 5 min hotplate annealing, when the temperature is increased to 300 ºC 5 min there is a reduction to 712 mV. The samples with Ti oxidized at 150 ºC show a mean value of 641 mV while the 200 ºC samples show a mean value of 643 mV. Again, the 150 ºC samples exhibit an improvement for all the annealing steps up to 300 ºC 5 min reaching a mean value of 680 mV, in contrast to the 200 ºC samples that the $i\text{-}V_{oc}$ decreases or stay the same when the 300 ºC 5 min annealing step is done. The mean value for the 200 ºC samples for this step is 650 mV.

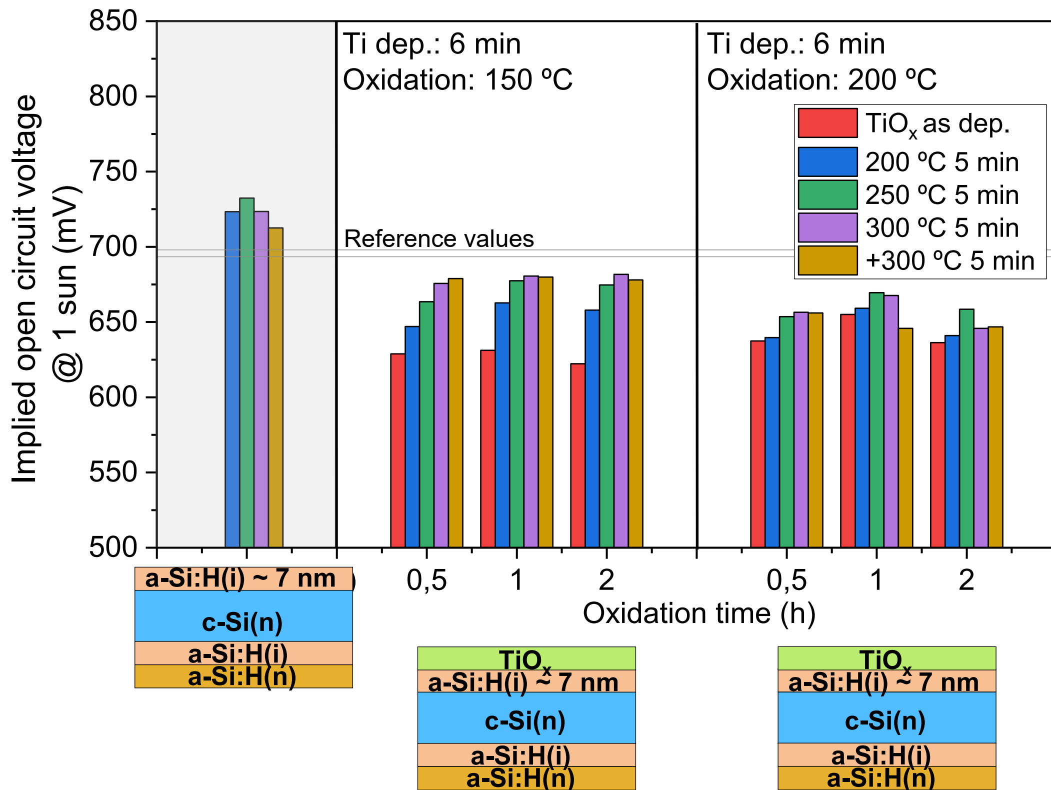

Figure 7-4 Implied open circuit voltage of TiOx/a-Si:H (~7 nm) samples with subsequent hotplate annealing processes.

The τ_{eff} and $i\text{-}V_{oc}$ evolution after the hotplate annealing at 300 °C reveals a distinct behavior depending on the oxidation temperature used for the formation of the TiO_x layer. Samples in which Ti was oxidized at 150 °C exhibit a clear increase in lifetime after annealing, whereas those oxidized at 200 °C show a degradation, showing a similar behavior to the control sample composed only with a-Si:H(i). XPS analysis (see Chapter IV) of TiO_x layers oxidized at both 150 °C and 200 °C (with oxidation times ≥1 h) indicates that the oxidation states of titanium are comparable at both temperatures, suggesting similar stoichiometry. However, the density of oxygen vacancies is reduced with increased oxidation time, indicating that the duration of the oxidation step plays a role in passivation quality. It is plausible that the TiO_x layer formed at 150 °C retains a higher concentration of oxygen vacancies prior to annealing, which may partially reorganize or be passivated during the 300 °C hotplate annealing, improving interface quality and lifetime. In contrast, the 200 °C samples initially containing fewer vacancies may undergo interfacial degradation during annealing, potentially due to hydrogen effusion from the a-Si:H(i) layer or structural relaxation effects. Additionally, field-effect passivation can also have an effect with TiO_x films since some works have found the presence of positive fixed charges due to oxygen vacancies [6]. These observations suggest that while the initial chemical states are similar, subtle differences in oxygen vacancy concentration and thermal response can critically impact the quality of TiO_x/a-Si:H(i) /c-Si(n) junction.

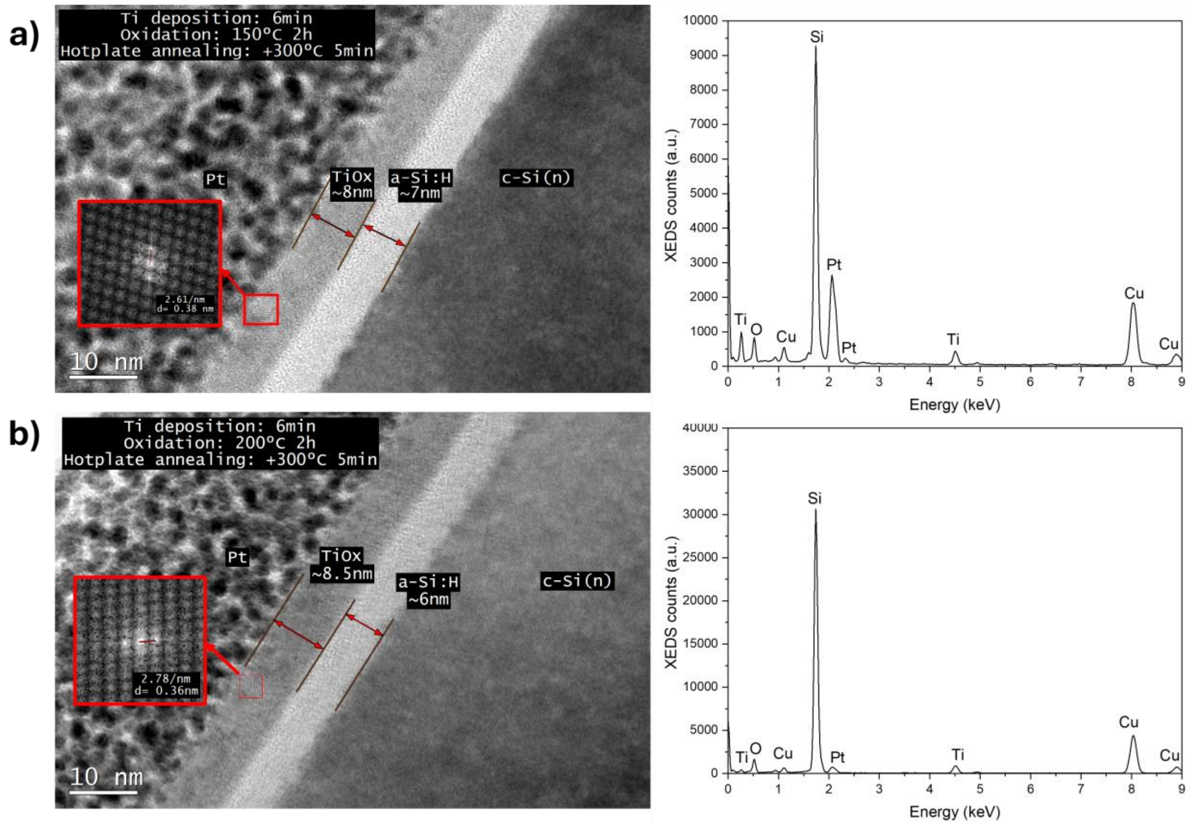

Figure 7-5 TEM images and XEDS spectra of a-Si:H(i)/TiO_x samples fabricated for measuring minority carrier lifetime.

Finally, TEM images were taken for the samples with a Ti oxidation process at 150 ºC 2 h and 200 ºC 2 h to compare between both temperatures. These are depicted in Figure 7-5. With these images the a-Si:H(i) is confirmed to have a thickness of 7 nm. Additionally, the TiO_x thickness is in good agreement with the deposition rate obtained in the previous chapter, 1.26 nm/h for 150 ºC and 2 nm/h for 200 ºC, recalling that ~5 nm of Ti is originally deposited following an oxidation step where a small quantity of TiO_x is deposited with such deposition rates. The XEDS confirms the presence of oxygen and titanium in the observed stack. The Cu signal appears due to the lamella holder. In both samples, there are some crystalline structures on the TiO_x layers that are depicted in the reciprocal-space in the inset. The interplanar distance obtained for the samples with 150 ºC and 200 ºC oxidation is 0.38 nm and 0.36 nm respectively. These can be related to the (101) plane for anatase TiO_x which has an interplanar distance of 0.35 nm. This is one of the more common planes observed in anatase TiO_x layer according to some works [7]. The most likely reason for the formation of such structures is because of the 300 ºC 5 min annealing step rather than the Ti oxidation temperature, since the TEM images of samples that were not exposed to the hotplate annealing show different interplanar distances (~0.20 nm), see Figure 6-13 and Figure 6-14 from previous chapter.

7.3 Flash Lamp Annealing process of a-Si:H(i) and TiO_x/a-Si:H(i) samples

Up to this point, all samples fabricated to measure the TiO_x/a-Si:H(i) passivation quality were annealed by hotplate or RTA under controlled atmospheres. Another annealing technique that was investigated was Flash Lamp Annealing (FLA). This technique differs from other annealing processes in that FLA has a duration of milliseconds. This could represent an advantage for the fabrication of solar cells since electricity consumption would be reduced. In the case of TiO_x, some work has been done exploring FLA to modify the TiO_x phase for photocatalysis applications [8][9], however, at the moment of writing this thesis no studies have been found where FLA on TiO_x is used for photovoltaic applications.

Since this was the first time that FLA was used to anneal these kinds of samples (TiO_x/a-Si:H(i)), a preliminary batch with symmetrical a-Si:H(n)/a-Si:H(i) stack was processed to determine the energy density range to be used with a flash time of 3.2 ms. The duration of 3.2 ms was chosen because this is the minimum time that allows reaching temperatures in the 200 – 800 ºC range at the Si surface. Naturally, the temperature reached by the sample depends on the energy density and duration of FLA process. Five different samples with symmetrical a-Si:H(n)/a-Si:H(i) stack were annealed with FLA varying the energy density from 38 to 70 Jcm^{-2}, which represents temperatures from 400 to 800 ºC. After that, the τ_{eff} and $i\text{-}V_{oc}$ were obtained by measuring the samples with the Sinton WCT-120 T and the results are depicted in Figure 7-6.

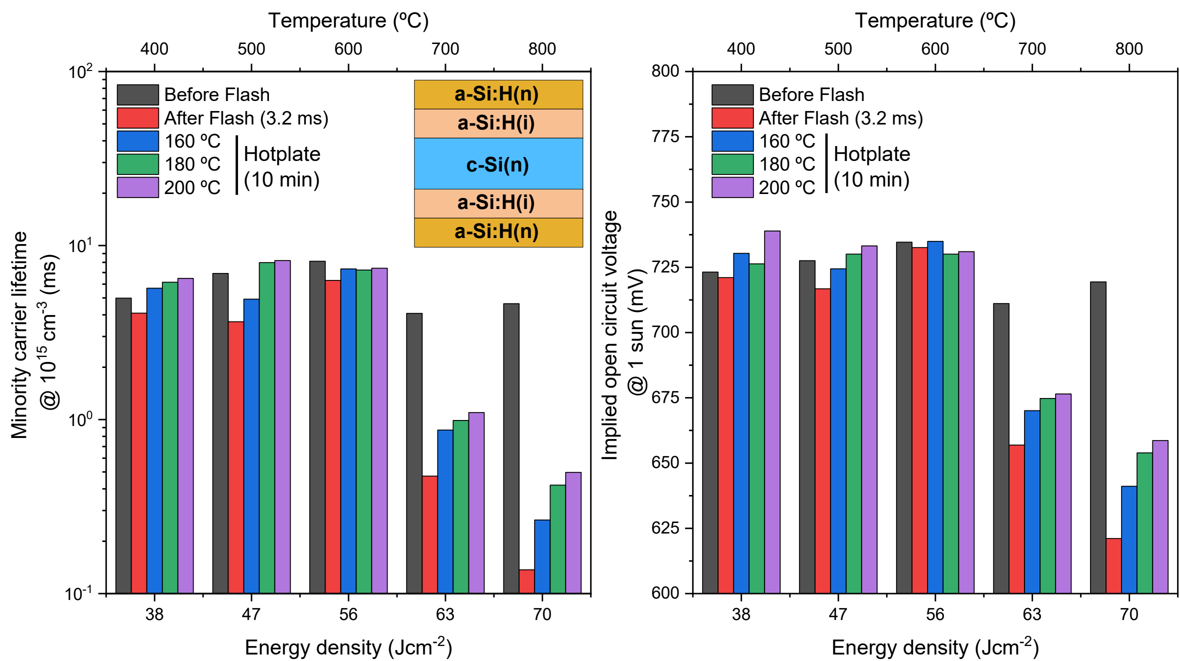

Figure 7-6 Minority carrier lifetime and implied open voltage circuit for symmetrical a-Si:H(n)/a-Si:H(i) samples annealed with flash lamp under different energy densities.

Interestingly, the results show that the a-Si:H(n)/a-Si:H(i) stack is capable of withstanding FLA processes reaching temperatures of 600 ºC (56 Jcm^{-2}). This temperature cannot performed with conventional annealing processes (hotplate or RTA) since the a-Si:H starts to degrade at ~300 ºC [5]. For all the samples processed with an energy density ≤ 56 Jcm^{-2}, there is a slight decrease in the τ_{eff} and $i\text{-}V_{oc}$. The τ_{eff} goes from a mean value of 6.6 to 4.6 ms after the FLA process. Additionally, the $i\text{-}V_{oc}$ goes from 728 to 723 mV. In contrast, when the energy density is increased to 63 Jcm^{-2} or higher, there is a strong decrease in both parameters. For instance, the sample with a FLA process of 70 Jcm^{-2} (800 ºC) goes from an original τ_{eff} and $i\text{-}V_{oc}$ value of 4.6 ms and 719 mV to 0.13 ms and 621 mV, respectively. To understand whether this degradation is permanent or not, subsequent annealing steps (160 ºC, 180 ºC, and 200 ºC) on hotplate were performed during 10 min. The samples with FLA process with energy density ≤ 56 Jcm^{-2} show a recovery to their original τ_{eff} and $i\text{-}V_{oc}$ values; however, for the samples with 63 or 70 Jcm^{-2} the annealing steps on hotplate are not able to recover their original values. The sample with a FLA process of 70 Jcm^{-2} recovers up to 0.49 ms and 658 mV. This indicates that the a-Si:H(n)/a-Si:H(i) stack has been permanently damaged due to the excessive temperature reached at the surface. The most likely reasons for this may be the effusion of the hydrogen contained in the a-Si:H(n)/a-Si:H(i) which plays a key role to passivate the dangling bonds in the interfaces or the partial crystallization of the a-Si:H layers that some works have shown that produce degradation [10].

With the previous results, it was decided to process a TiO_x/a-Si:H(i) sample with an energy density that would not affect the a-Si:H(i). In this case, it was decided to use 47 Jcm^{-2}. The TiO_x was fabricated by depositing ~5 nm of Ti (6 min deposition) plus an oxidation step of 200 ºC 1 h. This oxidation process was chosen since this showed some of the best results in terms of τ_{eff} and $i\text{-}V_{oc}$ in the previous experiments. In each step, the τ_{eff} and $i\text{-}V_{oc}$ was measured. The results are depicted in Figure 7-7. Before the TiO_x deposition, the sample exhibited 1.1 ms and 693 mV. As previously observed, when the TiO_x is deposited there is a degradation on the passivation, obtaining values 0.05 ms of 586 mV. Finally with the FLA step, the sample recovered up to 0.19 ms and 631 mV. Although the FLA process with 47 Jcm^{-2} and 3.2 ms is not able to fully recover the original passivation, it is clear that the FLA is positively affecting the TiO_x/a-Si:H(i). Further experiments varying the flash duration might be able to recover the original passivation or even improve it. Considering that the FLA process takes place in the range of milliseconds, in contrast to the minutes required for hotplate and RTA, this technique is promising for processing material for solar cells, as this can reduce the thermal budget during fabrication.

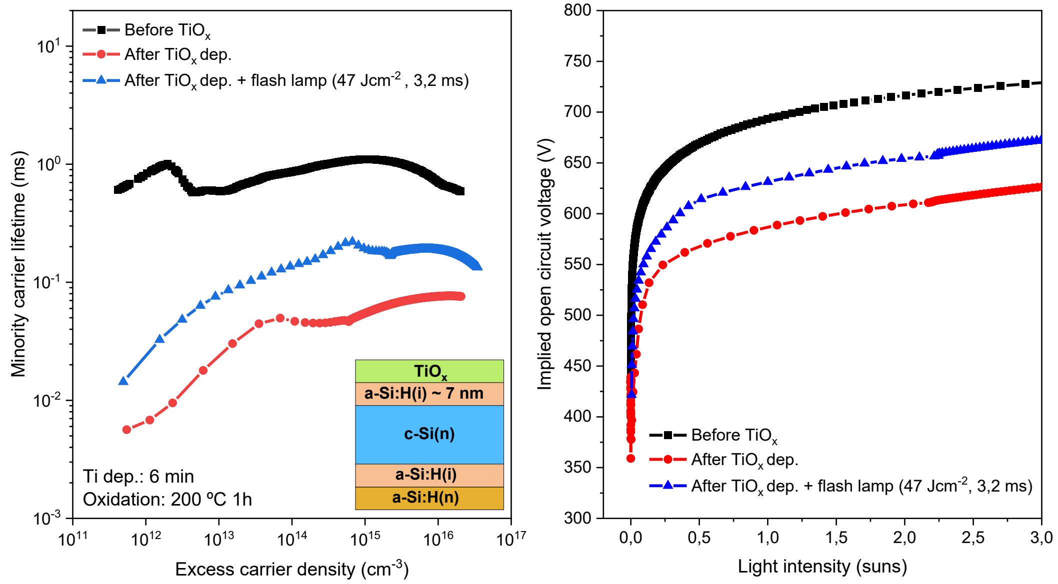

Figure 7-7 Minority carrier lifetime and implied open voltage circuit for TiO$_x$/a-Si:H(i) sample annealed with flash lamp with an energy density of 47 Jcm^{-2} with a duration of 3.2 ms.

7.4 Heterojunction solar cell with TiO$_x$ as electron-selective contact

Finally, to test the TiO$_x$ as electron-selective contact deposited by HPS, prototype solar cells were fabricated. A photograph of the fabricated device and a schematic of the structure are shown in Figure 7-8. The deposition of the a-Si:H(i), a-Si:H(n), a-Si:H(p), and ITO was done at *CIEMAT*. It is worth mentioning that the ITO was deposited by standard RF sputtering, and the front contacts were defined by photolithography.

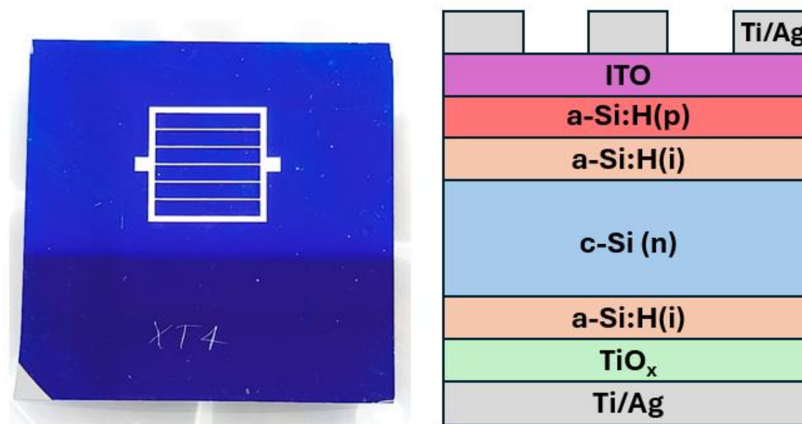

Figure 7-8 Photograph (left) and schematic diagram (right) of a silicon heterojunction solar cell incorporating TiO$_x$ as an electron-selective contact.

The fabrication steps of these solar cells were the following:

1. A 4'' n-type Si wafer (FZ, double side polished, <100>,1-5 Ωcm, 300 μm) from *TOPSIL* was used as a substrate.

2. The a-Si:H(i) and a-Si:H(p) layers were deposited by PECVD. The thicknesses for such layers are ~7 nm and ~10 nm, respectively.

3. Approximately 80 nm of ITO was deposited on the front side (i.e., on a-Si:H(i)/a-Si:H(p) stack) by standard RF sputtering.

4. The rear side was cleaned with diluted HF (1%) solution.

5. The TiO_x layers were deposited on the rear side of the sample. The Ti layer was deposited for 6 min to obtain ~ 5 nm. After that, the oxidation step is performed. Two oxidation conditions were tested, either 150 ºC for 1 h or 200 ºC for 1 h.

6. Negative photolithography was used to define the front contacts.

7. A Ti/Ag stack was deposited on both sides of the samples. The thicknesses for such layers were ~ 20 nm and ~ 500 nm, respectively.

Once the samples were finished, they were measured with a Sinus-70 solar simulator from *Wavelabs.* A shadow mask was placed on top of the samples to illuminate only the active area of the device, which is 1 cm^2. Solar cells were measured under standard conditions (AM1.5G, 25 ºC)

7.4.1 Evolution of J_{sc}, V_{oc}, FF, efficiency and resistances with low temperature annealing steps.

As is commonly done, subsequent annealing steps were performed to recover the samples from the damage caused by the sputtering deposition process, specifically the ITO and TiO_x deposition processes. After each annealing step, the IV curve under illumination was measured to study the evolution of the main solar cell parameters, i.e., short-circuit current density (J_{sc}), open-circuit voltage (V_{oc}), fill factor (*FF*), and efficiency. Additionally, the Sinus-70 solar simulator can extract the parallel resistance (R_p) and the series resistance (R_s) from the IV curve under illumination. The results on J_{sc}, V_{oc}, and *FF* are depicted in Figure 7-9, and the results on the efficiency, *Rs* and *Rp*, are depicted in Figure 7-10.

Without any annealing process, the samples exhibit similar values of J_{sc}, 28.95 mA/cm^2 for the sample with 150 ºC 1 h TiO_x and 29.59 mA/cm^2 200 ºC 1 h. These are reasonable values for a heterojunction solar cell without a texturized front side; besides, they are similar to those found by others using TiO_x deposited by standard RF sputtering [11] and e-beam [12]. Regarding the V_{oc}, there is a clear difference between the samples. The solar cell with a 150 ºC 1 h oxidized TiO_x shows a value of 426 mV, while the solar cell with 200 ºC 1 h oxidized TiO_x shows 478 mV. This is congruent with the carrier lifetime results explained previously as the samples oxidized at 200 ºC show higher τ_{eff} than samples oxidized at 150 ºC. The V_{oc} is really sensitive to the recombination current density (J_0), and thus, lower τ_{eff} can heavily penalize the V_{oc}. The *FF* is 0.47 and 0.57 for the samples oxidized at 150 ºC and 200 ºC, respectively.

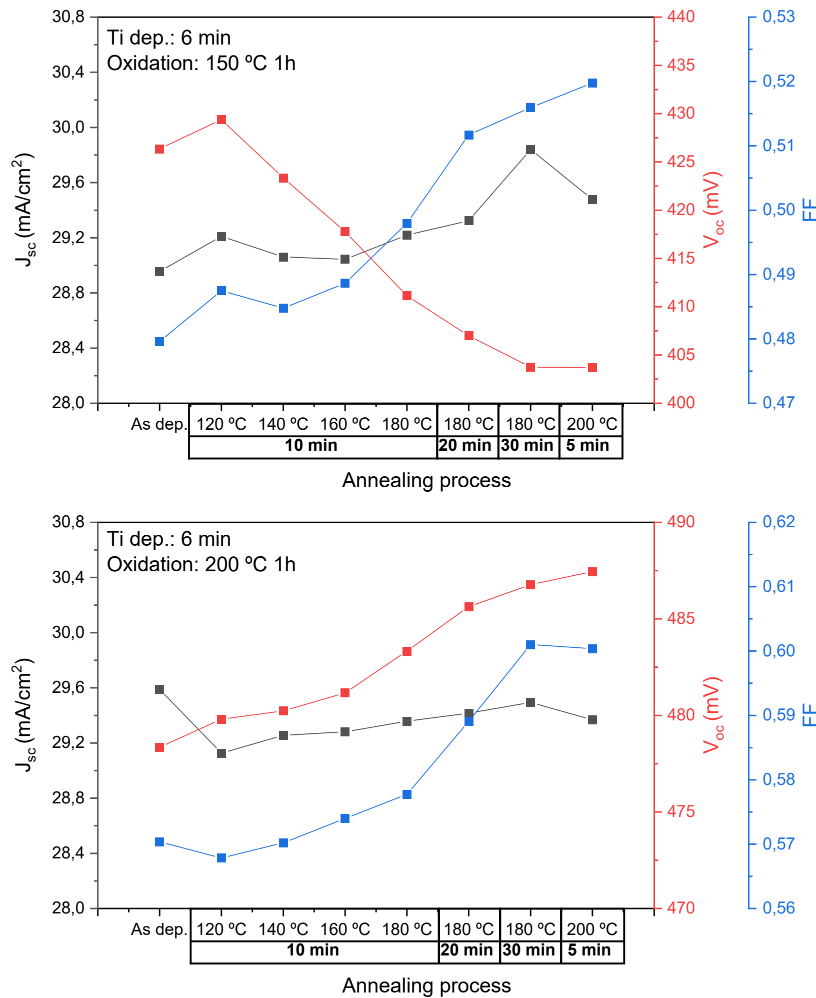

Figure 7-9 Evolution of J_{sc}, V_{oc}, and FF of TiO_x solar cells with subsequent annealing process performed with a hotplate.

With the annealing steps, the J_{sc} remains almost the same for both samples, reaching values of 29.47 mA/cm^2 (150 ºC 1 h samples) and 29.36 mA/cm^2 (200 ºC 1 h), the *FF* increases up to 0.52

(150 ºC 1 h samples) and 0.60 (200 ºC 1 h). Regarding the $V_{oc,}$ there is an opposite tendency between the samples. While the sample with TiO_x oxidized at 200 ºC 1 h shows the common trend of improving the V_{oc} with the annealing steps, going from 478 to 487 mV. The sample with TiO_x oxidized at 150 ºC 1 h shows an apparent reduction of V_{oc} as it goes from 426 to 403 mV. Typically, annealing steps at low temperature improve the V_{oc} by reducing the dangling bonds of the junctions, as such temperature facilitates the diffusion of hydrogen contained by the a-Si:H(i). In the previously explained lifetime results, the τ_{eff} for the 150 ºC samples increased with the annealing steps; thus, the decreases should be related to some layers not included in those samples. A possible reason could be the diffusion of the Ag into the a-Si:H(i)/TiO_x junction. In the previous chapter, TEM images showed that 200 ºC TiO_x samples exhibit crystalline structures on the surface, while the 150 ºC samples did not. It has been mentioned in some works that amorphous TiO_x films show greater diffusivity for the diffusion of Ag than crystalline TiO_x [13]. The diffusion into a-Si:H(i)/TiO_x (150 ºC) could explain the reduction in the V_{oc}.

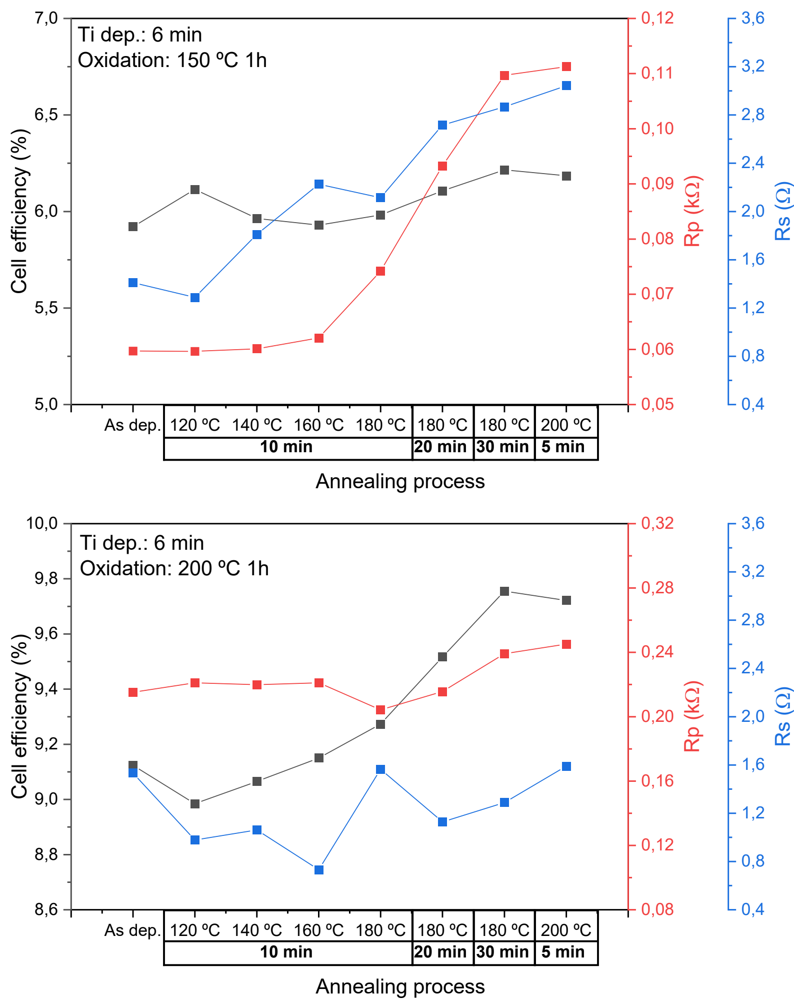

Figure 7-10 Evolution of efficiency, R_p, and R_s of TiOx solar cells with subsequent annealing process performed with a hotplate.

These solar cells have efficiencies of 6% (TiO_x at 150 ºC) and 9% (TiO_x at 200 ºC) without any annealing step. The *Rs* is almost the same for both samples, showing a value of 1.5 **Ω**. In contrast, the *Rp* is different for the samples. The sample with TiO_x at 150 ºC has an *Rp* of 60 **Ω**, while the sample with TiO_x at 200 ºC has 215 **Ω**. With the annealing steps, there is a slight improvement in the efficiency of the solar cells; the sample with TiO_x at 150 ºC increases to 6.2%, and the sample with TiO_x at 200 ºC increases to 9.7 %. Concerning the *Rp,* there is also an improvement, as they reach 111 **Ω** (TiO_x at 150 ºC) and 245 **Ω** (TiO_x at 200 ºC). The *Rp* values are considerably low and can indicate that even with the annealing steps, there are still some defects inside the a-Si:H(i) or TiO_x film that present an alternative path to the photo-generated carriers. Finally, the evolution of *Rs* with the annealing steps is different for both samples. While the sample with TiO_x at 150 ºC increases from 1.4 to 3 **Ω**, the sample with TiO_x at 200 ºC remains at the same value 1.5 **Ω**. All this information reveals that the main limiting factors for these solar cells are the low *Rp,* which in turn limits the *FF*, and the low V_{oc} resulting from the limited passivation quality of the TiO_x layer.

7.4.2 Comparison between Si solar cells with TiO_x as ESC and HIT solar cell

To compare the cells containing TiO_x as electron-selective contact, the illumination response (AM1.5G) of a heterojunction with intrinsic thin layer (HIT) cell developed by *CIEMAT* was also measured. This cell has an a-Si:H(n) film to replace the TiO_x function as an electron-selective contact. Both TiO_x cells and the HIT cell have the same a-Si:H(i), a-Si:H(p), and ITO layers; however, the HIT cell has a-Si:H(n) as the front layer, while the TiO_x cells have the electron-selective contact on the back side. In addition, the fingers have a different pattern, representing different percentages of shading on the illuminated side. In HIT-type cells, the area of the fingers represents ~16% of the active area, while the area for TiO_x cells represents only ~0.3%. The IV curves in illumination and the external quantum efficiency (EQE) of these cells are shown in Figure 7-11. It is worth noting that the IV and EQE curves were obtained after the samples were annealed with the last hotplate annealing step (200 ºC 5 min).

From the IV curves, it can be observed that the cells with TiO_x have a slightly higher J_{sc} than the HIT type cell, ~29 mA/cm^2 for the cells with TiOx and 28.8 mA/cm^2 for the HIT. This can be explained by the fact that the fingers have a different pattern, as described above. The V_{oc} is better for the HIT type cell, with a value of 647 mV, indicating less recombination at the junctions. The *FF* is also better with a value of 0.62, which is observable since the *Rp* of this cell is higher (563 kΩ). With respect to *Rs*, the HIT cell also shows a lower value (0.8 Ω) compared to TiO_x cells, which show values between 3 and 1.5 **Ω**. All of this gives an efficiency for the HIT solar cell sample of 11.55%.

In order to compare the spectral response of the cells, the EQE calculation (see Chapter III) was made considering a short circuit current density (J_{sc}) with the effective area of the cell following the next expression:

$$J_{sc,eff} = \frac{I_{sc}}{A_{eff}} = \frac{I_{sc}}{A_t(1-S)} \qquad 7.1$$

Where I_{sc} is the short circuit current obtained by the Sinus-70 solar simulator, A_t is the total active area of the sample, and S represents the percentage of the shadow due to the fingers.

From the Figure 7-11 b) it is noticeable that spectral response between 300 – 550 nm is similar for all the samples. This indicates that even when the TiO_x has shown a peak absorption at 300 nm (see Chapter IV), this is not observed in the final devices must likely due to the blue parasitic absorption of a-Si:H(n), a-Si:H(p), or even ITO [14] occurring at the front side. In the near-infrared (NIR) region (800 – 1200 nm), the HIT solar cell shows superior quantum efficiency. This improvement is likely due to enhanced rear-side passivation provided by the a-Si:H(i)/a-Si:H(p) stack, which is known to effectively suppress surface recombination. In comparison, the a-Si:H(i)/TiO_x interface likely introduces higher recombination rates, reducing the collection probability of long-wavelength (low-energy) photons, which are more sensitive to bulk and rear recombination losses. This has been observed in some works where the EQE of TiO_x solar cells and HIT are compared [15]. Additionally, the rear ITO layer present in the HIT solar cell may contribute to better carrier extraction by providing both optical transparency and lateral conductivity at the rear, further supporting improved EQE in the NIR. Finally, the inset shows a zoom in the 550 - 780 nm range to compare between the TiO_x solar cells. The sample with a TiO_x layer fabricated with 200 ºC 1 h oxidation step shows slightly higher EQE which can indicate a lower recombination rate at the rear side. This is congruent with the V_{oc} values obtained from the solar simulator (Figure 7-9).

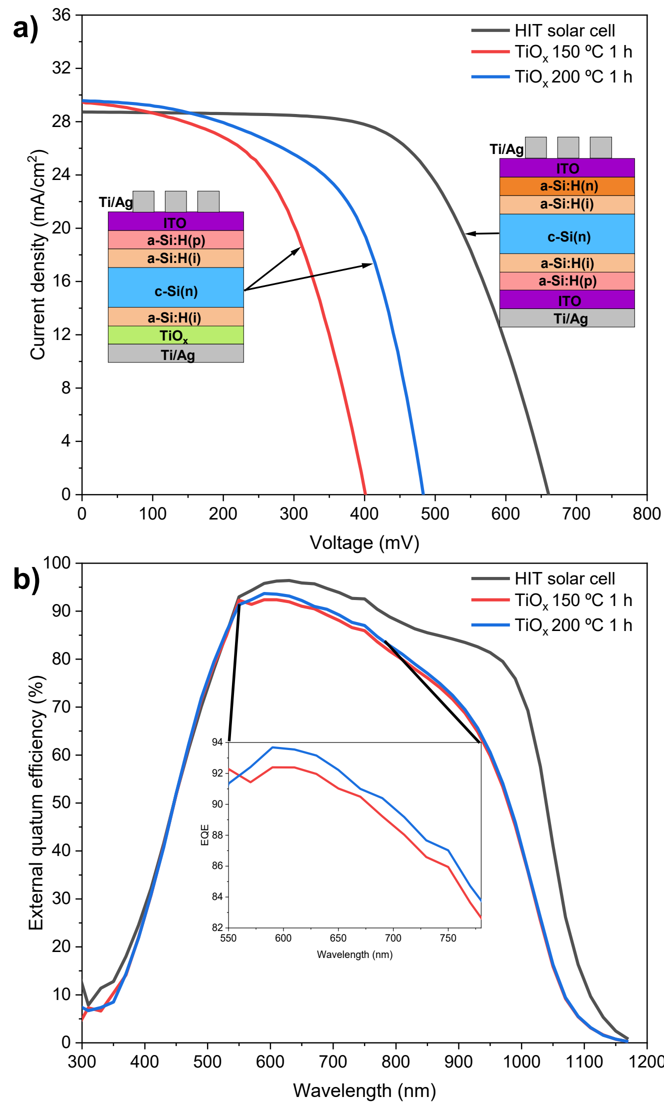

Figure 7-11 a) Illuminated current–voltage (IV) characteristics of silicon solar cells with TiO_x electron-selective contacts thermally oxidized at 150 °C and 200 °C (1 h), compared to a HIT cell. b) External quantum efficiency (EQE) spectra for the same devices.

Figure 7-12 shows the dark current–voltage (IV) curve of two of the samples: the HIT solar cell and a solar cell with TiO_x fabricated at 200 ºC 1 h oxidation step. The experimental curves are fitted using diode circuit models tailored to the dominant recombination and transport mechanisms in each structure. The fitting was done with by the *2/3-Diode Fit* Matlab program developed by Suckow [16]. For the sake of simplicity the ideality diode factor was fixed to $n_1 = 1$ and $n_2 = 2$. For the HIT cell, a standard two-diode model accurately reproduces the measured behavior, accounting for diffusion-related (*D1*) and Shockley-Read-Hall recombination-related (*D2*) currents, along with parallel resistance (*Rp*), and series resistance (*Rs*). In contrast, the TiO_x solar cell exhibits a more complex current behavior, particularly in the low-voltage region, which is better described by an extended three-diode model. This model includes an additional recombination pathway (*D3*),

associated with interface recombination losses, which is modeled with a diode and resistance (R_{rec}) in series. The three-diode model is well explained in the McIntosh dissertation [17]. In summary, he explains that the *D3* branch represents a high-recombination region caused by a resistive element such as an unpassivated region or local Schottky contacts between metal fingers and semiconductors. In the case of the solar cell with TiO_x the behavior should be related to the high recombination that takes place at the TiO_x/a-Si:H(i)/c-Si(n) stack.

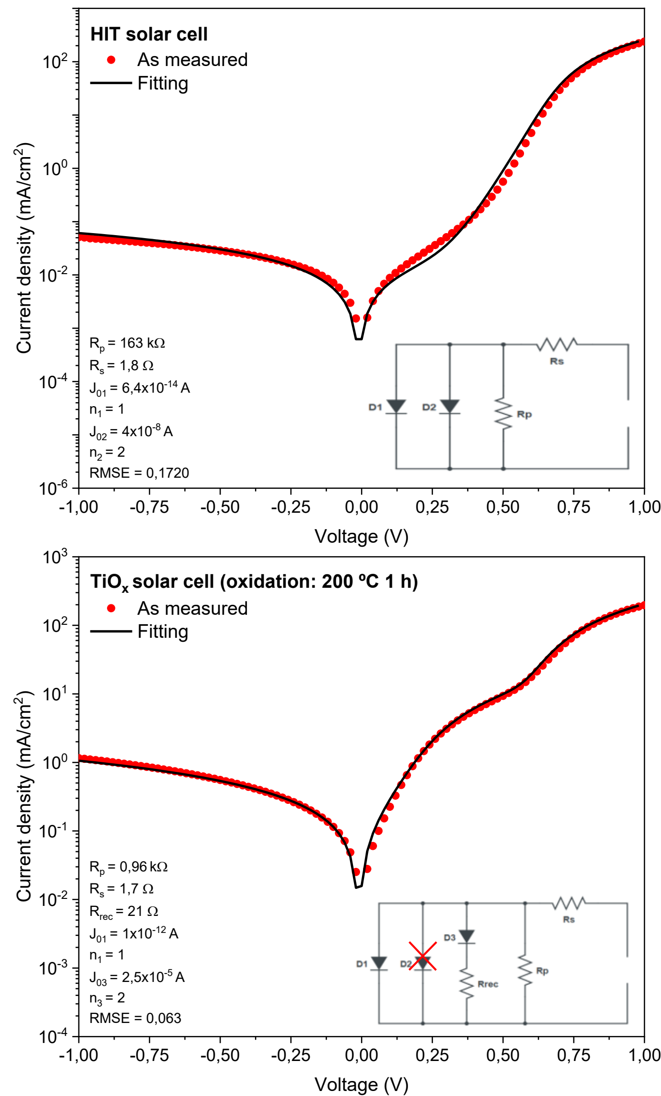

Figure 7-12 Dark current–voltage (IV) characteristics of silicon heterojunction solar cells and corresponding model fits. a) HIT solar cell fitted with the two-diode model, b) Solar cell with TiO_x as an electron-selective contact, modelled with an extended three-diode equivalent circuit.

As previously discussed, the HIT solar cell was accurately modelled using the standard two-diode equivalent circuit. The extracted saturation current densities were $J_{01} = 6.4x10^{-14}$ A/cm^2 with an ideality factor $n_1 = 1$, and $J_{02} = 4x10^{-8}$ A/cm^2 with $n_2 = 2$. These values are consistent with those typically observed in silicon heterojunction solar cells: J_{01} values in the range of 10^{-14} to 10^{-13} A/cm^2 which is

characteristic for the diffusion mechanism at high-voltage region, while J_{02} values on the order of 10^{-8} A/cm^2 that indicates moderate recombination in the depletion region, in this case the a-Si:H(p)/a-Si:H(i)/c-Si(n) junction.

In contrast, the TiO_x-based solar cell required a three-diode model to describe the dark IV behavior accurately. It exhibited a higher J_{01} = 1x10^{-12} A/cm^2 with an ideality factor n_1 = 1. The third recombination pathway, modeled by J_{03} = 2.5x10^{-5} A/cm^2 with an associated resistive component R_{rec} = 21 Ω, and ideality factor n_3 = 2, reflects a strong recombination mechanism, most likely at the TiO_x/a-Si:H(i)/c-Si(n) junction. This current density is several orders of magnitude higher than typical depletion recombination currents, indicating that the TiO_x contact might introduce a pronounced recombination path. As a result, the *D2* component was not necessary to fit the data, as the *D3* branch already captured the dominant recombination mechanism. Additionally, the extracted parallel resistance *Rp* = 0.96 kΩ for the TiO_x solar cell is substantially lower than that of the HIT solar cell (*Rp* = 163 kΩ), indicating greater leakage or localized defects. In contrast, the series resistance values *Rs* ≈ 1.7- 1.8 Ω were comparable in both devices as they exhibit similar slopes in the high-voltage region.

7.5 Summary and conclusions

This chapter presented a systematic characterization of TiO_x/a-Si:H(i) stacks as ESC for crystalline silicon solar cells. The stacks were fabricated using high-pressure sputtering (HPS) of Ti followed by low-temperature thermal oxidation at 150 °C and 200 °C for varying durations. An intrinsic a-Si:H layer (~10 nm) was explored to evaluate the impact on passivation quality and contact resistivity.

Key findings can be summarized as follows:

- **Contact Resistivity:** The inclusion of a thin a-Si:H(i) interlayer improves the passivation but increases the contact resistivity. Samples oxidized at 150 °C exhibited lower specific contact resistivity (as low as 271 mΩcm²) compared to those oxidized at 200 °C (up to 62 kΩcm²), likely due to increased interfacial oxidation of the a-Si:H layer and/or excessive TiO_x thickness. In comparison the lowest ρ_c obtained with only TiO_x was achieved with 150 ºC or 200 ºC < 2 h. Such ρ_c values were between 6 to 63 mΩcm².

- **Passivation Quality:** Minority carrier lifetime and implied open-circuit voltage measurements demonstrated that the 200 °C oxidized samples initially provided better passivation quality (up to 1.6 ms and 700 mV after annealing) due to enhanced TiO_x crystallinity. However, this was counterbalanced by higher contact resistivity.

- **Annealing Behavior:** Post-deposition annealing improved passivation properties. The samples with ~7 nm a-Si:H(i) and TiO_x shows an increase in the τ_{eff} with the 300 ºC 5 min annealing. The sample with only ~7 nm a-Si:H(i) shows a reduction in τ_{eff} with that annealing process. Although the reached τ_{eff} for the a-Si:H(i)/TiO_x is not the same as the original value (i.e., before TiO_x deposition), the increase of τ_{eff} with that annealing process indicates that the improvement in the a-Si:H(i)/TiO_x surpass the degradation of the a-Si:H(i).This behavior was more pronounced in the 150 °C oxidized samples.

- **Flash Lamp Annealing (FLA):** FLA was shown to be a viable low-thermal and energetically efficient method for enhancing the TiO_x/a-Si:H(i) interface. Moderate FLA conditions (e.g., 47 J/cm^2, 3.2 ms) partially restored passivation without inducing severe damage, highlighting its potential for exploring FLA as an annealing technique for Si solar cells.

- **Device Integration:** Heterojunction solar cells with rear-side TiO_x/a-Si:H(i) contacts were fabricated and compared against a HIT reference cell. Despite promising short-circuit current densities(~29 mA/cm^2), the devices suffered from lower V_{oc} and FF due to high recombination at the TiO_x interface. The HIT cell exhibited superior performance, underscoring the need to reduce contact resistivity and improve interfacial quality in TiO_x-based contacts.

In conclusion, while the TiO_x/a-Si:H(i) stack shows promising passivation and selectivity properties, optimization of the TiO_x thickness, oxidation temperature, and a-Si:H(i) thickness is necessary to mitigate contact resistance and interface recombination. Future work should explore ultrathin interlayers, modified oxidation schemes, and interface engineering approaches to optimize the silicon solar cells with TiO_x as ESC.

7.6 References

[1] H. Plagwitz, M. Nerding, N. Ott, H. P. Strunk, and R. Brendel, "Low-temperature formation of local Al contacts to a-Si:H-passivated Si wafers," *Prog. Photovoltaics Res. Appl.*, vol. 12, no. 1, pp. 47–54, 2004, doi: 10.1002/pip.522.

[2] M. A. Leilaeioun, W. Weigand, M. Boccard, Z. J. Yu, K. Fisher, and Z. C. Holman, "Contact resistivity of the p-Type amorphous silicon hole contact in silicon heterojunction solar cells," *IEEE J. Photovoltaics*, vol. 10, no. 1, pp. 54–62, 2020, doi: 10.1109/JPHOTOV.2019.2949430.

[3] Y. Nakagawa, K. Gotoh, T. Inoue, Y. Kurokawa, and N. Usami, "Improved Performance of Titanium Oxide/Silicon Oxide Electron-Selective Contacts by Implementation of Magnesium

Interlayers," *Phys. Status Solidi Appl. Mater. Sci.*, vol. 218, no. 19, pp. 1–6, 2021, doi: 10.1002/pssa.202100296.

[4] I. S. Yu, I. H. Chang, H. E. Cheng, and Y. S. Lin, "Surface passivation of c-Si by Atomic Layer Deposition TiO2 thin films deposited at low temperature," *2014 IEEE 40th Photovolt. Spec. Conf. PVSC 2014*, no. 100, pp. 1271–1274, 2014, doi: 10.1109/PVSC.2014.6925148.

[5] J. Shi, M. Boccard, and Z. Holman, "Plasma-initiated rehydrogenation of amorphous silicon to increase the temperature processing window of silicon heterojunction solar cells," *Appl. Phys. Lett.*, vol. 109, no. 3, 2016, doi: 10.1063/1.4958831.

[6] N. Beyraghi, M. C. Sahiner, O. Oguz, and S. Yerci, "Optimization of a Solution-Processed TiOx/(n)c-Si Electron-Selective Interface by Pre- and Postdeposition Treatments," *ACS Appl. Mater. Interfaces*, vol. 16, no. 13, pp. 16950–16961, 2024, doi: 10.1021/acsami.3c18134.

[7] R. S. Pessoa, F. P. Pereira, G. E. Testoni, W. Chiappim, H. S. Maciel, and L. V. Santos, "Effect of substrate type on structure of TiO2thin film deposited by atomic layer deposition technique," *J. Integr. Circuits Syst.*, vol. 10, no. 1, pp. 38–42, 2015, doi: 10.29292/jics.v10i1.403.

[8] S. Prucnal *et al.*, "TiO2 Phase Engineering by Millisecond Range Annealing for Highly Efficient Photocatalysis," *J. Phys. Chem. C*, vol. 127, no. 26, pp. 12686–12694, Jul. 2023, doi: 10.1021/ACS.JPCC.3C01165.

[9] R. Gago, S. Prucnal, J. Azpeitia, I. Jiménez, and L. Álvarez-Fraga, "Phase selectivity upon flash-lamp annealing of sputter deposited amorphous titanium oxide films," *Ceram. Int.*, vol. 50, no. March, pp. 49112–49118, 2024, doi: 10.1016/j.ceramint.2024.09.252.

[10] K. Gotoh *et al.*, "Hydrogen concentration at a-Si:H/c-Si heterointerfaces - The impact of deposition temperature on passivation performance," *AIP Adv.*, vol. 9, no. 7, 2019, doi: 10.1063/1.5100086.

[11] S. Fernández, I. Torres, and J. J. Gandía, "Sputtered Ultrathin TiO2 as Electron Transport Layer in Silicon Heterojunction Solar Cell Technology," *Nanomaterials*, vol. 12, no. 14, p. 2441, Jul. 2022, doi: 10.3390/nano12142441.

[12] J. He, Z. Ling, P. Gao, and J. Ye, "TiO2 Films from the Low-Temperature Oxidation of Ti as Passivating-Contact Layers for Si Heterojunction Solar Cells," *Sol. RRL*, vol. 1, no. 12, Dec. 2017, doi: 10.1002/SOLR.201700154.

[13] W. Zhang, Y. Liu, D. Zhou, H. Wang, W. Liang, and F. Yang, "Fast diffusion of silver in TiO2 nanotube arrays," *Beilstein J. Nanotechnol.*, vol. 7, no. 1, pp. 1129–1140, 2016, doi:

10.3762/bjnano.7.105.

[14] Z. C. Holman *et al.*, "Current losses at the front of silicon heterojunction solar cells," *IEEE J. Photovoltaics*, vol. 2, no. 1, pp. 7–15, 2012, doi: 10.1109/JPHOTOV.2011.2174967.

[15] J. Cho *et al.*, "Passivating electron-selective contacts for silicon solar cells based on an a-Si:H/TiOx stack and a low work function metal," *Prog. Photovoltaics Res. Appl.*, vol. 26, no. 10, pp. 835–845, 2018, doi: 10.1002/pip.3023.

[16] S. Suckow, "2/3-Diode Fit." 2014, [Online]. Available: http://nanohub.org/resources/14300.

[17] K. R. McIntosh, "Lumps, Humps and Bumps: Three Detrimental Effects in the Current-Voltage Curve of Silicon Solar Cells," *PhD thesis Univ. New South Wales*, no. September, 2001, doi: 10.13140/RG.2.2.19197.26083.

CHAPTER VIII: SUMMARY, CONCLUSIONS, AND FUTURE WORK

During this thesis, indium tin oxide (ITO) and titanium oxide (TiO_x) thin films were deposited using the non-conventional technique of high-pressure sputtering (HPS), aiming at their application on novel concepts of solar cells. For the ITO samples, the substrate holder was maintained at room temperature, while the argon partial pressure and radio frequency (RF) power density were systematically varied to study their influence on film properties. In the case of TiO_x, a two-step deposition process was developed. Initially, a thin titanium layer was sputtered from a metallic Ti target at room temperature using a power density of 2.2 W/cm^2 and a working pressure of 0.5 mbar. Subsequently, without breaking vacuum, the metallic Ti layer was oxidized using a low-temperature oxygen plasma, characterized by a substrate temperature in the range of 150–200 °C, an O_2/Ar gas ratio of 2%, a power density of 2.2 W/cm^2, and a working pressure of 0.5 mbar.

For both materials, extensive characterization was performed, including structural, electrical, optical, and minority carrier lifetime measurements, to evaluate their suitability for integration into silicon-based solar cell architectures.

Additionally, during the predoctoral stay at EPFL, the deposition of hydrogenated ITO (ITO:H) using conventional RF sputtering was also investigated. Several power densities and hydrogen flow ratios were tested to optimize the film properties. As with the HPS films, structural, electrical, optical, and minority carrier lifetime characterizations were carried out to assess the compatibility of ITO:H with the TOPCon solar cell fabrication process developed at EPFL's PV-Lab.

The following sections summarize the main conclusions of this thesis and propose potential directions for future works.

8.1 Conclusions

8.1.1 ITO deposited by HPS:

- ITO thin films deposition was explored with HPS, varying argon working pressures (0.5 – 2.3 mbar) and power densities (1.5–2.5 W/cm²). Electrical resistivity was found to be strongly influenced by the argon pressure, with higher pressures (≥ 1.0 mbar) leading to low-resistivity films in the range of 10^{-4} Ωcm.

- Hall effect measurements showed that carrier concentration increased with pressure, mainly due to the formation of oxygen vacancies in amorphous films. The highest electron mobility (~45 cm²/V·s) was achieved at 1.5 mbar. GIXRD analysis revealed a transition from polycrystalline to amorphous structure as pressure increased, with the amorphous regime offering better electrical performance.

- Optical measurements confirmed high transmittance (70–90%) in the visible range and low absorptance (~1–2%), with negligible impact from resistivity variations. Tauc plot analysis revealed direct optical bandgaps of 3.6–3.8 eV with no clear Burstein-Moss shift, indicating minimal band filling effects despite high carrier concentrations.

- A heterojunction solar cell prototype incorporating HPS-ITO achieved an efficiency of ~10% with a short circuit current density of 29.9 mA/cm^2, open circuit voltage of and 577 mV, and a fill factor of 0.60.

8.1.2 ITO:H deposited by RF sputtering:

- ITO:H showed potential as a passivating layer in TOPCon structures, acting as both a passivation and conductive layer. The best power density for depositing ITO:H was determined to be 1.6 W/cm², that balance low absorptance, low resistivity, and high mobility. Adding hydrogen (H_2) during deposition increases carrier concentration and mobility, but excessive H_2 increases free carrier absorption in the infrared (IR) range. The best results were obtained with 0.15 % O_2 and 0.9 % H_2 with 13.31 cm^2/Vs mobility, 4.38x10^{20} cm^{-3} carrier concentration, 1x10^{-3} Ωcm resistivity, and 1.35 % normalized absorptance (300-1000 nm).

- For the glass/ITO:H/Ag samples, the N_2 annealing process reduced the specific contact resistivity to $1x10^{-2}$ Ωcm^2. In contrast, the annealing in air produces a rectifying behavior which makes it impossible to measure contact resistivity. This indicates that an unwanted chemical reaction with the atmosphere is happening, most likely due to atmospheric oxygen or H_2O.

- For the poly-Si(n)/ITO:H samples, the best results regarding passivation were obtained with 80 nm ITO:H deposited with 0.1% O_2, 0.9 % H_2. We obtained a τ_{eff} at 10^{15} cm^{-3} of 5.87 ms, $i\text{-}V_{oc}$ of 730 mV, and J_0 of 4.29 $fAcm^{-2}$ after 90 min air annealing process (400 ºC). The contact resistivity of poly-Si(n)/ITO:H/Ag (between 1 and 3.4 Ωcm^2) was higher than for ITO:H/Ag alone (~10^{-2} Ωcm^2), possibly due to sputtering damage to the poly-Si layer.

8.1.3 TiO_x deposited by HPS:

- A novel approach to fabricate TiO_x thin films is achieved using a two-step deposition process. Following the growth of a thin Ti film, a low-temperature (150 ºC – 200 ºC) plasma process is performed to oxidize the Ti film. With this approach, the oxidization of the underlayer Si substrate is mitigated as it was confirmed by FTIR measurements and TEM images.

- Even though the OES analysis of the Ar/O_2 plasma did not show relevant Ti extraction from the target, a small quantity of TiO_x was deposited during the oxidation step. The mean deposition rate was 0.90 and 1.37 nm/h for the 150 ºC and 200 ºC process respectively. Thus, the final TiO_x thickness varied according to the oxidation step duration. From a starting Ti film thickness of 5 nm, the TiO_x films exhibited thicknesses between 6 – 11 nm.

- GIXRD showed that the low-temperature oxidation process led to mostly amorphous films. Some crystalline planes related to TiO_x anatase phase were observed with extended oxidation durations (150 ºC for 4 h or 200 ºC ≥ 2 h).

- The O/Ti atomic ratio was around 1.9 for all the samples fabricated with oxidation duration ≥ 1 h, for either temperature (150 ºC or 200 ºC). This indicates the presence of oxidation-states in the TiO_x films. Additionally, from the O 1s signal, a reduction in the oxygen vacancy content is observed as the oxidation process is extended.

- The optical band gap, extracted from Tauc plots, increased with oxidation time from 2.67 eV to 2.92 eV at 150 °C and remained in the range of 2.83–2.90 eV at 200 °C, reflecting reduced sub-gap absorption due to improved oxidation.

- TiO_x alone did not provide effective surface passivation, resulting in minority carrier lifetimes (τ_{eff}) below 10 µs and implied open-circuit voltages ($i\text{-}V_{oc}$) around 540–550 mV. The inclusion of a thin RCA-grown SiO_x interlayer followed by forming gas annealing enhanced τ_{eff} up to ~40 µs and $i\text{-}V_{oc}$ up to ~581 mV. However, this interlayer significantly increased the contact resistivity (ρ_c), with values rising from ~18 mΩcm² (no interlayer) to ~10^4–10^5 mΩcm² due to the tunnelling barrier imposed by the SiO_x. The lowest ρc values (13 - 63 mΩcm²) were achieved with a minimum Ti thickness of ~5 nm and oxidation durations around 0.5 – 1 h, underlining the importance of controlling interfacial oxide layers.

8.1.4 HPS - TiO_x with a-Si:H(i) passivating layer:

- The inclusion of a dedicated passivation layer, a-Si:H(i) with a thickness of 10nm, improved the τ_{eff} and $i\text{-}V_{oc}$. The best results were obtained for the 200 ºC 2 h TiO_x with 1.6 ms and 700 mV after hotplate annealing (200 ºC 5 min). For the 150 ºC 2 h, a τ_{eff} of 1.0 ms and $i\text{-}V_{oc}$ of 695 mV was obtained. Regarding the ρ_c, samples oxidized at 150 °C exhibited lower specific contact resistivity (as low as 271 mΩcm²) compared to those oxidized at 200 °C (up to 62 kΩcm²), likely due to increased interfacial oxidation of the a-Si:H layer and/or excessive TiO_x thickness.

- Post-deposition annealing improved passivation properties. The samples with ~7 nm a-Si:H(i) and TiO_x shows an increase in the τ_{eff} with the 300 ºC 5 min annealing. The sample with only ~7 nm a-Si:H(i) shows a reduction in τ_{eff} with that annealing process. Although the reached τ_{eff} for the a-Si:H(i)/TiO_x is not the same as the original value (i.e., before TiO_x deposition), the increase of τ_{eff} with that annealing process indicates that the improvement in the a-Si:H(i)/TiO_x surpass the degradation of the a-Si:H(i).This behavior was more pronounced in the 150 °C oxidized samples.

- FLA was shown to be a viable low-thermal-budget method for enhancing the TiO_x/a-Si:H(i) interface. Moderate FLA conditions (e.g., 47 Jcm^{-2}, 3.2 ms) partially restored passivation without inducing severe damage, highlighting its potential as an alternative annealing technique for Si solar cells.

- Prototype heterojunction solar cells with rear-side side TiO_x/a-Si:H(i) contacts were fabricated. The best result was obtained for the samples with 200 ºC 1 h TiO_x which showed short circuit current density of 29.36 mA/cm^2, open circuit voltage of 487 mV, fill factor of 0.60 and an efficiency of 9.7 %.

8.2 Future work

This thesis has studied the feasibility of using HPS to deposit ITO and TiO_x for solar cell applications. The fabricated heterojunction solar cells using these materials did not exhibit the S-shaped IV curve which is typically for heterojunctions and indicates poor band alignment due to Fermi-level pinning at the interfaces. Nevertheless, the open-circuit voltage is still low in comparison to conventional heterojunctions with doped a-Si:H. This indicates that the passivation quality can be further optimized. One potential strategy for improving passivation involves introducing hydrogen during the HPS deposition of ITO and TiO_x, as post-deposition annealing may activate hydrogen-related passivation mechanisms.

Additionally, in the case of TiO_x, the effect of varying the pressure during the low-temperature oxidation steps were not fully explored. Understanding the influence of this parameter could be crucial for optimizing the stoichiometry and defect density of the resulting films.

Finally, the fabrication of a fully dopant-free heterojunction solar cell combining both ITO and TiO_x layers deposited via HPS would represent a significant step forward. This device would enable a comprehensive understanding of the compatibility, interfacial properties, and overall performance of HPS-deposited layers in a complete solar cell architecture.

Regarding the ITO:H films deposited by standard RF sputtering, the passivation of defects in the c-Si(n)/SiO_x/poly-Si(n) structure has been successfully tested for ITO:H thicknesses of 80 nm. However, annealing processes in air negatively affect the electrical properties of the films. For that reason, similar annealing experiments in an N_2 atmosphere would be interesting to maintain the electrical properties while increasing the structure's lifetime. On the other hand, the ITO:H samples, as deposited, show relatively low mobility values. Therefore, the characterization of ITO:H deposited without including any oxygen could increase the mobility of the films, although the absorptance could be affected. In addition, increasing the substrate holder temperature during the deposition process could also be interesting in increasing mobility. Finally, samples with a thickness of ~20 nm should be investigated since this is the typically thickness used for PK/Si tandems.

LIST OF PUBLICATIONS

9.1 Journal papers

9.1.1 Related to this thesis

- **F. Pérez-Zenteno**, E. García-Hemme, I. Torres, R. Barrio, S. Duarte, R. Benítez-Fernández, D. Caudevilla, R. García-Hernansanz, J. Olea, D. Pastor, A. del Prado, and E. San Andrés, "*High-pressure sputtering deposition and in situ plasma oxidation of TiOx thin films as electron selective contact for photovoltaic applications*", Materials Science in Semiconductor Processing 186, 109038 (2025). https://doi.org/10.1016/j.mssp.2024.109038 Journal's impact factor: 4.2 (Q1)

- **F. Pérez-Zenteno**, E. San Andrés, E. García-Hemme, D. Caudevilla, S. Duarte, R. García Hernansanz, S. Algaidy, J. Olea, D. Pastor, A. del Prado. "*Fabrication of TiOx, by High Pressure Sputtering for Selective Contact in Photovoltaic Cells*," 2023 14th Spanish Conference on Electron Devices (CDE), Valencia, Spain, 2023, pp. 1-4, doi: 10.1109/CDE58627.2023.10339432.

- **F. Pérez-Zenteno**, E. San Andrés, E. García-Hemme, I. Torres, R. Barrio, D. Caudevilla, S. Duarte, R. García Hernansanz, J. Olea, D. Pastor, A. del Prado. "*High Pressure Sputtering of Mo Targets in Mixed Ar/O2/H2 Atmospheres for Hole Selective Contacts in Photovoltaic Cells*," 2023 14th Spanish Conference on Electron Devices (CDE), Valencia, Spain, 2023, pp. 1-4, doi: 10.1109/CDE58627.2023.10339461.

- D. Caudevilla, E. Garcia-Hemme, E. San Andrés, **F. Perez-Zenteno**, I. torres, R. Barrio, R. Garcia-Hernansanz, S. Algaidy, J.Olea, D. Pastor, A. del Prado. "*Indium tin oxide obtained by high pressure sputtering for emerging selective contacts in photovoltaic cells*". Materials Science in semiconductor processing. 137 (2021) 106189. https://doi.org/10.1016/j.mssp.2021.106189 Journal's impact factor: 4.2 (Q1)

9.1.2 Others

1. S. Algaidy, R. Benítez-Fernández, S. Duarte-Cano, **F. Pérez-Zenteno**, D. Caudevilla, E. Garcia-Hemme, J. Olea, E. San Andrés, R. García-Hernansanz, J. Siegel, J. Gonzalo, D. Pastor and A. del Prado. "*Characterization of Cr implanted GaAs processed with ArF and Nd-YAG laser melting*". Semiconductor Science and Technology 40 (5), 055008 pp 1-13 (2025). DOI 10.1088/1361-6641/adce25.

2. S. Duarte-Cano, **F. Pérez-Zenteno**, D. Caudevilla, J. Olea, E. San Andrés, A. del Prado, R. Benítez-Fernández, E. García-Hemme, M. Rezaei, J. A. Clemente, S. Algaidy, I. Torres, R. Barrio, E. Ros, J. Puigdollers, P. Ortega, C. Voz, R. García-Hernansanz, "*Proton Irradiation Effects on Silicon Heterojunction Solar Cells with MoOx Selective Contacts*", Material Science in Semiconductor processing 190, 109312 (2025). https://doi.org/10.1016/j.mssp.2025.109312

3. J. Olea, J. Gonzalo, J. Siegel, A.F. Braña, G. Godoy-Pérez, R. Benítez-Fernández, D. Caudevilla, S. Algaidy, **F. Pérez-Zenteno**, S. Duarte-Cano, A. del Prado, E. García-Hemme, R. García-Hernansanz, D. Pastor, E. San-Andrés, I. Mártil "*Optoelectronic properties of GaP:Ti photovoltaic devices*" Materials Today Sustainability28(2024) 101008. https://doi.org/10.1016/J.MTSUST.2024.101008

4. D. Caudevilla, **F. Pérez-Zenteno**, S. Duarte-Cano, S. Algaidy, R. Benítez-Fernández, G. Godoy-Pérez, J. Olea, E. San Andrés, R. García-Hernansanz, A. del Prado, I. Mártil, D. Pastor, and E. García-Hemme, "*Native oxide layer role during cryogenic-temperature ion implantations in germanium*", Physica Status Solidi A: Applications and Materials Science 2400124, https://doi.org/10.1002/pssa.202400124

5. S. Algaidy, D. Caudevilla, G. Godoy-Pérez, R. Benítez-Fernández, **F. Pérez-Zenteno**, S. Duarte-Cano, R. García-Hernansanz, E. San Andrés, E. García-Hemme, J. Olea, J. Siegel, J. Gonzalo, D. Pastor, and Á. del Prado, "*Optical, Electrical, and Optoelectronic Characterization of Ti-Supersaturated Gallium Arsenide*", Phys. Status Solidi A: Applications and Materials Science 2400123, (2024) https://doi.org/10.1002/pssa.202400123

6. S. Algaidy, D. Caudevilla, **F. Perez-Zenteno**, R. García-Hernansanz, E. García-Hemme, J. Olea, E. San Andres, S. Duarte-Cano, J. Siegel, J. Gonzalo, D. Pastor and A. del Prado, "*High-quality single-crystalline epitaxial regrowth on pulsed laser melting of Ti implanted GaAs*", Materials Science in Semiconductor Processing 153, 107191 (2023). https://doi.org/10.1016/j.mssp.2022.107191

7. J. Olea, G. González-Díaz, D. Pastor, E. García-Hemme, D. Caudevilla, S. Algaidy, **F. Pérez-Zenteno**, S. Duarte-Cano, R. García-Hernansanz, A. del Prado, E. San-Andrés, I. Mártil, Yao-Jen Lee, Tzu-Chieh Hong and Tien-Sheng Chao, "*Ti supersaturated Si by microwave annealing processes*", Semiconductor Science and Technology 38, 024004 (2023).

8. R. García-Hernansanz, S. Duarte-Cano, **F. Pérez-Zenteno**, D. Caudevilla, S. Algaidy, E. García-Hemme, J. Olea, D. Pastor, A. del Prado, E. San Andrés, I. Mártil, E. Ros, J. Puigdollers, P. Ortega and C. Voz, "*Transport mechanisms in hyperdoped silicon solar cells*", Semiconductor Science and Technology 38, 124001 (2023). https://doi.org/10.1088/1361-6641/ac9f63

9. J. Olea, G. González-Díaz, D. Pastor, E. García-Hemme, D. Caudevilla, S. Algaidy, **F. Pérez-Zenteno**, S. Duarte-Cano, R. García-Hernansanz, A. del Prado, E. San Andrés and I. Mártil, "*Electronic transport properties of Ti supersaturated Si and processed by rapid thermal annealing or pulsed-laser melting*", Semiconductor Science and Technology (2023).

10. D. Caudevilla, S. Algaidy, **F. Pérez-Zenteno**, S. Duarte-Cano, R. García-Hernansanz, J. Olea, E. San-Andrés, A. del Prado, R. Barrio, I. Torres, E. García-Hemme and D. Pastor, "*Electrical transport properties in Ge hyperdoped with Te*", Semiconductor Science and Technology 37, 124001 (2022). https://doi.org/10.1088/1361-6641/ac9a67

11. E. García-Hemme, D. Caudevilla, S. Algaidy, **F. Pérez-Zenteno,** R. García-Hernansanz, J. Olea, D. Pastor, A. del Prado, E. San Andrés, I. Mártil, G. González-Díaz. "*On the Optoelectronic Mechanisms Ruling Ti-hyperdoped Si Photodiodes*". Advanced Electronic Materials (2021) 2100788. Parámetro de Impacto: 7.295 (Q1). https://doi.org/10.1002/aelm.202100788

12. Caudevilla; Berenzén; Algaidy; **Pérez Zenteno**; Olea; San Andrés Serrano 1; García Hernanzanz; Pastor; del Prado; García Hemme. *Overcoming the solid solubility limit of Te in Ge by ion implantation and pulsed laser melting recrystallization*. 2021 13th Spanish Conference on Electron Devices. IEEE, 06/2021. DOI 10.1109/CDE52135.2021.9455720,

13. San Andrés Serrano; García Hernansanz; Moreno; García Hemme; Barrio; Torres; Caudevilla; Pastor; Olea; del Prado; Algaidy; **Pérez Zenteno**. *High Pressure Sputtering of materials for selective contacts in emerging photovoltaic cells*. 2021 13th Spanish Conference on Electron Devices. IEEE, 06/2021.DOI 10.1109/cde52135.2021.9455754

14. D. Caudevilla, E. Garcia-Hemme, E. San Andrés, **F. Perez-Zenteno**, I. torres, R. Barrio, R. Garcia-Hernansanz, S. Algaidy, J.Olea, D. Pastor, A. del Prado. "*Indium tin oxide obtained by*

high pressure sputtering for emerging selective contacts in photovoltaic cells". Materials Science in semiconductor processing. 137 (2021) 106189. https://doi.org/10.1016/j.mssp.2021.106189 Parámetro de Impacto: 3.927 (Q1).

9.2 Contributions in conferences

1. **F. Pérez-Zenteno,** R. Sakakibara, T. Schaller, J. Hurni, F. J. Haug, E. García-Hemme, E. San Andrés. "*Passivation of TOPCon Bottom Cell for Perovskite/Si Tandem Devices via RF-Sputtered ITO:H2*" EUPVSEC 2025. September 22th-26th, 2025, Bilbao, Spain. Type of presentation: poster.

2. J. Olea, R. Benítez-Fernández, **F Pérez-Zenteno**, S. Algaidy, S. Duarte-Cano, D. Pastor, E. García-Hemme, R. García-Hernansanz, A. Del Prado, E. San Andrés, I. Mártil, T. Hong, Y. Lee. "*Characterization of Ti supersaturated Si fabricated by microwave annealing*", IEEE 15th Spanish Conference on Electron Devices, Malaga (Spain), 2025. Type of presentation: Poster

3. **F. Pérez-Zenteno,** D. Caudevilla, R. Benítez-Fernández, S. Duarte-Cano, S. Algaidy, R. García-Hernansanz, J. Olea, D. Pastor, A. Del Prado, E. García-Hemme, E. San Andrés. "*Optimizing specific contact resistivity of TiOx/Si: A comparative study of different circular metal contacts*" IEEE 15th Spanish Conference on Electron Devices, Malaga (Spain), 2025. Type of presentation: Poster

4. S. Duarte-Cano, **F. Pérez-Zenteno**, E. San Andrés, S. Algaidy, R. Benítez-Fernández, D. Pastor, E. García-Hemme, R. García-Hernansanz, "*Radiation Effects on Vanadium Oxide Solar Cells for Energy Applications in Low Earth Orbit*" IEEE 15th Spanish Conference on Electron Devices, Malaga (Spain), 2025. Type of presentation: Poster

5. R. Benítez-Fernández, A. Rahman, G. Godoy-Pérez, D. Caudevilla, **F. Pérez-Zenteno**, S. Duarte-Cano, S. Algaidy, R. García-Hernansanz, J. Olea, D. Pastor, A. Del Prado, E. San Andrés, M. J. Sher, E. García-Hemme. "*Effects of soft annealing on the optoelectronic performance of Ti hyperdoped Si photodiodes*". EMRS 2024 Fall Meeting. September 16th-18th, 2024, Warsaw, Poland. Type of presentation: Oral.

6. S. Algaidy, **F. Perez-Zenteno**, R. Benítez Fernández, S. Duarte Cano, D. Caudevilla Gutierrez, R. Garcia Hernansanz, E. Garcia Hemme, J. Olea Ariza, E.San Andres Serrano, J. Siegel, J. Gonzalo, D. Pastor, A. Del Prado. "*A comparative study of GaAs hyperdoped with*

Chromium processed by ArF+ excimer and Nd-YAG pulsed laser melting". EMRS 2024 Fall Meeting. September 16th-18th, 2024, Warsaw, Poland. Type of presentation: Oral.

7. **F. Pérez-Zenteno**, S. Duarte, R. Benítez-Fernandez, G. Godoy-Pérez, I. Torres , R. Barrio, D. Caudevilla, S. Algaidy, R. García-Hernansanz, J. Olea, D. Pastor, Á. del Prado, Lars Rebohle, E. García-Hemme, E. San Andrés. "*Characterization of TiO_x as electron selective contact using low-temperature oxidation process via high-pressure sputtering*". EUPVSEC 2024. September 23th-27th, 2024, Vienna, Austria. Type of presentation: poster.

8. Sebastian Duarte-Cano, Laura Torrecilla, Daniel Caudevilla, **Francisco Perez-Zenteno**, Rafael Benitez-Fernandez, Guillermo Godoy-Perez, Rodrigo Garcia-Hernansanz, Eric Garcia-Hemme, Javier Olea, David Pastor, Alvaro Del Prado, Enrique San Andres, Sari Algaidy. "*Aluminum Zinc Oxide Layers by High-Pressure Sputtering for TOPCon Solar Cells*" EUPVSEC 2024. September 23th-27th, 2024, Vienna, Austria. Type of presentation: poster.

9. **F. Pérez-Zenteno**, E. San Andrés, E. García Hemme, R. Benítez, G. Godoy, I. Torres, R. Barrio, D. Caudevilla, S. Duarte Cano, R. García Hernansanz, J. Olea, D. Pastor, A. del Prado "*Deposition of alternative materials for selective contacts of novel heterojunction solar cells by High-Pressure Sputtering*". EUPVSEC 2023. Septembre 18th-22nd, 2023. Lisboa, Portugal. Type of presentation: poster

10. **F. Pérez-Zenteno**, R. Benítez, G. Godoy, I. Torres, R. Barrio, D. Caudevilla, S. Duarte, R. García-Hernansanz, J. Olea, D. Pastor, Á. del Prado, E. San Andrés and E. García-Hemme, "*Effect of dopant activation by rapid thermal annealing or pulsed laser annealing in interdigitated back-contacted solar cells*", 40th European Photovoltaic Solar Energy Conference and Exhibition (EU PVSEC), Lisbon (Portugal), 2023. Type of presentation: Poster.

11. D. Caudevilla, S. Prucnal, **F. Pérez-Zenteno**, S. Algaidy, S. Duarte-Cano, J. Olea, R. García-Hernansanz, A. del Prado, E. San Andrés, S. Zhou, D. Pastor, E. García-Hemme and Y. Berencén, "*On-chip photodetection at telecom wavelengths: a silicon-on-insulator hyperdoping approach with tellurium*", E-MRS Fall Meeting, Warsaw (Poland), 2023. Type of presentation: Oral.

12. D. Araña, A. Rahman, D. Caudevilla, **F. Pérez-Zenteno**, S. Algaidy, S. Duarte-Cano, R. García-Hernansanz, J. Olea, D. Pastor, A. Del Prado, E. San Andrés, E. García-Hemme, M. Sher. "*Lifetime and optoelectronic characteristics of Ti hyperdoped Si photodiodes*". European Materials Research Society (EMRS) 2023 Fall Meeting. Warsaw, Poland. Type of presentation: Oral.

13. D. Caudevilla, S. Algaidy, **F. Pérez-Zenteno**, S. Duarte-Cano, R. Benítez-Fernández, G. Godoy-Pérez, J. Olea, R. García-Hernansanz, A. del Prado, I. Mártil, E. San Andrés, D. Pastor, E. García-Hemme. "*Native Ge oxide layer role when implanting at cryogenic temperatures for hyperdoped materials*". European Materials Research Society (EMRS) 2023 Fall Meeting. Warsaw, Poland. Type of presentation: poster.

14. S. Algaidy, D. Caudevilla, **F. Perez-Zenteno**, R. García-Hernansanz, E. García-Hemme, J. Olea, E. San Andres, S. Duarte-Cano, J. Siegel, J. Gonzalo, D. Pastor, A. del Prado, R. Benitez-Fernández, G. Godoy-Pérez. "*Sub-bandgap Absorption in GaAs hyperdoped with (Ti, Cr)*". European Materials Research Society (EMRS) 2023 Fall Meeting. Warsaw, Poland. Type of presentation: Oral.

15. **F. Pérez-Zenteno**, D. Caudevilla, S. Duarte, S. Algaidy, E. San Andrés, E. García-Hemme, R. García-Hernansanz, J. Olea, D. Pastor and A. del Prado, "Fabrication of TiOx by High Pressure Sputtering for selective contacts in photovoltaic cells", IEEE 14th Spanish Conference on Electron Devices, Valencia (Spain), 2023. Type of presentation: Poster.

16. **F. Pérez-Zenteno**, E. San Andrés, E. García Hemme, I. Torres, R. Barrio, D. Caudevilla, S. Duarte Cano, R. García Hernansanz, J. Olea, D. Pastor, A. del Prado "*High-pressure sputtering of Mo targets in mixed Ar/O2/H2 atmospheres for hole selective contacts in photovoltaic cells*" 14th Conference on Electronic devices (CDE). Valencia, June 6th to 8th, 2023. Type: oral presentation.

17. S. Duarte-Cano, M. Rezaei, **F. Pérez-Zenteno**, D. Caudevilla, S. Algaidy, J. Olea, E. San Andrés, A. del Prado, D. Pastor, E. García-Hemme, F. J. Franco, J. A. Clemente. I. Torres, R. Barrio, E. Ros, J. Puigdollers, P. Ortega, C. Voz, C. Armenta-Deu and R. García-Hernansanz, "*Impact of Proton Irradiation on TMO-Based Solar Cells*", IEEE 14th Spanish Conference on Electron Devices, Valencia (Spain), 2023. Type of presentation: Oral.

18. J. Olea, G. Godoy, D. Caudevilla, S. Algaidy, **F Pérez-Zenteno**, S Duarte-Cano, A. del Prado, E. García-Hemme, R. García-Hernansanz, D. Pastor, E. San-Andrés, I. Mártil, G. González-Díaz, J. Gonzalo, J. Siegel and Alejandro F. Braña, "*Optoelectronic properties of GaP:Ti photovoltaic devices*", IEEE 14th Spanish Conference on Electron Devices, Valencia (Spain), 2023. Type of presentation: Poster.

19. D. Caudevilla, **F. Pérez-Zenteno**, S. Duarte, S. Algaidy, J. Olea, E. San Andrés, R. García-Hernansanz, A. del Prado, I. Mártil, D. Pastor, E. García-Hemme. "Stopping layer and oxygen incorporation during cryogenic-temperature implantations in germanium". IEEE 14th Spanish Conference on Electron Devices (CDE) Valencia, España (2023). Type of presentation: poster.

20. S. Algaidy, D. Caudevilla, S. Duarte-Cano, **F. Perez-Zenteno**, J. Olea, E. Garcia-Hemme, A. del Prado, D. Pastor, R. Garcia-Hernansanz, E. San- Andres, J. Siegel, J. Gonzalo. "*Sub-bandgap photoresponse induced by pulsed laser melting in GaAs*". 14th Conference on Electronic devices (CDE). Valencia, Spain (2023). Type of presentation: Poster.

21. D. Caudevilla, E. García-Hemme, **F. Pérez-Zenteno**, S. Algaidy, J. Olea, E. San Andrés, R. García-Hernansanz, A. Del Prado, I. Mártil, Y. Berencén, D. Pastor. "*Hyperdoping germanium by Ion Implantation and Pulsed Laser Recrystallization*". European Materials Research Society (EMRS) 2022 Spring Meeting. Strasburg, France (Virtual). Type of presentation: Oral.

22. R. García-Hernansanz, S. Duarte-Cano, **F. Pérez-Zenteno**, D. Caudevilla, S. Algaidy, E. García-Hemme, J. Olea, D. Pastor, A. del Prado, E. San-Andrés, I. Mártil, E. Ros, J. Puigdollers, P. Ortega and C. Voz, "*Transport mechanisms in hyperdoped silicon solar cells*", E-MRS Spring Meeting, virtual conference, 2022. Type of presentation: Póster.

23. J. Olea, G. González-Díaz, D. Pastor, E. García-Hemme, D. Caudevilla, S. Algaidy**, F. Pérez-Zenteno**, S. Duarte-Cano, R. García-Hernansanz, A. del Prado, E. San Andrés and I. Mártil, "*Electronic transport properties of Si supersaturated with Ti and processed by rapid thermal annealing or pulsed-laser melting*", E-MRS Spring Meeting, virtual conference, 2022. Type of presentation: Póster.

24. J. Olea, G. González-Díaz, D. Pastor, E. García-Hemme, D. Caudevilla, S. Algaidy, **F. Pérez-Zenteno**, S. Duarte-Cano, R. García-Hernansanz, A. del Prado, E. San-Andrés, I. Mártil, Y.-J. Lee, T.-C. Hong and T.-S. Chao, "*Ti supersaturated Si by microwave annealing processes*", E-MRS Spring Meeting, virtual conference, 2022. Type of presentation: Póster.

25. D. Montero, A. del Prado, J. Olea, G. González-Díaz, D. Pastor, E. García-Hemme, D. Caudevilla, S. Algaidy**, F. Pérez-Zenteno**, S. Duarte-Cano, R. García-Hernansanz, E. San Andrés and I. Mártil, "*Inferring the recrystallization regimes of silicon supersatured with titanium after Pulsed Laser Melting through Transmittance-Reflectance measurements*", E-MRS Spring Meeting, virtual conference, 2022. Type of presentation: Oral.

26. E. García-Hemme, D. Caudevilla, S. Algaidy, **F. Zenteno**, R. García-Hernansanz, J. Olea, D. Pastor, A. del Prado, E. San-Andrés, I. Mártil and G. González-Díaz, "*Unveiling the optoelectronic mechanisms ruling Ti hyperdoped Si photodiodes*", IEEE 13th Spanish Conference on Electron Devices, Sevilla (Spain), 2021. Type of presentation: Poster.

27. D. Caudevilla, Y. Berencén, S. Algaidy, **F. Zenteno**, J. Olea, E. San Andrés, R. García-Hernansanz, A. del Prado, D. Pastor and E. García-Hemme, "*Overcoming the solid solubility limit of Te in Ge by ion implantation and pulsed laser melting recrystallization*", IEEE 13th Spanish Conference on Electron Devices, Sevilla (Spain), 2021. Type of presentation: Oral